

Copyright
by
Jianyong Mo
2015

The Dissertation Committee for Jianyong Mo
certifies that this is the approved version of the following dissertation:

Short timescale Brownian motion and applications

Committee:

Mark G. Raizen, Supervisor

Mike C. Downer

Gregory A. Fiete

Roger D. Bengtson

Pawan Kumar

Short timescale Brownian motion and applications

by

Jianyong Mo, B.S.

DISSERTATION

Presented to the Faculty of the Graduate School of

The University of Texas at Austin

in Partial Fulfillment

of the Requirements

for the Degree of

DOCTOR OF PHILOSOPHY

THE UNIVERSITY OF TEXAS AT AUSTIN

August 2015

Dedicated to my parents, Falin Mo and Yuee Xu,
my wife, Juan,
my daughter, Emily,
my parents-in-law, Guoping Li and Lianzhen Wei,
my brother, sister-in-law and nephew, Jianbin, Jinlian and Zifan
and my brother-in-law, Xianlong Li
for their endless love and support.

Acknowledgments

First of all, I would like to thank my supervisor Prof. Mark Raizen for giving me the opportunity to work in such an outstanding group. Mark is a great advisor with an open mind to anything, which is the reason why the experiments we are doing in the lab are so diverse. I am very impressed by his confidence, creativity and attitude doing research.

I joined the lab in August 2009 to work on the lithium Fock State experiment with Gabriel Price, Kirsten Viering and David Medellin. Gabe is a great person to work with. He is very rigorous on research but would be very humorous in the daily life. Kirsten Viering is a well organized experimentalist and works efficiently with detailed plans. David is the person I worked with for the longest time in my Ph.D. career. I always appreciate his kindness, which made the research more enjoyable. He is very good at programming and theoretical understanding, which was very helpful to our work. Felix Schmidt joined the lithium experiment in the fall of 2012 for a half year. Felix is a self-motivated and talented young scientist. It was a great pleasure to have him.

In June 2013, I started to work on the Brownian motion experiment with Akarsh Simha and William Watson. I greatly appreciate Simon Kheifets and Akarsh for leaving me a working experimental setup. Their wonderful

experimental work gave me a high starting point and sped up this work significantly. Simon is a very talented scientist and has a variety of interests. Akarsh is a great guy to work with, I appreciate his patience and kindness. He gave me tremendous help both on experiments and theories. William is a very helpful undergraduate who works very hard. In the beginning of 2014, Will Plusnick and Jimmy Kennington started to work with me. David Riegler, a Würzburg student, joined us in the fall of 2014. He works hard on an optical microrheology project.

I would like to thank other students in the lab who have provided much help to me. They are Tongcang Li, Tom Mazur, Travis Bannerman, Adam Libson, Rob Clark, Isaac Chavez, Melissa Jenkins, Rodrigo Castillo-Garza, Bruce Klappauf, Karl Burkhardt, Igal Bucay, Georgios Stratis, Jamie Gardner, Kevin Melin, Erik Anciaux, Alina Blinova, Yu Lu, Matt Reay, Daniel Raimi-Zlatic, Tharon Morrison and David Dunskey. I especially appreciate the great help provided by Tongcang and Tom.

I would like to thank Jack Clifford, Allan Schroeder, George Sandefur and all other members of the machine shop, and Ed Baez and Lanny Sandefur in the cryo lab for their excellent work. I would like to thank Olga Vera, Rachael Salge, Marybeth Casias, and other members of CNLD for their administrative help. I especially appreciate the help from Olga through my whole Ph.D. career on all kinds of administrative things.

I also appreciate the friendships from Yu Chen, Xiang Hu, Liang Zhang, Liangfei Qiu, Xiaohui Gao, Zhenyan Li, Yuxuan Chen, Yang Gao, Qinjian Jin,

Yide Lin, Yihan Huang, Meng Li and many others.

I would like to give my unique thanks to my wife, my daughter, and my parents for their endless love. Without their support I could not achieve the level where I am right now.

Jianyong Mo

July, 2015

Austin, TX

Short timescale Brownian motion and applications

Publication No. _____

Jianyong Mo, Ph.D.

The University of Texas at Austin, 2015

Supervisor: Mark G. Raizen

This dissertation details our experiments and numerical calculations on short timescale Brownian motion and its applications. We test the Maxwell-Boltzmann distribution using micrometer-sized spheres in liquids at room temperature. In addition to that, we use Brownian particles as probes to study boundary effects imposed by a solid wall, viscoelasticities of complex fluids, slippage at solid-fluid interfaces, and fluid compressibility.

The experiments presented in this dissertation relies on the use of tightly focused laser beams to both contain and probe the Brownian motion of microspheres in fluids. A dielectric sphere near the focus of a laser beam scatters some of the incident photons in a direction which depends on the particle's position. Changes in the particle's position are encoded in the spatial distribution of the scattered beam, which can be measured with high sensitivity. It is important to emphasize that the Brownian motion in this dissertation is exclusive for translational Brownian motion.

We have reported shot-noise limited measurements of the instantaneous velocity distribution of a Brownian particle. Our system consists of a single micron-sized glass sphere held in an optical tweezer in a liquid in equilibrium at room temperature. We provide a direct verification of a modified Maxwell-Boltzmann velocity distribution and a modified energy equipartition theorem that account for the kinetic energy of the liquid displaced by the particle. Our measurements confirm the distribution over a dynamic range of more than six orders of magnitude in count-rate and five standard deviations in velocity.

We have reported high-bandwidth, comprehensive measurements of Brownian motion of an optically trapped micrometer-sized silica sphere in water near an approximately flat wall. At short distances, we observe anisotropic Brownian motion with respect to the wall. We find that surface confinement not only occurs in the long time scale diffusive regime but also in the short time scale ballistic regime, and the velocity autocorrelation function of the Brownian particle decays faster than that of particle in a bulk fluid. Furthermore, at low frequencies the thermal force loses its color due to the reflected flow from the no-slip boundary. The power spectrum of the thermal force on the particle near a no-slip boundary becomes flat at low frequencies.

We have numerically studied Brownian motion of a microsphere in complex fluids. We show that Brownian motion of immersed particles can be dramatically affected by the viscoelastic properties of the host fluids. Thus, this fact can be used to extract the properties of complex fluids via observing the motion of the embedded particles. This will be followed by two experimental

demonstrations of obtaining the viscosities of water and acetone.

We also study Brownian motion with partial and full slip boundary conditions both on the surface of a sphere and a boundary. We show that the motion of particles can be significantly altered by the boundary condition of fluid flow on a solid surface. We suggest that this fact can be used to measure the slippage, namely the slip length.

Lastly, I will discuss the efforts to study fluid compressibility and non-equilibrium physics using a short duration pulsed laser. We expect to increase the position sensitivity from current 10^{-15} m/ $\sqrt{\text{Hz}}$ to about 10^{-19} m/ $\sqrt{\text{Hz}}$ by using a pulsed laser with a peak power of 10^8 W. With such a high position sensitivity, we expect to be able to resolve the compressibility of fluids. We will also discuss a few future experiments studying non-equilibrium physics.

Table of Contents

Acknowledgments	v
Abstract	viii
List of Tables	xvi
List of Figures	xvii
Chapter 1. Introduction	1
1.1 History of Brownian motion	1
1.2 Brief description of Brownian motion	3
1.3 Testing the Maxwell-Boltzmann distribution	6
1.4 Brownian motion near a boundary	8
1.5 Brownian motion in complex fluids	9
1.6 Brownian motion with slip boundary conditions	10
1.7 Brownian motion in compressible fluids and non-equilibrium physics study	11
1.8 Contents of this dissertation	12
Chapter 2. Optical trapping and balanced beam detection	13
2.1 Optical trapping	14
2.1.1 Ray optics approximation	17
2.1.2 Rayleigh approximation	20
2.1.3 Generalized Lorentz-Mie theory	23
2.1.4 Predictions of trapping with experimental conditions	27
2.2 Balanced beam detection system	30
2.2.1 Balanced beam detection with quadrant detectors	33
2.2.2 Balanced beam detection: an improved version	34

Chapter 3. Theory for Brownian motion of a free sphere in a Newtonian fluid	39
3.1 Linear response theory: Kubo-Green formula	41
3.2 The Wiener-Khinchin theorem	44
3.3 Brownian motion in a Newtonian incompressible fluid	46
3.3.1 A free particle in a Newtonian incompressible fluid	46
3.3.1.1 A free particle in air	47
3.3.1.2 A free particle in liquid	49
3.3.2 An optically trapped microsphere in a Newtonian incompressible fluid	54
3.3.2.1 An optically trapped particle in air	55
3.3.2.2 An optically trapped particle in liquid	57
3.4 Implications for position and velocity measurement	60
3.4.1 Position measurement	61
3.4.2 Instantaneous velocity measurement	64
3.4.3 Shot noise estimation	67
Chapter 4. Testing the Maxwell-Boltzmann distribution using Brownian particles	68
4.1 Experimental setup	71
4.1.1 Optical setup	72
4.1.2 Microspheres and fluids	77
4.1.3 Flow cell	80
4.1.4 Imaging	83
4.1.5 Balanced beam detection system	85
4.1.6 Optical alignment procedure	88
4.1.7 Cut mirror and detector alignment	91
4.1.8 LabVIEW control and data acquisition system	92
4.2 Methods for data analysis	93
4.3 Experimental results and discussion	95
4.3.1 Mean square displacement	95
4.3.2 Position power spectral density	97
4.3.3 Velocity autocorrelation function	99

4.3.4	Instantaneous velocity measurements and Maxwell-Boltzmann distribution testing	100
4.3.5	Measurements of the thermal force	108
Chapter 5. Theory for Brownian motion with boundary effects		112
5.1	Anisotropic and hindered diffusion of a microsphere near a wall	114
5.1.1	Diffusion of a microsphere near a flat wall	115
5.1.2	Diffusion of a microsphere near a cylindrical wall	116
5.2	Boundary effects on unsteady Brownian motion	118
5.2.1	Linear hydrodynamics	119
5.2.2	Reaction field tensor	122
5.2.3	Effective mass with boundary effects	125
5.2.4	The flattening in the thermal force power spectral density	127
5.2.5	Boundary effects on Brownian motion of a trapped particle	130
5.3	Numerical predictions on boundary effects with experimental conditions	131
5.3.1	Position power spectral density	131
5.3.2	Velocity power spectral density	132
5.3.3	Mean square displacement	133
5.3.4	Velocity autocorrelation function	134
5.3.5	Thermal force power spectral density	135
5.4	Fluid dynamics simulation on boundary effects	136
Chapter 6. Observation of broadband boundary effects on Brownian motion		140
6.1	Experimental setup	142
6.1.1	Optical setup	143
6.1.2	Flow cell with fibers	144
6.1.3	Microspheres and fluids	146
6.1.4	Relative position control with a piezo-stage	146
6.1.5	Imaging	147
6.1.6	Data acquisition	148
6.2	Experimental results and discussion	148
6.2.1	Mean square displacement	149

6.2.2	Velocity autocorrelation function	151
6.2.3	Position power spectral density	153
6.2.4	Velocity power spectral density	154
6.2.5	Thermal power spectral density	156
6.2.6	The absolute sphere-wall separation calibration	158
6.2.6.1	The VACF calibration method	159
6.2.6.2	The diffusion calibration method	160
6.2.7	Boundary effects in the parallel direction	164
6.3	Summary	166
Chapter 7. Brownian motion in viscoelastic fluids		167
7.1	Simple complex fluid models	170
7.1.1	A Maxwell fluid	171
7.1.2	A Kelvin-Voigt fluid	172
7.1.3	A Jeffreys fluid	172
7.2	Brownian motion in a complex fluid	173
7.2.1	Position power spectral density	175
7.2.2	Velocity power spectral density	175
7.2.3	Mean square displacement	175
7.2.4	Velocity autocorrelation function	176
7.2.5	Thermal force power spectral density	176
7.3	Methods of estimating viscoelasticity of a fluid by measuring Brownian motion of an immersed particle	178
7.3.1	Mason-Weitz method (without hydrodynamic effects)	179
7.3.2	Felderhof method (with hydrodynamic effects)	180
7.3.3	Numerical testing of these two methods	182
7.4	Measurements of viscoelastic properties of fluids	183
Chapter 8. Brownian motion with slip boundary condition		185
8.1	Brownian motion of an unbounded microsphere with partial-slip boundary condition	188
8.1.1	Velocity autocorrelation function	189
8.1.2	Mean square displacement	191

8.1.3	Position power spectral density	191
8.1.4	Velocity power spectral density	192
8.1.5	Thermal force power spectral density	193
8.2	Brownian motion of a no-slip microsphere near a perfect-slip wall	195
8.2.1	Position power spectral density	196
8.2.2	Velocity power spectral density	197
8.2.3	Mean square displacement	198
8.2.4	Velocity autocorrelation function	200
8.2.5	Thermal force power spectral density	200
Chapter 9.	Brownian motion in compressible fluids and non-equilibrium physics study	205
9.1	Brownian motion in compressible fluids	206
9.1.1	Theory for Brownian motion of a microsphere in a compressible fluid	207
9.1.2	Numerical predictions of Brownian motion in compressible fluids	209
9.1.3	Experiments toward resolving compressibility of fluids	215
9.2	Non-equilibrium physics study	221
	Appendix	224
	Appendix 1. Kubo-Green formula derivation	225
	Bibliography	227
	Vita	255

List of Tables

4.1	The summary of the results for the three systems	107
-----	--	-----

List of Figures

2.1	Qualitative view of optical trapping of a dielectric sphere. . . .	18
2.2	Optical forces exerted by a 400 mW, 1064 nm laser beam on a 3 μm diameter silica microsphere in water with different NAs. . . .	24
2.3	Optical forces exerted by a 400 mW, 1064 nm laser beam on different sized silica microspheres in water with NA = 1.0. . . .	25
2.4	F_z^{min} on silica microspheres of different sizes	26
2.5	Optical forces exerted by a 400 mW, 1064 nm laser beam on a 3 μm diameter silica microsphere in water with NA = 1.0. . . .	28
2.6	Optical forces exerted by a 400 mW, 1064 nm laser beam on a 3 μm diameter silica microsphere in acetone with NA = 1.0. . . .	29
2.7	Optical forces exerted by a 400 mW, 1064 nm laser beam on a 3 μm diameter BaTiO ₃ microsphere in acetone with NA = 1.0. . . .	30
2.8	Illustration of a balanced detection system with a quadrant detector.	33
2.9	Illustration of a balanced detection system with a balanced detector	35
3.1	A linear time invariant system	42
3.2	Position PSDs and shot noise	62
3.3	Cumulative position power spectra with shot noise	63
3.4	Velocity power spectra of the two systems.	65
3.5	Cumulative velocity power spectra of the two systems.	66
4.1	A simplified schematic of experimental setup for measuring instantaneous velocity of a microsphere in liquid.	71
4.2	Detailed optical schematic of the experiment.	73
4.3	Scanning electron microscope images of the microspheres.	77
4.4	Optical microscope images of microspheres.	78
4.5	Illustration of a measurement of particle size using ImageJ.	79
4.6	The size distribution of the microspheres used in the experiments.	79

4.7	Flow cell and mount	80
4.8	Typical images of trapped microspheres.	85
4.9	AC detector transfer function	88
4.10	Dependence of signal-to-noise ratio and detection beam profile on the camera on axial position of the condensing objective.	90
4.11	Double logarithmic plot of the experimental and theoretical MSDs of a trapped microsphere in liquid in three systems.	96
4.12	The position power spectra of the three systems.	98
4.13	Semi-logarithmic plot of the experimental and theoretical velocity autocorrelation functions.	99
4.14	The VPSD and normalized cumulative VPSD of a silica microsphere in water.	101
4.15	The VPSD and normalized cumulative VPSD of a silica microsphere in acetone.	102
4.16	The VPSD and normalized cumulative velocity PSD of a BaTiO ₃ microsphere in acetone.	103
4.17	The normalized velocity distribution of a silica microsphere in water	104
4.18	The normalized velocity distribution of a silica microsphere in acetone	105
4.19	The normalized velocity distribution of a BaTiO ₃ microsphere in acetone	106
4.20	The arising resonance in the position PSD	109
4.21	The thermal force power spectra in the three systems	110
5.1	Boundary effects on the position power spectra	131
5.2	Boundary effects on the velocity power spectra	133
5.3	Boundary effects on the mean square displacement	134
5.4	Boundary effects on the velocity autocorrelation function	135
5.5	Boundary effects on the thermal power spectra	136
5.6	The fluid fields of steady Stokes flow near a sphere both in free space and bounded fluid	137
5.7	A study of the onset of boundary effects by observing the vorticity field	138
6.1	Schematic of experimental setup for boundary effects study	143

6.2	Flow cell for studying boundary effects.	145
6.3	Optical images of a trapped silica microsphere near a fiber . .	148
6.4	Experimental and theoretical MSDs with boundary effects . .	150
6.5	Experimental and theoretical velocity autocorrelation functions	152
6.6	Experimental and theoretical position power spectra	153
6.7	Experimental and theoretical velocity power spectra	155
6.8	Experimental and theoretical thermal force power spectra . . .	156
6.9	The VACF calibration method	159
6.10	Normalized position autocorrelation function	163
6.11	The absolute sphere-wall separation measurements obtained by measuring the hindered diffusion coefficients	164
6.12	Experimental and theoretical boundary effects on the parallel motion	165
7.1	Rheological schemes of three simple models	170
7.2	The numerical predictions of position power spectra in complex fluids	174
7.3	The numerical predictions of velocity power spectra in complex fluids	174
7.4	The numerical predictions of mean square displacements in a complex fluid	176
7.5	The numerical predictions of velocity autocorrelation function in a complex fluid	177
7.6	The numerical predictions of thermal force power spectra in a complex fluid	178
7.7	The viscoelasticity of fluids obtained by the Mason-Weitz method and the Felderhof Method	183
7.8	Experimental results of viscosities of water and acetone	183
8.1	Fluid flow boundary conditions at solid-fluid interfaces	186
8.2	The numerical predictions of velocity autocorrelation function of an unbounded microsphere with different slip lengths	190
8.3	The numerical predictions of the MSDs of an unbounded mi- crosphere with different slip lengths	191
8.4	The numerical predictions of the position PSDs of an unbound- ed microsphere with different boundary conditions	192

8.5	The numerical predictions of the velocity PSD of an unbounded microsphere with different boundary conditions	193
8.6	The numerical predictions of the velocity power spectral density of an unbounded microsphere with different boundary conditions	194
8.7	The numerical predictions of the position PSD of an no-slip microsphere near a flat infinite wall with different boundary conditions	197
8.8	The numerical predictions of the velocity PSD of an unbounded microsphere with different boundary conditions at a sphere-wall distance of $3 \mu\text{m}$	198
8.9	The numerical predictions of the mean square displacements of a no-slip microsphere in three cases	199
8.10	The numerical predictions of the VACFs of a no-slip microsphere in three cases	201
8.11	The numerical predictions of the FPSDs on a no-slip microsphere in three cases	202
9.1	The predictions of the position power spectra for the two systems	210
9.2	The predictions of the velocity power spectra for the two systems	211
9.3	The predictions of the MSDs for the two systems	212
9.4	The predictions of the VACFs for the two systems	213
9.5	The predictions of the FPSDs for the two systems	214
9.6	The schematic of the experiment studying Brownian motion with pulse probes	216
9.7	The schematic for instantaneous velocity measurements of a Brownian particle using probe pulses with calibrations	219
9.8	The simplified schematic of a “pump-probe” experiment. . . .	223

Chapter 1

Introduction

1.1 History of Brownian motion

Brownian motion is the random movement of particles agitated by the thermal motion of the molecules in a fluid. The observation of Brownian motion was first reported in 1785 by Jan Ingenhauz [1]. He described the irregular movement of coal dust on the surface of alcohol. The Brownian motion of a particle in bulk fluids was first discovered by Robert Brown in 1827 [2]. He observed the irregular motion of pollen as well as inorganic matter like wood, and nickel dust in water using a simple microscope. Today, this motion is known as Brownian motion.

In 1905, Albert Einstein explained in precise detail how a microscopic particle is agitated by the thermal motion of fluid molecules. This explanation of Brownian motion served as a definitive confirmation that atoms and molecules actually exist [3]. Einstein's prediction for the mean squared displacement (MSD) of a free spherical particle in a fluid in one dimension is

$$\langle \Delta x^2(t) \rangle = \langle [x(t + \tau) - x(\tau)]^2 \rangle = 2Dt \quad (1.1)$$

where $D = \frac{RT}{N_A 6\pi\eta a}$ is the diffusion constant and involves Avogadro's constant N_A , R is the gas constant, T is the absolute temperature, η is the viscosity of

the fluid and a is the radius of the sphere. M. von Smoluchowski also derived the expression of MSD in Eq. (1.1) independently in 1906 [4], but his result was off by a factor of 2. This result was confirmed experimentally by Jean Perrin in 1909 [5], which led to the measurements of Avogadro's number and thus proof of the existence of atoms and molecules. Because of this work, Perrin was awarded the Nobel Prize in Physics in 1926.

The result in Eq. (1.1) is correct only for Brownian motion on long time scales (typically ≥ 1 ms), conventionally called diffusive Brownian motion. Long time trajectories of Brownian particles are classic examples of fractals that are continuous everywhere but not differentiable anywhere [6]. Therefore, there is no definition for instantaneous velocity in this theory, as the root mean square velocity $\sqrt{\langle v^2 \rangle} = \frac{\sqrt{\langle \Delta x^2(t) \rangle}}{\Delta t} = \sqrt{\frac{2D}{\Delta t}}$ diverges when $\Delta t \rightarrow 0$. Einstein knew his diffusive Brownian motion theory [3] would break down at short time scales. In 1907, he gave the theory [7] that considers the instantaneous velocity of a Brownian particle, in which he gave the time scales at which thermal energy is exchanged between the particle and the fluid and the displacements of the particle during those time scales.

In 1908, Paul Langevin proposed a stochastic differential equation, the Langevin equation, which was quite different from Einstein's approach and "infinitely more simple" according to him, to describe Brownian motion [8,9]. This was the first mathematical description of the motion of particle in a fluid over the entire time domain. In Langevin's description, the force on the particle exerted by the fluid is separated into two components, the fluctuation force

(also called the thermal force) and the friction force. Both of them are due to the same physical mechanism, the collisions between the particle and the fluid molecules. They are related by the fluctuation-dissipation theorem [10]. Since then, the Langevin model has found broad applications in many fields [11].

1.2 Brief description of Brownian motion

In this section, we will consider a $3\ \mu\text{m}$ diameter silica sphere (with density $\rho_p = 2 \times 10^3\ \text{kg/m}^3$) in water ($\rho_f = 10^3\ \text{kg/m}^3$ and viscosity $\eta = 0.9 \times 10^{-3}\ \text{Pa}\cdot\text{s}$) at room temperature as an example to briefly discuss Brownian motion. Water is a strongly correlated medium with a mean free path of about $3\ \text{\AA}$, the average distance water molecules can travel between collisions [12]. The collision rate between the microsphere with surrounding water molecules is about $10^{20}\ \text{Hz}^1$. If one could resolve the motion of the particle at single collision level, Brownian motion would not be stochastic as conventionally considered anymore, but deterministic governed by Newton's laws. However, this would be extremely hard to do in practice. Instead, most successful theories [3, 4, 8] begin from a statistical point of view by averaging many collisions in a clever way. A similar situation happens in solid state physics when considering the interaction between a crystal containing Avogadro's number of atoms and electromagnetic waves. Instead of tackling this problem at single atom level, people treat the crystal as a collective entity of many atoms, forming energy

¹This is assuming purely two-body collisions and ignoring the cluster formation of water molecules. In reality, many-body collisions might not be negligible since water is a strongly correlated system. Therefore, it might be better to treat water as a continuum.

bands, refractive index and so on.

Because of the huge difference in mass between the microsphere (3×10^{-14} kg) and a water molecule (3×10^{-26} kg), the motion of the microsphere can only be changed significantly by a large number of collisions. Therefore, it is natural to study Brownian motion in an averaged manner, averaging on the order of 10^{12} collisions. One of the key questions to correctly study Brownian motion is how long should people average the collisions without losing information. Obviously, people want to average the collisions for a longer time to reduce the difficulty of describing Brownian motion. However in Einstein's 1905 work [3], he averaged too many collisions, resulting in only being correct on long time scales.

There are two important time scales setting limits on the longest time scale one can average the collisions to correctly describe Brownian motion. One of them is $\tau_p = m_p/(6\pi\eta a) = (2\rho_p a^2)/(9\eta)$, known as the momentum relaxation time of the particle [3, 4, 8, 13], where ρ_p is the density of the particle. It indicates how long the particle takes to lose its momentum to the surrounding fluid. τ_p increases with the size and density of the particle and decreases with the viscosity of the fluid. The other one is $\tau_f = \rho_f a^2/\eta$, the time for vorticity in the fluid to travel one microsphere radius a , where ρ_f is the density of the fluid. This directly relates to the hydrodynamic memory effects [14, 15]. For 3 μm diameter silica sphere in water, these two time scales are comparable, $\tau_p = 1 \mu\text{s}$ and $\tau_f = 2.25 \mu\text{s}$, during which about 10^{14} collisions occur. The averaging time interval should be shorter than both τ_p

and τ_f to fully resolve the momentum relaxation. Thus, the averaged number of collisions should be fewer than 10^{14} , indicating that the mass ratio (10^{12}) between the sphere and a water molecule is a good estimation for the optimal averaging collision number.

In spite of many successful studies of Brownian motion on long time scales, experimental measurements of the velocity and thus kinetic energy of the thermal motion of microscopic particles was not possible until recently [16–18], after many failed attempts [19, 20]. This is because it requires extreme resolutions of both time and position. As mentioned above, for a 3 μm diameter silica microsphere in water, the temporal resolution should be shorter than both τ_p and τ_f . With 2% uncertainty, the temporal resolution needs to be 20 ns. The corresponding spatial resolution is determined by the average displacement, due to Brownian motion, of the microsphere during that 20 ns. At room temperature, the average thermal velocity of the microsphere is about 400 $\mu\text{m/s}$, resulting in an 8×10^{-12} m average displacement. With 2% uncertainty in the position measurements, the position resolution must be at least 1.6×10^{-13} m in 20 ns, corresponding to 2×10^{-17} m/ $\sqrt{\text{Hz}}$ in position sensitivity. The position resolution of our experiments is on the level of 10^{-15} m/ $\sqrt{\text{Hz}}$, as shown in Chapter 4. Therefore, with current resolution, we can not resolve the instantaneous velocity of a 3 μm diameter silica microsphere in water with 2% uncertainty.

However, this requirement is reduced to 10^{-15} m/ $\sqrt{\text{Hz}}$ for a 5 μm barium titanate (BaTiO_3 , $n = 2.1$, $\rho_B = 4.2 \times 10^3$ kg/m³) microsphere in acetone

($n = 1.35$, $\rho_f = 789 \text{ kg/m}^3$ and $\eta = 3.1 \times 10^{-4} \text{ Pa}\cdot\text{s}$). This is because of two improvements: first, slowing down the dynamics by using acetone (lower viscosity compared to water) and BaTiO₃ microspheres (higher density compared to silica); and second, improving signal-to-noise by using BaTiO₃ microspheres (higher refractive index compared to silica improves the scattering efficiency). Therefore, instantaneous velocity measurements were made possible as discussed in detail in Chapter 4.

1.3 Testing the Maxwell-Boltzmann distribution

The one dimensional Maxwell-Boltzmann distribution (MBD) for the velocities of molecules in an ideal gas in thermal equilibrium is [21]

$$f(v) = \sqrt{\frac{m}{2\pi k_B T}} \exp\left(-\frac{mv^2}{2k_B T}\right) \quad (1.2)$$

where m is mass, k_B is Boltzmann's constant and v is the velocity. The energy equipartition theorem, $\frac{1}{2}m\langle v^2 \rangle = \frac{1}{2}k_B T$, can be derived from the MBD. The actual velocity distribution in certain systems has been predicted to deviate from the standard MBD, for example, due to particle-particle interactions or relativistic effects [22–25]. A simple thought experiment showing a change in the velocity distribution by adding an arbitrary potential was proposed by Lord Kelvin in 1892 [22]. Additional deviations from the MBD have been predicted for low density plasmas [23], interstellar molecular hydrogen [24], and in the solar plasma by measuring neutrino flux [25]. In spite of predicted deviations, the MBD still holds as a remarkably robust approximation for most physical systems.

Previous work has reported an experimental verification of the MBD and energy equipartition theorem for a microsphere in air [16]. This result is to be expected, since the interaction of a particle with the surrounding air is fairly weak. In the case of a particle in a liquid, it is not so clear whether the MBD and energy equipartition theorem still hold, due to the strong hydrodynamic coupling.

We have reported an accurate test of the Maxwell-Boltzmann distribution and the energy equipartition theorem using a barium titanate glass (BaTiO_3) microsphere in acetone [18]. We find that the velocity distribution follows a modified Maxwell-Boltzmann distribution

$$f(v) = \sqrt{\frac{m^*}{2\pi k_B T}} \exp\left(-\frac{m^* v^2}{2k_B T}\right) \quad (1.3)$$

where m^* is the effective mass of the microsphere in liquid which is the sum of the mass of the microsphere m_p and half of the mass of the displaced liquid m_f , $m^* = m_p + \frac{1}{2}m_f$ [26]. The liquid adds a virtual mass $\frac{1}{2}m_f$ to the microsphere, since accelerating the microsphere requires a force both on the microsphere and the surrounding liquid. As a result, the energy equipartition theorem also needs to be modified to $\frac{1}{2}m^*\langle(v^*)^2\rangle = \frac{1}{2}k_B T$.

The apparent conflict between our observation and the equipartition theorem can be resolved by considering the effects of compressibility of the liquid [26]. Below timescales on the order of $\tau_c = a/c$, where c is the speed of sound in the liquid and a is the radius of the microsphere, the compressibility of the liquid cannot be neglected and the velocity variance will approach the

energy equipartition theorem. This will be discussed in detail in Chapter 9.

1.4 Brownian motion near a boundary

When a particle approaches a boundary, its dynamics will be altered in a way that contains the information about the boundary. Brownian motion of particles near boundaries is relevant to many scientific fields. For instance, in microfluidics, the channel is so narrow that the influence of boundaries is inevitable. Many biological experiments are performed near a plane surface, namely, a glass coverslip. Understanding the influence of boundaries on particle dynamics is of great significance, from both a fundamental and an applied point of view.

It is well-known that the mobility of particles decreases as they approach boundaries at which the fluid does not slip. This effect of “surface confinement” was predicted by Lorentz in 1907 [27]. The increase of the drag force is attributed to the alteration of the hydrodynamic interaction between the particle and the fluid generated by the no-slip boundaries. The motion of the particle becomes anisotropic because the drag force parallel to the wall is typically less than that perpendicular to the wall. This effect is significant when the dimensions of the confining geometry and the suspended particles are comparable.

Despite many years of experiments on Brownian motion, the effects of boundaries over a wide range of time scales are still not well understood. Our experiments provide the first comprehensive study of boundary effects on

Brownian motion over a wide range of time scales. We report the observation of surprising and qualitatively new phenomena, such as fast memory loss of the particle's velocity near the boundary, and a flattening in the thermal force spectrum. This detailed understanding of boundary effects might enable the development of a new 3D microscope with a fast remote sensor to map out boundary contours.

1.5 Brownian motion in complex fluids

Brownian motion of a particle is caused by the constant collisions between the particle and the fluid molecules. Therefore, Brownian motion contains some information about the host medium.

Newtonian fluids can be characterized by a single coefficient of viscosity, which depends on temperature but does not change with the strain rate. Only a small group of fluids exhibit such constant viscosity. The large class of fluids, whose viscosity changes with the strain rate, are called non-Newtonian fluids (or complex fluids). Such materials are viscoelastic, exhibiting both a viscous and an elastic response. The study of the deformation and flow of such complex fluids is called rheology.

A new approach, called optical microrheology, using micron-sized immersed particles as probes to investigate the viscoelastic behavior of complex fluids is pioneered by Mason and Weitz [28]. Unlike traditional rheology, which requires a bulk of fluid, microrheology only requires micro- or even nano-liters of fluids. Therefore, unlike traditional rheology, which only gives averaged

properties, microrheology gives the local properties of the fluids with a spatial resolution of micrometers or even nanometers. This is especially valuable for studying highly non-homogeneous complex materials. Furthermore, microrheology typically has a higher bandwidth than the conventional bulk rheometry.

In the first part of Chapter 7, we will give the predictions of Brownian motion of a sphere in complex fluids with their properties known. We then present the procedure to measure the viscoelasticity of unknown fluids based on the measurements of Brownian motion of an embedded particle. This will be followed by two experimental demonstrations of obtaining the viscosities of water and acetone.

1.6 Brownian motion with slip boundary conditions

The boundary condition for the flow velocity of a viscous fluid at the solid-fluid interface is conventionally considered as no-slip, meaning the fluid molecules at the solid surface stick to the solid perfectly and have no relative velocity with the solid. Our experiments in Chapter 4 and 6 have shown that this is a good assumption for the interfaces between water and glass, as well as acetone and glass.

The slippage of a fluid on a solid surface can be characterized by the slip length δ or the contact angle θ_c , which are generally related through $\delta = \delta_0(1 + \cos(\theta_c))^{-2}$. δ_0 is an empirical quasi-universal length scale. When δ is much smaller than the dimensions of interest, the fluid flow boundary condition can be safely assumed to be no-slip. The contact angle between

water and glass typically lies in the range from 25° to 29° [29], resulting in a slip length of 0.1 nm. Therefore, the interface between water and micron-sized glass particles satisfies the no-slip boundary condition since the particle's size is 10^4 times larger than the slip length.

However, the no-slip boundary condition assumption has failed in many situations [30–34]. Partial-slip boundary conditions must be used when the slip length δ is comparable to the dimensions of interest. The effective slip length can be increased by microscopic structures on the surface of the solid [31, 32].

In the first part of Chapter 8, we will discuss the Brownian motion of a free particle with no-slip, partial-slip and perfect-slip boundary conditions. We will show that it is much easier to measure the instantaneous velocity of a microsphere with a perfect-slip boundary than that of a particle with a no-slip boundary condition. Secondly, we will discuss the dynamic motion of a microsphere with a no-slip boundary condition near a flat infinite wall with a perfect-slip boundary condition.

1.7 Brownian motion in compressible fluids and non-equilibrium physics study

We have observed that the velocity distribution of a microsphere in a liquid follows modified versions of the Maxwell Boltzmann distribution and the energy equipartition theorem in Chapter 4. As discussed before, this is because the current temporal resolution, which is limited by the position sensitivity and ultimately by the shot noise of the detection beam, is not able to resolve

the compressibility of the fluids. We have achieved a position sensitivity of 2×10^{-15} m/ $\sqrt{\text{Hz}}$ with 150 mW detection power as discussed in Chapter 4, which limits the temporal resolution to about 100 ns. One can increase the position sensitivity to about 10^{-19} m/ $\sqrt{\text{Hz}}$ using a pulsed laser with a peak power of 10^8 W. This leads to a temporal resolution of 0.1 ns, which is much shorter than typical τ_c (\sim ns); thus, one can resolve the compressibility of fluids. In the first part of Chapter 9, we will present the efforts that have been made to resolve the compressibility of fluids. We will also briefly discuss the possible future studies on non-equilibrium physics.

1.8 Contents of this dissertation

Chapter 2 provides the details of optical trapping and a balanced beam detection system. Chapter 3 introduces the theory of Brownian motion in incompressible Newtonian fluids. Chapter 4 provides the details of the experiments testing the Maxwell-Boltzmann distribution and the energy equipartition theorem. Chapter 5 gives the theory for Brownian motion of a microsphere near a flat infinite wall with a no-slip boundary condition. Chapter 6 provides the details of the experiments studying Brownian motion with boundary effects. Chapter 7 studies the viscoelastic properties of complex fluids using an immersed Brownian particle as a probe. Chapter 8 studies the slippage effects on Brownian motion. Chapter 9 presents the efforts to resolve the compressibility of a fluids using a pulsed laser and discusses non-equilibrium physics using a “pump-probe” scheme.

Chapter 2

Optical trapping and balanced beam detection

In this chapter, we will discuss the two main techniques used in our experiments: optical trapping and a balanced detection system. Trapping of particles (atoms, molecules, ions, nano-particles, micro-particles, biological cells and so on) is a powerful tool and has revolutionized many fields of science. In our experiments, particles are confined in a certain detection region by an optical trap created by tightly focused laser beams. The trapping beam also can serve as a detection beam used in a balanced beam detection system. In a balanced beam detection system, the detection beam is typically split into two roughly equal halves. A high gain balanced detector is typically used to amplify the power difference in the two branches, which is often directly related to essential physical quantities of the experiments. Thus, the common-mode noise in the laser beam can be substantially cancelled out. In our case, the power difference in the two branches has a linear dependence on the position of the trapped particles. Our balanced beam detection system provides us unprecedented bandwidth and precision in measuring Brownian motion at a tabletop scale.

2.1 Optical trapping

Optical trapping relies on momentum exchange between particles and photons. Photons, the particle aspect of the wave-particle duality of electromagnetic radiation, have momentum $p = h/\lambda$. The momentum of a single photon is very tiny. A 1064 nm photon has a momentum of 6.2×10^{-28} kg·m/s. The concept of radiation pressure was proposed by Johannes Kepler back in 1619 to explain the observation that a tail of a comet always points away from the Sun. The radiation pressure of light was first deduced theoretically by J. C. Maxwell in 1873 based on his electromagnetic theory [35] and measured experimentally by P. N. Lebedev [36], and E. F. Nichols and G. F. Hull in 1901 [37].

The invention of lasers made it possible to make use of the momentum of photons effectively, even a single photon provides a tiny momentum. 1 W of 1064 nm light, containing about 5×10^{18} photons per second, exerts about 7 nN on a totally reflecting mirror with perpendicular incidence. In contrast to classical light sources, a laser beam can be tightly focused onto a small particle with a diameter on the order of 1 μm . The radiation force on a 1 μm diameter silica sphere exerted by a 1 W focused laser beam can be 10^4 times greater than the gravitational force (3×10^{-13} N). Therefore, the optical trap can have huge effects on the motion of the particle. In fact, the gravitation force often can be neglected in most optical-tweezer experiments.

Shortly after the first laser was invented, Arthur Ashkin working in Bell labs, demonstrated that one could use focused laser beams to accelerate and

trap micrometer-sized transparent particles [38]. Ashkin and his coworkers also have shown that oil droplets and glass microspheres can be optically levitated in air [39] and vacuum [40]. In 1986, Ashkin along with Steven Chu, who won the 1997 Nobel Prize in Physics for using radiation pressure to cool and trap neutral atoms, observed stable trapping of dielectric particles with the gradient force of a strongly focused laser beam [41]. By then, a powerful tool was completely developed (mainly by Ashkin) to trap and manipulate microscopic particles using a tightly focused beam of light, now known as an optical tweezer. This technique soon became a standard tool in many fields [42–44].

The radiation pressure had a huge impact in atomic, molecular and optical physics as well, and led to the realization of Bose-Einstein condensation [45], degenerate Fermi gas [46], atomic clocks [47] and so on. Started in the 1970s, after the first observation of radiation pressure on microscopic particles, laser radiation pressure was soon used to manipulate a variety of atoms [48–51]. In 1986, cold sodium atoms (~ 1 mK) were optically trapped for the first time [52]. After that, neutral atoms were commonly trapped by a tightly focused laser beam, now known as an optical dipole trap. The basic forces of radiation pressure on atoms are conceptually similar to those on microscopic particles [53].

The radiation pressure exerted by a laser on a particle can be split into two components: the gradient force and the scattering force. The gradient force is a conservative force, which provides the trapping mechanism, whereas

the scattering force is a nonconservative force, which tends to push the particle out of the trap. The total force on the particle is $\vec{F}(\vec{r}) = \vec{F}_{scat}(\vec{r}) + \vec{F}_{grad}(\vec{r})$. The scattering force typically only exists in the axial direction of the laser beam and causes in a shift of the minimum of the trapping potential in the laser propagation direction, whereas the gradient force acts in all three dimensions. Thus, there is always a restoring force in the radial direction by a focused beam. In order to form a potential minimum in 3D, the total force on the particle in the axial direction $F_z = F_z^{scat} + F_z^{grad}$ must change sign. Equivalently, the minimum force in the axial direction $F_z^{min} = \min(F_z(\vec{r}))$ must be negative if we denote the magnitude of the scattering force as positive.

In summary, there are two requirements to stably trap particles. One is the formation of a trap, which requires F_z^{min} to be negative. Second is that the trap depth has to be deep enough to withstand thermal fluctuations. The trap depth typically needs to be 10 times greater than the averaged kinetic energy of the particle. This is due to the fact that the kinetic energy of a particle follows the Maxwell-Boltzmann distribution at thermal equilibrium. The particle has a significant probability for its instantaneous kinetic energy to be much higher than its average kinetic energy.

Depending on the ratio between the particle size and trapping laser beam wavelength, the interaction between a microscopic particle and a laser beam is commonly divided into three regimes: Ray optics regime [54] ($D \gg \lambda_0$, where D is the diameter of the particle and λ_0 is the wavelength of the laser in vacuum), Lorentz-Mie regime [55] ($D \sim \lambda_0$) and Rayleigh regime [56]

($D \ll \lambda_0$). In this section, we will first explain the principle of optical trapping in the ray optics regime. This will be followed by theoretical calculations of the optical forces on a particle with the Rayleigh approximation and with the generalized Lorentz-Mie theory.

2.1.1 Ray optics approximation

When the size of a particle is much larger than the wavelength of the trapping laser (usually $D > 10\lambda_0$), the optical forces on the particle can be calculated with the ray optics approximation [54].

In the ray optics regime (also called geometrical optics regime), diffractive effects typically can be neglected and the total light beam can be decomposed into individual rays, each with appropriate intensity, direction, and state of polarization, which propagate in straight lines in media of uniform refractive index. Each ray has the characteristics of a plane wave; thus, Fresnel formulas can be used to solve for light propagation. Each ray, reflected, refracted or absorbed by an object, transfers its momentum to the object, which is a microsphere in our case. The photons that are reflected and absorbed (absorption can be neglected in our experiments) by a microsphere exert the scattering force on the microsphere. The photons refracted by the microsphere exert the gradient force on the microsphere. The force from a laser beam can be calculated by splitting the beam as a collection of rays and summing the force from each one. The average force on the sphere is $F = (Pn_f/c) \sin \theta$, where P is the power of the ray, n_f is the index of refraction of the medium,

c is the speed of light in vacuum, and θ is the angle of deflection.

It is probably the most intuitive to explain optical trapping principles in this regime. Let's neglect the scattering force and just focus on the gradient force for a moment. A qualitative view of optical trapping of microspheres in the ray optics regime is shown in Fig. 2.1 [41, 54], illustrating that a displacement of the sphere in any direction from the focus of the laser results in a restoring force. If we neglect surface reflection from the microsphere, then the microsphere will be trapped at the focus of the laser beam as shown in Fig. 2.1(B). If the microsphere moves to the left of the focus (Fig. 2.1(A)), it will deflect the laser beam to the left and thus increase the momentum of photons to the left. The counter force from the deflected photons will push the

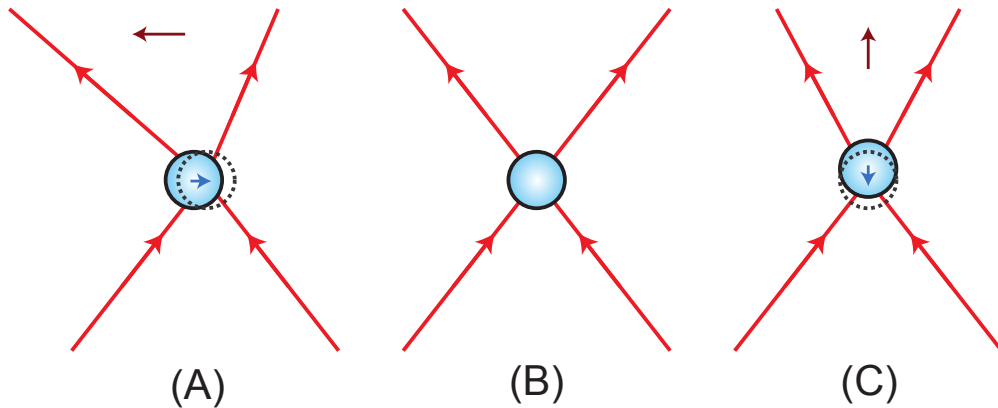


Figure 2.1: Qualitative view of optical trapping of a dielectric sphere. (A) displays the force on the particle when the particle is displaced laterally from the focus; (B) shows that there is no net force on the particle when the particle is trapped at the focus; and (C) displays the force on the particle when the particle is positioned above the focus. The scattering force is neglected here. (Figure courtesy of Dr. Tongcang Li.)

microsphere to the right, i.e. back to the focus of the laser beam. If the microsphere moves along the propagation direction of the laser beam (Fig. 2.1(C)), it will focus the laser more strongly and thus increase the momentum of photons along the propagation direction. The counter force from the deflected photons will push the microsphere back to the focus of the laser beam. The same thing will happen if the microsphere moves away from the focus in other directions. Thus a focused laser beam forms a stable optical trap in 3D.

In reality, one has to consider the scattering force. In order to form a trap in 3D, the gradient force has to be larger than the scattering force in the axial direction. The photons reflected back by the surface of a microsphere will push the microsphere forward. It has been reported that particles with a larger index mismatch are more difficult to trap [57]. In water ($n = 1.33$), it is more difficult to trap barium titanate microspheres (BaTiO_3 , $n = 2.1$, corresponding to a refractive index mismatch $m = n_p/n_f = 1.58$) than silica microspheres ($n = 1.46$, corresponding to $m = 1.1$). A dual-beam trap, with two counter-propagating laser beams cancelling the scattering force and doubling the gradient force, is necessary to trap BaTiO_3 microspheres in both water and acetone ($n = 1.35$), as demonstrated in Chapter 4.

The strength of both the gradient force and the scattering force linearly depends on the laser power, so increasing the trapping beam power will not make the F_z change sign. However, trap depth can be increased by increasing the trapping power provided a trap is formed. For fixed laser power, the gradient force in the axial direction $|F_z^{grad}|$ increases with increasing numerical

aperture ($\text{NA} \equiv n_f \sin \theta$, where θ is the $1/e^2$ half-angle of convergence of the trapping beam), while both the gradient force in the radial direction $|F_r^{grad}|$ and the scattering force $|F_z^{scat}|$ are maximized when $\text{NA} \rightarrow 0$, assuming that all the light is incident on the particle. Therefore, the laser beam should be tightly focused by a high NA objective lens to increase the gradient force and decrease the scattering force in the axial direction.

2.1.2 Rayleigh approximation

If the size of a microscopic particle is much smaller than the wavelength of the trapping laser beam (usually $D < \lambda_0/10$), the electric field of the laser beam is uniform over the entire particle. Therefore, the particle can be approximated as a point dipole (a Rayleigh scatterer). In this regime, the optical force on the particle can be calculated analytically with the Rayleigh scattering theory [41, 56].

As the electric field oscillates in time, it induces a dipole moment, whose oscillations follow that of the electric field. The oscillating dipole radiates a secondary, or scattered field, in all directions. The momentum flux of the resulting field is nonzero; some of it is transferred to the dipole in the form of the scattering force. The second component of radiation pressure is due to the Lorenz force exerted by the optical field on the induced dipole, which is proportional to the gradient of the laser field.

In the Rayleigh approximation, for a sphere (a nanosphere for example) with radius a in a fluid with refractive index n_f , the dipole moment \vec{P} induced

by an electric field \vec{E} is given by [56].

$$\vec{P}(\vec{r}, t) = 4\pi n_f^2 \epsilon_0 a^3 \frac{m^2 - 1}{m^2 + 2} \vec{E} \quad (2.1)$$

where ϵ_0 is the vacuum permittivity.

The scattering force of the laser on a sphere in a fluid with the Rayleigh approximation is [56]:

$$\vec{F}_{scat}(\vec{r}) = \hat{z} \left(\frac{n_f}{c} \right) C_{scat} I(\vec{r}) = \hat{z} \frac{128\pi^5 a^6}{3c\lambda_0^4} \left(\frac{m^2 - 1}{m^2 + 2} \right)^2 n_f^5 I(\vec{r}), \quad (2.2)$$

where c is the speed of light in vacuum, C_{scat} is the scattering cross section and $m = n_p/n_f$, where n_p is the refractive index of the microsphere. Because of the larger relative refractive index m , the scattering force on a BaTiO₃ nanosphere in water is about 5.2 times greater than the scattering force on the same size silica nanosphere in water with the same laser intensity.

The gradient force on a sphere in the Rayleigh regime is [56]:

$$\vec{F}_{grad}(\vec{r}) = [\vec{P}(\vec{r}, t) \cdot \nabla] \vec{E}(\vec{r}, t) = \frac{2\pi n_f a^3}{c} \left(\frac{m^2 - 1}{m^2 + 2} \right) \nabla I(\vec{r}), \quad (2.3)$$

The gradient force forms a trapping potential:

$$V(\vec{r}) = -\frac{2\pi n_f a^3}{c} \left(\frac{m^2 - 1}{m^2 + 2} \right) I(\vec{r}). \quad (2.4)$$

which is proportional to laser intensity.

Because the scattering force is proportional to a^6 while the gradient force is proportional to a^3 , the scattering force decreases much faster than the gradient force with decreasing size of the nanosphere. Thus it is easier

to achieve a negative F_z^{min} (forming a trap) for small particles than large particles. However, the depth of the trap decreases as the size of the particle decreases, whereas the average thermal energy is independent on particle size due to the energy equipartition theorem. Therefore, if the particle is too small, the trap lifetime will be very short, despite of the fact that the trap indeed is formed. As discussed above, in order to trap a nanosphere stably, as a rule of thumb, the trap depth should be at least 10 times larger than the average kinetic energy of the particle.

In many experiments, the laser beam is a linearly polarized Gaussian beam (TEM₀₀) with beam waist radius ω_0 at the focus. The intensity distribution of a Gaussian beam is

$$I(x, y, z) = \frac{2P}{\pi\omega^2(z)} e^{-2(x^2+y^2)/\omega^2(z)}, \quad (2.5)$$

where $\omega(z) = \omega_0 \left[1 + \left(\frac{\lambda_f z}{\pi\omega_0^2} \right)^2 \right]^{1/2}$, $\lambda_f = \lambda_0/n_f$ is the wavelength of the laser in the fluid and P is the power of the laser beam.

To estimate the trap depth and stiffness, we neglect the scattering force here. By combining Eq. (2.4) and Eq. (2.5), the trapping potential formed by a Gaussian beam can be obtained as

$$V(\vec{r}) = -\frac{2\pi n_f a^3}{c} \left(\frac{m^2 - 1}{m^2 + 2} \right) \frac{2P}{\pi\omega^2(z)} e^{-2(x^2+y^2)/\omega^2(z)}. \quad (2.6)$$

The trap depth is given by

$$V_0 = -\frac{2\pi n_f a^3}{c} \left(\frac{m^2 - 1}{m^2 + 2} \right) I(0). \quad (2.7)$$

where $I(0) = 2P/\pi w_0^2$ is the peak laser intensity. For displacements much smaller than w_0 , to first order, the potential is harmonic. The transverse trap stiffness is

$$K_r = \frac{16n_f a^3}{c\pi w_0^4} \left(\frac{m^2 - 1}{m^2 + 2} \right) P. \quad (2.8)$$

And the axial trap stiffness is

$$K_z = \frac{8a^3 n_f \lambda_f^2}{c\pi^2 w_0^6} \left(\frac{m^2 - 1}{m^2 + 2} \right) P. \quad (2.9)$$

The ratio between the radial trap stiffness and the axial trap stiffness is

$$\frac{K_r}{K_z} = \frac{2\pi n_f^2 w_0^2}{\lambda_0^2}, \quad (2.10)$$

which is about 10 with our experimental conditions.

The strength of the gradient force can be increased relatively to the scattering force by decreasing the waist of the focus, w_0 , which requires a larger NA. For a 50 nm silica sphere in water trapped by a 1 W 1064 nm laser beam with a beam waist of 1 μm , the trap depth is 1.4×10^{-19} J, corresponding to 22 times larger than the average kinetic energy ($\frac{3}{2}k_B T$) at room temperature. Therefore, the trap should be stable in this case. The trap stiffnesses are 180 nN/m and 18 nN/m in the radial and axial directions respectively. The scattering force will slightly shift the trap center, resulting in a shallower and less stiff trap.

2.1.3 Generalized Lorentz-Mie theory

In most optical-tweezer experiments, the sizes of the dielectric particles of interest are comparable with the wavelength of the trapping laser ($D \sim \lambda_0$).

For instance, in our experiments, the trapping laser beam wavelength is 1064 nm, and the diameters of the microspheres we used typically are between 3 μm and 6 μm .

In this case, neither ray optics nor the Rayleigh approximation is appropriate. Instead, the electromagnetic theory of light has to be used. For optical trapping of homogeneous and isotropic microspheres, one can use the generalized Lorenz-Mie theory. The mathematical calculation of the generalized Lorenz-Mie theory is quite complex. Here we will only use the computational toolbox developed by T. A. Nieminen *et al.* [55] to obtain some numerical results of the optical forces on a microsphere. This computational tool uses spherical partial wave expansion to characterize scattering fields.

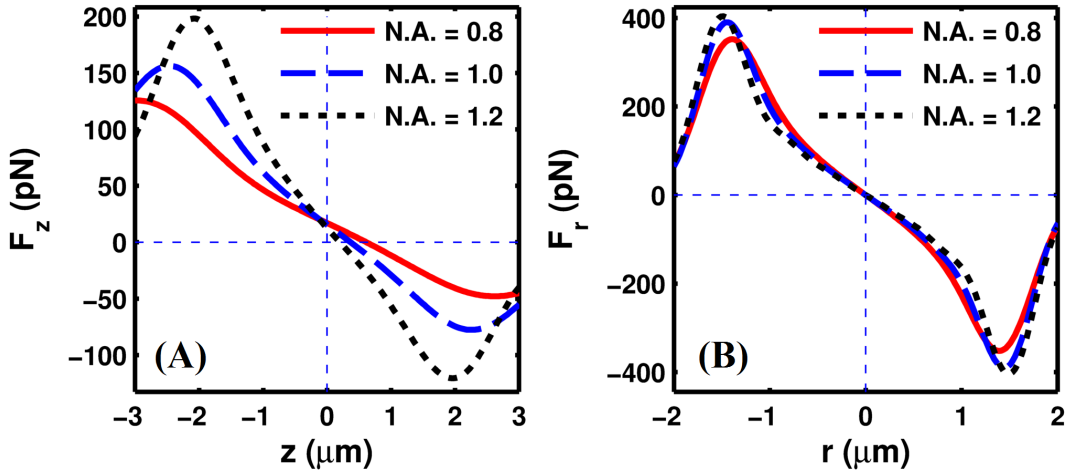


Figure 2.2: Optical forces exerted by a 400 mW, 1064 nm laser beam on a 3 μm diameter silica microsphere in water with different NAs. (A) In the axial direction, trapping strongly depends on NA. (B) In the radial direction, trapping weakly depends on NA.

The calculated total optical forces on a 3 μm diameter silica microsphere in water both in the axial and radial directions exerted by a 1064 nm, 400 mW laser beam focused by objective lenses with three different NAs (NA = 0.8, 1.0, 1.2) are shown in Fig. 2.2. A trap is formed for all three NAs, since the total forces change sign in both the axial and radial directions. The optical forces along the radial direction are similar for all three NA as shown in Fig. 2.2(B). On the other hand, the optical forces along the axial direction depend on the NA, as shown in Fig. 2.2(A). This is because the scattering force is only along the axial direction. The scattering force shifts the trapping center position in the laser beam propagation direction. It is worth noting that the trap depth and stiffness increase with increasing NA.

Fig. 2.3 shows the calculated total optical forces on silica microspheres

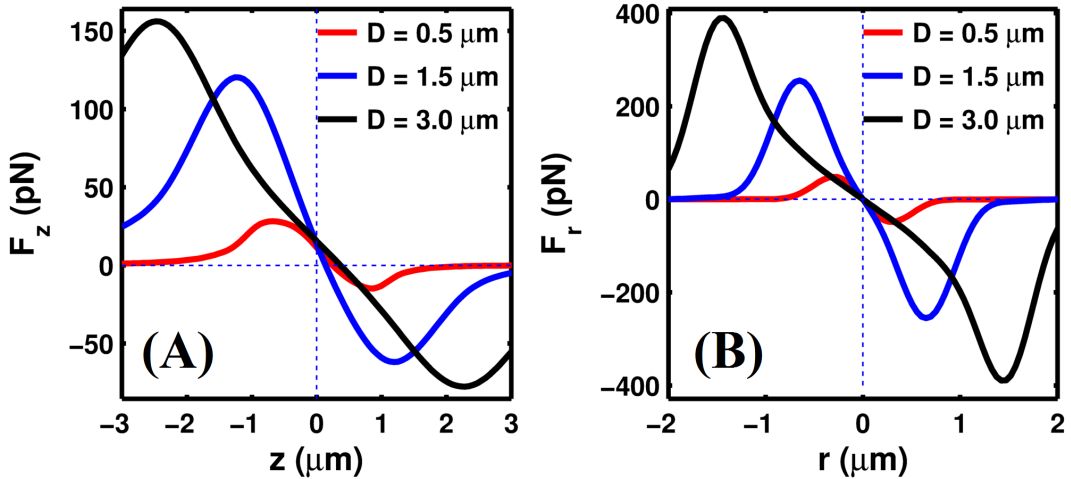


Figure 2.3: Optical forces exerted by a 400 mW, 1064 nm laser beam silica microspheres with different sizes in water with NA = 1.0. (A) In the axial direction. (B) In the radial direction.

with three different sizes in water both in the axial and radial directions exerted by a 400 mW, 1064 nm laser beam focused by an objective lens with $NA = 1.0$. The optical forces in the axial and radial directions have a similar dependence on the size of microspheres. These calculations show that the larger size of microsphere, the deeper the trap. However, it is worth noting that this is not always true, as shown in Fig. 2.4. It is interesting that the trap stiffness does not have a monotonic dependence on the size of microspheres.

The minimum axial forces F_z^{min} on a silica microsphere in water as a function of the size of the microsphere are shown in Fig. 2.4. F_z^{min} oscillates as the diameter of the microsphere changes. This is because of the interference

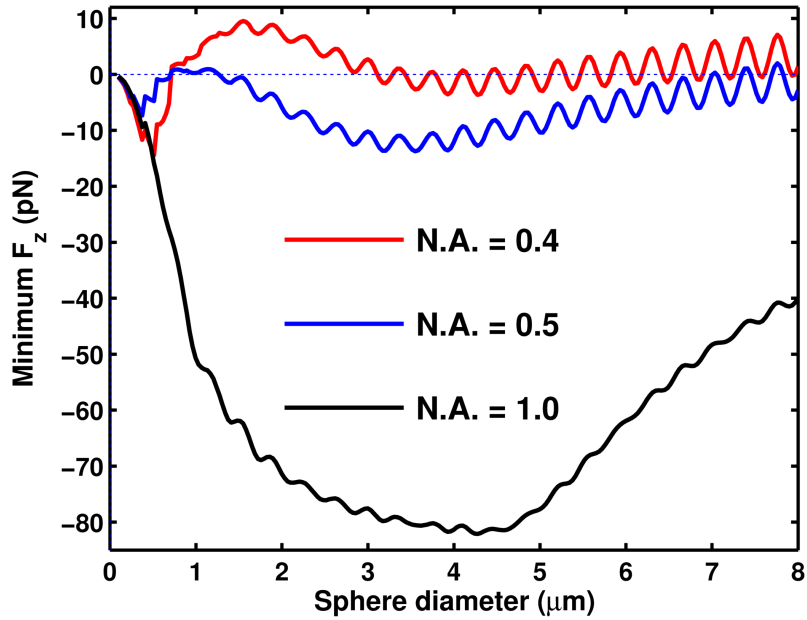


Figure 2.4: The minimum axial forces F_z^{min} on silica microspheres of different sizes in water exerted by a 400 mW, 1064 nm laser beam focused with different NAs ($NA = 0.4, 0.5, 1.0$).

between the scattered light and unscattered light. The oscillation period is about half the wavelength of the laser inside of the microsphere, which is $\lambda_0/(2n_p) = 364 \text{ nm}$ [58]. As discussed before, a trap can only be formed if F_z^{min} is negative. With $\text{NA} = 1.0$, microspheres with diameters up to at least $8 \text{ }\mu\text{m}$ can be trapped because F_z^{min} is negative. However, with smaller NAs ($\text{NA} = 0.4, 0.5$), the trap can only be formed with certain size microspheres. This feature may be used as a selection process to sort microspheres.

2.1.4 Predictions of trapping with experimental conditions

In this section, we will give our predictions of optical trapping with the experimental conditions discussed in Chapter 4 and 6. We study three systems: a silica glass microsphere in water, a silica glass microsphere in acetone and a BaTiO_3 microsphere in acetone. The trapping laser beam has a wavelength of 1064 nm and a power of 400 mW focused by an objective with $\text{NA} = 1.0$.

Fig. 2.5 shows the calculated total optical forces on a $3 \text{ }\mu\text{m}$ silica microsphere in water both in the axial and radial directions. The trap stiffnesses are predicted to be $42 \text{ }\mu\text{N/m}$ and $150 \text{ }\mu\text{N/m}$ in the axial and radial directions respectively, which are very good predictions as discussed in Chapter 4. In thermal equilibrium, the root mean square of the displacement of the particle can be obtained through $x_{rms} = \sqrt{k_B T / K}$. With this, the average displacements of the silica microsphere are predicted to be about 5 nm and 10 nm in the radial and axial directions respectively. The trap depth can be estimated to be a factor of 10^5 greater than the particle's averaged kinetic

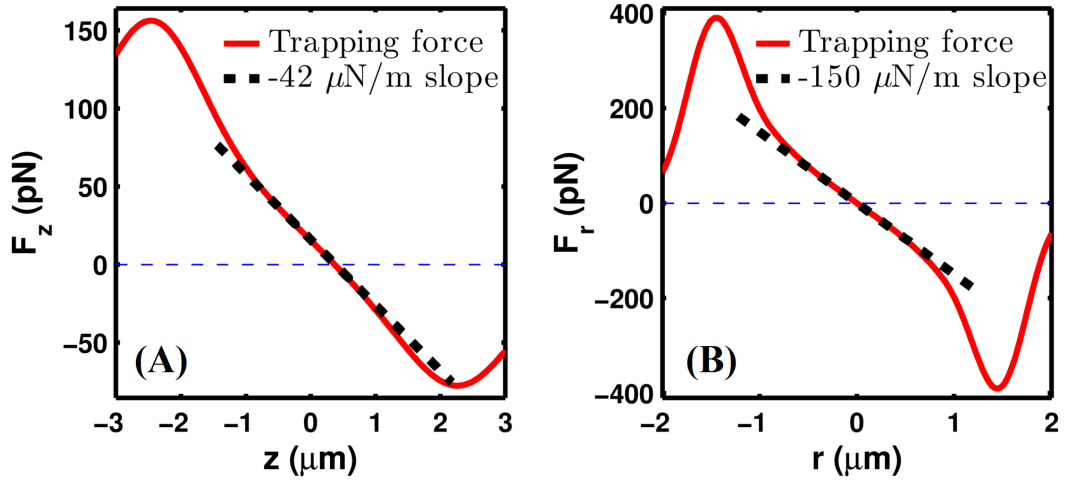


Figure 2.5: Optical forces exerted by a 400 mW, 1064 nm laser beam on a 3 μm diameter silica microsphere ($n = 1.46$) in water ($n = 1.33$) with $\text{NA} = 1.0$. (A) In the axial direction with a predicted trap stiffness of 42 $\mu\text{N}/\text{m}$. (B) In the radial direction with a predicted trap stiffness of 150 $\mu\text{N}/\text{m}$.

energy, indicating an ultra-stable trap. The trap can be approximated as a harmonic trap up to 500 nm away from the trap center, which is much larger than the root mean square of the displacement of the particle. Therefore, the trapping force on the particle can be approximated as a harmonic force in typical optical-tweezer experiments.

Fig. 2.6 shows the calculated total optical forces on a 3 μm silica microsphere in acetone ($n = 1.35$) both in the axial and radial directions. This optical trap is similar to the one shown in Fig. 2.5. The smaller relative refractive index of a silica microsphere in acetone ($m = 1.08$), as compared to that of a silica microsphere in water ($m = 1.10$), results in slightly less trap stiffness, 32 $\mu\text{N}/\text{m}$ and 120 $\mu\text{N}/\text{m}$ in the axial and radial directions respectively. It is

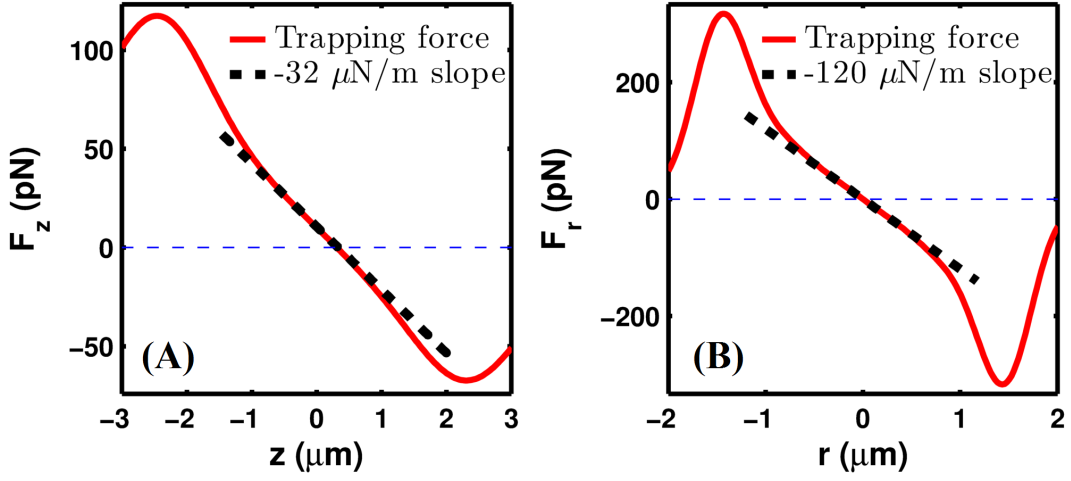


Figure 2.6: Optical forces exerted by a 400 mW, 1064 nm laser beam on a 3 μm diameter silica microsphere ($n = 1.46$) in acetone ($n = 1.35$) with $\text{NA} = 1.0$. (A) In the axial direction with a predicted trap stiffness of 32 $\mu\text{N}/\text{m}$. (B) In the radial direction with a predicted trap stiffness of 120 $\mu\text{N}/\text{m}$.

worth noting that the experimental trapping strength discussed in Chapter 4 is weaker than the predictions here. This is because that the focusing lens used in the experiments is a water immersion objective, resulting in a larger aberration in acetone as compared to that in water.

The calculated total optical forces on a 3 μm BaTiO_3 microsphere in acetone both in the axial and radial directions are shown in Fig. 2.7. The laser does provide strong confinement in the radial direction. However, the much larger relative refractive index between a BaTiO_3 microsphere and acetone ($m = 1.58$), as compared to that between a silica microsphere and water ($m = 1.10$), results in an overwhelming scattering force. As a result, the F_z^{min} is positive, indicating that no trap is formed. Therefore, one has to use two counter-propagating laser beams to cancel the scattering forces while doubling

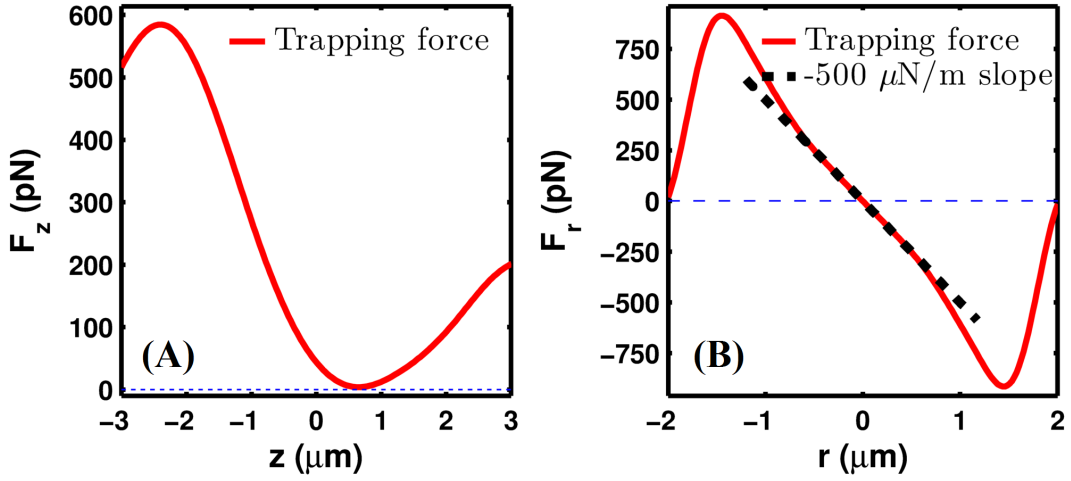


Figure 2.7: Optical forces exerted by a 400 mW 1064 nm laser beam on a 3 μm diameter BaTiO_3 microsphere ($n = 2.1$) in acetone ($n = 1.35$) with $\text{NA} = 1.0$. (A) In the axial direction (B) In the radial direction with a predicted trap stiffness of $500 \mu\text{N/m}$. Obviously, particles can not be trapped in 3D since there is no potential minimum in the axial direction.

the gradient force. This prediction is confirmed by the experiments discussed in Chapter 4.

2.2 Balanced beam detection system

A position sensitive detection system is needed to measure Brownian motion of particles. As discussed in Chapter 1, the temporal resolution required is determined by the particle momentum relaxation time τ_p , which is about $1 \mu\text{s}$ for a $3 \mu\text{m}$ diameter silica microsphere in water. The spatial resolution is determined by the displacement of the particle during time τ_p , which is sub-nanometer. In this section, we will briefly discuss and compare the main techniques developed for studying Brownian motion.

Video microscopy probably is the most common and intuitive technique to observe particles' motion. In video microscopy, successive images of one or more particles are taken using cameras, and centroid fitting algorithms are applied to track the particle's position with nanometer resolution, which is much higher than the resolution of the optical microscope itself [59]. The bandwidth of video microscopy detection is limited by the frame rate of the camera, which is typically between 10 Hz and 100 kHz.

Dynamic light-scattering (DLS) and diffusing wave spectroscopy (DWS) are typical for measurements of an ensemble of free Brownian particles. Particles' motion is encoded in multiply scattered light, which can be resolved by intensity autocorrelation interferometry. These two techniques can have a temporal resolution on the order of nanoseconds and a spatial resolution of sub-nanometers [60–62]. However, one can only get ensemble averaged results using these techniques; thus, they can not be used to measure the instantaneous velocity of a single Brownian particle.

Total internal reflection microscopy is another optical technique can be used to study Brownian motion. An evanescent wave is generated by a total internal reflection in a plate. A Brownian particle, located near the plate, scatters the evanescent wave differently with different distances to the plate. By measuring the light scattered by the particle, the separation between particle and plate can be determined. Often, the plate is fixed, thus the position of the particle in the perpendicular direction can be measured. The technique relies on the rapid exponential-decay evanescent wave, and achieves ~ 1 nm spatial

resolution and up to $\sim 1 \mu\text{s}$ temporal resolution [63]. In addition, this technique is only sensitive to particle's motion in the perpendicular direction to the plate since the evanescent wave is roughly homogeneous in the transverse direction.

Since 1990s, balanced beam detection, often also called back-focal-plane interferometry, became the standard tool to measure positions of microscopic particles [15, 64–68]. Typically, in this detection system, a dielectric particle (often a sphere) is trapped by a focused laser beam, and scatters some of the incident photons in a direction which depends on the particle's position. Changes in the particles' position are encoded in the spatial distribution of the scattered beam. The scattered and unscattered light forms the detection beam, which is split into two roughly equal halves. The difference between these two halves is directly related to the position of the particle. This small difference in the two halves can be amplified with a high gain, resulting in a high resolution in the position measurement of the particle. In addition, the common-mode noise, such as laser intensity noise, is substantially suppressed because it contributes equally to both halves.

The conventional way to split the detection beam and amplify the difference between halves is using a quadrant detector. We will discuss the limitations in this approach and present an improved version of the balanced beam detection system.

2.2.1 Balanced beam detection with quadrant detectors

As shown in Fig. 2.8, a microsphere is trapped by a focused laser beam. We refer the laser beam after the particle as the detection beam, which is re-collimated by a second lens. The movement of the particle results in changes in the scattering light, which is measured by a quadrant detector. A quadrant detector has four identical separated photodiodes (a, b, c, d as shown in Fig. 2.8), with approximately $100 \mu\text{m}$ gaps (dead zones) between them. The balanced beam detection requires that the detection beam to be incident in the center of the quadrant detector, shining the four photodiodes about equally. Thus, the four photodiodes generate nearly the same photocurrents that can be amplified with similar gains. Changes in the scattering light, thus the displacement of the particle, can be measured by linear combinations of the four photodiodes' outputs. The horizontal displacement of the particle can be obtained from the difference between the left and right sides of the quadrant detector, $V_a + V_c - V_b - V_d$; whereas, the vertical displacement of the particle is proportional to difference between the up and down sides of the quadrant detector, $V_a + V_b - V_c - V_d$.

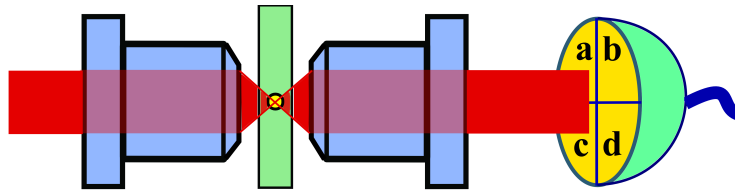


Figure 2.8: Illustration of a balanced detection system with a quadrant detector. A microsphere is trapped by a focused laser beam, which is re-collimated by a second lens and incident on a quadrant detector.

Despite of the fact that the balanced beam detection system with quadrant detectors had great success in many experiments [14, 15, 64–73], it has several limitations. First of all, the bandwidth of quadrant detector is limited to ~ 10 kHz to 1 MHz by the large capacitance of the photodiodes. This can be solved by reducing the area of the photodiode. For instance, a quadrant detector (Hamamastu, G6849-01) has a bandwidth of 120 MHz. However, an transimpedance amplifier operating at such high frequencies with a reasonable gain has never been achieved [74]. Second, crosstalk between 4 quadrants dominates the signals at high frequencies. This is unavoidable since the detector needs to be closely-packed to spatially split the light beam into four parts for differential detection.

2.2.2 Balanced beam detection: an improved version

The key problem of a quadrant detector in this system is that it does both jobs: balancing the detection beam and amplifying the photocurrent and these two can not compromise with each other well. An improved version of balanced detection system was developed [75], separating the spatial splitting and detection of the light. In this new system, the detection beam is split into halves by a fiber-optic bundle, and focused by two lens onto two photodiodes of a balanced detector (Thorlabs, PDB120C). The photodiodes in the balanced photodetector can be physically separated, and have much smaller area than those used in a quadrant detector because the split beams can be focused without having to maintain the beam profile. Therefore, unlike

quadrant detectors, crosstalk between two photodiodes is negligible and the capacitance of the photodiodes can be reduced down to ~ 10 pF. Furthermore, the photocurrent from each diode is amplified individually before subtraction in a typical quadrant detector. While, in a balanced detector, it is possible to wire the photodiodes in a “push-pull” configuration and only the difference in photocurrent is amplified. This allows much higher gain, higher bandwidth and lower noise.

A simpler and better way of splitting the detection beam is illustrated in Fig. 2.9. The spatial splitting of the detection beam is performed using a mirror with a sharp edge, which was not commercially available at the time when the work [75] was done. Half of the beam is reflected by the mirror while the other half is not. Each half is then focused onto one of the two inputs of a fast balanced detector. A low noise and high gain transimpedance amplifier is used to convert the difference in the photocurrents of the two photodiodes to a voltage signal. When the microsphere is displaced from the center of the trap,

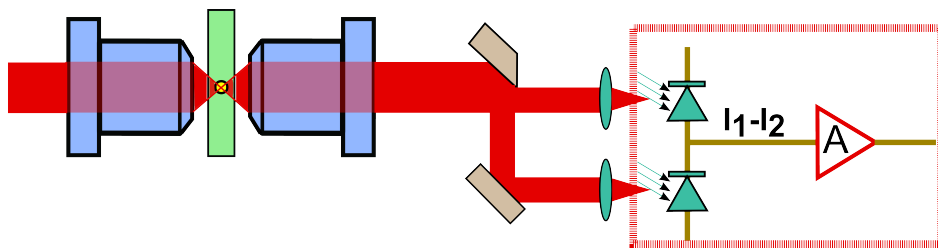


Figure 2.9: Illustration of the balanced detection system. The trapping beam is re-collimated by a second objective and split into two roughly equal halves by a cut mirror. Then, the two branches are focused onto two identical photodiodes by two lenses.

the beam is deflected, changing the power ratio of the two split beams. For small displacements, the detector output linearly depends on the displacement of the microsphere.

The output voltage signal V of the balanced detector is proportional to the displacement Δ of the microsphere. The relationship can be written as:

$$V = \Gamma P \chi Z \Delta, \quad (2.11)$$

where P is the detection beam power, Z is the detector transimpedance gain of the detector (volts/amp), χ is the responsivity of the photodiode (amps/Watt), and Γ is the optical gain of a particular system, which has a dimension of inverse length and has been discussed in the ray optics regime [76]. Based on this, the position sensitivity can be improved by increasing the optical gain, detection power, photodiodes' responsivity, and transimpedance gain. It is worth noting that the detector bandwidth is inversely proportional to the transimpedance gain; thus, they should compromise with each other [77].

This method has been extended to 3D to cool microspheres to mK in vacuum [78]. When studying Brownian motion in fluids, one-dimensional detection is sufficient because the equation of motion has no coupling terms and can be separated into three independent equations of motion, one for each Cartesian coordinate.

Noise in the Brownian motion measurements includes classical noise (mechanical vibration of the trapping and detection optics, laser intensity noise, laser pointing noise, electronic noise from the balanced photodetector

and acquisition card circuits) and quantum fluctuation noise (shot noise of the laser beam). Our experiments, discussed in detail in Chapter 4 and 6, are limited by classical noise at low frequencies and quantum shot noise at high frequencies.

One of the beauties of balanced beam detection is that the laser intensity noise, which is the major classical noise source in many experiments, is substantially cancelled out because it affects both balanced halves equally. Laser pointing noise can be significantly reduced by fiber coupling the laser into a single mode fiber. Noise caused by vibration of the optics can be minimized by mounting all the optics on a gas-bearing optical table. The laser pointing noise and noise caused by mechanical vibration can cause imbalance in two original balanced halves, which increases the leakage of laser intensity noise. Therefore, it is critical to align the cut mirror. Electronic noise can be reduced with our state-of-art detector design, which will be discussed in Chapter 4.

The fundamental limitation in our experiments is shot noise, the quantum fluctuations in the photon number arrives at the balanced detector. Photon number in a laser beam arrives the detector in a certain time interval obeys the Poisson statistics,

$$p(n) = \frac{\mu^{-n} e^{-\mu}}{n!} \quad (2.12)$$

with a expected value of μ and a standard deviation of $\sqrt{\mu}$. A 1064 nm laser beam with a power of 100 mW provides 5×10^{17} photons per second on average. Poisson statistics says we only know the photon flux per second within 7×10^8 .

Another great feature of balanced beam detection is that it is immune to phase fluctuation, which is about 1.3×10^{-9} radian in this example.

The absolute photon shot noise scales with \sqrt{P} , but the signal scales linearly with P , thus the noise floor in the position signal decreases as $1/\sqrt{P}$. Therefore, the signal-to-noise ratio can be improved by increasing the detection beam power. The maximum power can be limited by technical constraints of generating and detecting a high power laser beam, and by absorption and heating of the trapped particle or fluid.

Chapter 3

Theory for Brownian motion of a free sphere in a Newtonian fluid

The perpetual stochastic Brownian motion of particles in fluids is a result of fluctuations in the collisions with their surrounding fluid molecules. The fluid is often treated as a hydrodynamic continuum because the size of the particles of interest is much larger than that of the fluid molecules and the number of collisions averaged is huge during the time of interest.

The equation of motion for a particle exhibiting Brownian motion in a fluid can be described by the Langevin equation

$$m\ddot{\mathbf{x}} = \mathbf{F}_{fr} + \mathbf{F}_{th} + \mathbf{F}_{ext} \quad (3.1)$$

where \mathbf{F}_{ext} is any possible external force, which often refers to a harmonic optical trapping force $\mathbf{F}_{ext} = -K\mathbf{x}$. The gravitational force is often not considered in typical experiments. This is because the effect of the gravitational force is compromised by the optical trapping force, only resulting in a slight shift of the center of the trap. \mathbf{F}_{fr} is the friction force, which is a function of the particle's velocity $\dot{\mathbf{x}}$. Whereas, the randomly fluctuating thermal forces \mathbf{F}_{th} is assumed to be independent of velocity and varies extremely rapidly compared to the variations of velocity [74, 79]. The sum of \mathbf{F}_{fr} and \mathbf{F}_{th} is the total force

acting on the particle exerted by the fluid. \mathbf{F}_{fr} and \mathbf{F}_{th} are related through the fluctuation-dissipation theorem [10, 80] as

$$S_F(\omega) = 4k_B T \Re[\gamma(\omega)] \quad (3.2)$$

where \Re means the real part, $S_F(\omega)$ is the one-sided thermal force power spectral density and $\gamma(\omega)$ is the drag coefficient in frequency domain, which is related to the friction force as $\mathbf{F}_{fr}(\omega) = -\gamma(\omega)\mathbf{v}(\omega)$. The motion of the particle can be predicted by solving the Langevin equation [13, 14, 26, 81–85].

A more general and systematic approach to study Brownian motion is to utilize the Kubo-Green formula from the classical linear response theory [10, 80, 86–89], combined with the Wiener-Khinchin theorem [80]. In this chapter, we will give the frame work in terms of how to relate Brownian motion of a particle to its admittance, a generalized susceptibility. We will give a procedure of obtaining the position power spectral density (PPSD), velocity power spectral density (VPSD), mean square displacement (MSD), velocity autocorrelation function (VACF) and thermal force power spectral density (F-PSD) from the admittance. With this, the task turns to find the admittance for a specific system, which can be obtained based on the Langevin model. This approach will be used in this entire dissertation.

After establishing this general procedure, we will give the admittances in different systems: a free microsphere in a dilute fluid (air), a free microsphere in a dense liquid (water), an optically trapped microsphere in a dilute fluid and an optically trapped microsphere in a dense liquid, as well as the predictions

of Brownian motion in each system. In the end of this chapter, we will discuss the implications of the position and velocity measurements.

3.1 Linear response theory: Kubo-Green formula

Linear response theory describes how a system reacts to small magnitude external influences, which can be electromagnetic fields, forces, or temperature gradients and so on. Because of the small magnitude of the applied external influences, the response has a linear dependence on the external influences. For example, the response of a Newtonian fluid¹ to a small-magnitude external shear stress is to move with a shear rate of $\dot{\epsilon} = \sigma/\eta$, whose magnitude is determined by the viscosity η . This response does not depend on when the shear stress is applied, thus it is time-invariant.

Behaviors of linear time-invariant (LTI) systems can be described by linear response theory. What is a LTI system? For simplicity, we assume a LTI system only has one input $x(t)$ and one output $y(t)$, as shown in Fig. 3.1. If $y_1(t)$ and $y_2(t)$ are the two output signals corresponding to the two input signals $x_1(t)$ and $x_2(t)$ respectively, linearity of the system implies that the output of the system to input signal $\alpha_1 x_1(t) + \alpha_2 x_2(t)$ is $\alpha_1 y_1(t) + \alpha_2 y_2(t)$, where α_1 and α_2 are constants. Time-invariance requires that for any τ , $y(t+\tau)$ should be the output with input signal $x(t + \tau)$ if $y(t)$ is the output to the input $x(t)$, meaning the output of the system does not change with the same

¹Newtonian fluids are characterized by a single coefficient of viscosity, which depends on temperature but not on strain rate, as discussed in detail in Chapter 7.

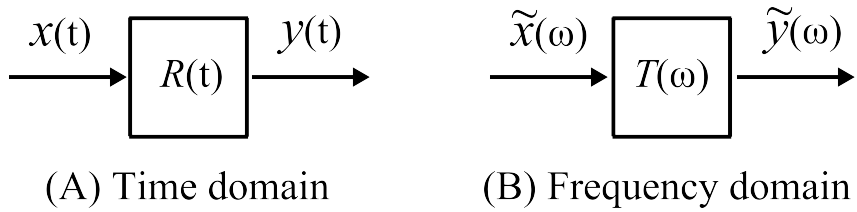


Figure 3.1: The response function of a linear time invariant system. (A) in time domain, (B) in frequency domain.

input applied at a different time.

The output of a LTI system can be obtained by the convolution of the input signal and its impulse response.

$$y(t) = \int_{-\infty}^{\infty} x(\tau)R(t - \tau)d\tau. \quad (3.3)$$

where $R(t)$ is the impulse response function of the system, which is the output of the system to a delta function impulse input. Because of the convolution theorem², the output in the frequency domain can be written as

$$\tilde{y}(\omega) = T(\omega)\tilde{x}(\omega). \quad (3.4)$$

where $\tilde{x}(\omega)$ and $\tilde{y}(\omega)$ are the Fourier transforms of the input and output signals respectively, and $T(\omega)$ is frequency response function, which is the Fourier transform of the impulse response $R(t)$. This frequency response function has many alternative names, such as susceptibility, admittance, mobility, transfer function and impedance, because of its many applications in physics, engineering and information theory.

²The Fourier transform of a convolution in the time domain equals the product of the Fourier transforms of each function in the frequency domain.

In this dissertation, we consider a micrometer-sized spherical particle in a liquid exhibiting Brownian motion at room temperature. We focus on the velocity response $\mathbf{v}(t)$ of a Brownian particle to a small magnitude external force $\mathbf{E}(t)$ exerted on the particle. Because the velocity of the microspheres is only on the order of $100 \mu\text{m/s}$, the Reynolds number $\text{Re} = 10^{-4} \sim 10^{-3}$. Thus, we can describe the fluid motion by the linearized time-dependent Navier-Stokes equation and the motion of the particle by the Langevin equation, which is a stochastic linear differential equation. Therefore, this system is linear. In addition, the response of the particle to the external force is independent of when the force is applied. Therefore, a particle undergoing Brownian motion is a linear time-invariant system. The corresponding frequency response function, exclusively called admittance in this dissertation, is defined as

$$\mathcal{Y}(\omega) = \frac{\tilde{\mathbf{v}}(\omega)}{\tilde{\mathbf{F}}(\omega)} \quad (3.5)$$

where $\tilde{\mathbf{v}}(\omega)$ and $\tilde{\mathbf{F}}(\omega)$ are the Fourier transforms of the velocity of the particle and the applied force in frequency respectively.

The Kubo-Green formula [10, 80, 86–89], sometimes is also called the first fluctuation-dissipation theorem, connects the dynamic admittance to the Fourier-Laplace transform of the velocity autocorrelation function by

$$\mathcal{Y}(\omega) = \frac{1}{k_B T} \int_0^\infty e^{i\omega t} C_v(t) dt, \quad (3.6)$$

where $C_v(t) = \langle v(t_0)v(t_0 + t) \rangle$ is the velocity autocorrelation function. As an example, the derivation of this relation for a Brownian particle described by

the Einstein-Ornstein-Uhlenbeck model [13, 81] is given in Appendix 1. Since the velocity autocorrelation function $C_v(t)$ is a real function, the admittance has a property,

$$\mathcal{Y}(-\omega) = \mathcal{Y}^*(\omega) \quad (3.7)$$

for all real ω , where $\mathcal{Y}^*(\omega)$ is the complex conjugate of $\mathcal{Y}(\omega)$.

3.2 The Wiener-Khinchin theorem

The Wiener-Khinchin theorem [80] states that the power spectrum $S_\epsilon(\omega)$ of a stationary random process $\epsilon(t)$ and its autocorrelation function are Fourier transform pairs³,

$$S_\epsilon(\omega) = \int_{-\infty}^{\infty} e^{i\omega t} \langle \epsilon(0)\epsilon(t) \rangle dt, \quad (3.8)$$

Here, we replace the arbitrary physical variable ϵ with the velocity of the particle,

$$S_v(\omega) = \int_{-\infty}^{\infty} e^{i\omega t} \langle v(0)v(t) \rangle dt, \quad (3.9)$$

We can get the velocity power spectral density $S_v(\omega)$ from the admittance $\mathcal{Y}(\omega)$ using Eq. (3.6) and Eq. (3.9).

$$S_v(\omega) = 2k_B T \Re[\mathcal{Y}(\omega)] \quad (3.10)$$

where $\Re[\mathcal{Y}(\omega)]$ means the real part of the admittance. This can be obtained simply by summing Eq. (3.6) and its complex conjugate and use the fact that

³The convention of the Fourier transform used in this dissertation is non-unitary, angular frequency.

the velocity autocorrelation function is even. The position power spectral density can be obtained from the velocity power spectral density

$$S_x(\omega) = \frac{S_v(\omega)}{\omega^2} = \frac{2k_B T \Re[\mathcal{Y}(\omega)]}{\omega^2} \quad (3.11)$$

Through the Wiener-Khinchin theorem, the velocity autocorrelation function $C_v(t)$ and position autocorrelation function $C_x(t) = \langle x(t_0)x(t_0 + t) \rangle$ can be obtained from their corresponding power spectra.

$$C_v(t) = \int_{-\infty}^{\infty} e^{-i\omega t} S_v(\omega) d\omega = 2k_B T \int_{-\infty}^{\infty} e^{-i\omega t} \Re[\mathcal{Y}(\omega)] d\omega \quad (3.12)$$

$$C_x(t) = \int_{-\infty}^{\infty} e^{-i\omega t} S_x(\omega) d\omega = 2k_B T \int_{-\infty}^{\infty} e^{-i\omega t} \frac{\Re[\mathcal{Y}(\omega)]}{\omega^2} d\omega \quad (3.13)$$

Furthermore, the mean square displacement (MSD) of the particle can be found from the position autocorrelation function $C_x(t)$ via this identity,

$$\langle \Delta x^2(t) \rangle = \langle [x(t_0 + t) - x(t_0)]^2 \rangle = 2\langle x(t)^2 \rangle - 2C_x(t) \quad (3.14)$$

Later, it will be shown in detail that the drag coefficient $\gamma(\omega)$ is directly related to the admittance. The thermal force power spectral density (FPSD, one-sided) acting on the particle can be obtained as,

$$S_F(\omega) = 4\pi k_B T \Re[\gamma(\omega)]. \quad (3.15)$$

If the admittance of the particle's velocity $\mathcal{Y}(\omega)$ and the drag coefficient $\gamma(\omega)$ in the system of interest are known, the statistical functions, such as MSD, PPSD, VPSD, VACF and FPSD, can be at least numerically obtained

from Eq. (3.10) to Eq. (3.15). Analytic solutions for these quantities might exist, however they are difficult to derive. The task in the next section will focus on obtaining an expression for the admittance in each different system.

3.3 Brownian motion in a Newtonian incompressible fluid

In this section, we will give the admittances for some systems and the corresponding predictions of Brownian motion. The fluid discussed in this section is incompressible and Newtonian, meaning its viscosity does not depend on frequency. It is necessary to note that we will only study Brownian motion in one dimension, which is sufficient since the Langevin equation has no coupling terms and can be decomposed into three independent equations of motion.

3.3.1 A free particle in a Newtonian incompressible fluid

The motion of a free particle in a fluid can be described by the Langevin equation,

$$m_p \ddot{x}(t) + \gamma(t) \dot{x}(t) = F_{th}(t). \quad (3.16)$$

where m_p and $x(t)$ are the mass and position of the particle respectively, $-\gamma(t)\dot{x}(t)$ and $F_{th}(t)$ are the drag force and thermal force on the particle respectively. To obtain the admittance, we replace $x(t)$ with $v(t) = \dot{x}(t)$

$$m_p \dot{v}(t) + \gamma(t)v(t) = F_{th}(t), \quad (3.17)$$

and take the Fourier transform the above equation

$$-i\omega m v(\omega) + \gamma(\omega)v(\omega) = F_{th}(\omega). \quad (3.18)$$

By definition, Eq. (3.5), the admittance of a free particle in a fluid is

$$\mathcal{Y}(\omega) = \frac{1}{-i\omega m + \gamma(\omega)}. \quad (3.19)$$

It is easy to verify the property of the admittance as given in Eq. (3.7).

3.3.1.1 A free particle in air

In a dilute fluid (whose density is much lower than that of a particle), such as gas, the friction force on a particle moving at velocity v is given by Stokes law $F_{fr} = -\gamma_s v$, where $\gamma_s = 6\pi\eta a$ is the Stokes drag coefficient, η is the viscosity of the air and a is the radius of the sphere. The drag coefficient is independent of frequency due to the fact that the density and viscosity of air are so small. Therefore, the admittance of a particle in air is

$$\mathcal{Y}(\omega) = \frac{1}{-i\omega m + \gamma_s} \quad (3.20)$$

According to Eq. (3.10), the velocity power spectral density of a free particle in air is

$$S_v(\omega) = \frac{2k_B T \gamma_s}{\gamma_s^2 + m^2 \omega^2} \quad (3.21)$$

Applying Eq. (3.11), the position power spectrum of a free particle in air is

$$S_x(\omega) = \frac{2k_B T \gamma_s}{\gamma_s^2 \omega^2 + m^2 \omega^4} \quad (3.22)$$

Furthermore, using Eq. (3.12), the velocity autocorrelation function of a free particle in air is

$$C_v(t) = \int_{-\infty}^{\infty} e^{-i\omega t} S_v(\omega) d\omega = \frac{k_B T}{m} e^{-\frac{\gamma_s}{m}|t|} \quad (3.23)$$

Finally, according to Eq. (3.13), the position autocorrelation function of a free particle in air is

$$C_x(t) = \frac{k_B T}{\gamma_s} t + \frac{m k_B T}{\gamma_s^2} - \frac{m k_B T}{\gamma_s^2} e^{-\frac{\gamma_s}{m} t} \quad (3.24)$$

The mean square displacement of the particle at thermal equilibrium with the air is [13]:

$$\langle \Delta x^2(t) \rangle = \frac{2m k_B T}{\gamma_s^2} \left(\frac{\gamma_s}{m} t - 1 + e^{-\frac{\gamma_s}{m} t} \right). \quad (3.25)$$

At long time scales, the MSD $\langle \Delta x^2(t) \rangle$ given here is the same as the prediction of Einstein's theory:

$$\langle \Delta x^2(t) \rangle = 2Dt \quad \text{for} \quad t \gg \tau_p \quad (3.26)$$

where $\tau_p = m_p / (6\pi\eta a) = \frac{2}{9} a^2 \rho_p / \eta$ is the momentum relaxation time of the particle. At very short time scales, the motion of the particle becomes ballistic and the MSD is

$$\langle \Delta x^2(t) \rangle = \frac{k_B T}{m} t^2 \quad \text{for} \quad t \ll \tau_p \quad (3.27)$$

There is no definition for the instantaneous velocity in the diffusive regime, whereas the instantaneous velocity is defined at very short time scales and can be measured as $v = \Delta x(\Delta t) / \Delta t$, when $\Delta t \ll \tau_p$ [13, 16]. The one

dimensional velocity distribution of the particle in air at thermal equilibrium can be described by the Maxwell-Boltzmann distribution

$$f(v) = \sqrt{\frac{m}{2\pi k_B T}} \exp\left(-\frac{mv^2}{2k_B T}\right). \quad (3.28)$$

This has been experimentally verified recently [16].

Based on the fluctuation-dissipation theorem, the thermal force power spectrum (one-sided) is

$$S_{th}(\omega) = 4k_B T \Re[\gamma] = 4k_B T \gamma_s. \quad (3.29)$$

The thermal force spectral density is flat, independent of frequency. The thermal force is completely random, and is often referred to as “white noise”, meaning the thermal force is delta correlated. Often, this system is referred to as the Einstein-Ornstein-Uhlenbeck model [13, 76, 81].

3.3.1.2 A free particle in liquid

The motion of a particle in a dense and viscous fluid is more complicated than that in air as hydrodynamic effects begin to manifest. The friction force on the particle at any instant depends on the history of the particle’s motion, not just the particle’s velocity at that instant, which is often called hydrodynamic memory effect. The expression for the friction force at time t_0 , exerted on a sphere with arbitrary velocity $v(t)$ defined in the interval $-\infty < t < t_0$, is [90]:

$$F_{fr}(t_0) = -\gamma_s v(t_0) - m_a \dot{v}(t_0) - \gamma_s \sqrt{\frac{\tau_f}{\pi}} \int_{-\infty}^{t_0} \frac{\dot{v}(t)}{\sqrt{t_0 - t}} dt \quad (3.30)$$

The first term on the right hand side is the Stokes friction force, and the second term is associated with the inertia of the co-moving fluid, where $m_a = \frac{1}{2}m_f = \frac{2}{3}\pi a^3 \rho_f$, which is often called the added mass, where ρ_f is the fluid density. The third term describes the hydrodynamic memory effect associated with the particle's acceleration history in a viscous unsteady flow. And $\tau_f = \frac{\rho_f a^2}{\eta}$ is the time for the vorticity in the fluid to travel one microsphere radius [15]. This leads to frequency dependent drag coefficient

$$\gamma(\omega) = \gamma_s(1 + \sqrt{-i\omega\tau_f}) - \frac{i\omega m_f}{2} = \gamma_s(1 + \tilde{\alpha} + \frac{1}{9}\tilde{\alpha}^2) \quad (3.31)$$

where $\tilde{\alpha} = \sqrt{-i\omega\tau_f}$. Compared to the Stokes drag coefficient γ_s in air, $\gamma(\omega)$ here has two more terms. The term, $-\frac{i\omega m_f}{2}$, leads to the effective mass of the microsphere in fluid which is the sum of the mass of the microsphere and half of the mass of the displaced fluid [26]:

$$m^* = m_p + \frac{1}{2}m_f, \quad (3.32)$$

The term, $\gamma_s\sqrt{-i\omega\tau_f}$, gives the memory kernel, which leads to the Basset force [91]

$$F_{Basset} = -6a^2\sqrt{\pi\rho_f\eta} \int_{-\infty}^t \frac{\dot{v}(t')}{\sqrt{t-t'}} dt' \quad (3.33)$$

The Langevin equation for a spherical particle in a liquid can be written as

$$m^* \ddot{x}(t) + 6\pi\eta a \dot{x}(t) + 6a^2\sqrt{\pi\rho_f\eta} \int_{-\infty}^t \frac{\dot{v}(t')}{\sqrt{t-t'}} dt' = F_{th}(t) \quad (3.34)$$

Strictly speaking, hydrodynamic effects exist in air as well. However they are roughly 10^3 times smaller than those in liquids and occur at time

scales 10^3 times shorter than the time scales of Brownian motion in air, namely $\tau_f = 10^{-3}\tau_p$.

By plugging Eq. (3.31) into Eq. (3.19), the admittance of a free particle in a liquid can be obtained as

$$\mathcal{Y}(\omega) = \frac{1}{-i\omega m + \gamma_s(1 + \sqrt{-i\omega\tau_f}) - \frac{i\omega m_f}{2}} \quad (3.35)$$

Following the procedure laid out early this chapter, Eq. (3.10) yields the velocity power spectrum of a free particle in a liquid as

$$S_v(\omega) = \frac{2k_B T \gamma_s (1 + \sqrt{\frac{1}{2}\omega\tau_f})}{\gamma_s^2 (1 + \sqrt{\frac{1}{2}\omega\tau_f})^2 + (m^*\omega + \gamma_s \sqrt{\frac{1}{2}\omega\tau_f})^2} \quad (3.36)$$

Next, according to Eq. (3.11), the position power spectrum of a free particle in a liquid is

$$S_x(\omega) = \frac{2k_B T \gamma_s (1 + \sqrt{\frac{1}{2}\omega\tau_f})}{\omega^2 \gamma_s^2 (1 + \sqrt{\frac{1}{2}\omega\tau_f})^2 + \omega^2 (m^*\omega + \gamma_s \sqrt{\frac{1}{2}\omega\tau_f})^2} \quad (3.37)$$

Finally, according to Eq. (3.12), the velocity autocorrelation function of a free particle in a liquid can be analytically solved [82, 83]

$$C_v(t) = \frac{k_B T}{m^*} \frac{\alpha_+ e^{\alpha_+^2 t} \operatorname{erfc}(\alpha_+ \sqrt{t}) - \alpha_- e^{\alpha_-^2 t} \operatorname{erfc}(\alpha_- \sqrt{t})}{\alpha_+ - \alpha_-}, \quad (3.38)$$

where

$$\alpha_{\pm} = \frac{3}{2} \cdot \frac{3 \pm (5 - 36\tau_p/\tau_f)^{1/2}}{\tau_f^{1/2} (1 + 9\tau_p/\tau_f)}. \quad (3.39)$$

At long time scales, the velocity autocorrelation function $C_v(t)$ approaches the famous $t^{-3/2}$ long time tail

$$C_v(t) \propto \frac{k_B T}{m^*} \frac{1}{t^{3/2}} \text{ for } t \rightarrow \infty. \quad (3.40)$$

This power law decay of the velocity autocorrelation function, which is normally referred to as long time tail and was first discovered by numerical simulations in late 1960s [92, 93], is drastically different from the exponential decay in the Stokes limit case, shown in Eq. (3.23). This prolonged correlation is due to the propagation of flow patterns within the fluid, which preserve the information of the particle's past motion.

At short time scales, the velocity autocorrelation function $C_v(t)$ approaches [17]

$$C_v(t) \propto \frac{k_B T}{m^*} (1 - \sqrt{t/\tau_v}) \quad \text{for } t \ll \tau_v, \quad (3.41)$$

where

$$\tau_v = \frac{\pi}{4} \cdot \frac{\tau_p^2}{\tau_f}.$$

At very short time scales, the velocity autocorrelation function $C_v(t)$ decreases faster as \sqrt{t} , rather than t in air due to the hydrodynamic effects.

The mean square displacement of a free microsphere in a liquid is [14, 85]

$$\langle \Delta x^2(t) \rangle = 2Dt \left[1 - 2\sqrt{\frac{1}{\pi}} \frac{\tau_f}{t} + \frac{8}{9} \frac{\tau_f}{t} - \frac{\tau_p}{t} + \Xi\left(\frac{\tau_p}{\tau_f}, \frac{t}{\tau_f}\right) \right], \quad (3.42)$$

where $D = k_B T / (6\pi\eta a)$ is the diffusion coefficient and the term $\Xi(\frac{\tau_p}{\tau_f}, \frac{t}{\tau_f})$ is

$$\Xi\left(\frac{\tau_p}{\tau_f}, \frac{t}{\tau_f}\right) = \frac{3}{t(5\tau_f - 36\tau_p)^{1/2}} \left(\frac{1}{\alpha_+^3} e^{\alpha_+^2 t} \operatorname{erfc}(\alpha_+ \sqrt{t}) - \frac{1}{\alpha_-^3} e^{\alpha_-^2 t} \operatorname{erfc}(\alpha_- \sqrt{t}) \right). \quad (3.43)$$

At long time scales, the MSD produces the same prediction as Einstein's theory:

$$\langle \Delta x^2(t) \rangle = 2Dt \quad \text{for } t \gg \tau_p, \tau_f. \quad (3.44)$$

At very short time scales, the Brownian motion becomes ballistic and the MSD reduces to

$$\langle \Delta x^2(t) \rangle = \frac{k_B T}{m^*} t^2 \quad \text{for } t \ll \tau_p \quad (3.45)$$

Based on the fluctuation-dissipation theorem, the thermal force power spectrum (one-sided) is

$$S_{th}(\omega) = 4k_B T \Re[\gamma(\omega)] = 4k_B T \gamma_s \left(1 + \sqrt{\frac{1}{2} \omega \tau_f} \right) \quad (3.46)$$

Because of the hydrodynamic effects, the thermal force spectral density is not flat anymore, but depends on frequency. The thermal force spectrum is not white anymore, instead it becomes colored. This means that the thermal force is not completely random. The thermal force autocorrelation function is

$$C_{F_{th}}(t) = 4\gamma_s k_B T \left[\delta(t) - \frac{1}{2} \sqrt{\frac{\tau_f}{\pi}} t^{-3/2} \right]. \quad (3.47)$$

The liquid adds a virtual mass $\frac{1}{2}m_f$ to the microsphere, since accelerating the microsphere requires a force both on the microsphere and the surrounding liquid. Therefore, the Maxwell-Boltzmann distribution needs to be changed to

$$f(v) = \sqrt{\frac{m^*}{2\pi k_B T}} \exp\left(-\frac{m^* v^2}{2k_B T}\right), \quad (3.48)$$

and the energy equipartition theorem need to be correspondingly modified as well to

$$\frac{1}{2} m^* \langle v^2 \rangle = \frac{1}{2} k_B T \quad (3.49)$$

where v is the velocity of the microsphere in one dimension. Thus the rms velocity is $v_{rms} = \sqrt{k_B T / m^*}$. This has been experimentally verified recently [18], and will be discussed in detail in Chapter 4.

This result apparently conflict with the equipartition theorem. The discrepancy can be resolved by considering the effects of compressibility of the liquid [94]. Below timescales on the order of $\tau_c = a/c$, where c is the speed of sound in the liquid, the compressibility of the liquid cannot be neglected. The particle will decouple from the surrounding liquid and the effective mass of the particle is just the bare mass of the particle.

3.3.2 An optically trapped microsphere in a Newtonian incompressible fluid

Experiments often require some sort of confinement of the particles to keep them in the detectable region. Often, the confinement is provided by an optical tweezer as discussed in Chapter 2, which provides a harmonic trapping force $F_{trap} = -Kx$ on the microsphere. This is true when the displacement of the microsphere is much smaller than 500 nm as discussed in Section 2.1.4.

The optical trap will change the admittance of the particle. Therefore, the MSD, PPSD, VPSD, XACF and VACF will change correspondingly. It is worth noting that the effective mass and thermal force spectrum are independent of optical trapping.

The motion of an optically trapped particle can be described by the

Langevin equation with a trapping term as

$$m\ddot{x}(t) + \gamma(t)\dot{x}(t) + Kx(t) = F_{th}(t). \quad (3.50)$$

The admittance can be obtained by replacing $x(t)$ with $v(t) = \dot{x}(t)$ and Fourier transform that equation

$$-i\omega mv(\omega) + \gamma(\omega)v(\omega) + \frac{Kv(\omega)}{-i\omega} = F_{th}(\omega). \quad (3.51)$$

So by definition, the admittance is

$$\mathfrak{Y}(\omega) = \frac{1}{-i\omega m + \gamma(\omega) + \frac{K}{-i\omega}}. \quad (3.52)$$

3.3.2.1 An optically trapped particle in air

As discussed before, the drag coefficient for a sphere in air is $\gamma(\omega) = \gamma_s$.

Therefore, the Langevin equation simplifies to

$$m\ddot{x}(t) + \gamma_s\dot{x}(t) + Kx(t) = F_{th}(t). \quad (3.53)$$

The cyclic frequency of the damped oscillator is $\omega_1 = \sqrt{\omega_0^2 - (2\tau_p)^{-2}}$, where $\tau_p = m/\gamma_s$ as defined before and $\omega_0 = \sqrt{m/K}$ is the trapping frequency. The system is underdamped when ω_1 is real ($\omega_0 > \frac{1}{2\tau_p}$), critically damped when $\omega_1 = 0$ and overdamped when ω_1 is imaginary ($\omega_0 < \frac{1}{2\tau_p}$). The motion of the particle behaves differently depending on whether the system is an underdamped or an overdamped system. Typical systems of a particle in air are underdamped due to strong trapping and low viscosity of air.

The admittance of an optically trapped particle in air is

$$\mathcal{Y}(\omega) = \frac{-i\omega}{m_p(\omega_0^2 - \omega^2) - i\omega\gamma_s} \quad (3.54)$$

According to Eq. (3.11), the position power spectrum of an optical trapped particle in air is [81]

$$S_x(\omega) = \frac{2k_B T \gamma_s}{m_p^2(\omega_0^2 - \omega^2)^2 + \omega^2 \gamma_s^2} \quad (3.55)$$

According to Eq. (3.10), the velocity power spectrum of an optical trapped particle in air is

$$S_v(\omega) = \frac{2k_B T \omega^2 \gamma_s}{m_p^2(\omega_0^2 - \omega^2)^2 + \omega^2 \gamma_s^2} \quad (3.56)$$

The position autocorrelation function and velocity autocorrelation function in underdamped systems (in air) are [81]

$$C_x(t) = \frac{A}{2\gamma_s m \omega_0^2} \left(\cos \omega_1 t + \frac{\sin \omega_1 t}{2\omega_1 \tau_p} \right) e^{-t/2\tau_p} \quad (3.57)$$

and

$$C_v(t) = \frac{A}{2\gamma_s m} \left(\cos \omega_1 t - \frac{\sin \omega_1 t}{2\omega_1 \tau_p} \right) e^{-t/2\tau_p} \quad (3.58)$$

The mean square displacement of an optically trapped particle at thermal equilibrium with the air is

$$\langle \Delta x^2(t) \rangle = \frac{2k_B T}{m \omega_0^2} \left[1 - e^{-t/2\tau_p} \left(\cos \omega_1 t + \frac{\sin \omega_1 t}{2\omega_1 \tau_p} \right) \right]. \quad (3.59)$$

At short times, the MSD has the same limit as that of the free particle, since for short intervals the trap appears as a constant force, whose time average is zero.

$$\langle \Delta x^2(t) \rangle = \frac{k_B T}{m} t^2 \quad \text{for} \quad t \ll \tau_p \quad (3.60)$$

The long time MSD of a trapped particle is very different from that of a free particle. Due to the confinement provided by the trap, the MSD reduces to a constant, which depends on trap strength and temperature

$$\langle \Delta x^2(t) \rangle = \frac{2k_B T}{m\omega_0^2} \quad (3.61)$$

The optical trap does not alter the velocity distribution of the particle and the thermal force spectral density on the particle. So they remain the unchanged.

$$f(v) = \sqrt{\frac{m}{2\pi k_B T}} \exp\left(-\frac{mv^2}{2k_B T}\right) \quad (3.62)$$

$$S_{th}(\omega) = 4k_B T \Re[\gamma(\omega)] = 4k_B T \gamma_s \quad (3.63)$$

In overdamped case, the position autocorrelation function of an optically trapped particle is [95]

$$C_x(t) = \frac{2\gamma_s k_B T}{2m^2} \left[\frac{e^{it/\tau_-}}{\tau_-^{-1}(\tau_+^{-2} - \tau_-^{-2})} - \frac{e^{it/\tau_+}}{\tau_+^{-1}(\tau_+^{-2} - \tau_-^{-2})} \right] \quad (3.64)$$

where

$$\tau_{\pm} = \frac{2\tau_p}{1 \pm 2\tau_p \omega_1} \quad (3.65)$$

and the velocity autocorrelation function of an optically trapped particle is

$$C_v(t) = \frac{2\gamma_s k_B T}{2m^2} \left[\frac{e^{-t/\tau_+}}{\tau_+(\tau_+^{-2} - \tau_-^{-2})} - \frac{e^{-t/\tau_-}}{\tau_-(\tau_+^{-2} - \tau_-^{-2})} \right] \quad (3.66)$$

3.3.2.2 An optically trapped particle in liquid

The Langevin equation for an optically trapped spherical particle in a liquid can be written as

$$m^* \ddot{x}(t) + 6\pi\eta a \dot{x}(t) + 6a^2 \sqrt{\pi\rho_f \eta} \int_{-\infty}^t \frac{\dot{v}(t')}{\sqrt{t-t'}} dt' + Kx(t) = F_{th}(t) \quad (3.67)$$

The admittance of an optically trapped particle in a liquid is

$$\mathfrak{Y}(\omega) = \frac{1}{-i\omega m + \gamma_s(1 + \sqrt{-i\omega\tau_f}) - \frac{i\omega m_f}{2} + \frac{K}{-i\omega}} \quad (3.68)$$

According to Eq. (3.10), the velocity power spectrum of an optically trapped particle in a liquid is

$$S_v(\omega) = \frac{2k_B T \omega^2 \gamma_s (1 + \sqrt{\frac{1}{2}\omega\tau_f})}{(m^*(\omega_0^2 - \omega^2) - \omega\gamma_s\sqrt{\frac{1}{2}\omega\tau_f})^2 + \omega^2\gamma_s^2(1 + \sqrt{\frac{1}{2}\omega\tau_f})^2} \quad (3.69)$$

According to Eq. (3.11), the position power spectrum of an optically trapped particle in a liquid is [85, 96]

$$S_x(\omega) = \frac{2k_B T \gamma_s (1 + \sqrt{\frac{1}{2}\omega\tau_f})}{(m^*(\omega_0^2 - \omega^2) - \omega\gamma_s\sqrt{\frac{1}{2}\omega\tau_f})^2 + \omega^2\gamma_s^2(1 + \sqrt{\frac{1}{2}\omega\tau_f})^2} \quad (3.70)$$

As $\omega \rightarrow 0$, the position power spectral density approaches

$$S_x(\omega \rightarrow 0) = \frac{2k_B T \gamma_s}{K^2}. \quad (3.71)$$

According to Eq. (3.12), the velocity autocorrelation function of a trapped microsphere in a liquid is [83, 85]

$$C_v(t) = \frac{k_B T}{m^*} \left[\frac{z_1^3 e^{z_1^2 t} \operatorname{erfc}(z_1 \sqrt{t})}{(z_1 - z_2)(z_1 - z_3)(z_1 - z_4)} + \frac{z_2^3 e^{z_2^2 t} \operatorname{erfc}(z_2 \sqrt{t})}{(z_2 - z_1)(z_2 - z_3)(z_2 - z_4)} \right. \\ \left. + \frac{z_3^3 e^{z_3^2 t} \operatorname{erfc}(z_3 \sqrt{t})}{(z_3 - z_1)(z_3 - z_2)(z_3 - z_4)} + \frac{z_4^3 e^{z_4^2 t} \operatorname{erfc}(z_4 \sqrt{t})}{(z_4 - z_1)(z_4 - z_2)(z_4 - z_3)} \right] \quad (3.72)$$

where $\operatorname{erfc}(z)$ is the complementary error function, and the coefficients z_1 , z_2 , z_3 , and z_4 are the four roots of the equation [85],

$$\left(\tau_p + \frac{1}{9}\tau_f \right) z^4 - \sqrt{\tau_f} z^3 + z^2 + \frac{1}{\tau_k} = 0, \quad (3.73)$$

where $\tau_k = \gamma_s/K$, and the coefficient of the z^3 term should be $-\sqrt{\tau_f}$, instead of $\sqrt{\tau_f}$ listed in [85]. The short time limit is the same as that of a free particle

$$C_v(t \rightarrow 0) = \frac{k_B T}{m^*} \quad (3.74)$$

At long time scales, the famous $t^{-3/2}$ long time tail in the velocity autocorrelation function is replaced by a more rapid decay [74, 97]

$$C_v(t \rightarrow \infty) \propto \frac{1}{t^{7/2}} \quad (3.75)$$

The mean square displacement of a trapped microsphere in a liquid is [83, 85]

$$\begin{aligned} \langle \Delta x^2(t) \rangle = & \frac{2k_B T}{K} + \frac{2k_B T}{m^*} \left[\frac{e^{z_1^2 t} \operatorname{erfc}(z_1 \sqrt{t})}{z_1(z_1 - z_2)(z_1 - z_3)(z_1 - z_4)} \right. \\ & + \frac{e^{z_2^2 t} \operatorname{erfc}(z_2 \sqrt{t})}{z_2(z_2 - z_1)(z_2 - z_3)(z_2 - z_4)} + \frac{e^{z_3^2 t} \operatorname{erfc}(z_3 \sqrt{t})}{z_3(z_3 - z_1)(z_3 - z_2)(z_3 - z_4)} \\ & \left. + \frac{e^{z_4^2 t} \operatorname{erfc}(z_4 \sqrt{t})}{z_4(z_4 - z_1)(z_4 - z_2)(z_4 - z_3)} \right] \quad (3.76) \end{aligned}$$

At short times, it has the same limit as the free particle shown in Eq. (3.45),

$$\langle \Delta x^2(t) \rangle = \frac{k_B T}{m^*} t^2 \quad \text{for } t \ll \tau_p \quad (3.77)$$

At long time scales, the optical trapping causes the MSD to plateau due to confinement

$$\langle \Delta x^2(t) \rangle = \frac{2k_B T}{K} = \frac{2k_B T}{m\omega_0^2} \quad (3.78)$$

The optical trap does not alter the velocity distribution of the particle nor the thermal force properties on the particle. So they remain the same as

those of a free particle,

$$f(v) = \sqrt{\frac{m^*}{2\pi k_B T}} \exp\left(-\frac{m^* v^2}{2k_B T}\right), \quad (3.79)$$

$$S_{th}(\omega) = 4k_B T \Re[\gamma(\omega)] = 4k_B T \gamma_s \left(1 + \sqrt{\frac{1}{2}\omega\tau_f}\right), \quad (3.80)$$

$$C_{F_{th}}(t) = 4\gamma_s k_B T \left[\delta(t) - \frac{1}{2}\sqrt{\frac{\tau_f}{\pi}} t^{-3/2}\right]. \quad (3.81)$$

3.4 Implications for position and velocity measurement

Am I really measuring this quantity correctly and precisely? This is probably one of the most frequent questions every experimentalist asks themselves. Every measurement system has noise, which sets a limit on the accuracy of the results. For example, one can not hear clearly on the phone in a noisy environment. To hear better, one can reduce the noise by blocking the other ear. Furthermore, one can not resolve a 1 MHz fluctuation in a voltage signal using a conventional multi-meter, because the multimeter, whose bandwidth is typically only around 10 kHz, simply cannot response that fast. To be able to measure some quantities precisely, the detection systems have to have high enough bandwidth and low enough noise level. The bandwidth is ultimately limited by the noise level. It is perhaps easier to interpret these systems in the frequency domain.

In this section, we will discuss the requirements (thus possible improvements) to measure the particle's position and instantaneous velocity precisely.

We consider a 3 μm diameter silica microsphere optically trapped (with stiffness $K = 150 \mu\text{N/m}$) in water and a 5 μm diameter BaTiO_3 microsphere optically trapped (with stiffness $K = 150 \mu\text{N/m}$) in acetone as two examples to understand the role of noise plays in our experiments. As discussed in Chapter 2, shot noise of the detection laser beam is the dominant noise source at high frequencies in our experiments, which is around $10^{-15} \text{ m}/\sqrt{\text{Hz}}$. In addition, shot noise is a “white” noise in position measurements, meaning it has a flat power spectrum in position.

3.4.1 Position measurement

The predictions of the position power spectral density S_x for the two systems are shown in Fig. 3.2. At low frequencies, the S_x in the two systems saturate at different levels due to the different particle sizes and fluid viscosities. Additionally, the signal dominates the shot noise in this range, and the area of the signal spectrum is larger than that of the noise. In the limit of large ω , the S_x in both systems decay with a slope of -3.5 on the log-log plot. Shot noise of three different levels ($10^{-16} \text{ m}/\sqrt{\text{Hz}}$, $10^{-15} \text{ m}/\sqrt{\text{Hz}}$, $10^{-14} \text{ m}/\sqrt{\text{Hz}}$) are shown as the dashed lines and set a limit on the detection bandwidth. At high frequencies, the signal is overwhelmed by shot noise. The lower the shot noise is, the higher the detection bandwidth is. The detection bandwidth is around 1.5 MHz, 6 MHz and 20 MHz (the frequencies where the S_x is equal to the shot noise) for the silica-water system with the three different shot noise levels respectively. As a comparison, the response bandwidth

of the detector used in this experiment is 58 MHz (Section 4.1.5), which is larger than the detection bandwidth set by the shot noise. For a fixed shot noise, the detection bandwidth is higher in the silica-water system than that in the BaTiO₃-acetone system. However, this does not necessary mean one can measure the position more accurately in the silica-water system than in the BaTiO₃-acetone system. What matters is the ratio of the area under the S_x within the bandwidth to the area under the S_x with infinite bandwidth, which gives the mean square value of the position signal. The mean square value of the position of the particles is directly related to the average kinetic

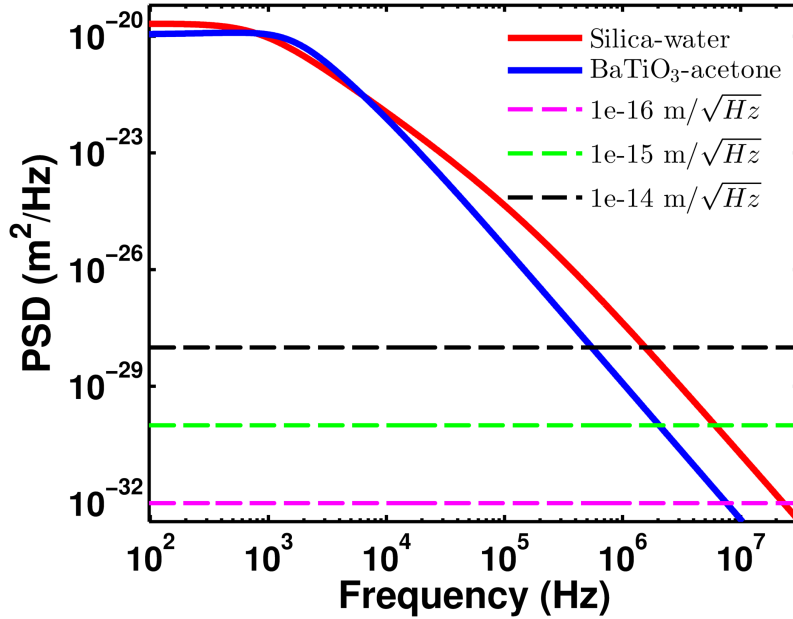


Figure 3.2: Comparison of position PSDs predicted for the two systems with different shot noise levels. The red solid line represents the silica-water system, the blue solid line is for the BaTiO₃-acetone system, and the dashed lines represent shot noise with three different levels ($10^{-16} \text{ m}/\sqrt{\text{Hz}}$, $10^{-15} \text{ m}/\sqrt{\text{Hz}}$, $10^{-14} \text{ m}/\sqrt{\text{Hz}}$).

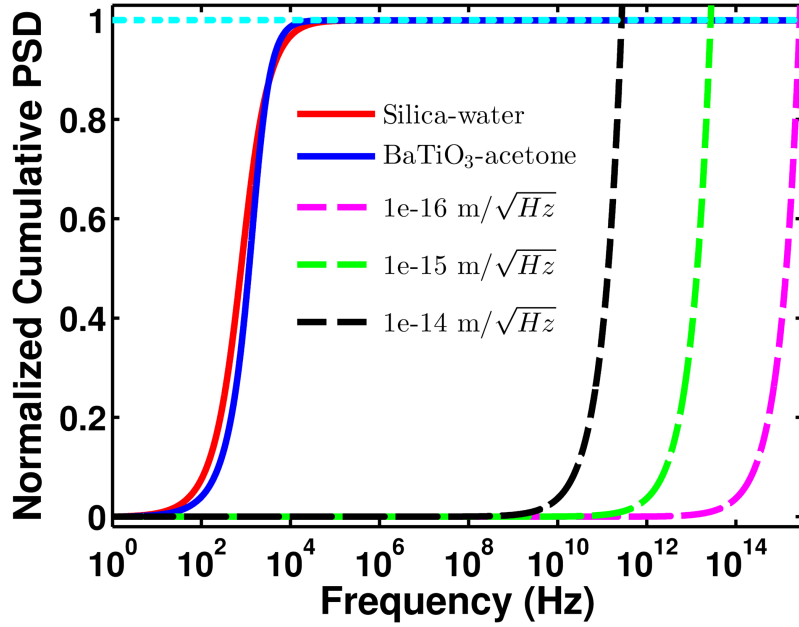


Figure 3.3: Cumulative position power spectra (normalized to $\langle x_{rms}^2 \rangle$) for the two systems. The red solid line represents the silica-water system, the blue solid line is for the BaTiO₃-acetone system, and the dashed lines represent the shot noise with three different levels (10^{-16} m/ $\sqrt{\text{Hz}}$, 10^{-15} m/ $\sqrt{\text{Hz}}$, 10^{-14} m/ $\sqrt{\text{Hz}}$).

energy through the energy equipartition theorem, $\langle x_{rms}^2 \rangle = k_B T / K$.

A better way to interpret this is to calculate the cumulative position power spectrum (the area under the S_x for a given bandwidth), denoted as CS_x . The cumulative position power spectra (normalized to the position mean square value $\langle x_{rms}^2 \rangle$) for the two systems are shown in Fig. 3.3. For both systems, the CS_x almost exactly reach the position variance $\langle x_{rms}^2 \rangle$ well before the shot noise becomes dominant. Therefore, we can measure the position quite precisely in both systems.

3.4.2 Instantaneous velocity measurement

Being able to measure the position accurately does not guarantee being able to measure the instantaneous velocity, because velocity measurement is much more vulnerable to high frequency noise. For a fixed magnitude noise in position, the higher the frequency of the noise is, the higher noise magnitude is in velocity.

Fig. 3.4 shows the predictions of the velocity power spectral densities, S_v , for the two systems. The velocity PSD can be obtained from position PSD through $S_v = \omega^2 S_x$. The flat shot noise in the position spectrum results in ‘violet’ noise⁴ in the velocity spectrum, with slope 2 on a log-log plot, as represented by the dashed lines. At low frequencies, the signal is much higher than the shot noise. Whereas at high frequencies, the shot noise dominates. In velocity PSD, the frequency range over which noise dominates the signal is the same as that in position PSD, but the shot noise impact on velocity measurements is much more significant than that on position measurements.

The cumulative velocity power spectra CS_v (normalized to the position variance $\langle v_{rms}^2 = k_B T / m^* \rangle$) for the two systems are shown in Fig. 3.5. Unlike the case of position measurements shown in Fig. 3.3, the shot noise becomes important before CS_v reaches the velocity mean square value $\langle v_{rms}^2 \rangle$. The CS_v in the BaTiO₃-acetone system reaches its $\langle v_{rms}^2 \rangle$ earlier than that in the silica-water system. Therefore, for a fixed shot noise level, one can measure the

⁴It is also known as differentiated white noise, due to its being the result of the differentiation of a white noise signal.

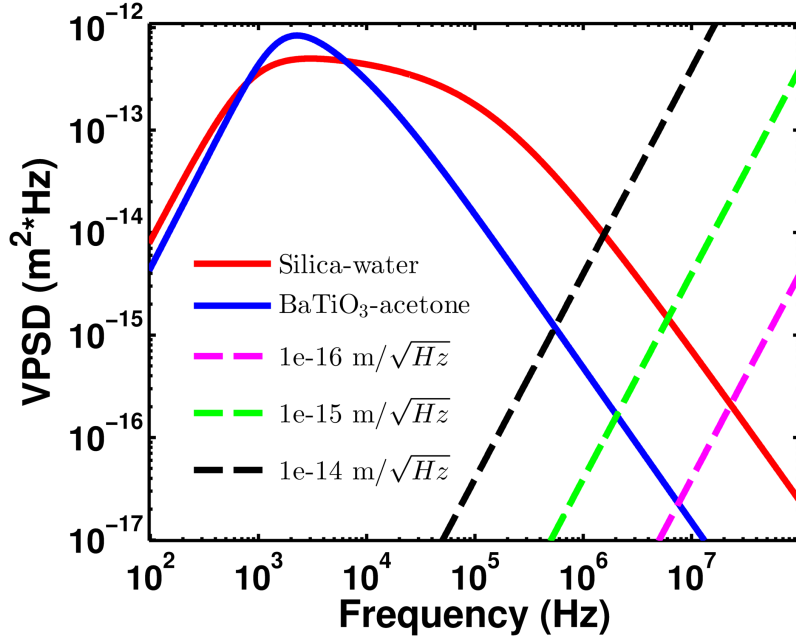


Figure 3.4: Velocity power spectra (normalized to $\langle x_{rms}^2 \rangle$) of the two systems with different shot noise levels. The red solid line represents the silica-water system, the blue solid line is for the BaTiO₃-acetone system, and the dashed lines represent the shot noise with three different levels (10^{-16} m/ $\sqrt{\text{Hz}}$, 10^{-15} m/ $\sqrt{\text{Hz}}$, 10^{-14} m/ $\sqrt{\text{Hz}}$).

instantaneous velocity in the BaTiO₃-acetone system more accurately than in the silica-water system. For instance, with a shot noise level of 10^{-15} m/ $\sqrt{\text{Hz}}$, one can measure 98% of the kinetic energy of the particle in the BaTiO₃-acetone system and only 89% of that in the silica-water system. It is worth noting that the contribution to the velocity from a frequency range from DC to 1 kHz is negligible, as shown in Fig. 3.5. Therefore the high pass filter (with a 3 dB cut-off frequency of 1 kHz) in the detector, will be discussed in Chapter 4, does not affect the instantaneous velocity measurements.

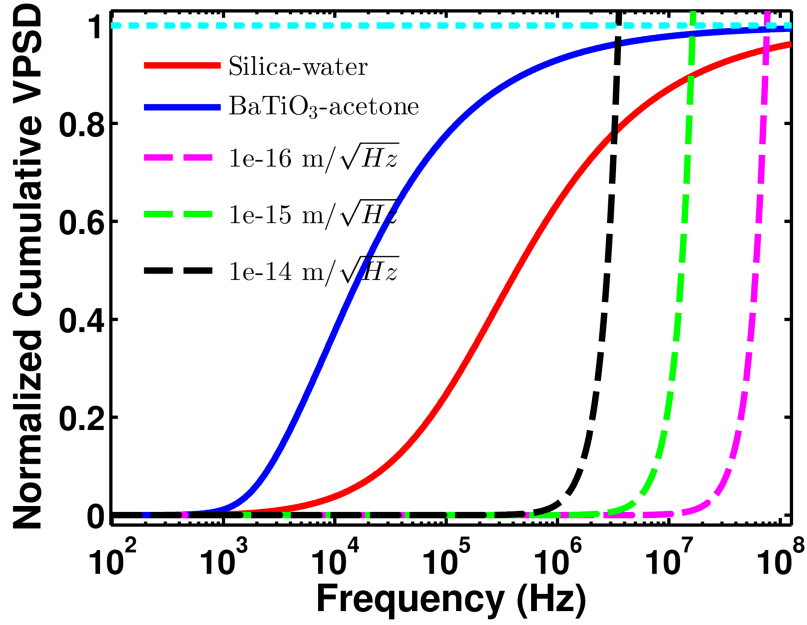


Figure 3.5: Cumulative velocity power spectra (normalized to $\langle v_{rms}^2 \rangle$) for the two systems. The red solid represent the silica-water system, the blue solid line is for the BaTiO₃-acetone system, and the dashed lines represent shot noise with three different levels ($10^{-16} \text{ m}/\sqrt{\text{Hz}}$, $10^{-15} \text{ m}/\sqrt{\text{Hz}}$, $10^{-14} \text{ m}/\sqrt{\text{Hz}}$). The cyan dotted line is for guiding the eye to 1.

In summary, to be able to measure the instantaneous velocity precisely, one needs to move the solid lines in Fig. 3.4 and 3.5 toward the left, namely, to slow down the dynamics of the particles and move the dashed lines toward the right, namely, to reduce the shot noise. To slow down the dynamics of a particle in a fluid, the particle's density needs to be high, the fluid's density needs to be low and the fluid's viscosity needs to be low as well. To reduce the shot noise level, the optical gain needs to be high, which can be optimized by optical alignments, and the detection beam power needs to be high.

3.4.3 Shot noise estimation

Our resolution of tracking a particle's motion is limited by the shot noise of the detection beam, which is the fundamental limitation in typical optical tweezer experiments. It is not trivial to predict the shot noise level, especially when the size of the microsphere is on the same order as the wavelength of the laser. Here we only discuss a simple estimation. The shot noise limited position sensitivity is estimated to be [98]

$$S_{shot} \approx 5 \times 10^{-16} G \left(\frac{a}{1\mu\text{m}} \right) \left(\frac{100\text{mW}}{P} \right)^{1/2} \left(\frac{1\mu\text{m}}{\lambda} \right)^{1/2} \text{ m}/\sqrt{\text{Hz}}, \quad (3.82)$$

where a is the particle's radius, λ is the wavelength of the laser in vacuum, P is the power of the detection beam and G is a geometrical factor that depends on a/λ and a/w_0 , where w_0 is the waist of the focused laser beam.

With our experimental conditions, the wavelength of the laser is $1.064 \mu\text{m}$, the detection power is around 150 mW and a is $1.5 \mu\text{m}$, thus Eq. (3.82) can be reduced to

$$S_{shot} \approx 3G \times 10^{-15} \text{ m}/\sqrt{\text{Hz}}, \quad (3.83)$$

Combining this and our experimental results on shot noise, the geometrical factor G is around 1 in our system.

Chapter 4

Testing the Maxwell-Boltzmann distribution using Brownian particles

As discussed in Section 3.4, a combination of high density microspheres, low density fluid, less viscous fluid, high refractive index mismatch, high optical gain, and high detection power is necessary to reach high signal-to-noise ratio (SNR) measurement of the velocity of a Brownian particle in liquid. In this chapter, we discuss the experiments measuring the instantaneous velocity of microspheres in fluids in detail. We will show how we optimize each aspect of the experiments to be able to measure the instantaneous velocity of a microsphere in liquid.

The exceptionally dense and high refractive index of BaTiO_3 microspheres in combination with acetone's low density and low viscosity slow the dynamic motion of the particle and improve our detection efficiency. Water-immersion objectives were used for diffraction-limited focusing and detection. A home made high power balanced detector was used to further improve the SNR.

Once the instantaneous velocity measurement becomes a reality, we will give the accurate test that we have done on the Maxwell-Boltzmann distribu-

tion and the energy equipartition theorem. The one dimensional Maxwell-Boltzmann distribution (MBD) for the velocities of molecules in an ideal gas in thermal equilibrium is

$$f(v) = \sqrt{\frac{m}{2\pi k_B T}} \exp\left(-\frac{mv^2}{2k_B T}\right) \quad (4.1)$$

where m is mass, k_B is Boltzmann's constant and v is the velocity. From the MBD, we can derive the energy equipartition theorem $\frac{1}{2}m\langle v^2 \rangle = \frac{1}{2}k_B T$. The actual velocity distribution in certain systems has been predicted to deviate from the standard MBD, for example, due to particle-particle interactions or relativistic effects [22–25]. A simple thought experiment showing a change in the velocity distribution by adding an arbitrary potential was proposed by Lord Kelvin in 1892 [22]. Additional deviations from the MBD have been predicted for low density plasmas [23], interstellar molecular hydrogen [24], and in the solar plasma by measuring neutrino flux [25]. In spite of predicted deviations, the MBD still holds as a remarkably robust approximation for most physical systems.

Previous work has reported an experimental verification of the MBD and energy equipartition theorem for a microsphere in air [16]. This result is to be expected, since the interaction of a particle with the surrounding air is fairly weak. In the case of a particle in a liquid, it is not so clear whether the MBD and energy equipartition theorem still hold, due to the strong hydrodynamic coupling. A measurement of the instantaneous velocity of a microsphere in a liquid has been reported [17], however, the sample size (2 million velocity

data points) was not sufficient to give a robust estimate of the distribution for velocities beyond 3 standard deviations from the mean.

In this chapter, we will report a more accurate test of the MBD and the energy equipartition theorem in three systems: a silica (SiO_2) glass microsphere in water, a silica glass microsphere in acetone and a barium titanate glass (BaTiO_3) microsphere in acetone. We find that the velocity distribution follows a modified Maxwell-Boltzmann distribution [21]

$$f(v) = \sqrt{\frac{m^*}{2\pi k_B T}} \exp\left(-\frac{m^* v^2}{2k_B T}\right) \quad (4.2)$$

where m^* is the effective mass of the microsphere in liquid, which is the sum of the mass of the microsphere m_p and half of the mass of the displaced liquid m_f , $m^* = m_p + \frac{1}{2}m_f$ [26]. As a result, the energy equipartition theorem also needs to be modified to $\frac{1}{2}m^*\langle v^2 \rangle = \frac{1}{2}k_B T$. The observation is based on a substantially larger number of data points compared to previous work [17], thus reducing the error in estimating the tails of the distribution.

These modifications to the Maxwell-Boltzmann distribution and the energy equipartition theorem are unnecessary when considering the effects of compressibility of the liquid [26]. At timescales below $\tau_c = a/c$, where c is the speed of sound in the liquid and a is the radius of the microsphere, the compressibility of the liquid cannot be neglected and the mean square value of velocity will approach the energy equipartition theorem. The effects of compressibility in our three systems are well separated from the regime of hydrodynamic Brownian motion and will be discussed in detail in Chapter 9.

4.1 Experimental setup

A simplified schematic of our experimental setup for measuring the instantaneous velocity of a Brownian particle in a liquid is shown in Fig. 4.1, containing two main parts: optical trapping and a high-bandwidth balanced detection which are discussed in detail in Chapter 2.

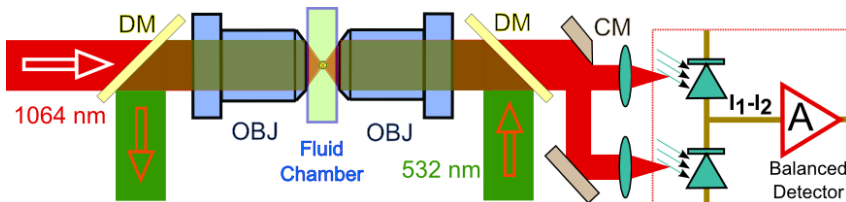


Figure 4.1: A simplified schematic of experimental setup for measuring the instantaneous velocity of a microsphere trapped by counter-propagating 1064 nm and 532 nm laser beams focused by microscope objectives (OBJ) in liquid. The 1064 nm laser is used to detect the horizontal motion of the particle using a high-power, high bandwidth balanced detector. DM: dichroic mirror, CM: D-shaped mirror.

As predicted in Section 2.1.4, we can use a single 1064 nm laser beam to trap silica microspheres both in water and acetone, while a dual-beam trap is required to trap BaTiO_3 microspheres. In the case of silica microsphere experiments, the microspheres are trapped by a single 1064 nm laser typically with a power of about 400 mW, focused by a water-immersion objective (denoted as the trapping objective). The trapping beam after passing through the trapped microsphere is re-collimated by an identical objective (denoted as the condensing objective). Now we refer the laser beam as the detection beam, which is split into two roughly equal halves before being focused onto a

home made balanced detector. The microsphere is introduced via a flow cell. In the case of BaTiO₃ microsphere experiments, another green 532 nm laser beam, focused by the condensing objective and counter-propagating with the 1064 nm laser beam, is used to cancel out the scattering force and double the gradient force. The 532 nm laser beam is used only for the purpose of trapping not for detection.

4.1.1 Optical setup

A detailed schematic of the optical setup is shown in Fig. 4.2. The red line represents the optical path of the 1064 nm trapping and detection beam. The green line represents the path of the 532 nm trapping beam. The 1064 nm trapping and detection beam is produced by an internally-stabilized non-planar ring oscillator (NPRO) laser (Innolight, Mephisto), with a maximum output power of 1.2 W. The 532 nm trapping beam is produced by a diode-pumped solid state laser (Coherent, Verdi V-10), with a maximum output power of 10 W. Both lasers are fiber coupled in order to reduce pointing noise and have a good spatial mode, which is important for tight focusing and high optical gain.

It is important that both lasers have low intensity fluctuations so as not to perturb the trapped particle. Much more critically, the detection laser has to have low intensity noise even with the significant suppression by the balanced beam detection system as discussed in Section 2.2. A home-made analog proportional-integral-derivative (PID) close loop controller [99] is used

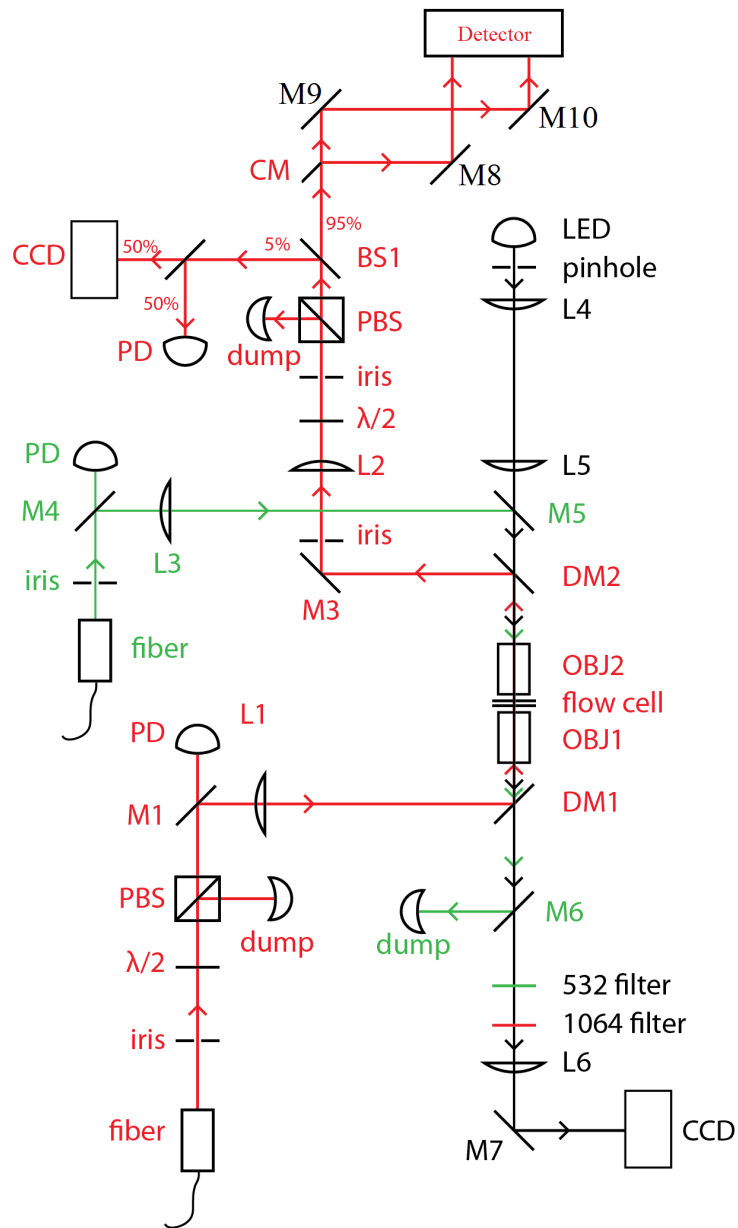


Figure 4.2: Schematic of optical setup for trapping and detection in liquids. The red line represents the optical path of the 1064 nm trapping and detection beam. The green line represents the path of the 532 nm trapping beam. The black line represents the optical path of the illumination beam. (Figure courtesy of Dr. Simon Kheifets.)

to both set the power and suppress the intensity noise for the 532 nm laser beam. The set point for the PID is generated by an analog-voltage-output board controlled by a LabVIEW control program, which will be discussed in Section 4.1.8. The output of the PID is fed into an acousto-optic modulator (AOM) controller which controls the radiofrequency (RF) power into an AOM, thus the optical power. The measurement point fed into the PID is provided by a photodiode collecting light leaked through mirror M4 downstream ($\sim 1\%$) of the fiber output, as shown in Fig. 4.2. It is important to place the AOM before the fiber input coupler since AOM typically degrades the beam profile and in some cases imparts pointing noise to the transmitted beam [100]. The resulting pointing noise can be eliminated by the fiber, resulting in intensity fluctuations that can be suppressed by the PID loop.

The power of the 1064 nm laser beam is controlled by a waveplate and a polarizing beam splitter (PBS) mounted before the fiber input coupler. Polarization of the laser beam, thus the transmission rate after the PBS, can be changed by rotating the waveplate. The waveplate is mounted on a motorized rotary mount which is controlled by the LabVIEW program to set the desired laser power. It is worth noting that we only set the 1064 nm beam to a certain power and do not use a PID-like close loop to stabilize the power since laser already has a built-in “noise eater”. In fact, we tried to do so and ended up producing more noise at certain frequencies. Because our 1064 nm laser beam has much less noise than the 532 nm laser beam does, it was used as the detection beam.

Two identical finite-conjugate (160 mm) water-immersion microscope objectives (LOMO, OM-25), with nominal NA 1.23, focal length 2.5 mm, and working distance 140 μm , are used in our experiments. Because the objectives are designed for visible light with a wavelength range from 400 nm to 700 nm, there was slight chromatic aberration for the 1064 nm laser beam, resulting in a slightly larger working distance and focal length than the numbers listed above. The cover-glass-correction-collar adjustment ring is set to its lowest setting, 0.1 mm, on both objectives. Because the objectives are designed for visible light, the transmission at 1064 nm is only 60%, which was estimated by measuring the transmission through the two lenses with the flow cell in between. Water immersion objectives are a better choice over oil immersion objectives as the fluids we use, water and acetone, more closely match water than typically used oils. Water-index-matching oil ($n = 1.33$, Carl Zeiss), instead of water, is used between the flow cell and each objective due to its low evaporation rate.

Both of the trapping lasers emerge from their fiber output couplers as collimated beams, with $1/e^2$ waists of 1.5 mm. Since the objectives are finite conjugate (160 mm), a lens is used to focus each beam 160 mm away from the objective: L1 for the 1064 nm beam and L3 for the 532 nm beam. These shall be referred to as the conjugate lenses. The 1064 nm beam is focused by L1, then reflected by DM1 and focused by OBJ1. It was then re-collimated by OBJ2, and reflected by DM1 to be used for detection. The 532 nm beam is focused by L3, reflected by M5, transmitted through DM2, focused by OBJ2,

re-collimated by OBJ1, transmitted through DM1 and reflected by M6 into a beam dump. DM1 and DM2 are dichroic mirrors with high transmission for 532 nm and high reflectivity for 1064 nm.

Although our 1064 nm laser has a maximum power of 1 W, the maximum power for trapping and detection are around 400 mW and 150 mW respectively after various losses from fiber coupling, the objectives, and scattering from a trapped particle. 150 mW detection power is close to the detector's damage threshold.

In the case of experiments with BaTiO₃ microspheres, the 532 nm laser is used to form a counter-propagation trapping configuration with the 1064 nm laser beam. This is necessary to cancel out the strong scattering force thus form a stable trap for BaTiO₃ microspheres. Although our 532 nm laser can easily produce more than 1 W power after the fiber, the best power ratio between the 1064 nm and 532 nm beams is around 1.5 to balance the scattering forces from two beams. This optimal power ratio depends on the alignment detail of the two trapping beams.

There are two reasons why we did not split our 1064 nm laser beam into two halves to form counter-propagation trapping configuration. One is if we do that the position sensitivity will be decreased since the maximum detector beam power will be cut in half. The other is that much effort is required to avoid forming interference between the two trapping beams, like shifting the laser frequencies by an AOM.

4.1.2 Microspheres and fluids

Experiments in this dissertation are performed using silica microspheres ($n = 1.46$, $\rho = 2.0 \text{ g/cm}^3$, Bangs Laboratories) and BaTiO_3 microspheres ($n = 1.9$, $\rho = 4.2 \text{ g/cm}^3$, Mo-Sci L.L.C) in either HPLC-grade water ($n = 1.33$, $\rho_f = 0.998 \text{ g/cm}^3$, $\eta = 0.9 \times 10^{-3} \text{ Pa}\cdot\text{s}$) or acetone ($n = 1.35$, $\rho_f = 0.789 \text{ g/cm}^3$, $\eta = 3.17 \times 10^{-4} \text{ Pa}\cdot\text{s}$) at $22 \pm 1 \text{ }^\circ\text{C}$.

High sphericity of the microspheres is necessary to eliminate the rotational motion contribution due to asymmetry of the microspheres, and this was confirmed by scanning electron microscope images (FEI Quanta 650 SEM) as shown in Fig. 4.3. The microspheres were sputtered with about 10 nm Au/Pd (with 60/40 ratio) before taking images. The silica microspheres have a much narrower size distribution than the BaTiO_3 microspheres do. We further investigate the size distribution of the microspheres used in this experiment using an optical microscope. The samples were prepared between two coverslips in a water solution and examined under an optical microscope (OMAX). Typical

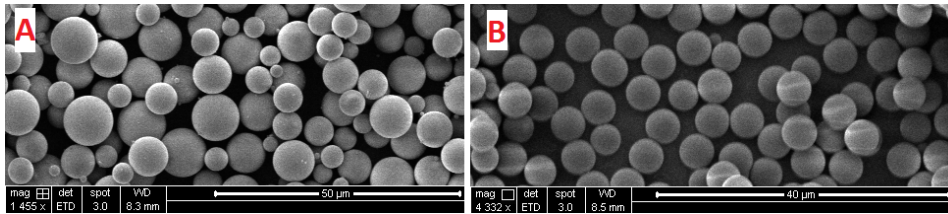


Figure 4.3: Scanning electron microscope images of the microspheres (sputtered with about 10 nm Au/Pd with 60/40 ratio) demonstrate high sphericity. A: The widely-dispersed (0.1-10 μm) BaTiO_3 glass microspheres; B: The mono-dispersed silica glass microspheres.

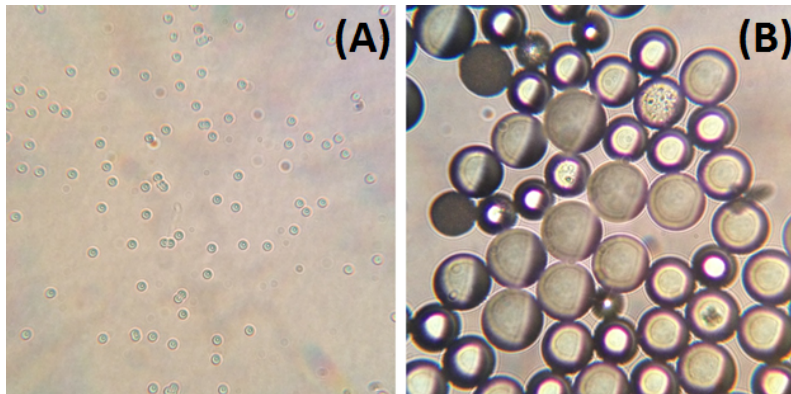


Figure 4.4: Optical microscope images of microspheres. (A), Silica microspheres have a uniform size (around $3 \mu\text{m}$). (B), BaTiO_3 microspheres have a wide range of size (1 to $15 \mu\text{m}$).

optical microscope images, shown in Fig. 4.4, are analyzed using ImageJ, an image processing program.

The procedure to measure particle size using ImageJ is first to convert images to monochrome and then set the contrast at the threshold such that only the particle can be recognized, as shown in Fig. 4.5. Then the reticles in the raw images are used to calibrate the image magnification. ImageJ provides a way to eliminate black spots shown in in Fig. 4.5(B) with sphericity below a certain threshold and calculate the area of individual black spots, thus the diameter of the particles.

We took about a thousand such images to achieve good statistics. As shown in Fig. 4.6, the silica microspheres have a much narrower size distribution, with a diameter of $3.22 \pm 0.12 \mu\text{m}$, corresponding to a 4% coefficient of variation (defined as the ratio of the standard deviation to the mean). While

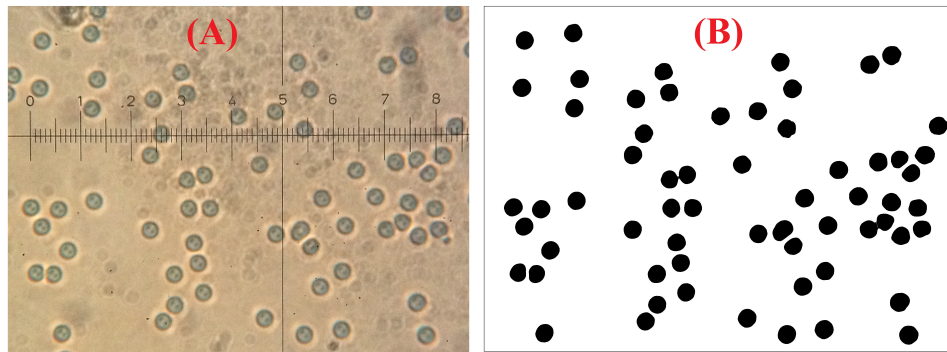


Figure 4.5: Illustration of a measurement of particle size using ImageJ. (A), The raw image of silica microspheres. The reticle is used to calibrate the image magnification. (B), The processed image of silica microspheres.

BaTiO₃ microspheres have a diameter of $10.6 \pm 2.7 \mu\text{m}$, corresponding to a 25% coefficient of variation.

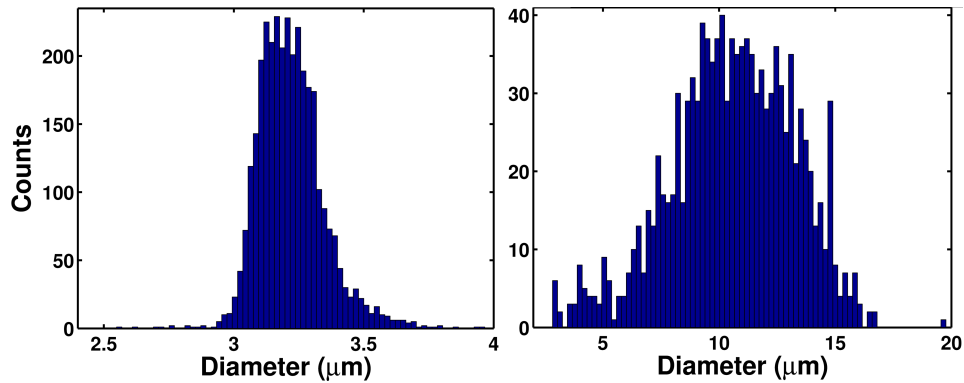


Figure 4.6: The size distribution of the microspheres used in the experiments. (A), Silica microspheres have a pretty uniform size, $3.22 \pm 0.12 \mu\text{m}$. (B), BaTiO₃ microspheres shows much broader size distribution, $10.6 \pm 2.7 \mu\text{m}$.

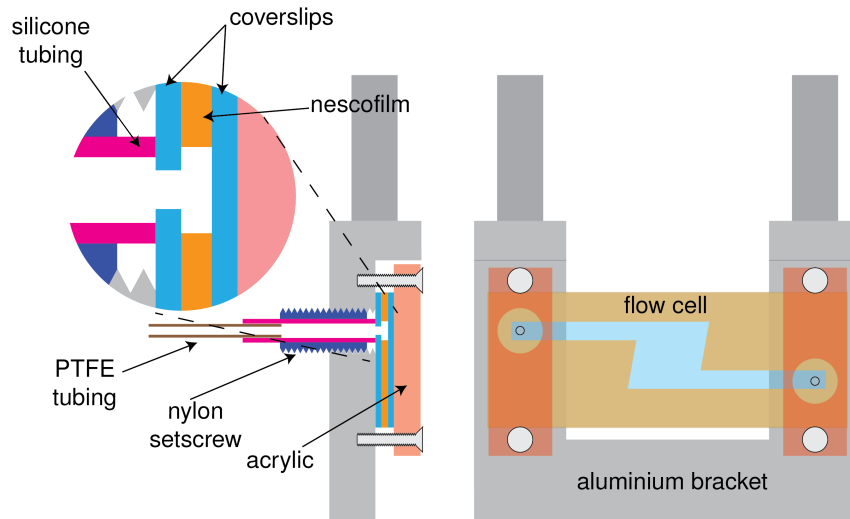


Figure 4.7: Schematic of the flow cell shape with cliff, mounting geometry, and fluid connections. (Figure courtesy of Dr. Simon Kheifets.)

4.1.3 Flow cell

The microspheres and fluids are introduced via a microfluidic flow cell to the optical trapping region, which is closely based on a design from the Minitweezers project in Dr. Bustamante's lab¹. An illustration of the chamber, mounting and plumbing connections is shown in Fig. 4.7. Once a particle is trapped, a pure solution is gently flowed through the cell to clear out stray microspheres and other contaminants.

The fluid chamber was constructed within a layer of thermoplastic nescofilm² (Bando Chemical Ind. LTD., 80 μm thickness) sandwiched be-

¹ <http://tweezerslab.unipr.it/cgi-bin/mt/home.pl> [Online; accessed July 20, 2015]

² Nescofilm is obsolete as of July 2015. Meltonix and PEEK films might be suitable

tween two number 0 microscope coverslips (Ted Pella, Gold Seal) with thickness $\sim 100 \mu\text{m}$. Therefore, the thickness of the flow cell is about $280 \mu\text{m}$. The inner dimension of flow cell is designed to be as wide as possible to avoid any boundary effects. As discussed in Chapter 5 and 6, a rule of thumb is that the sphere-wall distance needs to be 10 times larger than the microsphere radius. The maximum allowable thickness of the flow cell is limited by the combined working distance of the two objectives, which is roughly $300 \mu\text{m}$ (considering the chromatic aberration for the 1064 nm beam). It is important to note that the microspheres have to be confined by the optical trap in the center of the flow cell, leaving about $40 \mu\text{m}$ distance on each side to the coverslip wall. The microsphere can not be too large ($D \leq 8 \mu\text{m}$), otherwise boundary effects are inevitable with current flow cell design.

The coverslips have dimensions of $60 \text{ cm} \times 24 \text{ cm}$ and one of the two coverslips on each flow cell has a hole drilled in it with $\sim 1 \text{ mm}$ diameter on each side, which serve as the inlet and outlet of the flow cell. The holes were made on a CNC milling machine in the Physics department machine shop. The Nescofilm was cut with a “Z” shape removed slot that aligns with the holes on the coverslip, as shown in Fig. 4.7. The cut slot in the Nescofilm forms the fluid flow channel.

After careful holes-alignment, the “sandwich” was then placed on a hotplate with temperature set to around 150° C for about 5 minutes, with an

alternatives.

aluminium weight on top of it to apply pressure and distribute heat evenly. During this process, the thermoplastic Nescofilm melts and adheres to the coverslip firmly. The sealed flow cell was mounted to an aluminium bracket using acrylic plates. The aluminium bracket has threaded holes which align with the drilled holes in the coverslip. Silicone tubing was inserted inside a drilled nylon setscrew. When the set screw was screwed into the aluminium bracket, the tubing was pressed onto the coverslip and a pressure seal formed around the drilled hole. PTFE tubing was used to connect the needle of a syringe to the nylon tubing. The outside of the PTFE tubing was pressed into the inside of the silicone tubing and held by friction.

The flow cell and bracket were placed between the two objectives by a 3-axis translation stage. The translation stage provided adjustment of the location of the optical trap within the trapping chamber.

Commercially available microspheres are typically in dry powder form, which is quite convenient since we can dissolve them into any fluids of interest. The solution with appropriate concentration was prepared by adding a small quantity of the microsphere powder to a vial of high purity water or acetone. Ultra-sonication was used to separate the microspheres and degas possible micro-bubbles in the fluids. The sonicated solution was then transferred from the vial to a 1 cc syringe, which was mounted in a syringe pump (NE-300). The syringe pump allowed introduction of the solution into the flow cell at a precisely controlled flow rate. The exit port of the flow cell was connected to a waste collection vial mounted on the optical table below the flow cell.

BaTiO₃ microspheres are more difficult to trap than silica particles, since they have much faster terminal velocities than that of silica microspheres, due to their higher densities. This is even more apparent when trapping BaTiO₃ microspheres in acetone as compared to trapping silica microspheres in water due to acetone’s low viscosity. The terminal velocity of a 6 μm diameter BaTiO₃ microsphere in acetone can reach $\sim 100 \mu\text{m/s}$. As shown in Section 4.1.4, the imaging view is only about 50 μm , saying the BaTiO₃ microspheres only spend maximum 0.5 s in the view. It is worth noting that it was not possible to pick up a sunken microsphere at the bottom of the flow cell due to strong distortion in the trapping by the Nescofilm. The flow cell was designed to have a “cliff”, where the Nescofilm was over-cut at an angle so that falling microspheres fell away from the Nescofilm edge, as shown in Fig. 4.7. BaTiO₃ microspheres can be caught near the cliff region. Once a particle is trapped, the flow cell is translated to move the trap away from the cliff area to avoid boundary effects and reduce the odds of interference from stray particles.

4.1.4 Imaging

Optical imaging of the trapping region is necessary to make it easier to align optics, trap particle and detect stray particles in the trap. It also provided information about the size and type of trapped microspheres. We save the image of the trapping region for each experimental run.

The optical imaging, as shown in Fig. 4.2 (black optical path), is con-

structured under a bright-field imaging configuration (also known as Köhler illumination), in which the rays from any point of the light source in the specimen plane are parallel. The light source used for optical imaging is a ~ 100 mW red LED with a 15 degree angle of divergence. A red LED was used for the light source rather than a white one because much of the spectrum of the light emitted by a white LED would be blocked by the dichroic mirrors DM2 and M5. A short focal length lens (25 mm) near the LED was used to focus the LED light through a pinhole to achieve a better spatial mode.

The image of the microsphere will be located 160 mm away from the objective OBJ1. This virtual image plane is imaged onto a CCD camera using a single achromatic lens, M6. The CCD camera was installed on a translational stage to be able to adjust the location of the image plane with a range up to 8 cm. This was necessary because the trap minimum was not necessarily at the beam focus due to a shift in trap center caused by the scattering force, as discussed in Chapter 2.

Two typical images of trapped microspheres are shown in Fig. 4.8. The image of a BaTiO_3 microsphere in acetone has a much sharper interference pattern due to the high refractive index of BaTiO_3 microspheres. These images provide us a convenient estimate of the size of the trapped particles, the number of particles trapped and detection of stray trapped particles. They were also useful in aligning optics.

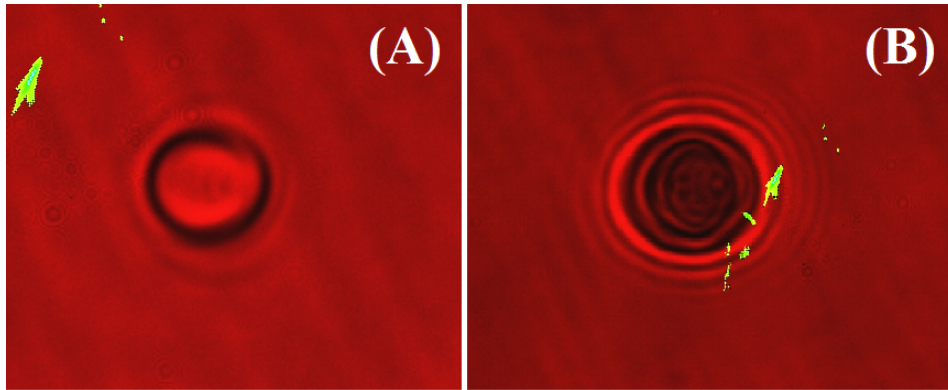


Figure 4.8: Typical images of trapped microspheres. (A), a silica microsphere in water; (B), a BaTiO_3 microsphere in acetone, which has a much sharper interference pattern due to high refractive index of BaTiO_3 microspheres. (Green spots are dead pixels in the camera.)

4.1.5 Balanced beam detection system

The 1064 nm beam after the objective OBJ2, referred as the detection beam, is reflected by a dichroic mirror DM2, and a mirror with a specific coating for 1064 nm, M3 before re-collimated by lens L2. This was followed by a half waveplate and PBS, which were used to adjust the power to the detector. A beam splitter (BS1) was used to reflect a small portion of the detection beam (5%) for monitoring, which was split again with a 50/50 beam splitter between a photodiode and a CCD camera. The photodiode was used to monitor the power to the detector, which is based on the power ratio between the light on the photodiode and the balanced detector is fixed. The CCD camera was used to monitor the beam profile, which contained information about the location (or absence) of the trapped microspheres within the trapping beam. It was also used to investigate the dependence of the optical gain on the optical alignment,

as shown Fig. 4.10.

The remaining light (95%) was split into roughly equal halves by a cut mirror CM before shining on a home-made, high power, AC-coupled balanced detector, which is one of key improvements to increase the position sensitivity to 2×10^{-15} m/ $\sqrt{\text{Hz}}$ and resolved the instantaneous velocity of microspheres in liquids. The home-made detector has a much higher operating power (up to 100 mW per photodiode) than commercially available detectors (Thorlabs balanced detectors, 5 mW per photodiode). The main limitation to the maximum operating power is thermal damage to the photodiodes, which can be increased by using larger area photodiodes and a lower bias voltage. However, both of them increase the detector's capacitance C_p , thus decrease the bandwidth of a transimpedance amplifier as the bandwidth goes with $\sqrt{1/C_p}$ [77]. The photodiodes (Excelitas, C30641) used in our detector have a 1 mm diameter, a responsivity of 0.75 A/W at 1064 nm, and a capacitance of less than 50 pF with a more than 5 V reverse bias. The detail of the electronic circuits has been already presented [76].

The bandwidth of the detector can be increased by reducing the gain, as the bandwidth is reversely proportional to gain [77]. The high detection power, thus high photocurrents made this possible. The gain of our home-made detector is around 1 kV/A, while commercially available balanced detectors have gains on the order of 10^5 V/A. With a 75 mW beam incident on each photodiode, 56 mA photocurrents are created per photodiode. In our experiments, the imbalance between two balanced beam halves is about 0.5% due

to Brownian motion of microspheres. Therefore, a $280 \mu\text{A}$ photocurrent imbalance is amplified by the transimpedance amplifier with a gain of about 1 kV/A , resulting in a 280 mV output.

However, the low frequency noise, particularly noise caused by vibrations and the harmonics of the 60 Hz AC power line, would create a large imbalance in the photocurrent, which can saturate the op-amp in the transimpedance amplifier and the digitizer. A high pass filter, with a -3 dB cutoff frequency at $\sim 1 \text{ kHz}$, is placed before the transimpedance amplifier to overcome this potential problem. As discussed in Section 3.4, this high pass filter does not affect the instantaneous velocity measurements since the contribution from frequency range between DC and 1 kHz is negligible.

Although high pass filtering did not significantly affect velocity measurement, it increased the complexity of data analysis. The detail of the transfer function of the detection system, combination of the balanced detector and digitizer board, is needed to correctly analyze the data. This transfer function was measured using a high-speed function generator (6060B, Fluke) and a 1300 nm wavelength telecommunications LED (HFBR-1119TZ, Avago Technologies) with a flat response function from DC up to as 500 MHz , as a variable frequency input source. The detection system has a flat band from 1 kHz to 58 MHz (at -3 dB points), as shown in Fig. 4.9 [17, 76]. The fall-off at high frequencies is not only due to the detector bandwidth but also the bandwidth of the digitizer, which is 125 MHz .

In summary, there are three main advantages of our home-made de-

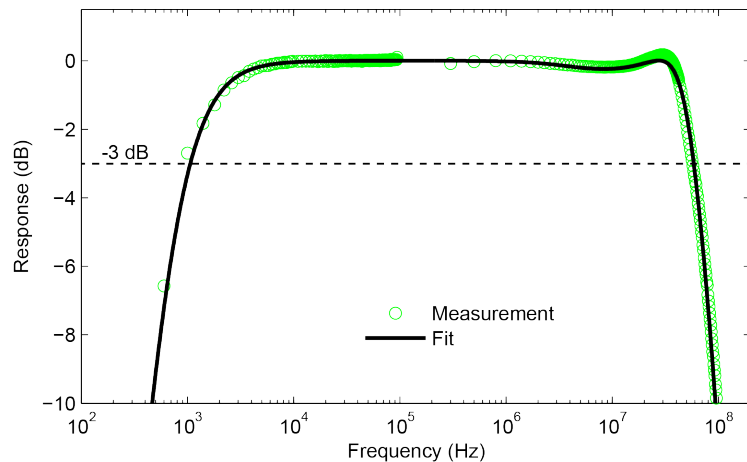


Figure 4.9: Measured AC detector transfer function and its fit. The green dots show the amplitude of the response function recorded through a 125 MHz bandwidth digitizer. The black line shows a fit. The resonant peak near 30 MHz is due to the digitizer [17].

tector as compared to commercially available detectors: larger photodiodes enables higher damage threshold, lower transimpedance gain enables larger bandwidth, and AC coupling before the transimpedance amplifier avoids saturation in op-amp and digitizer.

4.1.6 Optical alignment procedure

In this section, we will list the procedure to align the optics to achieve stable trapping and high optical gain.

To align the 1064 nm trapping beam, the conjugate lens L1 was removed and mirrors M1 and DM1 were used to align the 1064 nm beam such that it was perpendicular to and centered on the fixed objective OBJ1. The back-reflections from the multiple internal surfaces OBJ1, transmitted through

dichroic mirrors DM1 and M6, were incident on the imaging CCD camera. During this process, the 1064 nm filter was removed to let 1064 nm back-reflections pass through. The two mirrors M1 and DM1 were used to adjust the beam angle and position until the back reflections were symmetric and concentric.

Then both objectives were temporarily removed, and the path of the collimated beam marked with two irises to define the optical axis on the detection side of the trap. Both objectives were then installed, along with the flow cell. The conjugate lens L1 was replaced, and its position was adjusted until the back reflections on the CCD were again symmetric and concentric. OBJ2 was aligned so that the transmitted beam was collimated and centered on both irises.

The signal-to-noise ratio (SNR) is extremely sensitive to the axial position of the condensing objective, as shown in Fig. 4.10. The condensing objective was moved along a range of about 60 μm , showing there was a position with minimum SNR, which is obtained by comparing the mean square displacement at long time scales with and without a silica microsphere. The correlation between SNR and detection beam profile made it easy to optimize the SNR.

In the case of experiments with BaTiO_3 microspheres, counter-propagating dual-beam optical traps are particularly sensitive to misalignment, which can create artificial heating through non-conservative trajectories. We make use of the stable trapping of silica microspheres to align the dual beam trap.

With a silica microsphere trapped in the 1064 nm tweezer, conjugate lens L3 was removed, and M4 and M5 were used to align the 532 nm trapping beam to be symmetric and concentric around the trapped silica microsphere, observing from the image camera. Then the conjugate lens L3 was placed in a position where it focused the 532 nm beam at roughly 160 mm away from the condensing objective. With the 1064 nm beam aligned using the procedure given above, the 532 nm beam can be precisely aligned by minimizing the change in position when blocking one of these two laser beams, which was physically realized by moving the conjugate lens L3. This alignment method is based on the fact that silica microspheres can be trapped in both single 1064 nm and 532 nm beams. If the green beam was misaligned, the position of the

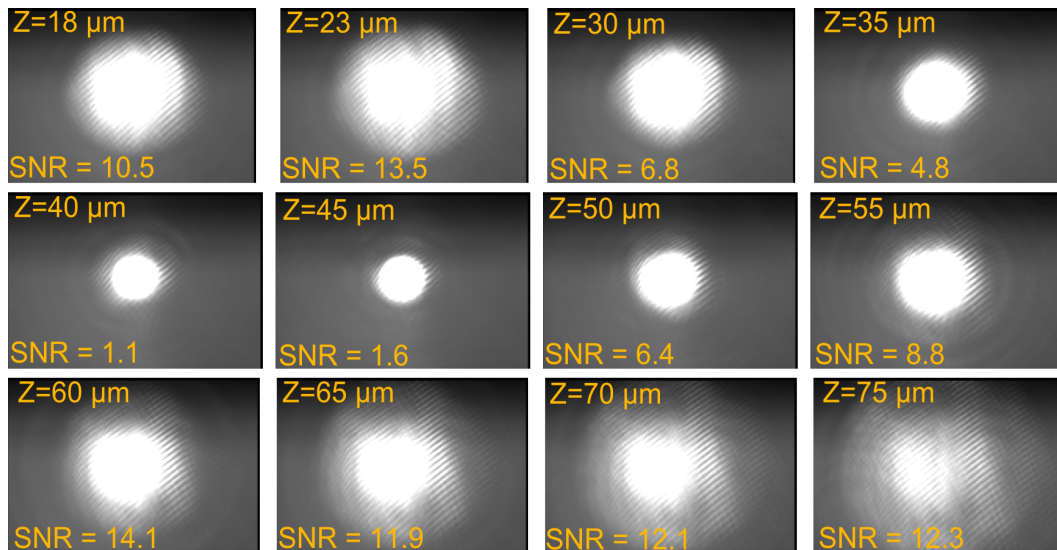


Figure 4.10: Dependence of signal to noise ratio and detection beam profile on the camera on axial position of the condensing objective. Z is micrometer reading of the position of the condensing objective.

trapped silica microsphere would shift. It is worth noting that the optimal power ratio between the 1064 nm and 532 nm beams is around 1.5.

4.1.7 Cut mirror and detector alignment

As discussed before, it is critical to balance the two detection beam halves. This requires near perfect alignment of the cut mirror. With a DC coupled detector, the cut mirror can be aligned by zeroing the output of the detector. To align the cut mirror for an AC coupled detector, we applied a 2 MHz (at which, the classical noise is negligible) intensity modulation on the 1064 nm laser. The cut mirror can be aligned by minimizing a 2 MHz intensity modulation in the output of the detector, if misaligned, the 2 MHz signal is visible. When the cut mirror is perfectly aligned, this intensity modulation will vanish. The 2 MHz intensity modulation on the 1064 nm is generated by applying an oscillating voltage signal to an electro-optic modulator (EOM) on 1064 nm optical path between the waveplate and PBS, as discussed in Section 4.1.1. The polarization of the 1064 nm laser beam, as well as the transmission power after the PBS, can be altered by changing the voltage to the EOM. This allowed for precise alignment of the cut mirror. The amplitude modulation was switched off during acquisition of Brownian motion data.

In order to automatically align the cut mirror, we installed it on a motorized stage (Thorlabs, MT1-Z8), which can be controlled by a motor controller (Thorlabs, TDC001). The LabVIEW program recorded the 2 MHz modulation signal from the balanced detector and has an algorithm to decide

which way to move the cut mirror to minimize the 2 MHz modulation signal. This automation makes it possible to take huge amount of data, which is necessary to test the Maxwell Boltzmann distribution with a high statistical precision.

As shown in Fig. 4.2, the split beams were guided by mirrors M8, M9 and M10 to the AC-coupled detector. This alignment was optimized for each photodiode with the LabVIEW program in alignment mode, which is discussed in detail in Section 4.1.8. The detection power was typically set to 10 mW with the 2 MHz modulation on, and the cut mirror was placed in a position that the detection beam was completely guided to one or the other photodiode. The alignment for each photodiode was done by maximizing the 2 MHz modulation signal. The strength of the 2 MHz signal of the two branches with the same modulation strength was roughly the same, indicating that the gains in the two branches were similar. This is necessary to eliminate the common mode noise.

4.1.8 LabVIEW control and data acquisition system

The whole experiment was controlled by a home written LabVIEW program, which can be operated in three modes: experimental conditions setting mode, alignment mode and data saving mode. In the experimental conditions setting mode, the power of both the 1064 nm and 532 nm laser beams can be remotely set by this program. In the alignment mode, the 2 MHz modulation signal is turned on automatically for aligning the cut mirror and the AC

detector. In the data saving mode, the 2 MHz modulation signal is turned off automatically and program acquires the signal from the balanced detector and saves it in binary files. Along with the data from the detector, with each acquisition the control program also save images from the optical imaging and beam profile monitoring cameras, the powers of the trapping beams, and the power of the beam entering the detectors.

The outputs of the balanced detector were digitized using a high bandwidth, ultra low noise board (GaGe, Razor 1622 Express CompuScope). The board had two channels, 16 bits of resolution, a maximum sampling rate of 200 Ms/s, and a maximum sample length of 2^{27} consecutive samples, which enables about 1 s of continuous recording for one continuous trajectory at maximum sampling rate.

4.2 Methods for data analysis

The voltage signal recorded by the digitizer is, to a very good approximation, proportional to the displacement of the particle in the trap. We first compute the voltage power spectral density (voltage PSD) by means of a Fast Fourier Transform (FFT) of the voltage signal, followed by taking the magnitude squared and appropriately scaling it [96]. The measured magnitude of the transfer function of the detection system is then squared and divided out of this voltage PSD. We also calculate the PSD of velocity fluctuations (velocity PSD) by applying a discrete derivative operator appropriately (in the frequency domain) on the position PSD.

The Wiener-Khinchin theorem [80] states that for wide-sense stationary random processes, the power spectral density and auto-correlation of a physical quantity are Fourier transform pairs. We make use of this to calculate the position auto-correlation function (PACF), up to a calibration constant, by FFT of the voltage PSD. In doing so, we discard data points at frequencies much lower than the trap frequency (~ 1 kHz), which are plagued by low-frequency noise in the system, and assume that the power spectrum is flat in this region. We then calculate the MSD from the PACF.

A least squares fit of the experimental MSD to the theory is then used to extract three parameters: the calibration factor that converts the voltage to length scales, the particle's diameter and the trapping constant. We use the velocity PSD to compute the VACF, again by use of the Wiener-Khinchin theorem.

The stochastic thermal force PSD is calculated from the position PSD using the Green's function obtained from using the hydrodynamic drag coefficient in the Langevin equation, but without assuming the fluctuation-dissipation theorem. The Green's function for the Langevin equation may be written as [15],

$$\hat{G}(\omega) = \frac{1}{-\omega^2 m_p - i\omega\gamma(\omega) + K} \quad (4.3)$$

The position is related to the driving thermal force through

$$\hat{x}(\omega) = \hat{G}(\omega)\hat{F}_{th}(\omega) \quad (4.4)$$

Thus, having numerically calculated the position PSD from experimental data, the thermal force PSD can be calculated from it through

$$S_F(\omega) = |\hat{G}(\omega)|^{-2} S_x(\omega) \quad (4.5)$$

4.3 Experimental results and discussion

This section describes the results of our analysis of Brownian motion trajectories acquired from the digitizer. We took many trajectories of the same microsphere in the three systems: a silica microsphere in water (677 trajectories), a silica microsphere in acetone (143 trajectories) and a BaTiO₃ microsphere in acetone (43 trajectories). The number of trajectories was limited by the maximum time for which the particles could be trapped without contamination. Each trajectory contains 2^{27} position data points, corresponding to ~ 1 s, recorded at the digitizer's maximum sampling rate of 200 MSa/s. The data was acquired with the digitizer's 25 MHz anti-aliasing filter enabled.

4.3.1 Mean square displacement

The voltage to position conversion factor C , trapping strength K as well as particle diameter d were obtained by a least-squares fit of the measured MSD to the hydrodynamic prediction, given by Eq. (3.76). The experimental and theoretical MSDs for each system are shown in Fig. 4.11. For the silica microsphere in water, fitting gives a diameter of $d = 3.06 \pm 0.05 \mu\text{m}$ and a trap strength of $K = 188 \pm 15 \mu\text{N/m}$. For the silica microsphere in acetone, fitting gives a diameter of $d = 3.98 \pm 0.06 \mu\text{m}$ and a trap strength of $K = 50 \pm 8$

$\mu\text{N}/\text{m}$. For the BaTiO_3 microsphere in acetone, fitting gives a diameter of $d = 5.36 \pm 0.06 \mu\text{m}$, and a trap strength of $K = 342 \pm 13 \mu\text{N}/\text{m}$. The uncertainty of each fit parameter is determined from the variance in the results of independent MSD fits of all measured trajectories for each system. It is worth noting that the measured trapping stiffness in the case of silica in water is pretty close the trapping stiffness prediction calculated by generalized Lorentz-Mie scattering as discussed in Section 2.1.4. Whereas the measured trapping stiffness in the case of silica in acetone is much lower than the prediction, which is due to non-diffraction limited focusing caused by the larger aberration in

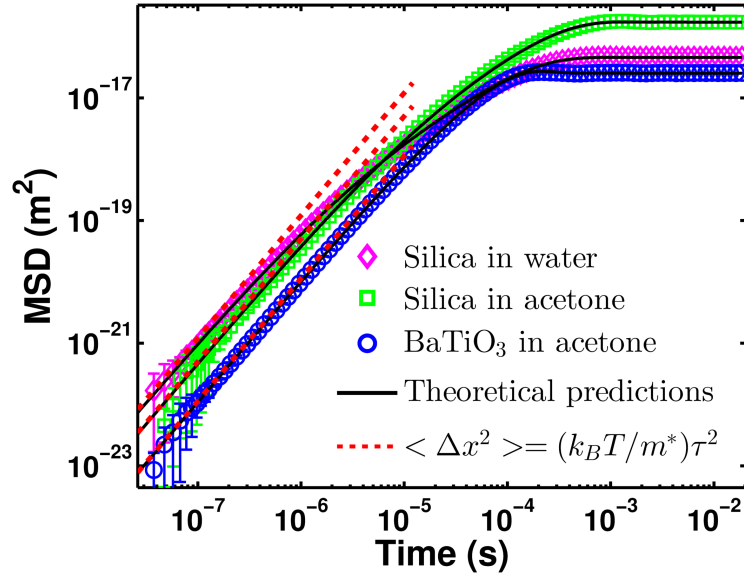


Figure 4.11: Double logarithmic plot of the experimental and theoretical MSDs of a typical 1-s trajectory for a trapped microsphere in liquid in three systems. Red dashed lines indicate the MSD of a particle moving at constant velocity $v_{rms}^* = \sqrt{k_B T / m^*}$; black lines are theoretical MSDs; magenta diamonds represent silica in water data; green squares represent silica in acetone data; blue circles represent BaTiO_3 in acetone data.

acetone using a water immersion objective.

The optical trapping causes the MSD to plateau around $\tau_k = \gamma_s/K$, the time scale during which the particle experiences a drift back towards the trap center, before the purely diffusive regime is reached. The red dotted lines in Fig. 4.11 represent the MSD of a microsphere moving at a constant velocity of $v_{rms}^* = \sqrt{k_B T/m^*}$, as the modified equipartition predictions predicts. The predicted v_{rms}^* are 327 $\mu\text{m/s}$, 227 $\mu\text{m/s}$ and 104 $\mu\text{m/s}$ for systems with the silica microsphere in water, silica microsphere in acetone, and BaTiO₃ microsphere in acetone respectively. At short timescales, the measured MSDs overlap with the red dash-dot lines, a signature that the motion of the particles is well into the ballistic regime.

4.3.2 Position power spectral density

The position power spectral densities for the three systems are shown in Fig. 4.12. At high frequencies, the signal is dominated by photon shot noise of the detection beam. As a result, the position PSD flattens at high frequencies. The level of shot noise was obtained by a least-squares fit of the measured position PSD to the sum of the theoretical position PSD and a constant noise level. The position PSD flattens at high frequencies due to shot noise of the detection beam at $2.4 \times 10^{-15} \text{ m}/\sqrt{\text{Hz}}$, $9.1 \times 10^{-15} \text{ m}/\sqrt{\text{Hz}}$ and $1.8 \times 10^{-15} \text{ m}/\sqrt{\text{Hz}}$ for a silica microsphere in water, a silica microsphere in acetone and a BaTiO₃ microsphere in acetone respectively. The detection beam power was maximized to reduce the relative shot noise. The system with

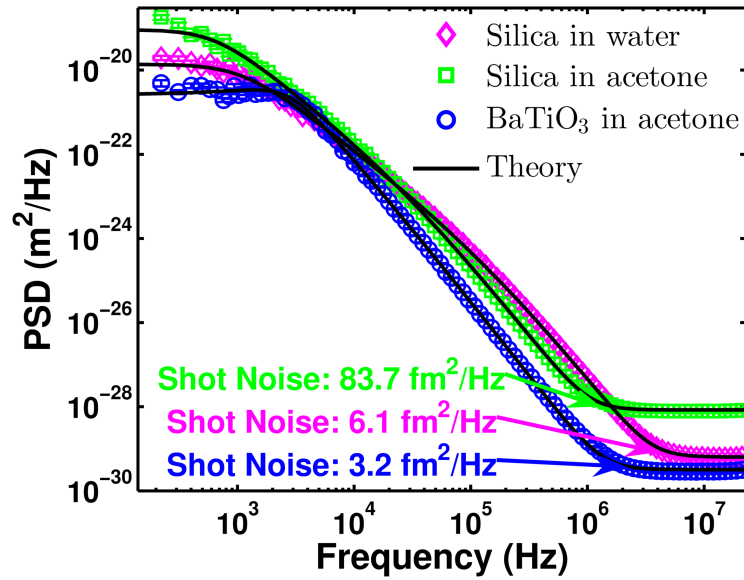


Figure 4.12: The position power spectra of the same trajectories as shown in Fig. 4.11. The position PSD flattens at high frequencies due to shot noise of the detection beam at $2.4 \times 10^{-15} \text{ m}/\sqrt{\text{Hz}}$, $9.1 \times 10^{-15} \text{ m}/\sqrt{\text{Hz}}$ and $1.8 \times 10^{-15} \text{ m}/\sqrt{\text{Hz}}$ for a silica microsphere in water, a silica microsphere in acetone and a BaTiO₃ microsphere in acetone respectively. Black lines are the sum of theoretical position PSD and a constant shot noise; magenta diamonds represent silica in water data; green squares represent silica in acetone data; blue circles represent BaTiO₃ in acetone data.

a silica microsphere in acetone has less refractive index mismatch compare to the system with a silica microsphere in water, which results in a lower position sensitivity. Due to the high refractive index of BaTiO₃ microspheres, the system with a BaTiO₃ microsphere in acetone has the highest position sensitivity.

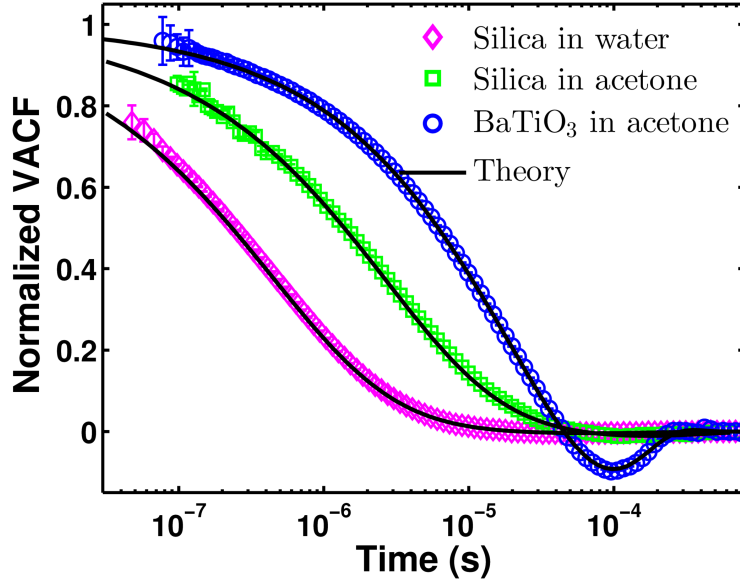


Figure 4.13: Semi-logarithmic plot of the experimental and theoretical velocity autocorrelation functions $C_v(t)$ for the same trajectories as shown in Fig. 4.11. The $C_v(t)$ are normalized by $\langle (v_{rms}^*)^2 \rangle$ for each system. Black lines correspond to the full hydrodynamic theory [83]; magenta diamonds represent silica in water data; green squares represent silica in acetone data; blue circles represent BaTiO₃ in acetone data.

4.3.3 Velocity autocorrelation function

The velocity autocorrelation function $C_v(t)$ (normalized by $\langle (v_{rms}^*)^2 \rangle$) for the three systems are shown in Fig. 4.13. The experimentally resolved maximum normalized VACF values are 0.75, 0.85 and 0.95 for three systems: a silica microsphere in water, a silica microsphere in acetone and a BaTiO₃ microsphere in acetone respectively. The VACF of the silica microsphere in acetone decays slower than the one in water, which is because of the lower viscosity of acetone as compared to water. The VACF of the BaTiO₃ microsphere in acetone decays slower than that of the silica microsphere in acetone,

which is because of the higher density of the BaTiO₃ microsphere as compared to that of the silica microsphere. Therefore, the use of BaTiO₃ microspheres and acetone facilitates instantaneous velocity measurement. The oscillation in the VACF observed in the BaTiO₃ microsphere in acetone system is due to the strong optical trapping. In fact, the oscillation also exists in the other two systems as well, however this is not obvious in a log-linear plot.

4.3.4 Instantaneous velocity measurements and Maxwell-Boltzmann distribution testing

In this section, we will show that our detection bandwidth is not limited by the time response of the detection system, rather than being limited by the noise, particularly the shot noise in the detection beam, as discussed in Section 3.4. We then illustrate the improvements we made to achieve instantaneous velocity measurements in the frequency domain.

The velocity power spectral density (velocity PSD) and cumulative velocity PSD (normalized to $k_B T/m^*$) for the three systems for the same data as in Fig.4.11 are shown in Fig. 4.14, 4.15 and 4.16. The velocity PSD represents how the power of the velocity of the microspheres is distributed over the different frequencies. The cumulative velocity PSD shows the fraction of velocity signal contained in a frequency from DC to a given frequency, and can be interpreted as showing the minimum measurement bandwidth necessary to measure the average kinetic energy within a given uncertainty. Magenta lines in Fig. 4.14 represent the shot noise contribution as calculated using the re-

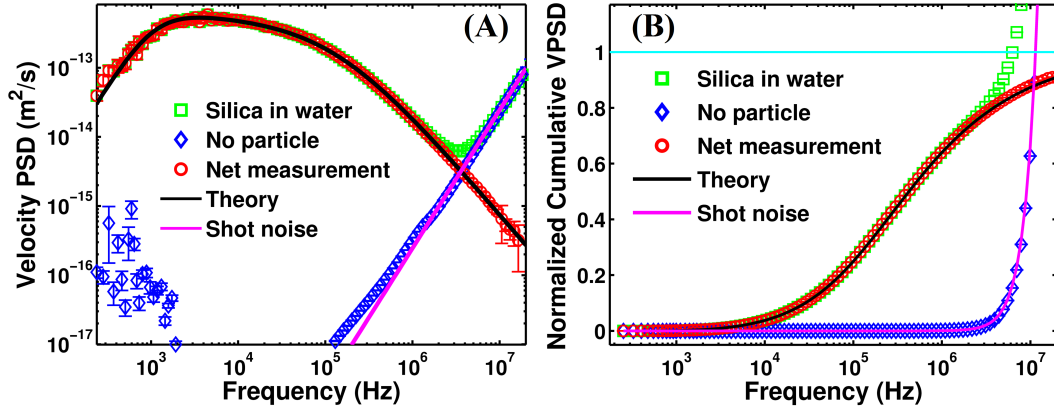


Figure 4.14: The velocity PSD (A) and normalized cumulative velocity PSD (B, normalized to $k_B T/m^*$) of a silica microsphere in water for the same trajectories as in Fig. 4.11 in the system with a silica microsphere in water. In both plots: green squares represent the measurements with trapped particles; blue diamonds represent the noise measured without particles present but with the same detection power; red circles represent the net measurement with noise subtracted; black lines are the theoretical prediction; magenta lines are the shot noise using the results shown in Fig.4.12, indicating that it is the dominant noise source.

sults shown in Fig. 4.11. The blue diamonds represent the noise measured without particles present but with the same detection power. The agreement between the magenta lines and blue diamonds in each system indicates that it is indeed the dominant source of noise. The velocity PSD of the shot noise is proportional to ω^2 , while the cumulative velocity PSD of the shot noise is proportional to ω^3 , which set a sharp bandwidth limit, as shown in Fig. 4.14, above which the signal is dominated by the noise. The useful bandwidth is not directly limited by the detection system response time but by the quantum noise of the detection beam.

To be able to measure the instantaneous velocity, we need increase the

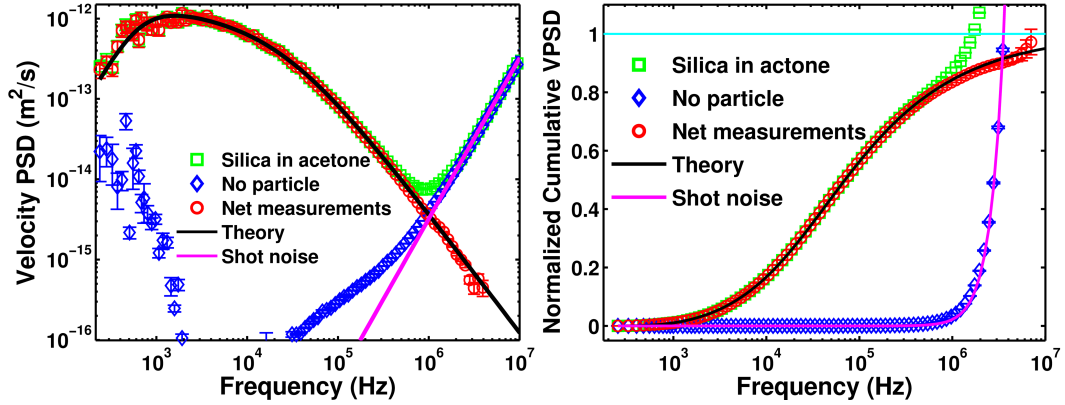


Figure 4.15: The velocity PSD (A) and normalized cumulative velocity PSD (B, normalized to $k_B T/m^*$) of a silica microsphere in acetone for the same trajectories as in Fig. 4.11 in the systems with a silica microsphere in acetone. In both plots: green squares represent the measurements with trapped particles; blue diamonds represent the noise measured without particles present but with the same detection power; red circles represent the net measurement with noise subtracted; black lines are the theoretical prediction; magenta lines are the shot noise using the results shown in Fig. 4.12, indicating that it is the dominant noise source.

area under velocity PSD (namely, a larger cumulative velocity PSD) before it is dominated by the shot noise by moving the velocity PSD of the microsphere (the black lines in Fig. 4.14, 4.15 and 4.16) towards the left (equivalently, slowing down the dynamics of the microsphere) and (or) moving the shot noise curve (the magenta lines in Fig. 4.14, 4.15 and 4.16) towards the right (equivalently, reducing shot noise and increasing position sensitivity). As compared to the system of a silica microsphere in water, by using the system of a silica microsphere in acetone, we can move the velocity PSD of the microsphere towards the left (due to less viscosity of acetone) but we move the shot noise curve towards the left as well (due to a less refractive index mismatch, thus a

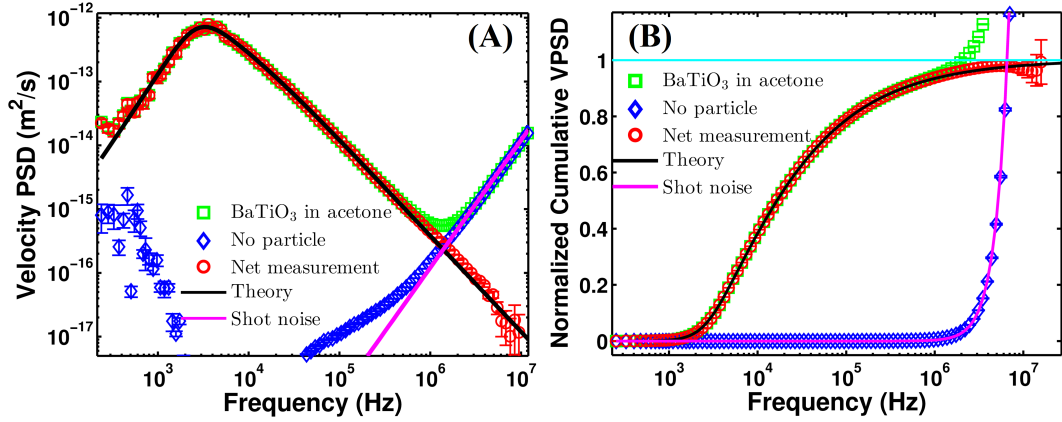


Figure 4.16: The velocity PSD (A) and normalized cumulative velocity PSD (B, normalized to $k_B T/m^*$) of a BaTiO₃ microsphere in acetone for the same trajectories as in Fig. 4.11 in the systems with a BaTiO₃ microsphere in acetone. In both plots: green squares represent the measurements with trapped particles; blue diamonds represent the noise measured without particles present but with the same detection power; red circles represent the net measurement with noise subtracted; black lines are the theoretical prediction; magenta lines are the shot noise using the results shown in Fig.4.12, indicating that it is the dominant noise source.

lower optical gain). As a result, the improvement was marginal. Instead, by using the system of a BaTiO₃ microsphere in acetone, we can not only move the velocity PSD of the microsphere towards the left but also move the shot noise towards the right, resulting a much bigger improvement.

The velocity distributions for the three systems, calculated from 3.6 billion, 200 million and 144 million velocity points, are shown in Fig. 4.17, 4.18 and 4.19. Blue lines (overlapping almost perfectly with the black line in Fig. 4.19) are Gaussian fits of the measurements, from which the fraction of the mean kinetic energy observed was determined. We observed 78%, 83%

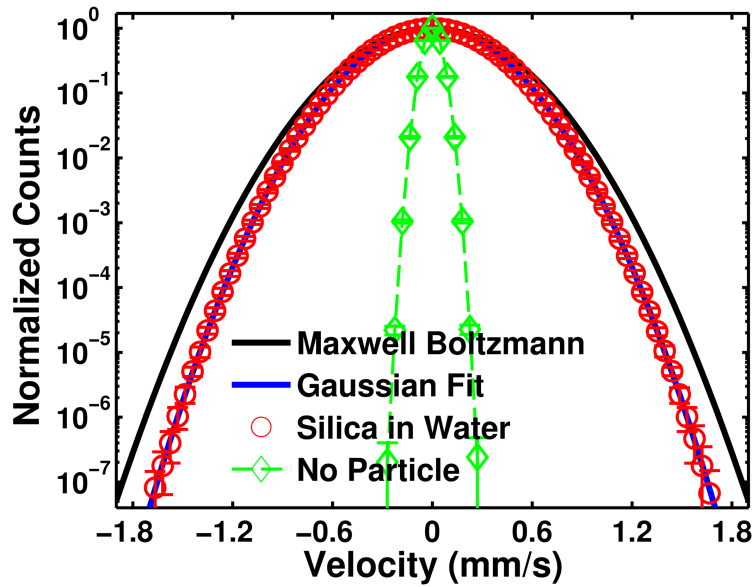


Figure 4.17: The normalized velocity distribution of a silica microsphere in water ($v_{rms}^* = 327 \mu\text{m/s}$), calculated from 3.6 billion data points. The histogram bin size for each velocity distribution was set to the rms magnitude of the corresponding noise. Red circles represent the measurements with trapped microspheres; green diamonds represent the measurements acquired without particles present, but with matching detection power; black line is the modified MBD prediction; blue line is a Gaussian fit of the measurements, from which the fraction of the mean kinetic energy observed was determined.

and 100% of the mean kinetic energy predicted by the modified energy equipartition theorem, to which the noise contributes about 4%, for the three systems respectively. The three systems give a trend of approaching the instantaneous velocity measurement, showing the importance of using BaTiO_3 microspheres and acetone. It is worth emphasizing that the instantaneous velocity measurement was made possible by two improvements: first, slowing down the dynamics by using acetone (lower viscosity compared to water) and BaTiO_3 microspheres (higher density compared to silica); and second,

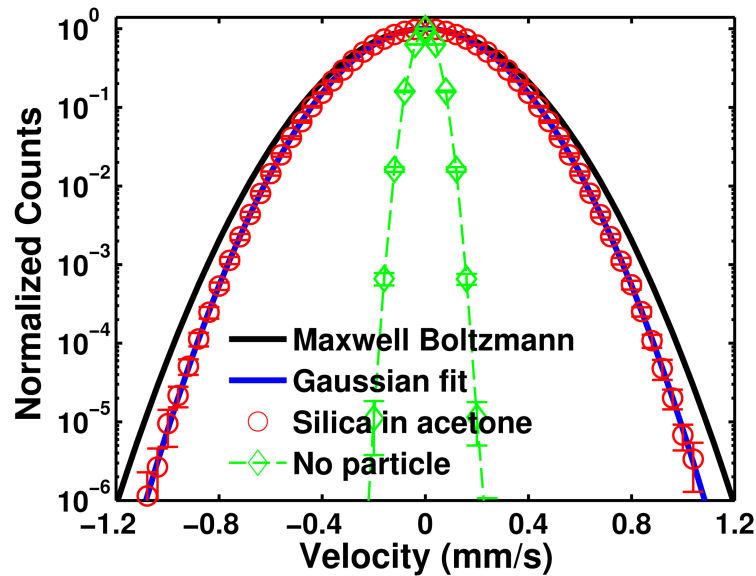


Figure 4.18: The normalized velocity distribution of a silica microsphere in acetone ($v_{rms}^* = 227 \mu\text{m/s}$), calculated from 200 million data points. The histogram bin size for each velocity distribution was set to the rms magnitude of the corresponding noise. Red circles represent the measurements with trapped microspheres; green diamonds represent the measurements acquired without particles present, but with matching detection power; black line is the modified MBD prediction; blue line is a Gaussian fit of the measurements, from which the fraction of the mean kinetic energy observed was determined.

improving signal-to-noise by increasing the detected beam power and using BaTiO_3 microspheres (higher refractive index compared to silica improves the scattering efficiency).

The instantaneous velocity of the microspheres was calculated by a numerical derivative of the position data, which is averaged using binning. A shorter averaging time would increase the fraction of kinetic energy observed

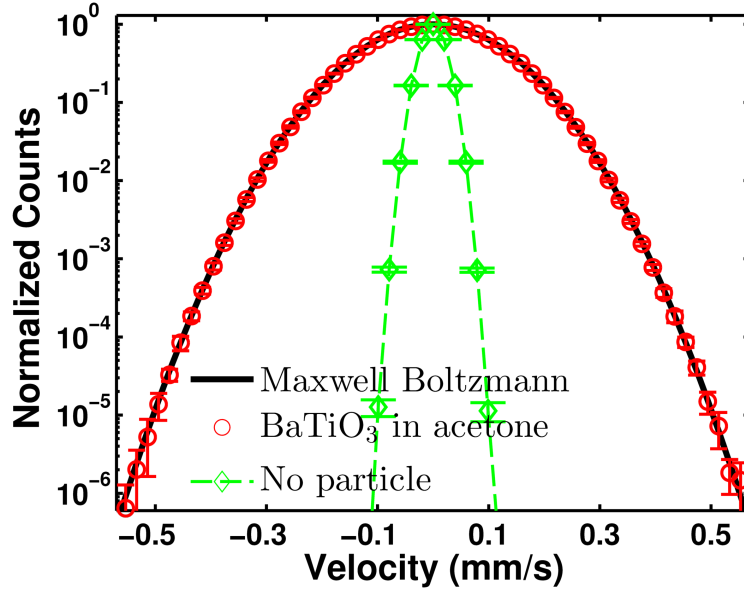


Figure 4.19: The normalized velocity distribution of a BaTiO₃ microsphere in acetone ($v_{rms}^* = 104 \mu\text{m/s}$), calculated from 144 million data points. The histogram bin size for each velocity distribution was set to the rms magnitude of the corresponding noise. For all plots: red circles represent the measurements with trapped microspheres; green diamonds represent the measurements acquired without particles present, but with matching detection power; black line is the modified MBD prediction.

but at the cost of a lower signal-to-noise ratio (SNR), which is defined as

$$SNR = 10 \log_{10} \left(\frac{\langle v^2 \rangle}{\langle n^2 \rangle} \right) \quad (4.6)$$

where $\langle v^2 \rangle$ and $\langle n^2 \rangle$ are the mean square values of the velocity and noise measurements respectively. We choose bin size $n = 25, 85$ and 40 for the three systems respectively with $SNR \approx 14$ dB for each system.

The detailed experimental conditions and results are listed in Table 1 for all the three systems. The instantaneous velocity of a microsphere in a

liquid follows the modified MBD (and thus, the modified energy equipartition theorem) over a dynamic range of more than six orders of magnitude in count-rate and five standard deviations in velocity, as shown in Fig. 4.19. Assuming ergodicity [21], the same conclusion should also be true for an ensemble of identical particles.

Systems	Silica in water	Silica in acetone	BaTiO ₃ in acetone
d (μm)	3.06 ± 0.05	3.98 ± 0.06	5.36 ± 0.06
P (mW)	144 ± 6	144 ± 6	135 ± 6
K ($\mu\text{N/m}$)	188 ± 15	50 ± 8	342 ± 13
C (mV/nm)	25.3 ± 0.5	6.3 ± 0.3	31.8 ± 0.6
SN (fm/ $\sqrt{\text{Hz}}$)	2.3 ± 0.1	8.9 ± 0.4	1.7 ± 0.1
Velocity points	3.6 billion	200 million	144 million
Bandwidth	8 MHz	2.4 MHz	5 MHz
$E_{kinetic}$	78%	83%	100%

Table 4.1: The summary of the results for the three systems. d is the sphere diameter, P is the detection power, K is the trap stiffness, C is the volts-per-meter calibration factor, SN is the position shot noise and $E_{kinetic}$ is measured kinetic energy in percentage.

To measure the actual instantaneous velocity in liquid as predicted by the equipartition theorem, the temporal resolution must be shorter than the time scales of acoustic damping, which are 1.0 ns, 1.7 ns and 2.3 ns for three systems: a silica microsphere in water, a silica microsphere in acetone and a BaTiO₃ microsphere in acetone respectively. By using a pulsed laser as the detection beam, one can significantly reduce the shot noise and it may be possible to measure the true instantaneous velocity, which will be discussed more in Chapter 9. Our setup can also be used to measure the velocity distribution

of a particle in non-Newtonian fluids [101], where deviations from the modified MBD may result from the viscoelasticity of the complex fluid.

4.3.5 Measurements of the thermal force

As discussed in Chapter 3, the dynamics of the Brownian particle may be modeled using a Generalized Langevin equation with a stochastic driving force that captures the effect of the thermal fluctuations in the fluid acting on the particle. In the Einstein-Ornstein-Uhlenbeck model [13], which is valid only when the inertia of the fluid is negligible, the thermal force exerted on Brownian particles is assumed to be spectrally white, meaning it is delta correlated and has a flat power spectral density $S_{F_{th}} = 4k_B T \gamma_s$. Addition of the Basset force to the Einstein-Ornstein-Uhlenbeck model results in the colored thermal force spectral density $S_{F_{th}} = 4k_B T \gamma_s (1 + \sqrt{\omega \tau_f / 2})$ [83] acting on a particle in an unbounded fluid.

The color of the thermal force emerges as a resonance in the position PSD, which has been suggested [102] and verified recently [15, 103]. A very strong trap is necessary to explore this resonance. The equation of motion for a trapped particle doing Brownian motion in a fluid can be described by the Langevin equation

$$m\ddot{x} = F_{fr} + F_{th} - Kx \quad (4.7)$$

At low frequencies (long time scales), the optical trapping force dominates over the inertia of the particle and the friction force. Thus, the Langevin equation can be reduced to $F_{th} = Kx$. The stronger the trap is the larger

frequency range in which the reduced Langevin equation holds. Consequently, the thermal force PSD can be obtained as

$$S_{F_{th}} = K^2 S_x. \quad (4.8)$$

Because of the color of the thermal force, $S_{F_{th}} = 4k_B T \gamma_s (1 + \sqrt{\omega \tau_f / 2})$, the position PSD increases with increasing frequency up to the corner frequency $f_c = K / (2\pi \gamma_s)$. As the frequency increases more than f_c , the friction force and the inertia of the particle become increasingly important, resulting in a corresponding decrease in the position PSD. Therefore, a resonance arises in the position PSD. Among the three systems, the BaTiO₃ in acetone system has a trapping strength to be able to observe such a resonance at $f_c = 3.5$ kHz.

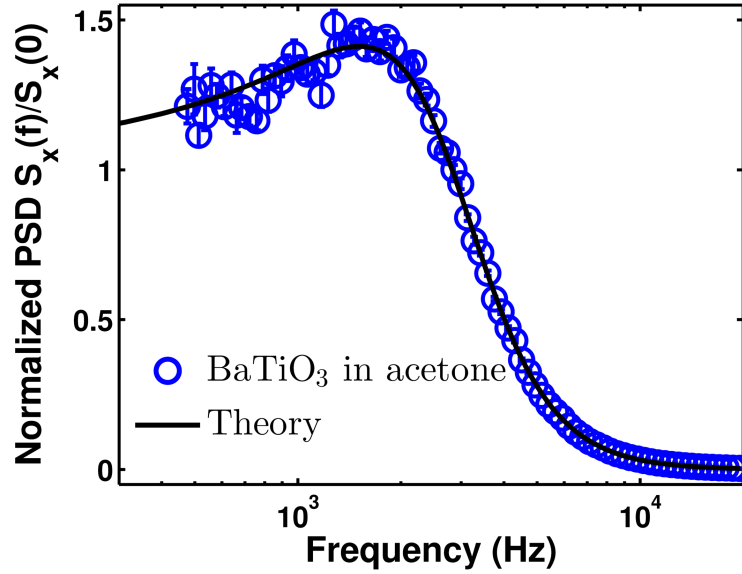


Figure 4.20: Log-linear plot of the position PSD of a trapped BaTiO₃ microsphere in acetone, reflecting the color of the thermal force. This is re-plotting the BaTiO₃-acetone data shown in Fig. 4.12.

The position PSD (normalized by $S_x(0)$, averaged over all 43 trajectories) for the BaTiO₃ in acetone system is shown in Fig. 4.20, which is re-plotting the BaTiO₃ in acetone data in Fig. 4.12 on a log-linear plot. This arising resonance is remarkable, since a microsphere in a liquid is conventionally considered as an overdamped system.

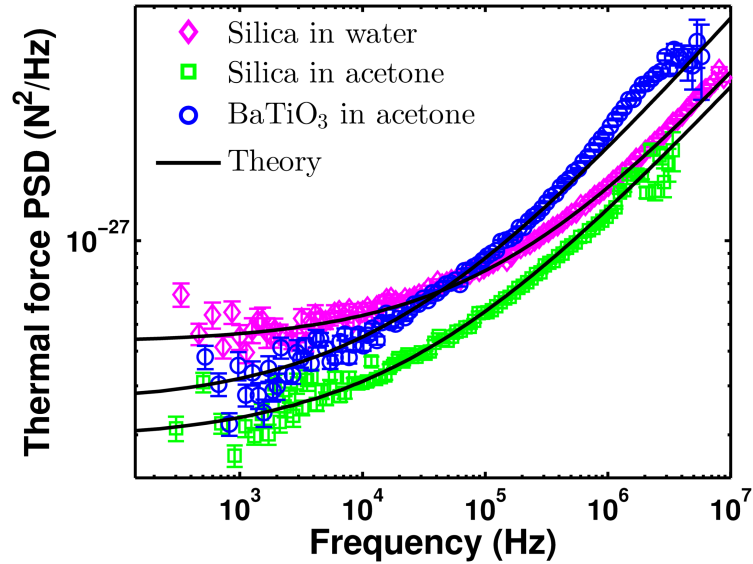


Figure 4.21: Double logarithmic plot of the colored thermal force in the three systems for the same data as shown in Fig. 4.11. Black lines are the theoretical predictions of the thermal force PSD for the three systems. Magenta diamonds represent silica in water data; green squares represent silica in acetone data; blue circles represent BaTiO₃ in acetone data. The deviation from the theory around 2 MHz for the system of a BaTiO₃ microsphere in acetone is due to the laser intensity noise leakage caused by slight misalignment of the cut mirror.

In addition to the above indirect way of studying the color of the thermal force, the thermal force spectral densities for the three systems can be directly calculated from position PSD using Eq. (4.5), as shown in Fig. 4.21.

The DC values of the $S_{F_{th}}$ in the three systems are different due to different sizes of the particles and different viscosities of the liquids. Where as at high frequencies, they all increase with a $\sqrt{\omega}$ dependence, with a slop of 0.5 on a log-log plot. The deviation from the theory around 2 MHz for the system of a BaTiO₃ microsphere in acetone is due to the laser intensity noise leakage caused by a slight misalignment of the cut mirror.

Chapter 5

Theory for Brownian motion with boundary effects

Understanding the influence of boundaries on particle dynamics is of great significance, from both a fundamental and an applied point of view. For example, blood cells moving in vessels, particles migrating in porous media, and macromolecules diffusing in membranes are all affected by the presence of boundaries. Because of this, the Brownian motion of particles near a boundary is more complicate and interesting than that in bulk.

It is well-known that the mobility of particles decreases as they approach boundaries at which the fluid does not slip. This effect of “surface confinement” was predicted by Lorentz in 1907 [27]. The increase of the drag force is attributed to the alteration of the hydrodynamic interaction between the particle and the fluid generated by the no-slip boundaries. The motion of the particle becomes anisotropic because the drag force parallel to the wall is typically less than that perpendicular to the wall. This effect is significant when the dimensions of the confining geometry and suspended particles are comparable.

Surface confinement has conventionally been considered one of many

boundary effects which will influence Brownian motion in the long time scale diffusive regime. We pointed out that this effect can also occur in the short time scale ballistic regime [104]. In addition to that, there are many other boundary effects that occur in the ballistic regime as well. In the short time scale ballistic regime, the velocity autocorrelation function of the Brownian particle decays faster than that of particle in a bulk fluid. Furthermore, at low frequencies the thermal force loses its color due to the reflected flow from the no-slip boundary. The power spectrum of the thermal force on the particle near a no-slip boundary becomes flat at low frequencies.

In this chapter, we will first give the theory for boundary effects on Brownian motion in the diffusive regime, namely the predictions of diffusion coefficients near a boundary as a function of sphere-wall separation. We consider two systems: a microsphere near a flat infinite wall and a microsphere outside a cylindrical wall. This will be followed by the theory for boundary effects on Brownian motion over the entire time scales. Furthermore, we will give numerical predictions of a variety of statistical properties of Brownian motion using the conditions in our experiments. These numerical results serve as a guide for our experiments. It is important noting that in this chapter, the fluid flow has no-slip boundary conditions both at the surface of the walls and the particle. We also would like to emphasize again that the particle only has translational motion and does not rotate.

5.1 Anisotropic and hindered diffusion of a microsphere near a wall

The fluid drag force on a particle with radius a , moving freely at velocity \mathbf{v} in a fluid with viscosity η , i.e., far from any borders, in the case of the low Reynolds number, is simply described by the Stokes law [105]

$$\mathbf{F} = 6\pi\eta a\mathbf{v}. \quad (5.1)$$

The corresponding diffusion coefficient can be obtained through Stokes-Einstein relation

$$D_0 = \frac{k_B T}{6\pi\eta a}. \quad (5.2)$$

A particle diffusing close to a no-slip wall will experience increased viscous drag compared with its motion in the bulk. The motion of the particle also becomes anisotropic due to the hydrodynamic interactions between the particle and the nearby wall, which depends on the particle's shape, orientation, relative position to the wall, the shape of the wall as well as the fluid flow boundary conditions both at surface of the particle and the wall.

In this section, we will first give the diffusion coefficients of a particle near a flat wall. This is followed by the theoretical predictions of diffusion coefficients near a cylindrical wall, which is the actual experimental system discussed in Chapter 6.

5.1.1 Diffusion of a microsphere near a flat wall

The system of a spherical particle moving near an infinite flat wall has cylindrical axial symmetry, with an axis in the normal direction to wall through the center of the spherical particle. Therefore, the particle's motion can be decomposed into parallel and perpendicular directions. The drag force on a spherical particle in both parallel and perpendicular directions has been given using method of reflection [106]. The method of reflections is an iterative series solution technique that decomposes the velocity and the pressure fields into a linear superposition of terms of successively higher order in the number of wall and sphere boundary interactions. The terms in the expansion are constrained to alternately satisfy the boundary conditions on the sphere and on the confining walls.

The anisotropic and hindered diffusion coefficients of the particle in parallel and perpendicular directions are [106]

$$\frac{D_{\parallel}(h)}{D_0} = 1 - \frac{9}{16}\xi + \frac{1}{8}\xi^3 - \frac{45}{256}\xi^4 - \frac{1}{16}\xi^5 \quad (5.3)$$

$$\begin{aligned} \frac{D_0}{D_{\perp}(h)} &= \frac{4}{3} \sinh(\beta) \sum_{n=1}^{\infty} \frac{n(n+1)}{(2n-1)(2n+3)} \\ &\times \left[\frac{2 \sinh((2n+1)\beta) + (2n+1) \sinh(2\beta)}{4 \sinh^2((n+1/2)\beta) - (2n+1)^2 \sinh^2 \beta} - 1 \right] \end{aligned} \quad (5.4)$$

where D_0 is the diffusion coefficient of a free sphere with the same size in the same fluid at the same temperature, $\xi = \frac{a}{h}$ and $\beta = \cosh^{-1}(\frac{h}{a})$, h is the distance between the center of the sphere and the surface of the wall, denoted as sphere-wall separation. It is worth noting that boundary effects imposed

by a flat wall on diffusion at the same position always satisfy $D_{\perp} < D_{\parallel}$.

5.1.2 Diffusion of a microsphere near a cylindrical wall

Since the experiments as discussed in Chapter 6 on boundary effects is actually performed near a cylindrical wall. Unlike the case with a sphere near a flat wall, this system no longer has cylindrical axial symmetry. The motion of the particle behaves differently in all three directions \hat{r} , \hat{z} and $\hat{\theta}$.

We here give the predictions of the anisotropic and hindered diffusion of a point-like sphere outside a cylinder, which has been studied previously [107]. We can get a better approximation by adding a geometric series summation for higher order reflections, as suggested by Happel and Brenner [106]

$$D_{\hat{r}} = D_0(1 - r_n \Gamma_{\hat{r}}) \quad (5.5)$$

$$D_{\hat{z}} = D_0(1 - r_n \Gamma_{\hat{z}}) \quad (5.6)$$

$$D_{\hat{\theta}} = D_0(1 - r_n \Gamma_{\hat{\theta}}) \quad (5.7)$$

where D_0 is the diffusion coefficient of a free sphere with the same size in the same fluid at the same temperature, r_n is radius of the particle normalized by

the radius of the cylinder, and

$$\begin{aligned}
\Gamma_{\hat{r}} &= \frac{3}{2\pi} \hat{\Sigma} \left[H_n - \frac{1}{4}(L_{n-1} + L_{n+1} - 2r_0 L_n) \right. \\
&\quad \left. \times (L_{n-1} + L_{n+1} - (L'_{n-1} + L'_{n+1})r_0 + 2L'_n)/E_n \right] \\
\Gamma_{\hat{z}} &= \frac{3}{2\pi} \hat{\Sigma} \left[H_n + \left(\lambda \frac{\partial L_n}{\partial \lambda} \right) \left(L_n - \frac{1}{2}(L_{n-1} + L_{n+1})r_0 \right) / E_n \right] \\
\Gamma_{\hat{\theta}} &= \frac{3}{2\pi} \left[H_n - \frac{1}{4} \hat{\Sigma} (L_{n-1} - L_{n+1}) \left(\frac{2nL_n}{r_0} - (n-2)L_{n-1} - (n+2)L_{n+1} \right) / E_n \right] \\
H_n &= I_n(\lambda) \frac{K_n^2(\lambda r_0)}{K_n(\lambda)}; L_n = \frac{K_n(\lambda r_0)}{K_n(\lambda)}; L'_n = \frac{\lambda K'_n(\lambda r_0)}{K_n(\lambda)} \\
E_n &= 1 + \chi'_n(1) - \frac{1}{2} (\chi'_{n-1}(1) + \chi'_{n+1}(1)) \\
\chi'_n(1) &= \frac{\lambda K'_n(\lambda)}{K_n(\lambda)}; \hat{\Sigma} = \int_0^\infty \sum_{n=-\infty}^\infty d\lambda
\end{aligned}$$

where I_n, K_n are modified Bessel functions and r_0 is the distance from the center of the sphere to the center of the cylinder normalized by the radius of the cylinder.

These results are true only when the radius of the cylinder is much bigger than both the radius of the particle and sphere-cylinder separation (the distance between the center of sphere and the surface of the cylinder). When the particle is very close to the cylinder, within the point particle approximation, the curvature of the boundary can be neglected. Thus, the diffusion coefficients can be calculated using Eq. (5.3) and Eq. (5.4), $D_{\hat{r}} \sim D_{\perp}$ and $D_{\hat{z}} \sim D_{\hat{\theta}} \sim D_{\parallel}$. It is worth noting that the boundary effects imposed by the cylindrical wall on diffusion for the same position always satisfy $D_{\hat{r}} < D_{\hat{z}} < D_{\hat{\theta}}$.

$D_{\hat{r}}$ is less than both $D_{\hat{z}}$ and $D_{\hat{\theta}}$ is consistent with the flat wall case ($D_{\perp} < D_{\parallel}$). $D_{\hat{z}} < D_{\hat{\theta}}$ is due to the orientation of the curvature of the cylindrical boundary. If the particle is inside of a cylinder, this relation should be modified to $D_{\hat{z}} > D_{\hat{\theta}}$. Because of the curvature of the cylindrical boundary, with the same sphere-wall separation, these relations, $D_{\perp} < D_{\hat{r}}$ and $D_{\parallel} < D_{\hat{r}} < D_{\hat{\theta}}$, always hold, as discussed more in Chapter 6.

5.2 Boundary effects on unsteady Brownian motion

The effect of a plane wall on the unsteady motion of a sphere in a viscous fluid in the parallel direction to the wall has been studied by Wakiya [108] and in the perpendicular direction by Gotoh et al. [109]. These authors showed that the famous long-time tail of the velocity autocorrelation function in bulk is obliterated by the wall. The first complete theory on boundary effects imposed by a flat wall on Brownian motion over the entire time scales was not available until recently [110]. However, this work seems inconsistent, and we have proposed a correction. The modifications to Felderhof's theory will be justified and discussed in detail in a future publication [111].

In this section, we review briefly Felderhof's theory, including our proposed modifications, for boundary effects on the Brownian motion of a spherical particle in an incompressible fluid near a flat and infinite no-slip wall. We consider a spherical particle of radius a and mass m_p , immersed in a viscous incompressible fluid with shear viscosity η and mass density ρ_f near a flat and infinite wall. The fluid does not slip both the surface the boundary and the

sphere. The sphere-wall separation is h , defined as the distance between the center of the sphere and the surface of the wall.

5.2.1 Linear hydrodynamics

For small magnitude motion of the sphere, the fluid velocity and pressure field are governed by the linearized Navier-Stokes equations

$$\rho_f \frac{\partial \mathbf{v}}{\partial t} = \eta \nabla^2 \mathbf{v} - \nabla p, \quad (5.8)$$

$$\nabla \cdot \mathbf{v} = 0. \quad (5.9)$$

The pressure field is determined by the condition of incompressibility. More conveniently, the linearized Navier-Stokes equations can be written in the frequency domain as

$$\eta \nabla^2 \mathbf{v}_\omega - i\omega \rho_f \mathbf{v}_\omega = -\nabla p, \quad (5.10)$$

$$\nabla \cdot \mathbf{v}_\omega = 0. \quad (5.11)$$

The equation of motion for the sphere is governed by Newton's law

$$-i\omega m_p \mathbf{U}_\omega = \mathbf{E}_\omega + \mathbf{K}_\omega \quad (5.12)$$

where \mathbf{U}_ω is the Fourier transform of the particle velocity, \mathbf{K}_ω is the Fourier transform of the force on the particle exerted by the fluid, namely the drag force, and \mathbf{E}_ω is the Fourier transform of the time dependent external force acting on the sphere, which can be the optical trapping force or the thermal force in the Langevin model.

The location of the sphere itself shall be assumed to have negligible motion, so that the boundary may be assumed to be stationary. In other words, the boundary is fixed but the velocity conditions at the boundary are changing all the time. The force on the sphere exerted by the fluid \mathbf{K}_ω in the presence of an incident flow $\mathbf{v}'(\omega)$ that satisfies the linearized incompressible Navier-Stokes equations can be obtained through the generalized Faxén theorem [112, 113].

$$\mathbf{K}_\omega = -\gamma_0(\omega)\mathbf{U}(\omega) + 6\pi\eta a \left[(1 + \tilde{\alpha})\bar{\mathbf{v}}'_S(\omega) + \frac{1}{3}\tilde{\alpha}^2\bar{\mathbf{v}}'_V(\omega) \right], \quad (5.13)$$

where $\bar{\mathbf{v}}'_S$ and $\bar{\mathbf{v}}'_V$ denote the averages of the incident flow $\mathbf{v}'(\omega)$ on the surface and volume of the sphere respectively. $\gamma_0(\omega)$ is the free-space drag coefficient $\gamma_0(\omega) = 6\pi\eta a \left(1 + \tilde{\alpha} + \frac{1}{9}\tilde{\alpha}^2 \right)$, where $\tilde{\alpha} = \sqrt{-i\omega\rho_f a^2/\eta}$.

The boundary effects imposed by the wall can be treated as the change in the incident flow $\mathbf{v}'(\mathbf{r}_0, \omega)$. In Felderhof's frame work [110], the flow reflected from the wall is treated as the incident flow to calculate the drag on a sphere near a wall. The reflected flow is calculated by assuming that the force on the fluid exerted by the spherical particle may be approximated by an appropriate point force \mathcal{F}_ω . And the the incident flow can be calculated via $\mathbf{v}'(\mathbf{r}_0, \omega) = \mathbf{R}(\mathbf{r}_0, \omega) \cdot \mathcal{F}_\omega$, where $\mathbf{R}(\mathbf{r}_0, \omega)$ is the reaction field tensor discussed later in detail in Section 5.2.2.

Within the point particle approximation [110], the inhomogeneities of flow over the small size of the sphere are neglected, and we replace the surface and volume averages in the generalized Faxén theorem simply with the flow generated by the incident flow at the particle's position $\bar{\mathbf{v}}'_S = \bar{\mathbf{v}}'_V = \mathbf{v}'(\mathbf{r}_0, \omega) =$

$\mathbf{R}(\mathbf{r}_0, \omega) \cdot \mathcal{F}_\omega$. Thus, the drag force with point approximation becomes

$$\mathbf{K}_\omega = -\gamma_0(\omega)\mathbf{U}_\omega + 6\pi\eta a [(1 + \alpha a + \alpha^2 a^2/3)\mathbf{R}(\mathbf{r}_0, \omega) \cdot \mathcal{F}(\omega)]. \quad (5.14)$$

Felderhof simply uses the external for \mathbf{E}_ω acting on the particle as the point force \mathcal{F}_ω . Therefore, the drag force calculated in [110] is

$$\mathbf{K}_\omega = -\gamma_0(\omega)\mathbf{U}_\omega + 6\pi\eta a [(1 + \tilde{\alpha} + \tilde{\alpha}^2/3)\mathbf{R}(\mathbf{r}_0, \omega) \cdot \mathbf{E}_\omega], \quad (5.15)$$

which we believe is incomplete. The correct expression for \mathbf{K}_ω using Faxén theorem is given by [111]

$$\mathbf{K}_\omega = -\gamma_0(\omega)\mathbf{U}_\omega + \gamma_s [(1 + \tilde{\alpha} + \tilde{\alpha}^2/3)\mathbf{R}(\mathbf{r}_0, \omega) \cdot (\mathbf{E}_\omega + i\omega(m_p - m_f)\mathbf{U}_\omega)]. \quad (5.16)$$

The key idea is that the point force $\mathcal{F}(\omega)$ must reproduce the momentum flux through the surface of the sphere between two situations: one is an immersed point particle exerted by an external force \mathbf{E}_ω and the other is the region occupied by the sphere is filled with fluid (particle is removed), and the point force \mathcal{F}_ω acted at the center of this spherical region. The net force exerted by the sphere on the fluid is given by $-\mathbf{K}_\omega = \mathbf{E}_\omega + i\omega m_p \mathbf{U}_\omega$ (Eq. (5.12)). To produce the same net force on the boundary, we must have a point force of value $\mathcal{F}_\omega = -\mathbf{K}_\omega - i\omega m_f \mathbf{U}_\omega$ acting on the fluid at position \mathbf{r}_0 , since some of the momentum from this force will go toward accelerating the fluid. Thus, in the case of unsteady Stokes flow, it is only for neutrally buoyant particles that the induced force \mathcal{F}_ω is the same as the external force \mathbf{E}_ω .

Combining Eq. (5.12) and Eq. (5.16) and with the definition $\mathbf{U}_\omega = \boldsymbol{\mathcal{Y}}_\omega \mathbf{E}_\omega$, the admittance tensor of a sphere in fluid near a flat infinite no-slip boundary can be written as

$$\boldsymbol{\mathcal{Y}}_\omega = \frac{\mathbf{I} + \gamma_s(1 + \tilde{\alpha} + \tilde{\alpha}^2/3)\mathbf{R}(\mathbf{r}_0, \omega)}{(\gamma_0(\omega) - i\omega m_p)\mathbf{I} + i\omega(m_f - m_p)\gamma_s(1 + \tilde{\alpha} + \tilde{\alpha}^2/3)\mathbf{R}(\mathbf{r}_0, \omega)}, \quad (5.17)$$

where \mathbf{I} is the identity matrix.

Combining Eq. (5.12) and Eq. (5.16) and with the definition $\mathbf{K}(\omega) = -\gamma(\omega)\mathbf{U}(\omega)$, the drag-coefficient tensor of a sphere in fluid near a flat infinite no-slip boundary can be written as

$$\gamma(\omega) = \frac{\gamma_0(\omega) + i\omega m_f \gamma_s(1 + \tilde{\alpha} + \tilde{\alpha}^2/3)\mathbf{R}(\mathbf{r}_0, \omega)}{\mathbf{I} + \gamma_s(1 + \tilde{\alpha} + \tilde{\alpha}^2/3)\mathbf{R}(\mathbf{r}_0, \omega)}. \quad (5.18)$$

As compared to a particle undergoing Brownian motion far away from any boundaries, the admittance and drag coefficient now become much more complicated. Both of them depend on the detail boundary geometry and in general are anisotropic, namely become a tensor.

5.2.2 Reaction field tensor

The reaction field tensor as defined by Felderhof is the difference, as $\mathbf{r} \rightarrow \mathbf{r}_0$, between the Green's function of the unsteady Stokes equations $\mathbf{G}(\mathbf{r}|\mathbf{r}_0; \omega)$ that respects no-slip boundary conditions on the wall, and $\mathbf{G}_0(\mathbf{r} - \mathbf{r}_0; \omega)$ the free-space Green's function, i.e.

$$\mathbf{R}(\mathbf{r}_0, \omega) = \lim_{\mathbf{r} \rightarrow \mathbf{r}_0} [\mathbf{G}(\mathbf{r}|\mathbf{r}_0; \omega) - \mathbf{G}_0(\mathbf{r} - \mathbf{r}_0; \omega)]. \quad (5.19)$$

Here, \mathbf{r}_0 denotes the location of the point force, which is the same as that of the point particle.

Within the point approximation, the non-diagonal elements of the reaction field tensor $R_{xy}(\mathbf{r}_0, \omega)$, $R_{yx}(\mathbf{r}_0, \omega)$, $R_{xz}(\mathbf{r}_0, \omega)$, $R_{zx}(\mathbf{r}_0, \omega)$, $R_{yz}(\mathbf{r}_0, \omega)$ and $R_{zy}(\mathbf{r}_0, \omega)$ vanish by axial symmetry. And only the diagonal elements of the reaction field tensor $R_{xx}(\mathbf{r}_0, \omega)$, $R_{yy}(\mathbf{r}_0, \omega)$ and $R_{zz}(\mathbf{r}_0, \omega)$ are nonzero. By the same symmetry, $R_{xx}(\mathbf{r}_0, \omega)$ equals $R_{yy}(\mathbf{r}_0, \omega)$. We denote $R_{\parallel}(\mathbf{r}_0, \omega) = R_{xx}(\mathbf{r}_0, \omega) = R_{yy}(\mathbf{r}_0, \omega)$ and $R_{\perp}(\mathbf{r}_0, \omega) = R_{zz}(\mathbf{r}_0, \omega)$. Therefore, the reaction field tensor in this limit is a diagonalized tensor, meaning the motion in the parallel and perpendicular is uncoupled.

The reaction field tensor element $R_{\parallel}(\mathbf{r}_0, \omega)$ is given by [110]

$$\begin{aligned}
R_{\parallel}(\mathbf{r}_0, \omega) = & \frac{-1}{192\pi\eta h\nu^4} \left[36 + 27\nu + 6\nu^2 + 6(6 + 12\nu + 11\nu^2 + 6\nu^3 + 4\nu^4)e^{-2\nu} \right. \\
& - (144 + 144\nu + 72\nu^2 + 24\nu^3 - 6\nu^4 + 2\nu^5 - \nu^6 + \nu^7)e^{-\nu} \\
& + 6\pi\nu^3 \left(2\nu(Y_{-2}(2\nu) - H_{-2}(2\nu)) + 3(Y_{-3}(2\nu) - H_{-3}(2\nu)) \right) \\
& \left. + \nu^8 E_1(\nu) + 12\nu^3(2\nu K_2(2\nu) + 3K_3(2\nu)) \right] \quad (5.20)
\end{aligned}$$

And the perpendicular element $R_{\perp}(\mathbf{r}_0, \omega)$ is given by [114]

$$\begin{aligned}
R_{\perp}(\mathbf{r}_0, \omega) = & \frac{-1}{96\pi\eta h\nu^4} \left[36 + 6\nu^2 + 48\nu^3 + 6(6 + 12\nu + 9\nu^2 + 2\nu^3)e^{-2\nu} \right. \\
& - (144 + 144\nu + 48\nu^2 - 6\nu^4 + 10\nu^5 + \nu^6 - \nu^7)e^{-\nu} \\
& + 6\pi\nu \left(2\nu(3 - \nu^2)(Y_0(2\nu) - H_0(2\nu)) - (6 - 5\nu^2)(Y_1(2\nu) - H_1(2\nu)) \right) \\
& \left. + \nu^6(12 - \nu^2)E_1(\nu) + 72\nu^2 K_0(2\nu) + 36\nu(2 + \nu^2)K_1(2\nu) \right] \quad (5.21)
\end{aligned}$$

where $\nu = \sqrt{-i\omega\rho_f h^2/\eta} = \sqrt{-i\omega\tau_w}$, τ_w is the time taken for vorticity in the fluid to traverse the distance from the wall to the sphere. $Y_n(2\nu)$ is the Bessel function, $K_n(2\nu)$ is the modified Bessel function, $E_1(\nu)$ is the exponential integral function, $H_n(2\nu)$ is the Struve function. We have verified these sophisticated calculations.

Until now, we can give the admittance of particle in the parallel direction

$$\mathbf{y}_\omega^\perp = \frac{1 + \gamma_s(1 + \tilde{\alpha} + \tilde{\alpha}^2/3)R_\perp(\mathbf{r}_0, \omega)}{(\gamma_0(\omega) - i\omega m_p) + i\omega(m_f - m_p)\gamma_s(1 + \tilde{\alpha} + \tilde{\alpha}^2/3)R_\perp(\mathbf{r}_0, \omega)}, \quad (5.22)$$

and in the parallel direction

$$\mathbf{y}_\omega^\parallel = \frac{1 + \gamma_s(1 + \tilde{\alpha} + \tilde{\alpha}^2/3)R_\parallel(\mathbf{r}_0, \omega)}{(\gamma_0(\omega) - i\omega m_p) + i\omega(m_f - m_p)\gamma_s(1 + \tilde{\alpha} + \tilde{\alpha}^2/3)R_\parallel(\mathbf{r}_0, \omega)}. \quad (5.23)$$

With these, the dynamics of the particle can be at least numerically calculated, although the analytic expressions remain unknown.

The low-frequency expansion of the reaction field tensor elements $R_\perp(\mathbf{r}_0, \omega)$ and $R_\parallel(\mathbf{r}_0, \omega)$ are given [110]

$$\begin{aligned} R_\perp(\mathbf{r}_0, \omega) &\sim \frac{1}{6\pi\eta h} \left(-\frac{9}{8} + \nu - \frac{3}{8}\nu^2 + \frac{19}{192}\nu^4 \right) \\ R_\parallel(\mathbf{r}_0, \omega) &\sim \frac{1}{6\pi\eta h} \left(-\frac{9}{16} + \nu - \frac{9}{8}\nu^2 + \nu^3 + \frac{3}{16}\nu^4 \log(\nu) \right). \end{aligned} \quad (5.24)$$

Thus, the zero-frequency mobility in the two directions are

$$\mu_\perp = \mathbf{y}^\perp(\omega = 0) = \frac{1 - \frac{9a}{8h}}{6\pi\eta a} \quad (5.25)$$

$$\mu_\parallel = \mathbf{y}^\parallel(\omega = 0) = \frac{1 - \frac{9a}{16h}}{6\pi\eta a}. \quad (5.26)$$

These expressions lead to the diffusion coefficients with first order of $\frac{a}{h}$ in the two directions via Einstein-Smoluchowski relation $D = \mu k_B T$,

$$\mathcal{D}_{\parallel} = \frac{k_B T}{6\pi\eta a} \left(1 - \frac{9a}{16h} \right) \quad (5.27)$$

$$\mathcal{D}_{\perp} = \frac{k_B T}{6\pi\eta a} \left(1 - \frac{9a}{8h} \right) \quad (5.28)$$

In the parallel direction, Eq. (5.27) obviously is Eq. (5.3) with up to the first order. In the perpendicular direction, this is not so obvious as comparing Eq. (5.28) to Eq. (5.4).

5.2.3 Effective mass with boundary effects

As discussed in Section 3.3.1.2, in an unbounded fluid, the effective inertial mass (which accounts for the inertia of the entrained fluid) of a spherical particle is given by the mass of the particle m_p , plus an added mass of $m_a = m_f/2$, namely $m^* = m_p + m_f/2$, where m_f is the mass of the liquid displaced by the particle [26].

The presence of the boundary alters this effective mass, which becomes anisotropic and also depends on the distance to the wall. The effective mass can be obtained from mean square of the velocity since $\langle (v^*)^2 \rangle = k_B T / m^*$, as the modified equipartition-theorem predicts. The mean square of the velocity can be obtained from Kubo-Green formula Eq. (3.6) using the initial value

theorem¹ [115]

$$\begin{aligned} C_{\perp}(0) &= \frac{k_B T}{m_p + \frac{1}{2}m_f \left(1 + \frac{3}{8} \left(\frac{a}{h}\right)^3\right)} \\ C_{\parallel}(0) &= \frac{k_B T}{m_p + \frac{1}{2}m_f \left(1 + \frac{3}{16} \left(\frac{a}{h}\right)^3\right)}. \end{aligned} \quad (5.29)$$

Therefore, the effective masses of the particle near a no-slip wall in perpendicular and parallel directions become

$$m_{\perp}^* = m_p + \frac{1}{2}m_f \left(1 + \frac{3}{8} \left(\frac{a}{h}\right)^3\right) \quad (5.30)$$

$$m_{\parallel}^* = m_p + \frac{1}{2}m_f \left(1 + \frac{3}{16} \left(\frac{a}{h}\right)^3\right). \quad (5.31)$$

These results are consistent with many authors [105,116]. However, Felderhof's framework produces the spurious results:

$$m_{\perp,F}^* = \frac{m_p + \frac{1}{2}m_f}{1 - \frac{1}{8} \left(\frac{a}{h}\right)^3} \quad (5.32)$$

$$m_{\parallel,F}^* = \frac{m_p + \frac{1}{2}m_f}{1 - \frac{1}{16} \left(\frac{a}{h}\right)^3}. \quad (5.33)$$

The modification due to boundary effects on the effective mass only applies to the added mass, whereas the bare mass of the particle remains unchanged.

According to modified energy equipartition theorem [26], the velocity variance becomes anisotropic as well and is

$$\langle (v_{\parallel}^*)^2 \rangle = \frac{k_B T}{m_{\parallel}^*} \quad (5.34)$$

$$\langle (v_{\perp}^*)^2 \rangle = \frac{k_B T}{m_{\perp}^*} \quad (5.35)$$

¹With $F(s) = \int_0^{\infty} f(t)e^{-st}dt$, one can get $\lim_{t \rightarrow 0} f(t) = \lim_{s \rightarrow \infty} sF(s)$

in the parallel and perpendicular directions respectively.

5.2.4 The flattening in the thermal force power spectral density

The thermal force power spectral density in the perpendicular direction is given by

$$S_{F,\perp}(\omega) = 4k_B T \Re[\gamma_\omega^\perp] \quad (5.36)$$

and in the parallel direction is given by

$$S_{F,\parallel}(\omega) = 4k_B T \Re[\gamma_\omega^\parallel] \quad (5.37)$$

where \Re means real part, and $\gamma^\perp(\omega)$ and $\gamma^\parallel(\omega)$ are

$$\gamma^\perp(\omega) = \frac{\gamma_0(\omega) + i\omega m_f \gamma_s (1 + \tilde{\alpha} + \tilde{\alpha}^2/3) R_\perp(\mathbf{r}_0, \omega)}{1 + \gamma_s (1 + \tilde{\alpha} + \tilde{\alpha}^2/3) R_\perp(\mathbf{r}_0, \omega)}, \quad (5.38)$$

$$\gamma^\parallel(\omega) = \frac{\gamma_0(\omega) + i\omega m_f \gamma_s (1 + \tilde{\alpha} + \tilde{\alpha}^2/3) R_\parallel(\mathbf{r}_0, \omega)}{1 + \gamma_s (1 + \tilde{\alpha} + \tilde{\alpha}^2/3) R_\parallel(\mathbf{r}_0, \omega)}. \quad (5.39)$$

The thermal force (and the drag coefficients) on the particle should not depend on the mass m_p or the density of the particle, as derived here. However, Felderhof's results spuriously does. The the drag coefficients derived from Felderhof's theory [110] are

$$\gamma^\perp(\omega) = \frac{\gamma_0(\omega) - i\omega m_p}{1 + \gamma_s (1 + \tilde{\alpha} + \tilde{\alpha}^2/3) R_\perp(\mathbf{r}_0, \omega)} + i\omega m_p, \quad (5.40)$$

$$\gamma^\parallel(\omega) = \frac{\gamma_0(\omega) - i\omega m_p}{1 + \gamma_s (1 + \tilde{\alpha} + \tilde{\alpha}^2/3) R_\parallel(\mathbf{r}_0, \omega)} + i\omega m_p. \quad (5.41)$$

In the Einstein-Ornstein-Uhlenbeck model [13] of Brownian motion, which is valid only when the inertia of the fluid is negligible, the corresponding

thermal force is white noise, with the flat (one-sided) spectrum $S_F = 4k_B T \gamma_s$. Addition of the Basset force to the Einstein-Ornstein-Uhlenbeck model results in the colored thermal force spectral density $S_F = 4k_B T \gamma_s (1 + \sqrt{\omega \tau_f / 2})$ on a particle in an unbounded fluid [83]. This has been experimentally verified [15, 17].

Surprisingly, the thermal force loses its color at low frequencies in the presence of a boundary. The thermal force power spectral density (FPSD) on the particle near a no-slip wall becomes flat at low frequencies ($\omega \tau_f \ll 1$ and $\omega \tau_w \ll 1$). The low frequency asymptotic behavior of the thermal force PSD on a particle near a flat wall is found by expanding the reaction field tensor and the expression for the drag coefficient to lowest few orders in ω . We find as $\omega \rightarrow 0$, the asymptotic form of the (one-sided) thermal force power spectrum on the particle in the parallel direction near a no-slip flat wall is given by

$$S_{F,\perp}(\omega) = 4k_B T \gamma_s \left(\frac{1}{1 - \frac{9a}{8h}} - \frac{32\sqrt{2}h^2}{3(8h - 9a)^2} (\omega \tau_f)^{\frac{3}{2}} \right), \quad (5.42)$$

and the parallel direction is given by

$$S_{F,\parallel}(\omega) = 4k_B T \gamma_s \left(\frac{1}{1 - \frac{9a}{16h}} + \frac{128\sqrt{2}(3h^4 - a^2h^2)}{3a^2(16h - 9a)^2} (\omega \tau_f)^{\frac{3}{2}} \right). \quad (5.43)$$

In contrast, the (one-sided) PSD of the thermal force on the sphere in bulk is given by

$$S_{F,0}(\omega) = 4k_B T \Re[\gamma_0(\omega)] = 4k_B T \gamma_s \left(1 + \sqrt{\frac{\omega \tau_f}{2}} \right). \quad (5.44)$$

The DC values of $S_{F,\parallel}$ and $S_{F,\perp}$ increase to $4k_B T \gamma_s \frac{1}{1 - \frac{9a}{16h}}$ and $4k_B T \gamma_s \frac{1}{1 - \frac{9a}{8h}}$ from the bulk value of $4k_B T \gamma_s$ respectively. The increase in the thermal force is con-

sistent with the increase in the drag force, in accordance with the fluctuation-dissipation theorem [10].

The enhanced flatness of the thermal force PSD observed in the presence of a no-slip plane wall, which can be understood as resulting from destructive interference of the reflected flow, is seen in the above expressions through the lack of $\sqrt{\omega\tau_f}$ and $\omega\tau_f$ terms. In contrast, this effect is not seen in the parallel direction in the case of a perfect slip plane wall, presumably due to constructive interference from the reflected flow. However, in the perpendicular direction to a perfect slip wall, the flatness is still seen, presumably due to the no penetration boundary condition keeping the reflected flow out of phase. This will be discussed in detail in Section 8.2.

A good analogy to this destructive interference interpretation is the reflection from a fixed (and a loose) end rope. The fixed end boundary condition for the rope is similar to the no-slip boundary condition for the fluid, while the loose end boundary condition for the rope is similar to the perfect slip boundary condition. It is well known that the reflection from a fix end rope is out of phase with the incident wave, therefore resulting in a destructive interference, while the reflection from loose end rope is in phase with the incident wave, resulting constructive interference. We believe the destructive interference leads the lacking of $\sqrt{\omega\tau_f}$ and $\omega\tau_f$ terms and flattening in the thermal force power spectrum, although further studies are needed.

5.2.5 Boundary effects on Brownian motion of a trapped particle

In our experiments studying the boundary effects, the particle was confined by an optical tweezer. The theory on boundary effects including optical trapping has been proposed recently [97].

The equation of motion of an optically trapped sphere is

$$-i\omega(m_p - m_f)\mathbf{U}_\omega = \mathbf{E}_\omega - \mathcal{F}_\omega - K\mathbf{X}_\omega \quad (5.45)$$

where $-K\mathbf{X}_\omega$ is the harmonic force provided by the optical trap. The admittance in the perpendicular direction can be written as [97]

$$y_\perp^t(\omega) = \frac{-i\omega y_\perp(\omega)}{-i\omega + Ky_\perp(\omega)}, \quad (5.46)$$

and in the parallel direction as

$$y_\parallel^t(\omega) = \frac{-i\omega y_\parallel(\omega)}{-i\omega + Ky_\parallel(\omega)}. \quad (5.47)$$

It is worth noting that the optical trap does not change the effective mass and thermal force properties. With this, the entire dynamics of Brownian motion of a trapped sphere near a flat infinite wall is known at least numerically.

It is much harder to obtain the theory of unsteady Brownian motion of a sphere outside of a cylindrical wall over the entire time scales due to the complications caused by the curvature of cylinder. Efforts are currently being undertaken to pursue this.

5.3 Numerical predictions on boundary effects with experimental conditions

In this section, we give the numerical predictions of a variety of statistical quantities for our experiments. We consider a $3\ \mu\text{m}$ silica sphere ($n = 1.46$, $\rho = 2.0\ \text{g/cm}^3$) in water ($n = 1.33$, $\rho_f = 1\ \text{g/cm}^3$, $\eta = 0.9 \times 10^{-3}\ \text{Pa}\cdot\text{s}$) near an infinite flat no-slip wall. A trap stiffness of $150\ \mu\text{N/m}$ is used, which is the typical value in our experiments.

5.3.1 Position power spectral density

The position power spectral density predictions of a microsphere near a flat no-slip wall with three different sphere-wall separations ($h = 2.5\ \mu\text{m}$,

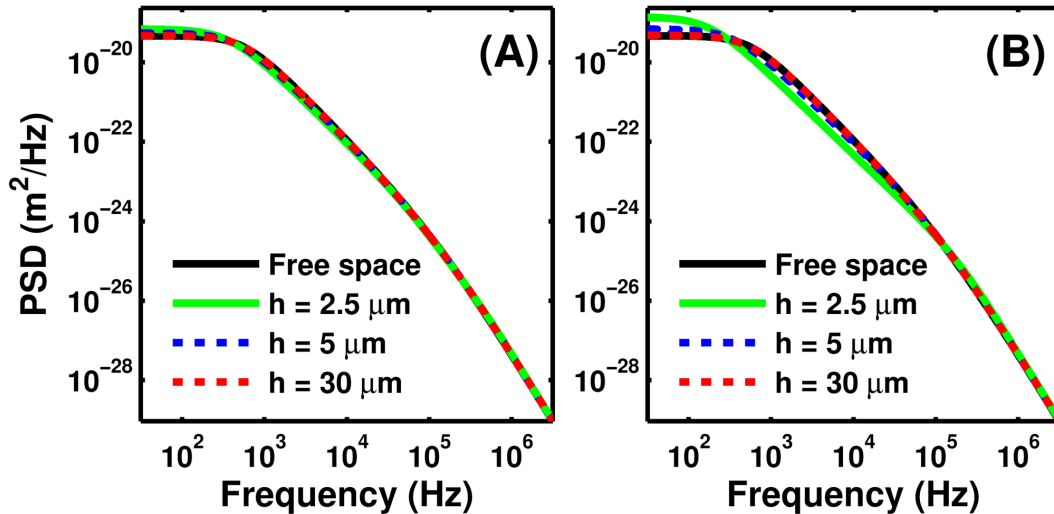


Figure 5.1: Boundary effects on the position power spectra of a $3\ \mu\text{m}$ diameter silica in water with three sphere-wall separations ($h = 2.5\ \mu\text{m}$, $5\ \mu\text{m}$, and $30\ \mu\text{m}$). The trap stiffness is $150\ \mu\text{N/m}$. (A), In the parallel direction. (B), In the perpendicular direction.

5 μm , and 30 μm) in both parallel and perpendicular directions are shown in Fig. 5.1. At high frequencies, the boundary effects are negligible in both directions. In both directions, the smaller the sphere-wall separation is the bigger the boundary effects on the sphere become. Interestingly, as compare to the free particle case, position PSD with boundary effects is enhanced at low frequencies due to boundary effects and suppressed at intermediate frequencies, thus keeping the area under the curve to $\langle x^2 \rangle = \frac{k_B T}{K}$. The boundary effects are more pronounced in the perpendicular direction than in the parallel direction. As show in Fig. 5.1, the boundary effects are negligible with a large sphere-wall separation ($h = 30 \mu\text{m}$) in both directions.

5.3.2 Velocity power spectral density

The velocity power spectral density predictions of a microsphere near a flat no-slip wall with three different sphere-wall separations ($h = 2.5 \mu\text{m}$, 5 μm , and 30 μm) are shown in Fig. 5.2. Boundary effects on velocity PSD is very similar to that on position PSD. An increased flatness of the velocity PSD due to boundary effects is consistent with the reduced correlation seen in the VACF as discussed in more detail later. The suppression of the velocity PSD from the free-space theory seen at these scales is complemented by an increase in the velocity PSD at short time scales, thus keeping the area under the curve to $\langle (v_{\parallel}^*)^2 \rangle$ and $\langle (v_{\perp}^*)^2 \rangle$ in parallel and perpendicular directions respectively.

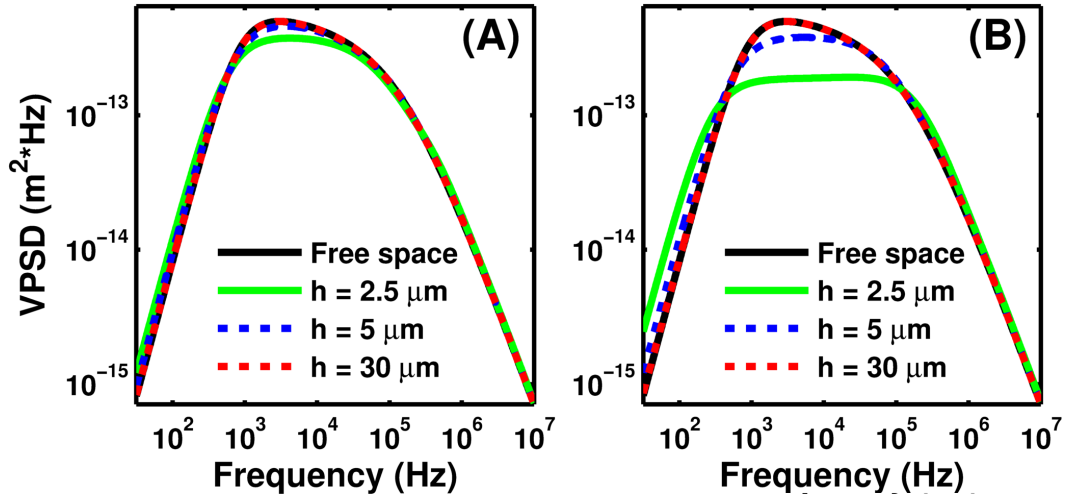


Figure 5.2: Boundary effects on the position power spectra of a $3 \mu\text{m}$ diameter silica in water with three sphere-wall separations ($h = 2.5 \mu\text{m}$, $5 \mu\text{m}$, and $30 \mu\text{m}$). The trap stiffness is $150 \mu\text{N/m}$. The black line is the theory without boundary effects. (A), In the parallel direction. (B), In the perpendicular direction.

5.3.3 Mean square displacement

The mean square displacement predictions of a microsphere near a flat no-slip wall with three different sphere-wall separations ($h = 2.5 \mu\text{m}$, $5 \mu\text{m}$, and $30 \mu\text{m}$) are shown in Fig. 5.3. Optical trapping causes the MSD to plateau around $\tau_k = \gamma_s / K$, the time scale during which the particle experiences a drift back towards the trap center, before the purely diffusive regime is reached. As shown in Fig. 5.3, the “surface confinement” occurs not only in the long time scales diffusive regime but also in the ballistic regime for small sphere-wall separations. The closer to the wall, the more suppression in the MSD.

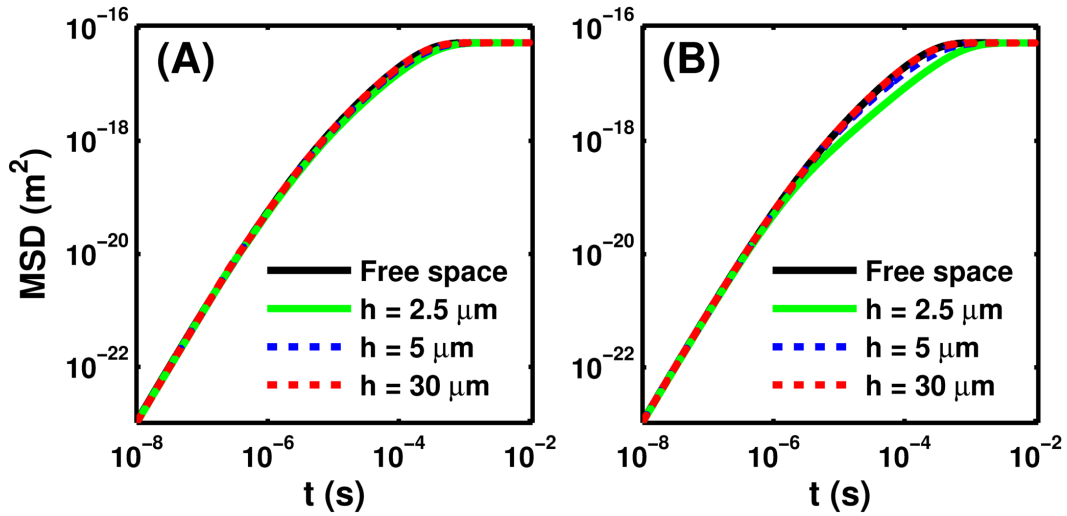


Figure 5.3: Boundary effects on the mean squared displacement (MSD) of a $3 \mu\text{m}$ diameter silica in water with three sphere-wall separations ($h = 2.5 \mu\text{m}$, $5 \mu\text{m}$, and $30 \mu\text{m}$). The trap stiffness is $150 \mu\text{N/m}$. (A), In the parallel direction. (B), In the perpendicular direction.

5.3.4 Velocity autocorrelation function

The predictions of the velocity autocorrelation function of a microsphere near a flat no-slip wall with three different sphere-wall separations ($h = 3 \mu\text{m}$, $5 \mu\text{m}$, and $30 \mu\text{m}$) are shown in Fig. 5.4. The VACF of the particle near a boundary decreases faster as the sphere-wall separation decreases. The long time tail of the VACF in the bulk case is largely cancelled by reflected flow from the wall, resulting in a more quickly decaying VACF. This rapid decay of the relaxation function reflects the loss of fluid momentum at the no-slip boundary, which is consistent with numerical simulations in Section 5.4.

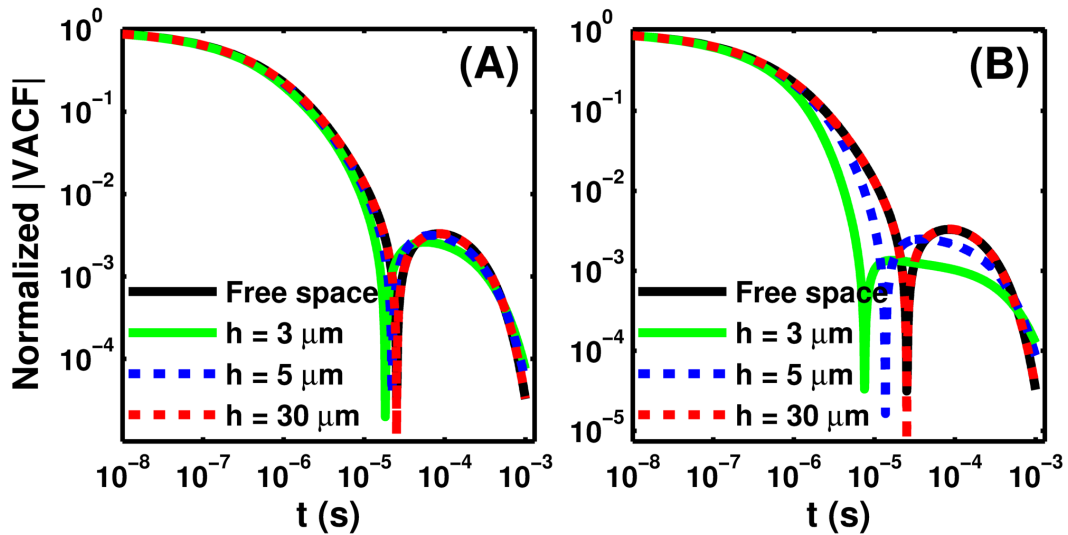


Figure 5.4: Boundary effects on velocity autocorrelation function (VACF) of a $3 \mu\text{m}$ diameter silica in water with three sphere-wall separations ($h = 3 \mu\text{m}$, $5 \mu\text{m}$, and $30 \mu\text{m}$). The trap stiffness is $150 \mu\text{N/m}$. (A), In the parallel direction. (B), In the perpendicular direction.

5.3.5 Thermal force power spectral density

The predictions of the thermal force spectrum of a microsphere near a flat no-slip wall with three different sphere-wall separations ($h = 3 \mu\text{m}$, $5 \mu\text{m}$, and $30 \mu\text{m}$) are shown in Fig. 5.5. As discussed in Section 5.2.4, it is very surprising that the thermal force loses its color at low frequencies in the presence of a boundary. The thermal force power spectral density (FPSD) acting on the particle near a no-slip wall becomes flat at low frequencies. This is believed to be a result of destructive interference between the incident and reflected flows. The smaller sphere-wall separation is, the larger flattening frequency range.

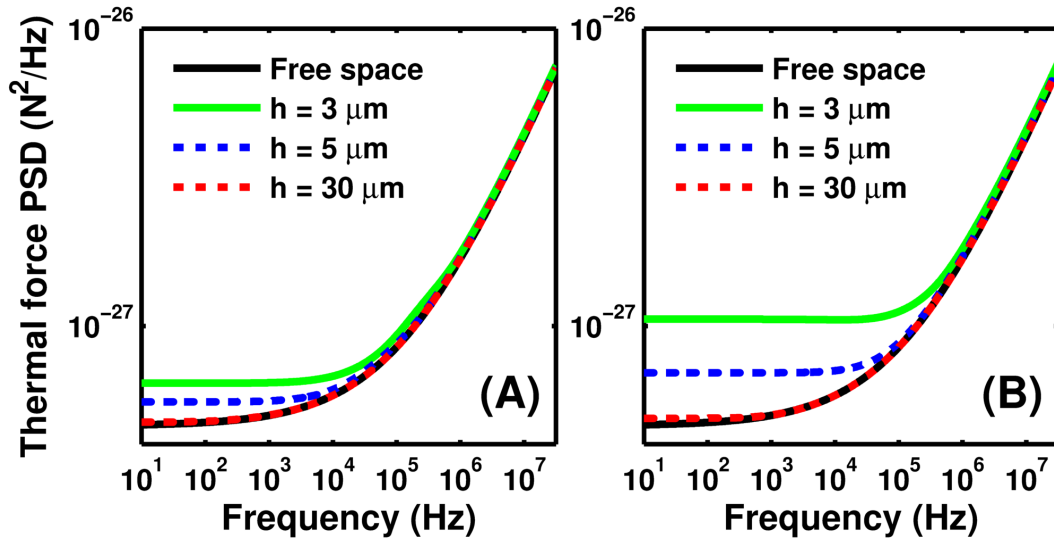


Figure 5.5: Boundary effects on the thermal force power spectra of a $3 \mu\text{m}$ diameter silica in water with three sphere-wall separations ($h = 3 \mu\text{m}$, $5 \mu\text{m}$, and $30 \mu\text{m}$). The trap stiffness is $150 \mu\text{N/m}$. (A), In the parallel direction. (B), In the perpendicular direction.

In summary, the boundary effects on Brownian motion are anisotropic, they are more pronounced in the perpendicular direction than in the parallel direction. In both directions, the closer to the wall, the bigger boundary effects are, the earlier boundary effects occur in timewise.

5.4 Fluid dynamics simulation on boundary effects

We study the fluid dynamics around a sphere both in free-space and near a no-slip wall numerically using COMSOL Multiphysics with a 2D axial symmetrical configuration [117,118]. The fluid in this simulation has the same properties as water and the diameter of the sphere is $3 \mu\text{m}$.

Fig. 5.6 shows the longitudinal section of Stokes flow field around a moving sphere both in an unbounded and bounded fluid. The white half circle represents the sphere, which is moving downwards at $1 \mu\text{m/s}$. The pressure field, shear stress magnitude field, velocity magnitude field and vorticity field (azimuthal component) are plotted in a $20 \mu\text{m}$ by $20 \mu\text{m}$ view. The left-edge represents the axis of cylindrical symmetry. The fields around the free-space sphere have up-down symmetry, while the wall (purple solid line) breaks this symmetry. In the bounded case, the sphere-wall separation h is $3 \mu\text{m}$. The fields above the sphere both in the bounded case and unbounded case are similar. The fields below the sphere are significantly altered by the wall. The

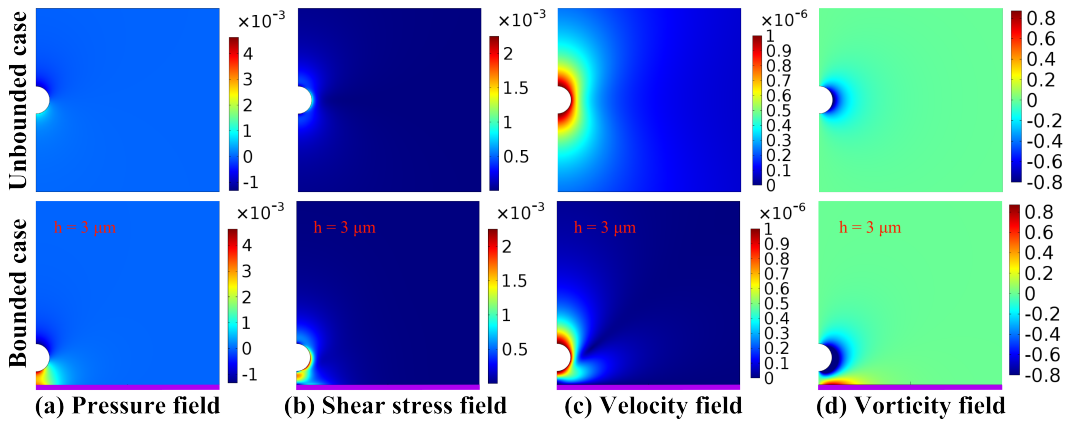


Figure 5.6: The fluid fields of steady Stokes flow near a sphere both in free space and bounded fluid (a), pressure field. (b), shear stress magnitude field. (c), velocity magnitude field. (d), vorticity field (azimuthal component). The top four figures are for unbounded case and the bottom four figures are for bounded case. The white half circle represents the sphere ($3 \mu\text{m}$ diameter) and the left boundary corresponds to the axis of cylindrical symmetry. The purple solid lines represent the no-slip wall and all other boundaries are open boundaries. The sphere is moving downwards at $1 \mu\text{m/s}$. In the bounded case, the sphere is at position with a sphere-wall separation of $3 \mu\text{m}$.

fluid builds up much higher pressure and shear stress, which is responsible for the faster-decay VACF of a bounded sphere. The same conclusion has been drawn for a sphere in a confined fluid between two flat walls by numerical simulation [119]. The fluid creates a significant transverse flow parallel to the wall due to the presence of the no-slip boundary. Vorticity is generated not only on the surface of the sphere but also on the surface of the wall but with a opposite sign.

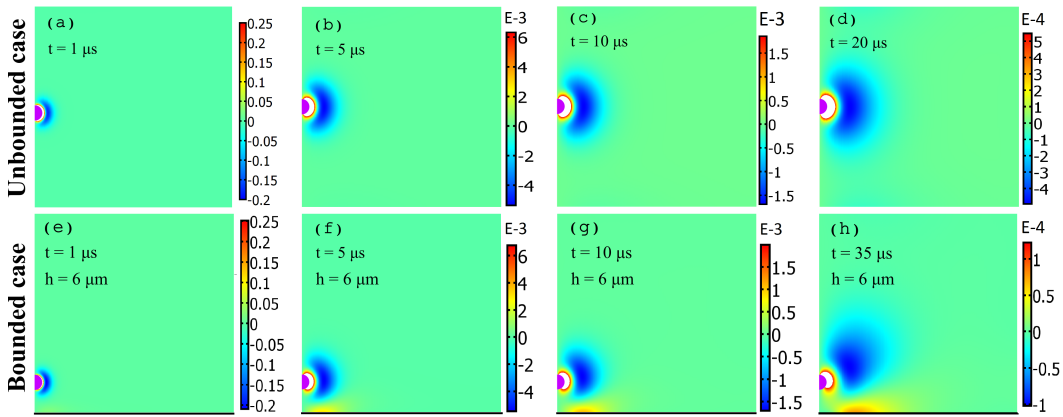


Figure 5.7: A study of the onset of boundary effects by observing the vorticity field (azimuthal component). The sphere (purple half circle, $3 \mu\text{m}$ diameter), initially at rest, receives a 1-s impulse and at position in the downward direction, with an acceleration of 2 m/s^2 in the first $0.5 \mu\text{s}$ and a deceleration of 2 m/s^2 in the second $0.5 \mu\text{s}$. Unbounded case (a), vorticity field at $t = 1 \mu\text{s}$. (b), vorticity field at $t = 5 \mu\text{s}$. (c), vorticity field at $t = 10 \mu\text{s}$. (d), vorticity field at $t = 20 \mu\text{s}$. Bounded case with the sphere initially at a sphere-wall separation of $6 \mu\text{m}$. (e), vorticity field at $t = 1 \mu\text{s}$. (f), vorticity field at $t = 5 \mu\text{s}$. (g), vorticity field at $t = 10 \mu\text{s}$. (h), vorticity field at $t = 35 \mu\text{s}$. The left edge is the axis of cylindrical symmetry and top and right boundaries are open boundaries. The white areas are out-of-range clippings: the white areas should be redder than their surrounding color. The bottom edge is an open boundary in the unbounded case and a no-slip boundary in the bounded case.

Conventionally, the boundary effects are assumed to start becoming important around $\tau_w = \rho_f h^2 / \eta$, which is the time scale over which the vorticity generated on the surface of the sphere (or the wall) propagates across the sphere-wall separation. It turns out that τ_w is just a rough estimation. As discussed in Chapter 6, our data (both in VACF and MSD) starts to deviate from the free-space theory well before τ_w . We study the onset of boundary effects by observing the dynamics of the vorticity field (azimuthal component), as shown in Fig. 5.7. Initially, both the 3 μm diameter sphere and fluid are at rest. At $t = 0$ the sphere receives a 1- μs downwards impulse accelerating with a constant acceleration of 2 m/s^2 for 0.5 μs and then decelerates with a constant deceleration of 2 m/s^2 to a stop in another 0.5 μs . The vorticity field (40 μm by 40 μm) shows up-down symmetry in the unbounded case, which is plotted in the top half (Fig. 5.7(a-d)). In the bounded case (Fig. 5.7(e-h)), the sphere moves in the same way except near a no-slip wall with a sphere-wall separation 6 μm . The wall starts to break the vorticity field symmetry in a visible way around 5 μs , which is well before $\tau_w = 36 \mu\text{s}$. It must be noted that in addition to vorticity diffusion, there are inertial effects of the boundary at much shorter time-scales due to the propagation of sound waves. To the approximation that the fluid is incompressible, these effects occur almost instantaneously. However, these effects are difficult to discern in our experimental work.

Chapter 6

Observation of broadband boundary effects on Brownian motion

There have been many experiments verifying the surface confinement effect in the diffusive regime, mainly focusing on measuring the changes in the diffusion coefficient of micron-sized particles near surfaces using dynamic light scattering [120, 121], video microscopy [72, 122], total internal reflection microscopy [63, 123] or oscillating optical tweezers [73, 124].

In addition to surface confinement, it has been reported that the presence of a no-slip boundary also affects the velocity autocorrelation function [97, 125]. The long time tail of the VACF in the bulk case is largely cancelled by reflected flow from the wall, resulting in a more quickly decaying VACF. Boundary effects on the position power spectral density in a limited frequency window have been reported [15, 103]. These experiments have observed a resonance in the position PSD caused by the color of the thermal force, which we have observed as well and is shown in Section 4.3.5. They also observed a suppression of this resonance caused boundary effects as the sphere-wall separation decreases.

A broadband, comprehensive experimental study of effects of the bound-

ary via hydrodynamic interaction on Brownian motion was still lacking until recently [104], in spite of the previous work on boundary effects mentioned above [15, 63, 73, 97, 103, 120, 122, 125] and the fact that Brownian motion of a sphere in bulk has been well studied [15–18, 126].

In this chapter, we investigate the effects of a boundary on the Brownian motion of a sphere in water both in the diffusive and ballistic regime. We report high-bandwidth, comprehensive measurements of Brownian motion of an optically trapped micrometer-sized silica sphere in water near an approximately flat wall. At short distances we observe anisotropic Brownian motion with respect to the wall. We find that surface confinement not only occurs in the long time scale diffusive regime but also in the short time scale ballistic regime, and the velocity autocorrelation function of the Brownian particle decays faster than that of particle in a bulk fluid. Furthermore, at low frequencies the thermal force loses its color due to the reflected flow from the no-slip boundary. The power spectrum of the thermal force on the particle near a no-slip boundary becomes flat at low frequencies.

It is important to note that the boundary effects in this article occur only through hydrodynamic interaction. Other close-range forces between particles and boundary, like the electrostatic force [127], van der Waals force [128], and Casimir force [70] can be neglected because we keep the sphere-wall separation ($h \geq 3 \mu\text{m}$) much larger than the length scales at which those forces become relevant.

6.1 Experimental setup

Since most of the setup has been discussed in detail in Chapter 4, this chapter only emphasizes the modifications specifically made for studying Brownian motion with boundary effects in detail.

A simplified schematic of our experimental setup for measuring the Brownian motion of a micrometer-sized silica sphere in water near an approximately flat wall, both in perpendicular and parallel directions, is shown in Fig. 6.1. An approximately $3\ \mu\text{m}$ diameter silica glass microsphere is trapped by a $1064\ \text{nm}$ laser focused by the same water-immersion microscope objective as in Chapter 4. The trapping laser beam also serves as the detection beam, which is collected by an identical objective and then split into two roughly equal halves in the horizontal direction in the lab frame. The same home-made balanced detector as in Chapter 4 was used to amplify the power difference between the halves, which depends linearly on the position of the trapped particle, as shown in Fig. 6.1(A). A fluid chamber, containing two $80 \pm 1\ \mu\text{m}$ diameter cylindrical glass fibers with their axes in the vertical and horizontal directions respectively, is used to introduce the microspheres to the trap, as shown in Fig. 6.1(B). The fibers provide well-defined cylindrical boundaries with no-slip boundary conditions. The geometry of the sphere and cylindrical boundary is shown to scale in Fig. 6.1(C).

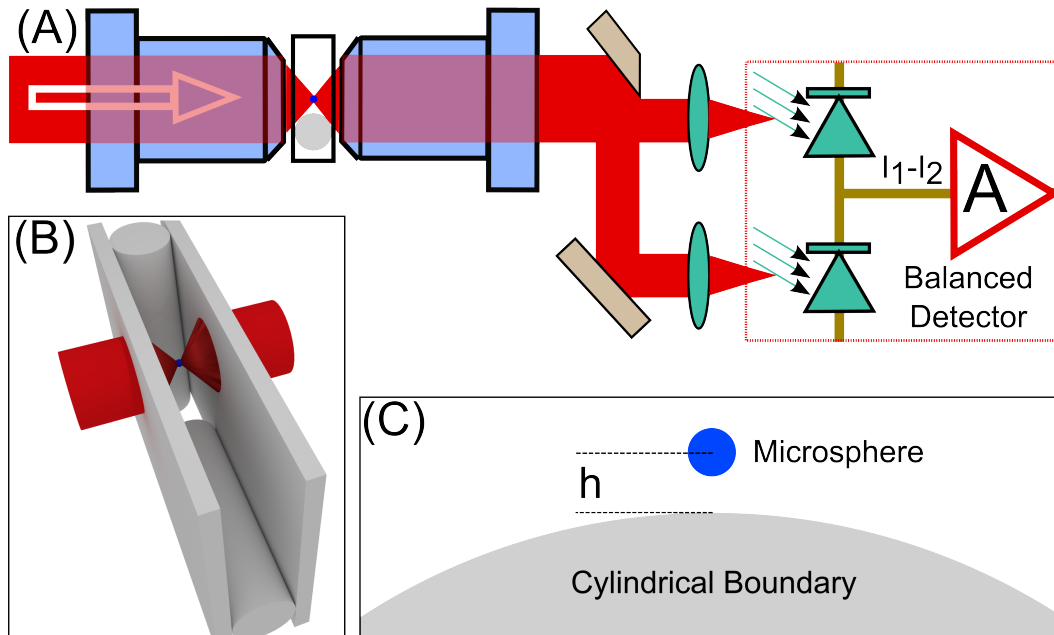


Figure 6.1: Schematic of Brownian motion of an optically trapped glass microsphere in water near a boundary. (A), Simplified schematic showing a glass microsphere ($3 \mu\text{m}$ diameter) trapped at the focus of a 1064 nm optical tweezer near a boundary. The trapping beam is used to detect the horizontal motion of the particle using a high bandwidth balanced detection system. (B), Two $80 \pm 1 \mu\text{m}$ diameter cylindrical fibers are sealed in the chamber with their axes in the vertical and horizontal directions respectively, providing well-defined no-slip cylindrical boundaries. (C), The geometry of the sphere and cylindrical boundary to scale. The sphere-wall separation refers to the distance between the center of the sphere and the surface of the boundary.

6.1.1 Optical setup

The trapping 1064 nm laser beam (Mephisto, Innolight) is introduced by a polarization-maintaining single mode fiber (Thorlabs, P3-1064PM-FC-5) and focused by a water-immersion microscope objective (LOMO, OM-25). The trapping laser beam also serves as the detection beam, which is collected

by an identical objective and then split into two roughly equal halves in the horizontal direction using a D-shaped mirror (Thorlabs, BBD05-E03). The same AC-coupled detector discussed in Chapter 4 is used to amplify the power difference between the halves, which depends linearly on the position of the trapped particle. The position of the D-shaped mirror is adjusted to balance the laser power in the two halves. In this experiment, the trapping laser beam power is around 400 mW and the detection beam power is set to approximately 150 mW. The detailed schematic of the optical setup is shown in Fig. 4.2.

6.1.2 Flow cell with fibers

The fluid flow cell is constructed in a similar way as in Section 4.1.3. It is constructed within a layer of nescofilm (Bando Chemical Ind. LTD., 80 μm thickness) sandwiched between two number 0 microscope coverslips (Ted Pella, 100 μm thickness). Two 80 ± 1 μm diameter bare fibers (Thorlabs SM980G80, with coating layer stripped by fiber stripping tool, Thorlabs T04S10) are heat-sealed in the chamber with their axes in the vertical and horizontal directions respectively, providing well-defined cylindrical no-slip boundaries. The length of the bare fibers are typically around 3 cm. We sonicate and examine them under an optical microscope to ensure the surface of the stripped fiber is smooth. The schematic for the flow cell with embedded fibers is shown in Fig. 6.2. We are able to measure the Brownian motion in perpendicular and parallel directions to the wall independently with vertical and horizontal fibers respectively since our detection system measures the horizontal motion of the

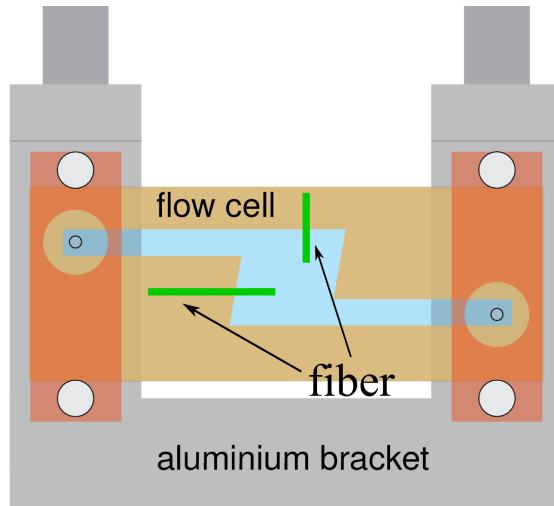


Figure 6.2: The fluid flow cell with two cylindrical fiber embedded for studying boundary effects.

microsphere.

The cylindrical boundary is chosen intentionally to avoid clipping the laser beam with the boundary for small sphere-wall separations. In our setup, the waist of the trapping beam is estimated to be around $1 \mu\text{m}$, and as long as the sphere-wall separation h is more than $3 \mu\text{m}$, the clipping effect can be neglected. We confirm the lack of clipping by monitoring the trapping beam transmission rate through the chamber and by the stability of the fitting parameters at different positions with various sphere-wall separation.

The optical trap confines the particle to the center of the chamber in the beam propagation direction to minimize boundary effects on the motion of the particle imposed by the coverslips. Therefore, coverslip boundary effects can be neglected since the sphere-coverslip separation is $40 \mu\text{m}$, which is considerably

larger than the size of the sphere.

6.1.3 Microspheres and fluids

Experiments are performed using silica microspheres (Bangs Laboratories SS05N, $n = 1.46$, $\rho = 2.0 \text{ g/cm}^3$) in HPLC-grade water ($n = 1.33$, $\rho_f = 1 \text{ g/cm}^3$, $\eta = 0.9 \times 10^{-3} \text{ Pa}\cdot\text{s}$) at $22 \pm 1 \text{ }^\circ\text{C}$. High sphericity of the microspheres is necessary to eliminate the rotational motion contribution due to asymmetry of the microspheres, and was confirmed by scanning electron microscope images as shown in Chapter 4.

6.1.4 Relative position control with a piezo-stage

The whole chamber is mounted onto a piezo-stage, which is constructed of two feedback piezo elements with differential micrometers (Thorlabs DRV517), controlled by a piezo controller (Thorlabs, BPC301). The built in strain gauge¹ conveniently reads the absolute piezo length, namely the relative positions of fiber to the trapped microsphere, and displays it on a LCD screen. With this, we have the ability to position the cylindrical fibers with a precision of $\sim 10 \text{ nm}$ and a range of up to $30 \text{ }\mu\text{m}$ in two directions.

It was a surprising find that the close piezo-stage PID control loop actually disturbed the fluid resulting in a non-equilibrium system. The close

¹The metallic strain gauge consists of a very fine wire or metallic foil, arranged in a grid pattern, which is bonded to the piezo. Therefore, any strain experienced by the piezo is transferred directly to the strain gauge, which expands or contracts, causing a proportional change in electrical resistance. Such small change in resistance is measured by a bridge configuration, like Wheatstone bridge.

PID loop constantly adjusts the voltage to the piezo trying to maintain the constant strain, which stabilizes the piezo strain at long time scale but makes it more noisy at high frequencies. Therefore, the piezo stage PID control loop is kept open while taking data.

There are three main sources causing fluctuations in the sphere-wall separation: relative vibrational motion between the fibers and laser trapping focus, the thermal motion of the microsphere in the trap, and the drifting in piezo length. The relative vibration is reduced to on the order of 10 nm by using a gas floating optical table (TMC Vibration Control). The thermal motion fluctuations in the trap can be reduced by increasing the trap strength, resulting in $\sqrt{\frac{k_B T}{K}} \sim 10$ nm in our system. The piezo length drifting can be minimized by waiting for a long time (a few minutes) after applying a certain voltage to the piezo, which lengthens the amount of time required to take data.

6.1.5 Imaging

Two typical images of trapped microspheres near a fiber are shown Fig. 6.3. These images provide us the convenience to estimate the sphere-wall separation. Due to the strong interference patterns, this estimation is limited with a uncertainty up to 1 μm . We developed two more precise ways to calibrate the absolute distance between the sphere and wall, as discussed in Section 6.2.6.

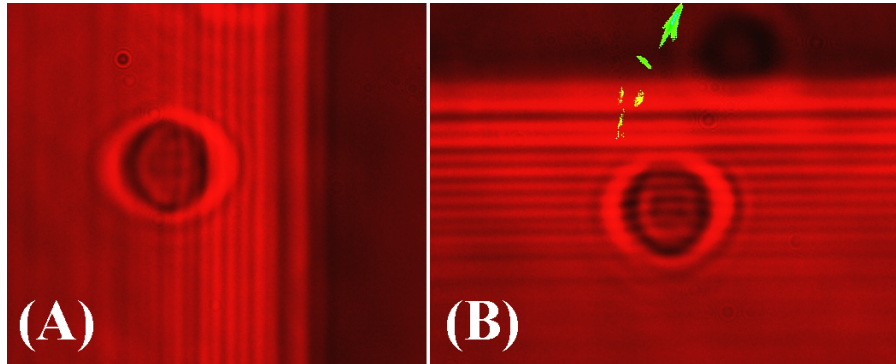


Figure 6.3: Typical images of a trapped silica microsphere in water near a glass cylindrical fiber. (A), a silica microsphere near a vertical fiber; (B), a silica microsphere near a horizontal fiber. (Green spots are the dead pixels on the camera).

6.1.6 Data acquisition

The voltage signal recorded by the same balanced detector as in Chapter 4, is recorded by the same 16-bit digitizer (GaGe applied, CS1622) at a sampling rate of 200 MSa/s. Each continuous trajectory contains 2^{27} samples, corresponding to about 0.7 s. We take at least 10 such measurements at each position. The data was acquired with the digitizer's 25 MHz anti-aliasing filter enabled.

6.2 Experimental results and discussion

This section describes results of the boundary effects on a $3\ \mu\text{m}$ silica microsphere near a $80\ \mu\text{m}$ diameter cylindrical glass fiber in water. It is important to note that the cylindrical boundary can be approximated as a flat wall with small sphere-wall separations ($\leq \sim 7\ \mu\text{m}$). Therefore, the theory for

a flat infinite wall can be adapted to analyze the experimental data.

6.2.1 Mean square displacement

A least-squares fit of the mean square displacement (MSD) of the recorded trajectories to the theory of Brownian motion near a no-slip flat wall [97, 110] is used to determine the sphere diameter d , the trap stiffness K , and the detector volts-per-meter calibration factor C . The MSDs at four different positions (with sphere-wall separations of $30 \mu\text{m}$, $6.1 \mu\text{m}$, $4.6 \mu\text{m}$ and $3.1 \mu\text{m}$) in the perpendicular direction to the wall are shown in Fig. 6.4. The sphere diameter ($d = 3.06 \pm 0.19 \mu\text{m}$), trap stiffness ($K = 151 \pm 31 \mu\text{N/m}$) and detector volts-per-meter calibration factor ($C = 20.1 \pm 2.0 \text{ mV/nm}$) are similar at those four positions, which indicates that the laser is not clipped by the cylindrical boundary. The uncertainty of each fit parameter is determined from the variance in the results of independent MSD fits of 10 trajectories per position.

At all four positions, the optical trapping causes the MSD to plateau around $\tau_k = \gamma_s/K$, the time scale during which the particle experiences a drift back towards the trap center, where $\gamma_s = 6\pi\eta a$ is the Stokes drag coefficient, before the purely diffusive regime is reached. The boundary effects are negligible on MSD with a large sphere-wall separation, $h = 30 \mu\text{m}$, as shown in Fig. 6.4(A). The experimental data agrees well with both free-space theory and boundary theory. Fig. 6.4(B-D) shows that the surface confinement effects appear on the time scale of $\tau_w = \rho_f h^2/\eta$, which is the time taken for vorticity

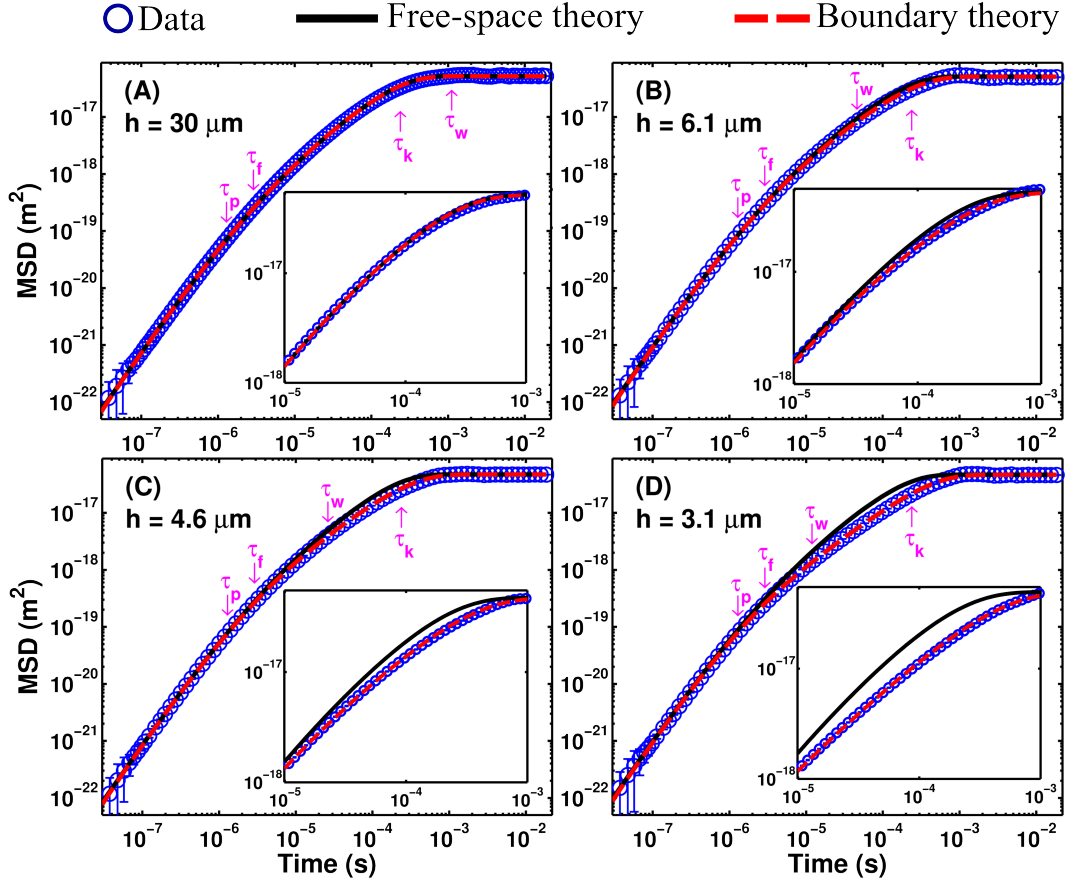


Figure 6.4: Experimental and theoretical mean square displacements at 4 positions in perpendicular direction with respect to the wall. (A), with a sphere-wall separation of $30 \mu\text{m}$ ($\tau_w=0.9 \text{ ms}$). (B), with a sphere-wall separation of $6.1 \mu\text{m}$ ($\tau_w=37 \mu\text{s}$). (C), with a sphere-wall separation of $4.6 \mu\text{m}$ ($\tau_w=21 \mu\text{s}$). (D), with a sphere-wall separation of $3.1 \mu\text{m}$ ($\tau_w=9.6 \mu\text{s}$). The blue circles are the experimental data ($\tau_p = 1 \mu\text{s}$, $\tau_f = 2.3 \mu\text{s}$, $\tau_K = 190 \mu\text{s}$); the black lines are the unbounded theoretical predictions [83] and the red dashed lines correspond to the bounded theoretical predictions at various sphere-wall separations [111]. The MSD becomes suppressed as the sphere approaches the wall. The insets show higher resolution of the suppression of the MSD.

to traverse the distance from the wall to the sphere [15, 110]. As discussed in Section 5.4, τ_w is just a rough estimation. In fact, the boundary effects could

occur a decade earlier than the prediction by τ_w . The MSD is suppressed as the sphere-wall separation decreases. When τ_w is comparable to τ_p and τ_f , the surface confinement on the motion of the particle due to boundaries not only occurs in the diffusive regime, but also in the ballistic regime, as shown clearly in Fig. 6.4(D).

6.2.2 Velocity autocorrelation function

The velocity autocorrelation functions, normalized to $\langle (v_{\perp}^*)^2 \rangle$, in the perpendicular direction to the wall, are shown in Fig. 6.5, for the same positions as in Fig. 6.4 (with $h = 30 \mu\text{m}$, $6.1 \mu\text{m}$, $4.6 \mu\text{m}$ and $3.1 \mu\text{m}$). The boundary effects are negligible on VACF with a large sphere-wall separation $h = 30 \mu\text{m}$, as shown in Fig. 6.5(A). Fig. 6.5(B-D) show that the VACF of a particle near a boundary decreases faster as the sphere-wall separation decreases. The rapid decay of the relaxation function reflects the loss of fluid momentum at the no-slip boundary, which is consistent with numerical simulations as discussed in Section 5.4. The time at which the VACF near a wall starts falling remarkably below that in an unbounded fluid is related to the time scale τ_w . It is worth to emphasize again that τ_w is just a rough estimation, as discussed in Section 5.4. As shown here, the boundary effects could occur a decade earlier than the predicted τ_w .

The VACF is very sensitive to the sphere-wall separation, and therefore can be used to precisely measure this separation, which will be discussed in detail in Section 6.2.6.

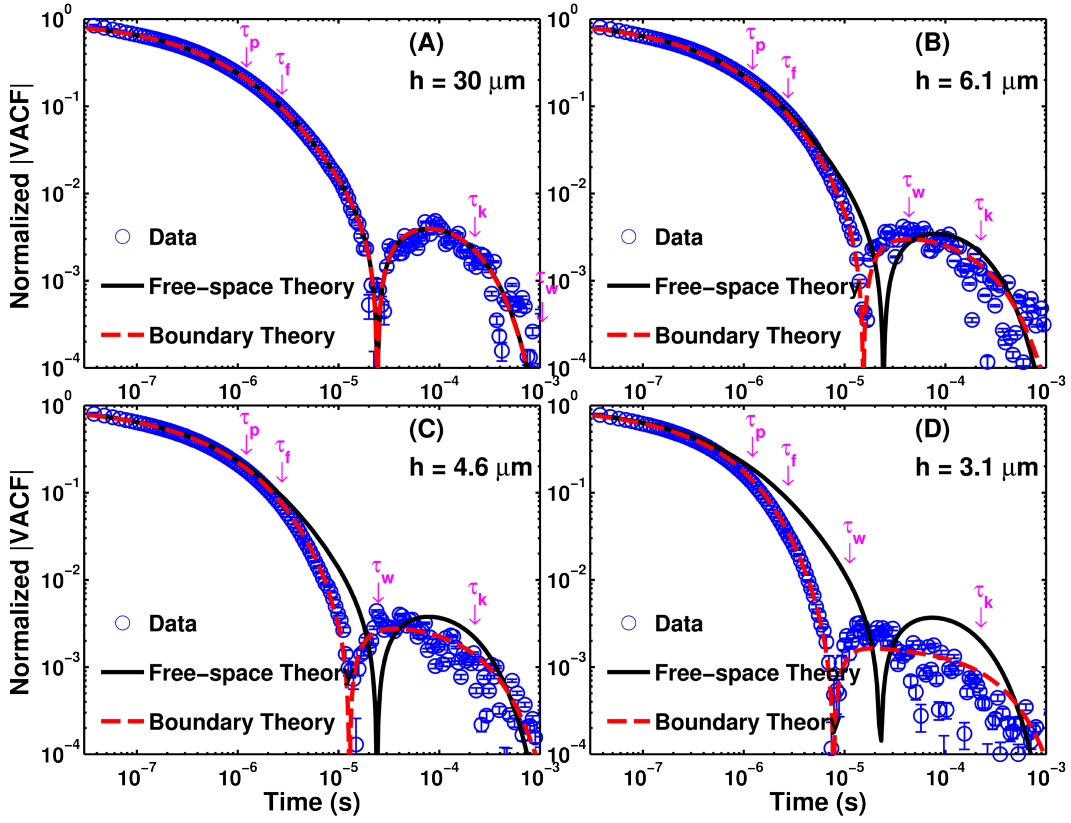


Figure 6.5: Experimental and theoretical velocity autocorrelation function (VACF) at the same positions as in Fig. 6.4 in the perpendicular direction with respect to the wall. The plots show the absolute value (normalized to $\langle(v_{\perp}^*)^2\rangle$) on a log-log scale. The sharp cusp-like features correspond to zero crossings. (A), with a sphere-wall separation of $30\ \mu\text{m}$ ($\tau_w = 0.9\ \text{ms}$). (B), with a sphere-wall separation of $6.1\ \mu\text{m}$ ($\tau_w = 37\ \mu\text{s}$). (C), with a sphere-wall separation of $4.6\ \mu\text{m}$ ($\tau_w = 21\ \mu\text{s}$). (D), with a sphere-wall separation of $3.1\ \mu\text{m}$ ($\tau_w = 9.6\ \mu\text{s}$). The blue circles are the experimental data ($\tau_p = 1\ \mu\text{s}, \tau_f = 2.3\ \mu\text{s}, \tau_K = 190\ \mu\text{s}$); the black lines are the theoretical predictions for an unbounded particle [83] and the red dashed lines correspond to the bounded theoretical predictions with various sphere-wall separations [111]. The VACF decays faster as the sphere approaches the wall.

6.2.3 Position power spectral density

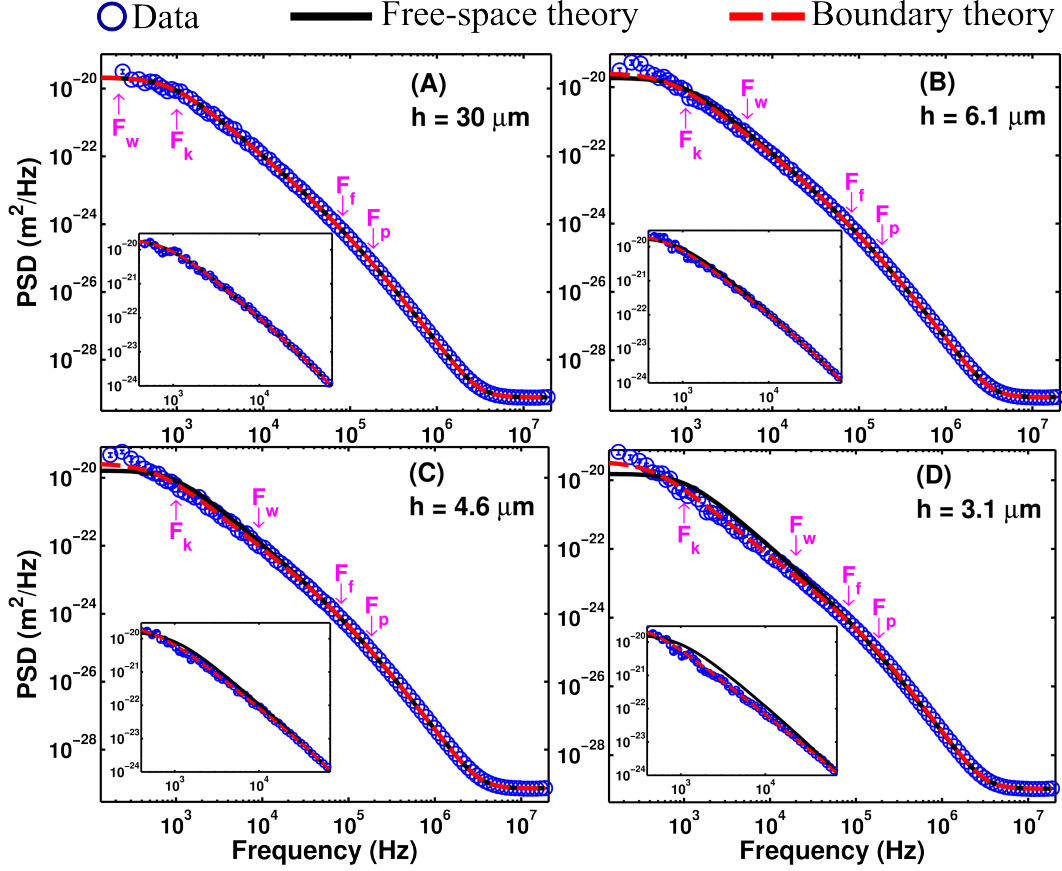


Figure 6.6: Experimental and theoretical position power spectra at the same positions as in Fig. 6.4 in the perpendicular direction to the wall. (A), $h = 30 \mu\text{m}$ ($F_w = 177 \text{ Hz}$). (B), $h = 6.1 \mu\text{m}$ ($F_w = 4.3 \text{ kHz}$). (C), $h = 4.6 \mu\text{m}$ ($F_w = 7.5 \text{ kHz}$). (D), $h = 3.1 \mu\text{m}$ ($F_w = 16.6 \text{ kHz}$). The blue circles are the experimental data ($F_p = 153 \text{ kHz}$, $F_f = 68 \text{ kHz}$, $F_K = 833 \text{ Hz}$); the black lines are the sum of the unbounded theoretical predictions and a constant shot noise and the red dashed lines correspond to the sum of the bounded theoretical predictions at various sphere-wall separations [111] and a constant shot noise. At high frequencies, the PSDs flatten at $3 \times 10^{-15} \text{ m}/\sqrt{\text{Hz}}$, limited by the shot noise of the detection beam [17, 18]. The insets show higher resolution of the suppression of the position PSD at intermediate frequencies.

The position PSD for motion perpendicular to the wall at four different wall-to-sphere distances (with $h = 30 \mu\text{m}$, $6.1 \mu\text{m}$, $4.6 \mu\text{m}$ and $3.1 \mu\text{m}$) is shown in Fig. 6.7 . The DC-value of the PSD increases as we go closer to the wall, which was not evident in previous work [15, 103] due to normalization. Observation of this in the experiment is obscured by low-frequency noise. However, we have observed that the position PSD decays faster than it would in free-space, which is corresponding to the increased flatness of the thermal force near the wall. The frequency at which the position PSD near a wall starts deviating remarkably from that in an unbounded fluid is related to the frequency scale $F_w = 1/(2\pi\tau_w)$. It is worth noting that F_w is a rough estimation as well. In reality, the boundary effects occur at frequencies one decade higher than the predicted F_w . At larger sphere-wall separations (for example, $h = 30 \mu\text{m}$), the boundary effects on position PSD are negligible. At high frequencies, the PSDs flatten at around $3 \times 10^{-15} \text{ m}/\sqrt{\text{Hz}}$, limited by the shot noise of the detection beam [17, 18].

6.2.4 Velocity power spectral density

The velocity power spectral density (velocity PSD) is the Fourier transform of the VACF, and characterizes the distribution of power in the fluctuations of the velocity at various frequencies. The velocity PSD for motion perpendicular to the wall is shown in Fig. 6.7 with the same sphere-wall separations as in Fig. 6.4 (with $h = 30 \mu\text{m}$, $6.1 \mu\text{m}$, $4.6 \mu\text{m}$ and $3.1 \mu\text{m}$). The reduced correlation seen in the VACF close to the wall is seen as an increased

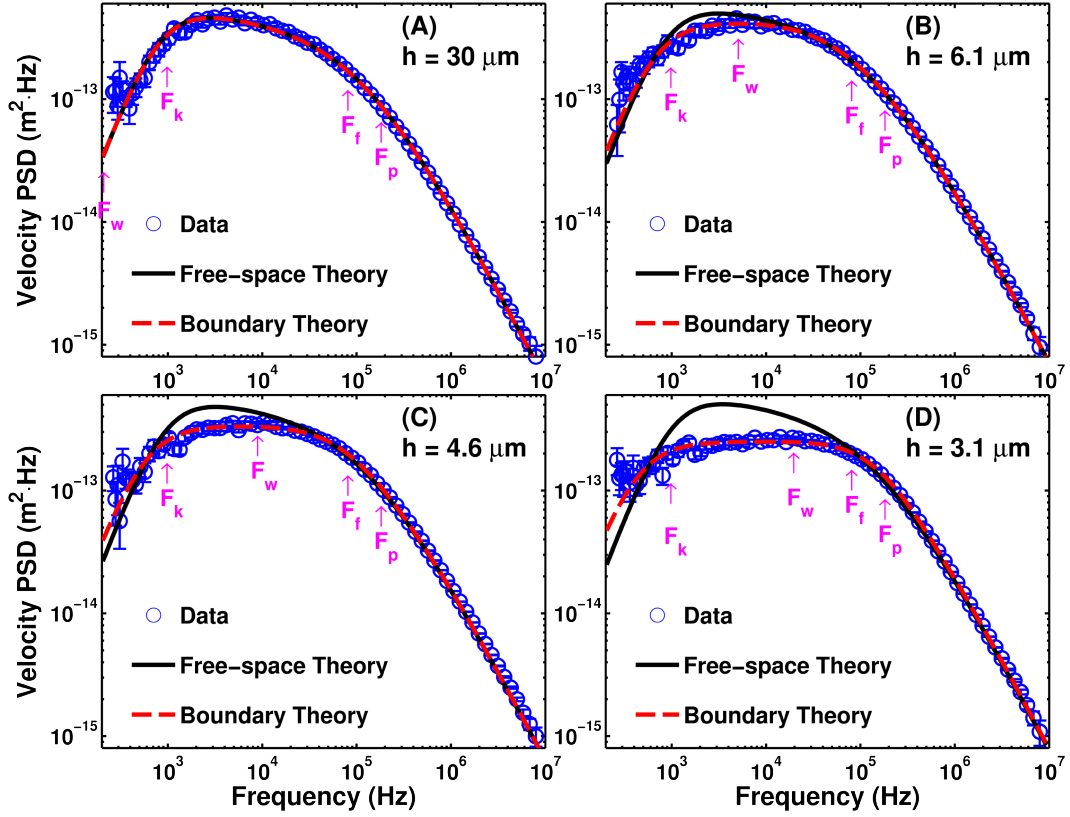


Figure 6.7: Experimental and theoretical velocity power spectra (velocity PSD) at the same positions as in Fig. 6.4 in perpendicular direction to the wall. (A), $h = 30 \mu\text{m}$ ($F_w = 177 \text{ Hz}$). (B), $h = 6.1 \mu\text{m}$ ($F_w = 4.3 \text{ kHz}$). (C), $h = 4.6 \mu\text{m}$ ($F_w = 7.5 \text{ kHz}$). (D), $h = 3.1 \mu\text{m}$ ($F_w = 16.6 \text{ kHz}$). The blue circles are the experimental data ($F_p = 153 \text{ kHz}$, $F_f = 68 \text{ kHz}$, $F_K = 833 \text{ Hz}$); the black lines are the sum of the unbounded theoretical predictions and the red dashed lines correspond to the bounded theoretical predictions at various sphere-wall separations [111].

flatness of the velocity PSD at similar time-scales (or corresponding frequency-scales). The frequency at which the velocity PSD near a wall starts to deviate remarkably from that in an unbounded fluid is related to the frequency scale $F_w = 1/(2\pi\tau_w)$. The suppression of the velocity PSD from the free-space the-

ory seen at these scales is complemented by an increase in the velocity PSD at short time scales, thus keeping the area under the curve to $\langle (v_{\perp}^*)^2 \rangle$.

6.2.5 Thermal power spectral density

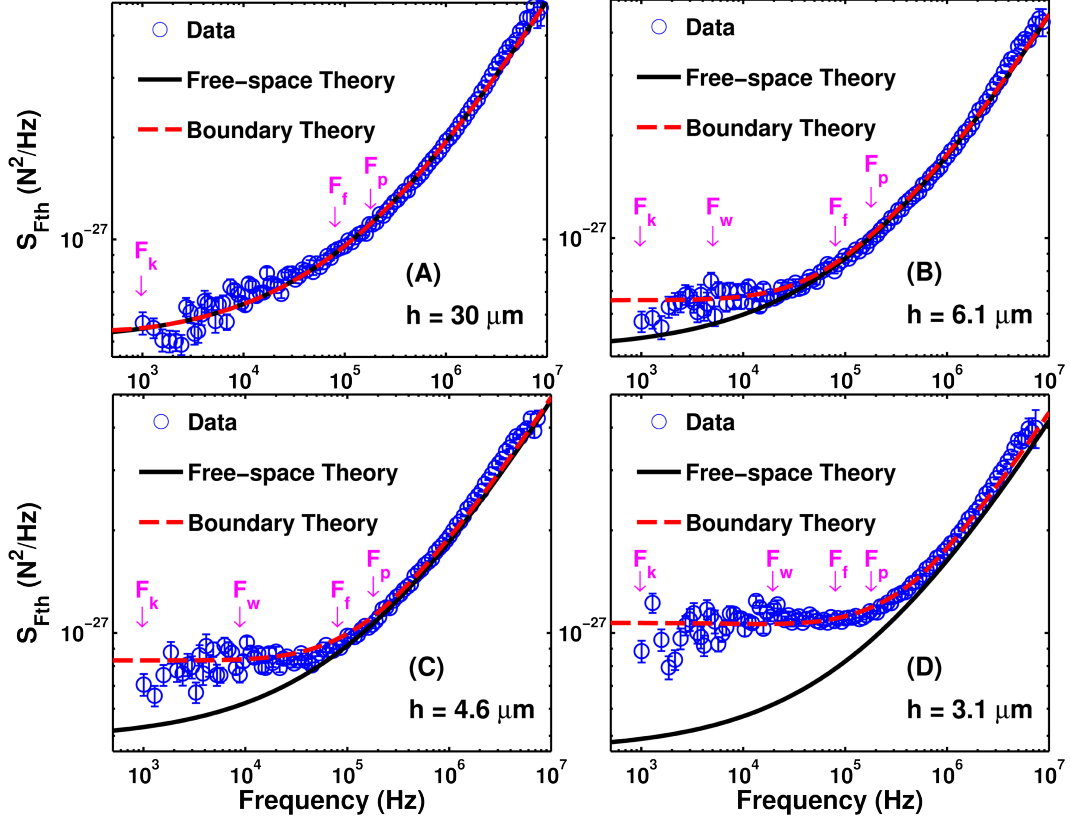


Figure 6.8: Experimental and theoretical thermal force power spectral density (FPSD) at the same positions as in Fig. 6.4 in perpendicular direction to the wall. ((A), $h = 30 \mu\text{m}$ ($F_w = 177 \text{ Hz}$). (B), $h = 6.1 \mu\text{m}$ ($F_w = 4.3 \text{ kHz}$). (C), $h = 4.6 \mu\text{m}$ ($F_w = 7.5 \text{ kHz}$). (D), $h = 3.1 \mu\text{m}$ ($F_w = 16.6 \text{ kHz}$). The blue circles are the experimental data ($F_p = 153 \text{ kHz}$, $F_f = 68 \text{ kHz}$, $F_K = 833 \text{ Hz}$); the black lines are the unbounded theoretical predictions and the red dashed lines correspond to the bounded theoretical predictions at various sphere-wall separations [111].

As discussed in Chapter 3, in the Einstein-Ornstein-Uhlenbeck model [13], which is valid only when the inertia of the fluid is negligible, the thermal force exerted on Brownian particles is assumed to be spectrally “white,” meaning it is delta correlated and has a flat power spectral density $S_{F_{th}} = 4k_B T \gamma_s$. Addition of the Basset force to the Einstein-Ornstein-Uhlenbeck model results in the colored thermal force spectral density $S_{F_{th}} = 4k_B T \gamma_s \left(1 + \sqrt{\omega \tau_f / 2}\right)$ [83]. This has recently been experimentally verified [15, 17, 103]. We have verified this as well, as discussed in Section 4.3.5.

More interestingly, the thermal force loses its color at low frequencies in the presence of a boundary. The thermal force power spectral density (FPSD) acting on the particle near a no-slip wall becomes flat at low frequencies ($\omega \tau_f \ll 1$ and $\omega \tau_w \ll 1$). This is believed to be a result of destructive interference between the incident and reflected flows, though more study is needed. The FPSDs in the direction perpendicular to the wall are shown in Fig. 6.8, for the same positions as in Fig. 6.4 (with $h = 30 \mu\text{m}$, $6.1 \mu\text{m}$, $4.6 \mu\text{m}$ and $3.1 \mu\text{m}$). Fig. 6.8(A), which has a large sphere-wall separation of $h = 30 \mu\text{m}$, shows that the boundary effects are negligible and verifies the colored thermal force spectral density. Fig. 6.8(B-D) show that the FPSDs in the perpendicular direction flatten at low frequencies and their DC values increase to $4k_B T \gamma_s \frac{1}{(1 - \frac{9a}{8h})}$ from the bulk value of $4k_B T \gamma_s$. The increase in the thermal force is consistent with the increase in the drag force, in accordance with the fluctuation-dissipation theorem [10].

It is worth noting that this flattening of the FPSD explains the un-

explained suppression of a resonance in the position PSD of a particle near a wall observed in previous experiments [15, 103]. The detailed origin of the resonance in position PSD has been discussed in Section 4.3.5, which is due to the color of the thermal force. The flattening in the thermal force PSD at low frequencies, caused by boundary effects, fades the thermal force's color and thus results in the suppression of the resonance in the position PSD. With small enough sphere-wall separations, this resonance would disappear.

All of the observed statistical properties, namely MSD, VACF, position PSD, velocity PSD, thermal force PSD, in the presence of the wall approach the corresponding free-space theories for time-scales much shorter than τ_w (or frequency-scales much larger than F_w). This is expected, as the numerical simulations, shown in Section 5.4, suggest that the vorticity from the wall takes time on the order of τ_w to reach the sphere. The inertial effects due to the boundary, which persist at high-frequencies in the form of an increased effective mass, are too insignificant to discern.

6.2.6 The absolute sphere-wall separation calibration

The piezo-stage used in the experiment only gives us precise measurements of the position of the particle relative to an arbitrary origin. The sphere-wall separations shown sub-figures (B-D) in Fig. 6.4 to 6.8 have a relative distance of $1.5 \mu\text{m}$ from the piezo reading. We developed two precise ways to calibrate the absolute distance between the particle and the wall, which will be discussed in detail in this section. These two methods of calibration yield

similar results.

6.2.6.1 The VACF calibration method

The absolute separation between the sphere and wall can be obtained by a least-squares fit of the experimental VACF (or MSD, PSD, VPSD, FPSD) to their corresponding boundary theory. It turns out that the fitting of VACF gives the most reliable results.

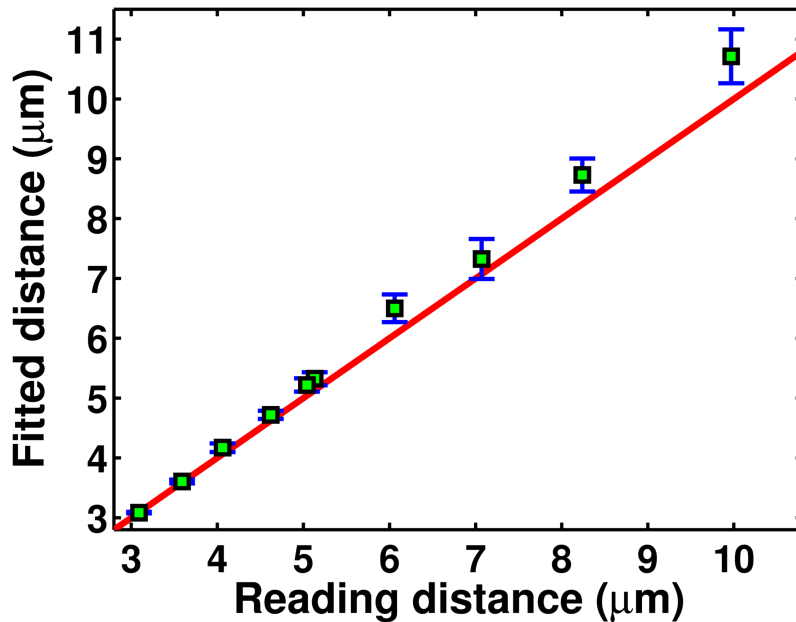


Figure 6.9: The absolute sphere-wall separation measurements obtained from fitting the data recorded by the AC-coupled detector to the no-slip flat-wall theoretical VACF. The green squares with error bars represent the experimental data and statistical errors obtained by averaging from 10 measurements at each position. The horizontal axis denotes the distance measured by the strain gauge after subtraction of the fitted offset. The red line is the $y = x$ line; The VACF fitting gives reliable results as long as the sphere-wall separation is smaller than $7 \mu\text{m}$.

The VACF is measured at multiple positions near the wall, whose relative separations are known by means of the piezo strain gauge. The VACF fitting gives reliable results as long as the sphere-wall separation is smaller than $7\ \mu\text{m}$. The VACF fitting results with sphere-wall separations larger than about $7\ \mu\text{m}$ suggest the curvature of the cylindrical fiber becomes important. The boundary effects with sphere-wall separations larger than $10\ \mu\text{m}$ become so weak that the VACF fitting becomes unreliable. The piezo strain gauge reading and the absolute positions h obtained by fitting the VACF to the theory are fit to a straight line of unitary slope to determine the offset of the origin of the piezo system from the wall. The absolute positions reported in Fig. 6.4 to 6.8 are obtained using this method.

6.2.6.2 The diffusion calibration method

We also measure the absolute distance by the measurement of the diffusion coefficients. The variation of the diffusion coefficient near a no-slip wall has been well-studied by numerous experiments [63, 72, 73, 120–124]. We reduce the optical trap strength so as to permit the MSD to enter the diffusive regime before flattening out, and acquire data with the same microsphere, with which the AC data was recorded and is shown in Fig. 6.4 to 6.8, using a DC-coupled detector. We then fit the measured hindered diffusion coefficients at various distances to the theoretical prediction of a sphere near a no-slip flat wall.

To measure the diffusion coefficient experimentally, we record the mo-

tion of a trapped microsphere near the boundary at long time scales. In this limit, the translational motion of a spherical particle in a liquid trapped by an optical tweezer can be described as [129]

$$Kx(t) + \gamma\dot{x}(t) = F_{th}(t). \quad (6.1)$$

The inertial force is neglected here because it is much smaller compared to the viscous drag at long time scales, $t \gg \tau_f$. The damping factor γ is approximately frequency independent but depends on the distance to nearby boundaries h , which can be computed from the position autocorrelation function if the trapping strength K is known [129],

$$C_x(t) = \langle x(\tau)x(\tau+t) \rangle = \langle x^2 \rangle e^{-\frac{K}{\gamma(h)}t} = \langle x^2 \rangle e^{-\frac{t}{\tau_k}} \quad (6.2)$$

where $\tau_k = \gamma(h)/K$ gives the time scale during which the particle experiences a drift back toward the trap center. With the trapping strength K fixed and a larger damping factor $\gamma(h)$, the bead takes a longer time to drift back to the center of the trap. The diffusion coefficient D can be obtained from the damping factor γ using the Stokes-Einstein relation

$$D(h) = \frac{k_B T}{\gamma(h)} \quad (6.3)$$

where k_B is the Boltzmann constant, T is the absolute temperature.

We reduce the trapping beam power from 400 mW to 50 mW to insure that the diffusive regime can be reached. We redirect the detection laser beam to a DC-coupled balanced detector (Thorlabs, PDB120C, with transimpedance

gain 1.8×10^5 V/A) to amplify the power difference in the two branches of the detection system. The detection power was only approximately 0.5 mW due to the high gain of the detector. The data is recorded by the same digitizer at a lower sampling rate of 5 MSa/s. Each continuous trajectory contains 2^{25} samples, corresponding to about 7 s. We take 10 such measurements at each position.

The voltage to position conversion factor C and trapping strength K as well as particle radius a were obtained by a least-squares fit of the measured mean square displacement (MSD), taken at $h > 100\mu\text{m}$, to free boundary theoretical MSD [85]. The data taken far away from any boundary gives us the experimental conditions: the diameter of the microsphere $a = 2.98 \pm 0.11 \mu\text{m}$, the trapping strength $K = 13.3 \pm 0.6 \mu\text{N/m}$ and the volts-per-meter calibration factor $C = 16.9 \pm 0.4 \text{ mV/nm}$. The uncertainty of each fit parameter is determined from the variance in the results of independent MSD fits of all measured trajectories.

Normalized position autocorrelation functions of the particle in the perpendicular direction at four different sphere-surface separations $h = 1.0 \mu\text{m}$, $2.2 \mu\text{m}$, $4.2 \mu\text{m}$ and $20 \mu\text{m}$ are shown in Fig. 6.10. The smaller sphere-wall separation, the larger the drag force, thus the longer τ_k . It is worth noting that the trapping strength is assumed to be constant at various sphere-wall separations. This is valid as long as the clipping effect is negligible, which has been verified by monitoring the trapping beam transmission rate through the chamber and by the stability of the fitting parameters at different positions

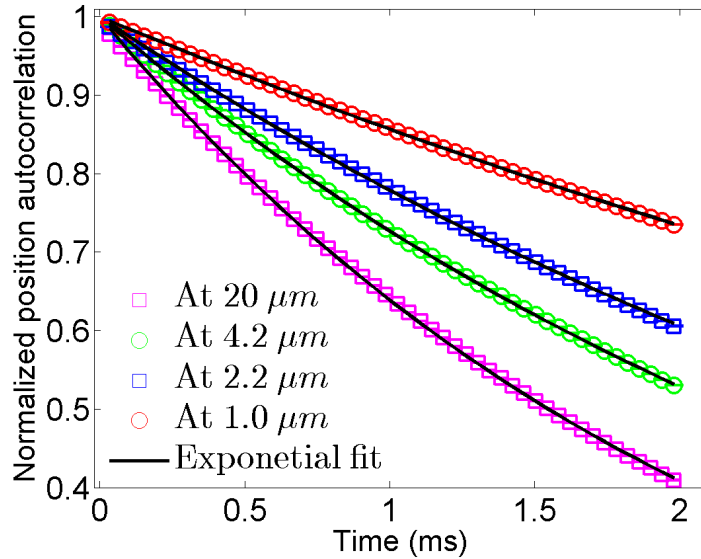


Figure 6.10: The position autocorrelation functions (normalized to $k_B T/K$) of the particle at four different sphere-wall separations $h = 1.0 \mu\text{m}$, $2.2 \mu\text{m}$, $4.2 \mu\text{m}$ and $20 \mu\text{m}$. The corresponding τ_k are 2.1 ms, 3.0 ms, 3.8 ms and 5.7 ms respectively.

with various sphere-wall separations.

The hindered diffusion coefficients of the particle in the perpendicular direction (normalized to its bulk value $D_0 = 0.14 \mu\text{m}^2/\text{s}$) as a function of sphere-wall separation from $2.5 \mu\text{m}$ to $30 \mu\text{m}$ are shown in Fig. 6.11. The data suggests that the curvature of the cylindrical fiber becomes important when sphere-wall separation is larger than $\sim 7 \mu\text{m}$, which agrees with the VACF fitting method. The rapid decrease at small sphere-wall separations makes this calibration relatively reliable.

The discrepancy in the absolute offset determined by the two methods

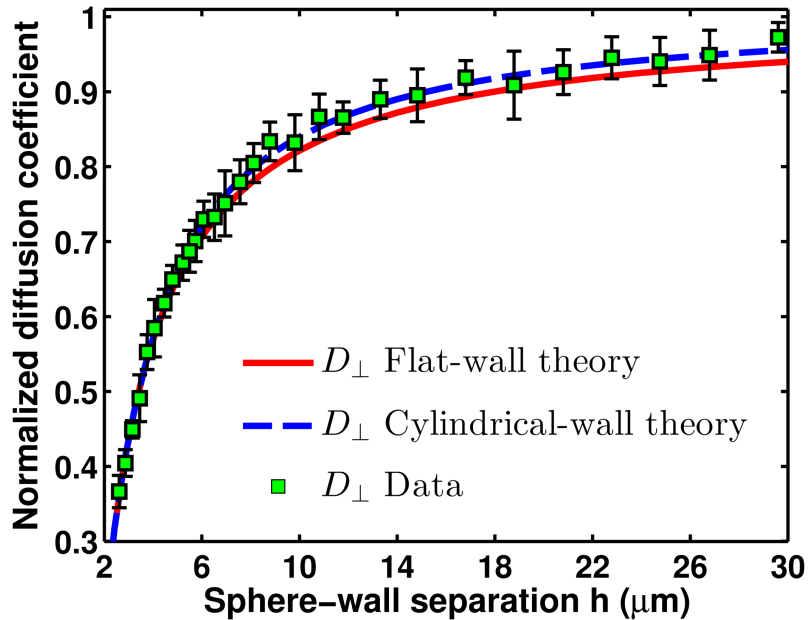


Figure 6.11: The absolute sphere-wall separation measurements obtained by measuring the hindered diffusion coefficients (normalized to its bulk value $D_0 = 0.14 \mu\text{m}^2/\text{s}$) of a $3 \mu\text{m}$ silica microsphere using the DC-coupled detector with a sphere-wall separation range from $2.5 \mu\text{m}$ to $30 \mu\text{m}$. The red line is the flat-wall theory Eq. (5.4). The blue dashed line is the modified cylindrical-wall theory Eq. (5.5). The green squares with error bars represent the experimental data and statistical errors obtained by averaging from 10 measurements at each position.

is within 300 nm. It is worth noting that these two methods can be applied to the calibration of the absolute sphere-wall separation calibration in the parallel direction as well.

6.2.7 Boundary effects in the parallel direction

The presence of a no-slip boundary has similar effects on the dynamics of the particle in the direction parallel to the boundary, except less pronounced.

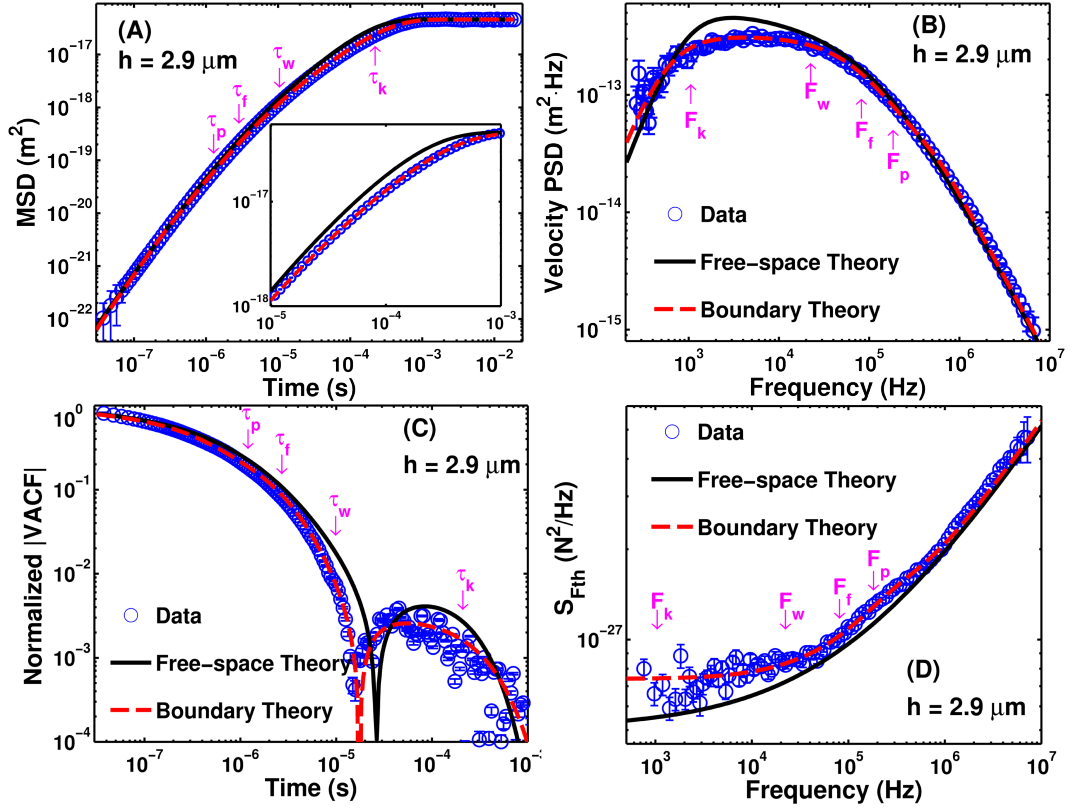


Figure 6.12: Experimental and theoretical Brownian dynamics in the parallel direction with a sphere-wall separation of $2.9 \mu\text{m}$. (A), MSD. (B), Velocity PSD. (C), Absolute VACF (normalized to $\langle (v_{\parallel}^*)^2 \rangle$). (D), Thermal force PSD. The blue circles are the experimental data; the black lines are the unbounded theoretical predictions and the red dashed lines correspond to the bounded theoretical predictions [111].

Thus the motion of the sphere becomes anisotropic. For brevity, we show boundary effects in the parallel direction only for a sphere-wall separation of about $3 \mu\text{m}$. We acquire and analyze the data in the parallel direction in the same way as in the perpendicular direction. The MSD, VPSD, VACF and FPSD on the parallel direction are shown in Fig. 6.12. It is noted that these

boundary effects are expected to be different near a partial or full slip wall, as discussed in Chapter 8.

6.3 Summary

A Brownian particle located near a flat wall provides a model system to study the behavior of more complex systems whose boundaries can be modeled as effective walls, such as blood vessels, cell membranes, and a variety of microfluidic geometries. Our techniques will find broad applications in precise biophysical measurements [130, 131], and in particular are capable of significantly speeding up the technique of thermal noise imaging [69]. Using a micro- or nano-sphere as a remote sensor to measure the distances to nearby boundaries in porous media can potentially map out boundary contours and build a 3D microscope.

Chapter 7

Brownian motion in viscoelastic fluids

Solids are the materials that conserve their shapes indefinitely in the absence of external forces. Solids deform under external forces. This deformation is small and reversible when the external force is moderate and disappears once the stress is removed. In such cases, it is called elastic deformation, during which dissipation is negligible. Elasticity is one of the defining properties of solids. Fluids, on the other hand, do not conserve their shape, and always end up taking the shapes of their container. This process can take a relatively short time for some fluids, such as water; and longer time for more viscous fluids, like honey.

A more systematic way to define solids and fluids is probably using the strain-stress relation. Strain ϵ is a description of deformation in terms of relative displacement of particles in the body. Stress σ is the force per unit area. The stress in elastic solids is linearly proportional to strain, $\sigma = E\epsilon$, where E is the elastic modulus. While in fluids, the shear stress does not depend on the strain itself, but depends on the strain rate $\sigma = \eta\dot{\epsilon}$, where η is the dynamic viscosity.

Until the beginning of the 19th century, people contented themselves

with classifying materials either in the family of elastic solids or Newtonian viscous fluids. People then realized that solids are not purely elastic whereas fluids are not purely viscous. To some degree, all materials are viscoelastic, can act both like fluids and like solids, depending on the time scales of interest. Even water, conventionally considered as a purely Newtonian viscous fluid, exhibits elasticity at time scales below 10^{-12} s (with a viscosity 10^{-3} Pa·s and the shear modulus G of (ice), 10^9 Pa) [132]. We will show that at time scales below 10^{-12} s, water actually is a complex fluid, which can be described using the Maxwell model, in section 7.2. On the other hand, solids can behave like fluids at long time scales, for example the Earth's mantle flow on time scales larger than 10^{10} s [132]. A more common example is Silly Putty, containing silicone polymers. When squeezed slowly, it deforms and flows like a liquid; however, when thrown against a wall, it bounces like a rigid elastic solid.

The stress in viscoelastic materials depends on both strain and strain rate. Therefore, it is convenient to use a complex elastic modulus $G(\omega)$ to describe the material's mechanical properties in frequency domain as $\sigma(\omega) = G(\omega)\epsilon(\omega)$. The complex elastic modulus can be decomposed into $G(\omega) = G'(\omega) - iG''(\omega)$, where the real part $G'(\omega)$ refers to the storage modulus and the imaginary part $G''(\omega)$ is the loss modulus. The corresponding frequency-dependent complex dynamic viscosity is $\eta(\omega) = G(\omega)/(-i\omega)$.

Rheology is the study of the flow and deformation of matter under the influence of a mechanical force, nowadays is an interdisciplinary subject. Microrheology, a branch of rheology, studies viscoelasticity of complex fluids by

measuring motion of immersed particles, and works at micron length scales and with microliter sample volumes. Microrheology techniques can be classified as either passive or active, depending on whether the particles' motion is governed by the thermal fluctuations of the surrounding fluid's molecules or an external force exerted on the particles. Any deviation from the normal diffusive behavior of the particle (in Newtonian fluids) is then interpreted as a response to the material properties of its complex environment [133].

Optical microrheology is a subset of microrheology, which relies on optical methods to measure motion of the immersed particles. This method was first reported by Mason *al et.* in 1995 [28], and then has been intensively used to study complex fluids [134–144]. However, the hydrodynamic effects are neglected in this approach. Therefore, this method is not suitable for high frequency rheology, in spite of the fact that viscoelasticity at high frequencies has been reported to be important [145,146]. A theory including hydrodynamics effects is proposed by Felderhof recently [147], which has been adapted to measure high-frequency viscoelasticity of a worm-like micelles solution [148].

A particle exhibiting Brownian motion in a viscoelastic fluid can be used as a probe to measure the properties of the host medium. This approach has a much higher spatial resolution, which is limited by the size of the probe particle, than conventional bulk rheometry. One assumption embedded in this method is that probe particles have to be bigger than the host fluids's structural constituents [101].

In the first part of this chapter, we will discuss Brownian motion in

two simple models of complex fluids, showing how the properties of the fluids affect the dynamics motion of a particle immersed inside. Then, we will discuss the procedures to estimate the properties of an unknown complex fluid by observing the Brownian motion of an immersed particle, followed by two experimental demonstrations of obtaining the viscosities of water and acetone with a high bandwidth.

7.1 Simple complex fluid models

There are many linear models describing the viscoelasticity of complex fluids. The Maxwell model is the simplest one for describing the properties of a viscoelastic liquid. The Kelvin-Voigt model is a better model for some viscoelastic solids. The Jeffreys model applies to systems composed of a solvent, which can be considered as purely viscous, containing elastic macromolecules, such as polymers [132].

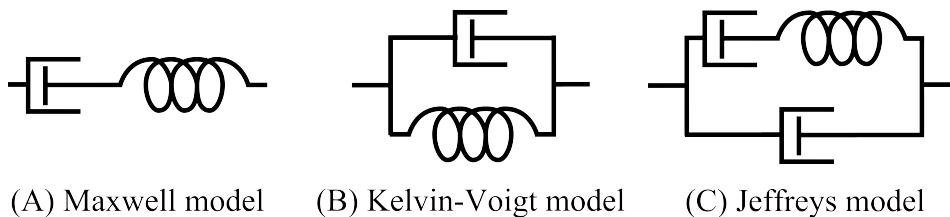


Figure 7.1: Rheological schemes of three simple models. (A) the Maxwell model, (B) the Kelvin-Voigt model, (C) the Jeffreys model. The spring represents the purely elasticity, whereas the dashpot means a purely viscous damper.

7.1.1 A Maxwell fluid

The simplest approach to describe viscoelasticity, already proposed by J. C. Maxwell in 1867, assumes that viscoelasticity can be represented by a purely viscous damper and a purely elastic spring connected in series, as shown in Fig. 7.1(A). So the stress-strain relation reads [101]

$$\frac{\dot{\sigma}(t)}{G_\infty} + \frac{\sigma(t)}{\eta_0} = \dot{\epsilon}(t) \quad (7.1)$$

In the frequency domain, a Maxwell fluid can be described by a single characteristic time τ_M , called the viscoelastic time, which marks the transition from a high-frequency elastic regime to a purely viscous fluid at low frequencies. The frequency dependent shear modulus is

$$G_M(\omega) = \frac{-i\omega\tau_M G_\infty}{1 - i\omega\tau_M} = \frac{\omega^2\tau_M^2 G_\infty}{1 + \omega^2\tau_M^2} - i\frac{\omega\tau_M G_\infty}{1 + \omega^2\tau_M^2} \quad (7.2)$$

and the frequency dependent shear viscosity is

$$\eta_M(\omega) = \frac{\tau_M G_\infty}{1 - i\omega\tau_M} \quad (7.3)$$

$\eta_M \rightarrow 0$ as $\omega \rightarrow \infty$, meaning there is no dissipation at high frequencies. It is worth noting that there are only a few materials that obey this model strictly. Silicone is among these few materials, and is highly transparent to radiation in the visible range all the way down to UV, which is suitable for using optical microrheology.

In reality, the constituent mesoscopic particles in a viscoelastic material are immersed in a solvent giving rise to a background viscosity $\eta(\omega \rightarrow \infty) =$

η_∞ . To account for the dissipation in the solvent, a generalized Maxwell model is often used

$$\eta_M^G(\omega) = \eta_\infty + \frac{\tau_M G_\infty}{1 - i\omega\tau_M} \quad (7.4)$$

This generalized Maxwell model was mistaken as the Jeffreys model [101]. The Jeffreys model [149, 150] gives different frequency dependent shear viscosity, as discussed below.

7.1.2 A Kelvin-Voigt fluid

A Kelvin-Voigt fluid assumes that viscoelasticity can be represented by a purely viscous damper and a purely elastic spring connected in parallel, as shown in Fig. 7.1(B). So the stress-strain relation reads

$$\sigma(t) = \eta_0 \dot{\epsilon}(t) + G\epsilon(t) \quad (7.5)$$

The frequency dependent shear modulus can be written as

$$G_K(\omega) = G_0 - i\omega\eta_0 \quad (7.6)$$

7.1.3 A Jeffreys fluid

The Jeffreys model [149, 150], assumes that viscoelasticity can be represented by a purely viscous damper and a purely elastic spring connected in series, connecting to another purely viscous damper in parallel as shown in Fig. 7.1(C). So the stress-strain relation reads

$$\frac{\dot{\sigma}(t)}{G_1} + \frac{\sigma(t)}{\eta_1} = \left(1 + \frac{\eta_2}{\eta_1}\right) \dot{\epsilon}(t) \quad (7.7)$$

The frequency dependent shear modulus can be written as

$$G_J(\omega) = \frac{-i\omega\eta_1 G_1 \left(1 + \frac{\eta_2}{\eta_1}\right)}{i\omega\eta_1 + G_1} \quad (7.8)$$

7.2 Brownian motion in a complex fluid

In this section, we will describe Brownian motion in a viscoelastic fluid with its properties known. We assume the fluid has a frequency dependent viscosity $\eta(\omega)$. To the first order, the frequency dependent drag coefficient can be written as [101]

$$\gamma_{vs}(\omega) = 6\pi\eta(\omega)a \left(1 + \sqrt{\frac{-i\omega\rho_f a^2}{\eta(\omega)}} - \frac{i\omega\rho_f a^2}{9\eta(\omega)}\right) \quad (7.9)$$

The frequency dependence of the drag coefficient is due to two reasons: $\eta(\omega)$ is frequency dependent, which is caused by viscoelasticity of fluids; the hydrodynamics effects of the fluids. The admittance of the optically trapped particle in such viscoelastic fluids can be obtained by

$$y_{vs}^t(\omega) = \frac{-i\omega}{-m\omega^2 - i\omega\gamma_{vs}(\omega) + K} \quad (7.10)$$

Again, the numerical prediction for the Brownian motion of a particle in a viscoelastic fluid can be easily obtained. Here, we consider a 3 μm diameter silica microsphere both in a Maxwell fluid and in a generalized Maxwell fluid with different properties, which can be characterized using two parameters τ_M and G_∞ . The η_∞ in the generalized Maxwell fluid case is the same as the viscosity of water, 10^{-3} Pa·s. A trap stiffness of 150 $\mu\text{N/m}$ is used in this

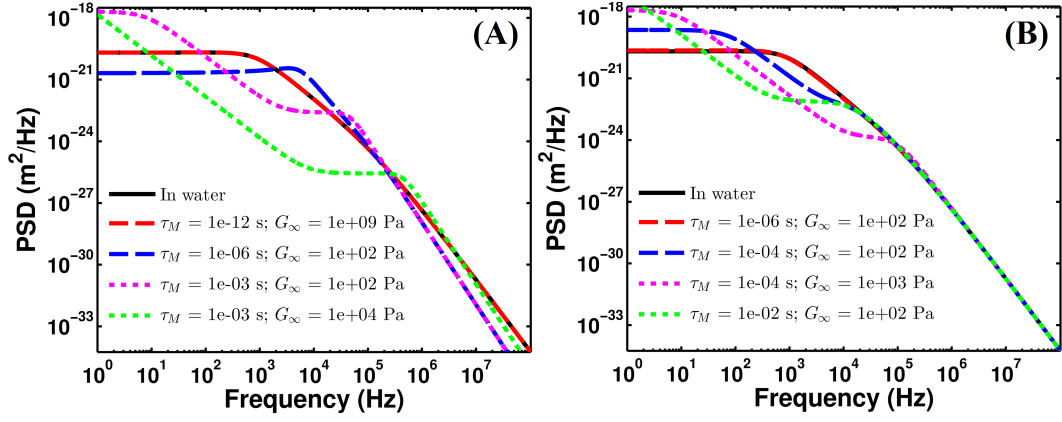


Figure 7.2: The numerical predictions of position power spectral density (PPSD) of a $3 \mu\text{m}$ diameter silica in complex fluids with different properties. (A), In Maxwell fluids. (B), In generalized Maxwell fluids.

numerical calculation. The frequency dependent viscosity $\eta(\omega)$ in Eq. (7.9) should be replaced by Eq. (7.3) and Eq. (7.4).

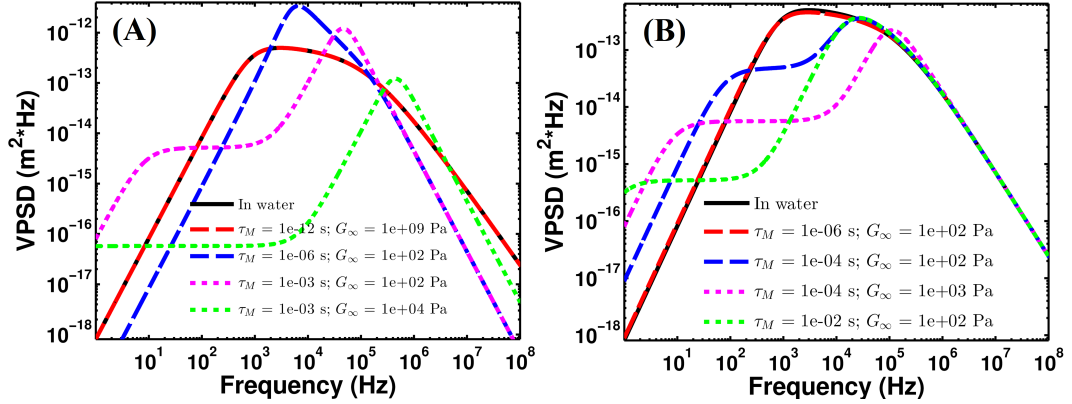


Figure 7.3: The numerical predictions of velocity power spectral density (VPSD) of a $3 \mu\text{m}$ diameter silica in complex fluids with different properties. (A), In Maxwell fluids. (B), In generalized Maxwell fluids.

7.2.1 Position power spectral density

The position power spectral density predictions of a microsphere in a Maxwell fluid are highly dependent on the properties of the Maxwell fluids, as shown in Fig. 7.2(A). The black line is the prediction of the microsphere in pure water. The red dashed line is the prediction of the particle in a Maxwell fluid with $\tau_M = 10^{-12}$ s and $G_\infty = 10^9$ Pa. The perfect agreement between them proves that water can be modeled as a Maxwell fluid. Its elasticity becomes important at time scales below 10^{-12} s though. The position power spectral density predictions of a microsphere in a generalized Maxwell fluid also highly depend on the properties of the Maxwell fluids, as shown in Fig. 7.2(B).

7.2.2 Velocity power spectral density

As shown in Fig. 7.3, the velocity PSD predictions of the microsphere immersed in Maxwell fluids and generalized Maxwell fluids are highly dependent on the properties of the fluids. At high frequencies, the Brownian motion of a particle in the generalized Maxwell fluid is the same as that in water. This is because the viscoelasticity of the generalized Maxwell fluid at high frequencies is dominated by the background solvent viscosity, which is the same as water in this case.

7.2.3 Mean square displacement

The mean square displacement predictions of the microsphere immersed in Maxwell fluids and generalized Maxwell fluids are shown in Fig. 7.4. The

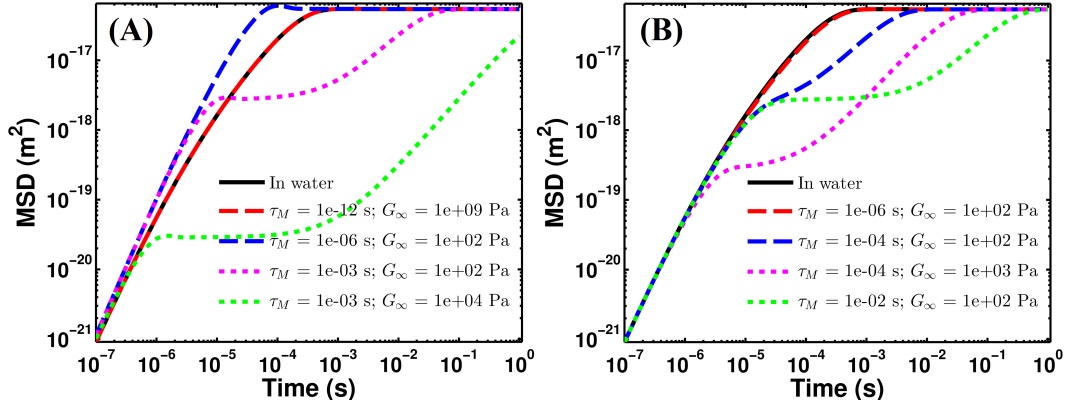


Figure 7.4: The numerical predictions of mean square displacement (MSD) of a $3 \mu\text{m}$ diameter silica in complex fluids with different properties. (A), In Maxwell fluids. (B), In generalized Maxwell fluids.

optical trapping causes the MSD to plateau at $2k_B T/K$. Both model fluids with certain viscoelastic properties can cause another plateau in MSD, which is conventionally considered as one of the defining features of viscoelasticity.

7.2.4 Velocity autocorrelation function

As shown in Fig. 7.5, the normalized velocity autocorrelation function predictions of the microsphere immersed in Maxwell fluids and generalized Maxwell fluids differ drastically from the the simple behavior in pure water. The elasticity of the complex fluid can cause oscillations in the VACF.

7.2.5 Thermal force power spectral density

The numerical predictions of thermal force power spectral densities exerted on the microsphere immersed in Maxwell fluids and generalized Maxwell fluids differ significantly from the the simple behavior in pure water, as shown

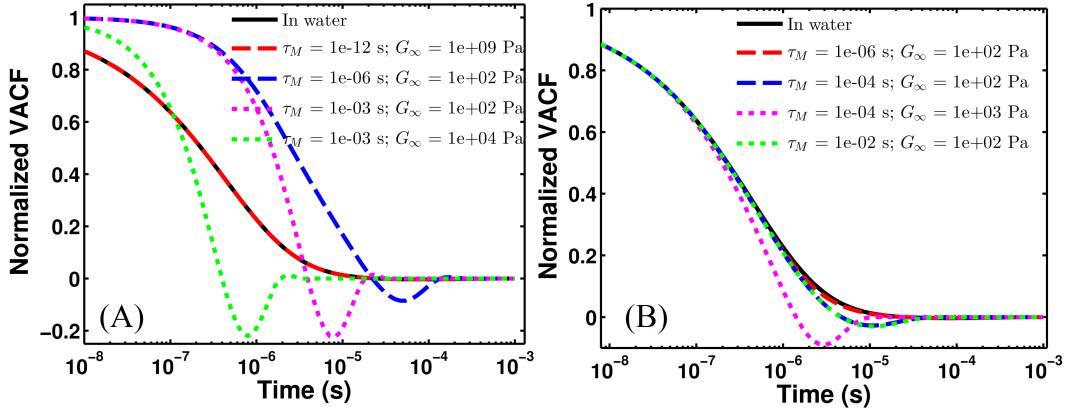


Figure 7.5: The numerical predictions of velocity autocorrelation function (VACF) of a 3 μm diameter silica in complex fluids with different properties. (A), In Maxwell fluids. (B), In generalized Maxwell fluids.

in Fig. 7.6. The FPSDs no longer monotonically increase with increasing frequency. The FPSDs in the Maxwell model flattens at frequencies higher than $1/\tau_M$,

$$S_F^M(\omega \gg 1/\tau_M) = 12\sqrt{2}\pi^2 a^2 k_B T \sqrt{\rho_f G_\infty} \quad (7.11)$$

Surprisingly, this saturation level does not depend on the relaxation time scale τ_M .

In summary, the viscoelasticity of a complex fluid can have dramatic impacts on Brownian motion of an immersed particle. In return, this dependence can be utilized to extract the properties of an unknown viscoelastic fluid, which will be discussed in detail in Section 7.3. It is worth to emphasize that the perfect agreement in Fig. 7.2(A), 7.3(A), 7.4(A), 7.5(A), 7.6(A) between the black lines, which are the predictions of the microsphere in pure water and the red dashed lines, which are the prediction of the particle in a Maxwell fluid

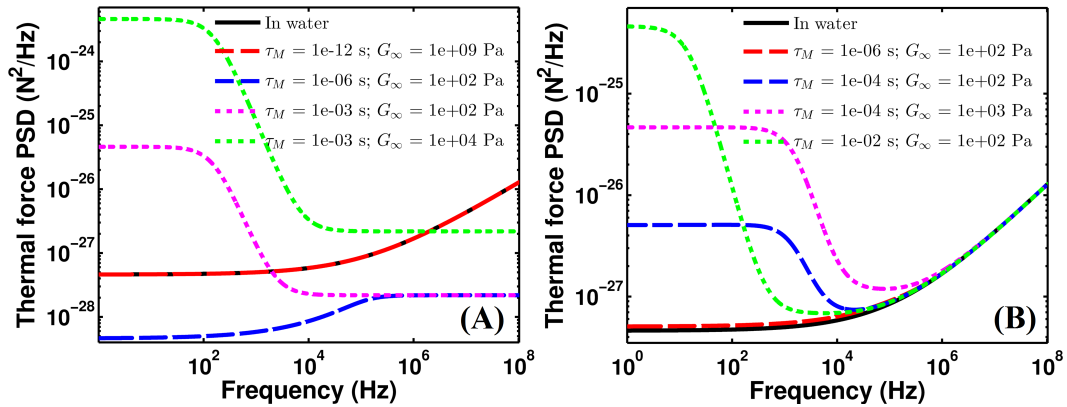


Figure 7.6: The numerical predictions of thermal force power spectral density (FPSD) of a 3 μm diameter silica in complex fluids with different properties. (A), In Maxwell fluids. (B), In generalized Maxwell fluids.

with $\tau_M = 10^{-12}$ s and $G_\infty = 10^9$ Pa, indicates that water is indeed a Maxwell fluid at frequencies up to about 1 THz.

7.3 Methods of estimating viscoelasticity of a fluid by measuring Brownian motion of an immersed particle

Last section we have discussed the Brownian motion in property-known complex fluids, showing the properties of the fluid can dramatically change the dynamics of the particle. Perhaps, it will be more interesting if one can measure the properties of the complex fluids by studying Brownian motion of a particle in such fluids.

7.3.1 Mason-Weitz method (without hydrodynamic effects)

Mason and Weitz pioneered an approach that relies on detecting the displacement of colloidal probe particles embedded in a complex fluid to extract the viscoelastic properties of the fluid [28]. The frequency-dependent viscosity of a medium can be estimated from the MSD of a free particle immersed in the host medium as

$$\eta(s) = \frac{k_B T}{3\pi a s^2 \langle \Delta \hat{x}^2(s) \rangle} - \frac{ms}{6\pi a} \quad (7.12)$$

where the first term reflects the viscoelasticity of the medium, the second term is related to the inertia of the particle, $s = -i\omega$ and $\langle \Delta \hat{x}^2(s) \rangle$ denotes the Laplace transform of the MSD.

$$\langle \Delta \hat{x}^2(s) \rangle = \int_0^\infty e^{-st} \langle \Delta x^2(s) \rangle dx \quad (7.13)$$

The term representing the inertia of the particle typically can be neglected in many experiments, in which the maximum accessible frequency is less than 1 MHz. Commonly, in optical microrheology experiments, the particle is trapped by an optical tweezer. The frequency-dependent viscosity extracted from MSD of an trapped particle is [138]

$$\eta(s) = \frac{k_B T}{3\pi a s^2 \langle \Delta \hat{x}^2(s) \rangle} - \frac{ms}{6\pi a} - \frac{K}{6\pi a s} \quad (7.14)$$

In spite of the tremendous success in many experiments [28, 135, 136, 139, 141, 143, 144], Mason's method [28] typically is only correct at low frequencies (up to ~ 100 kHz). This is because it does not include hydrodynamic effects by assuming the friction kernel $\gamma(\omega) = 6\pi\eta(\omega)a$.

7.3.2 Felderhof method (with hydrodynamic effects)

The observation of viscoelasticity at short timescales, or equivalently at high frequencies, requires disentangling the frequency-dependent elastic modulus and the hydrodynamic effects. The theory including hydrodynamic effects has been proposed [147, 151].

The dynamic viscosity of a complex fluid may be generalized as

$$\eta(\omega) = \eta_0 G_r(\omega) \quad (7.15)$$

where $G_r(\omega = 0) = 1$. The Kubo-Green formula relates the admittance and the velocity autocorrelation $C_v(t)$ as

$$\mathfrak{y}(\omega) = \frac{1}{k_B T} \int_0^\infty e^{i\omega t} C_v(t) dt, \quad (7.16)$$

We consider a microsphere with a no-slip boundary condition on its surface immersed in an incompressible fluid, within the linear hydrodynamics approximation, the translational admittance is given by [83]

$$\mathfrak{y}(\omega) = \frac{1}{-i\omega m + \gamma(\omega) + \frac{K}{-i\omega}}. \quad (7.17)$$

The correct friction kernel considered hydrodynamic effects should be

$$\gamma(\omega) = 6\pi\eta(\omega)a \left(1 + \sqrt{\frac{-i\omega\rho_f a^2}{\eta(\omega)} - \frac{i\omega\rho_f a^2}{9\eta(\omega)}} \right), \quad (7.18)$$

instead of $\gamma(\omega) = 6\pi\eta(\omega)a$ in the Mason-Weitz method. By combining Eq. (7.15) to 7.18, the frequency-dependent viscosity of the complex fluid can be obtained from the VACF

$$\eta(\omega) = \eta_0 \left[\sqrt{\frac{k_B T}{6\pi\eta_0 a C_v(\omega)} + \frac{1}{i\omega\tau_K} + i\omega \left(\tau_p - \frac{5\tau_f}{36} \right) - \frac{1}{2}\sqrt{-i\omega\tau_f}} \right]^2 \quad (7.19)$$

where $\hat{C}_v(\omega) = \int_0^\infty e^{i\omega t} C_v(t) dt$, $\tau_K = 6\pi\eta_0 a/K$, $\tau_p = 2\rho_p a^2/(9\eta_0)$ and $\tau_f = \rho_f a^2/\eta_0$.

We give the frequency-dependent viscosity in terms of the MSD instead of the VACF, since the VACF has more noise than the MSD in typical optical tweezer experiments due to the fact that VACF has zero crossing whereas MSD does not. The VACF can be related to MSD via the identity [139]

$$\hat{C}_v(\omega) = -\frac{\omega^2}{2} \Delta \hat{x}^2(\omega) \quad (7.20)$$

where $\Delta \hat{x}^2(\omega) = \int_0^\infty e^{i\omega t} \Delta x^2(t) dt$. Therefore, the frequency-dependent viscosity can be extracted from MSD as

$$\eta(\omega) = \eta_0 \left[\sqrt{-\frac{k_B T}{3\pi\eta_0 a \omega^2 \Delta x^2(\omega)} + \frac{1}{i\omega\tau_k} + i\omega \left(\tau_p - \frac{5\tau_f}{36} \right) - \frac{1}{2} \sqrt{-i\omega\tau_f}} \right]^2 \quad (7.21)$$

It is worth noting that this result reduces to Mason-Weitz's result Eq. (7.14) as $\tau_f \rightarrow 0$, meaning hydrodynamic effects are negligible at all time scales. This result will be used to extract the viscosity of fluids from experimental Brownian motion data.

Numerically calculating the Laplace-Fourier transform of the MSD and the VACF is not trivial. The Laplace-Fourier transform of any time dependent function $g(t)$ sampled at a finite set of data points $(t_n, g(t_n))$, where $n = 1, 2, \dots, N$, is defined as $\hat{g}(\omega) = \int_0^\infty e^{i\omega t} g(t) dt$. An algebraic method of estimating this transform has been proposed [141, 152, 153], in which $g(t)$ is linearly interpolated between data points $(t_n, g(t_n))$. This transform can be simply obtained by summing the Laplace-Fourier transform of each linear interpolated

piece of $g(t)$, which can be analytically calculated,

$$\hat{g}(\omega) = \frac{-1}{\omega^2} \left[-i\omega g(0) + (1 - e^{i\omega t_1}) + \dot{g}_\infty e^{i\omega t_N} + \sum_{n=2}^N \left(\frac{g_n - g_{n-1}}{t_n - t_{n-1}} \right) (e^{i\omega t_{n-1}} - e^{i\omega t_n}) \right] \quad (7.22)$$

where $g(0)$ is the value of $g(t)$ extrapolated to $t = 0$, \dot{g}_∞ is the gradient of $g(t)$ extrapolated to $t = \infty$. This method is used to calculate the Laplace-Fourier transform of the MSD and the VACF.

7.3.3 Numerical testing of these two methods

Here, we give two examples for comparing the results obtained from these two methods, as shown in Fig. 7.7. As it is well known, water and acetone are purely viscous fluids at frequencies less than 10^{10} Hz. Water has a viscosity of 0.9×10^{-3} Pa·s, while the viscosity of acetone is 3.1×10^{-4} Pa·s. The MSD and VACF used here are the theoretical predictions [83, 85]. At low frequencies, these two methods give the same results, which is to be expected. However the Felderhof method gives much more reliable results than the Mason-Weitz method at high frequencies. This is exactly due to the fact that the Mason-Weitz method does not include hydrodynamic effects while the Felderhof method does. In the Mason-Weitz method, the hydrodynamic effects are mistaken as viscoelasticity of the fluid, which cause the deviation at high frequencies.

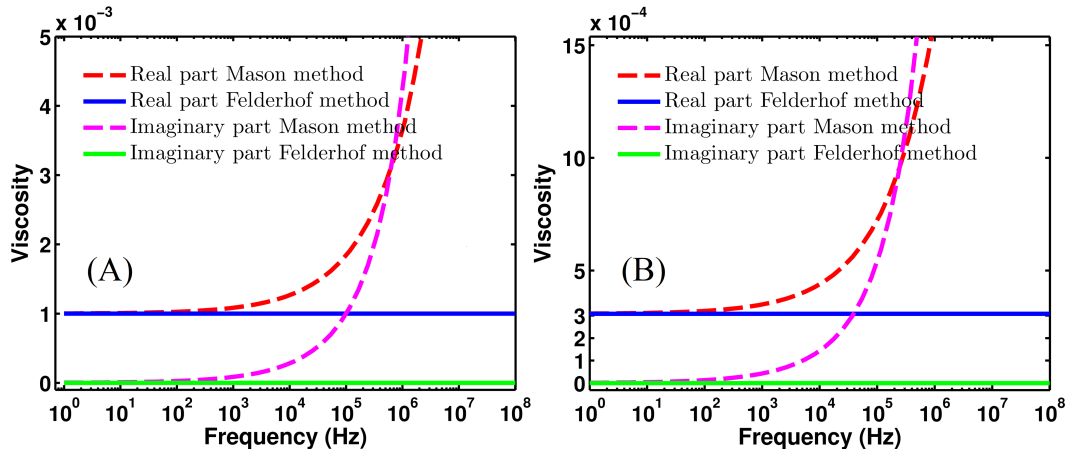


Figure 7.7: The viscoelasticity of water (A) and acetone (B) obtained by the Mason-Weitz method and the Felderhof Method.

7.4 Measurements of viscoelastic properties of fluids

In this section, through two demonstrations, we will analyze the experimental data to extract the viscosity of water and acetone using the Felderhof method. The data used here is the same as the two systems in Chapter 4, a silica microsphere in water and a silica microsphere in acetone.

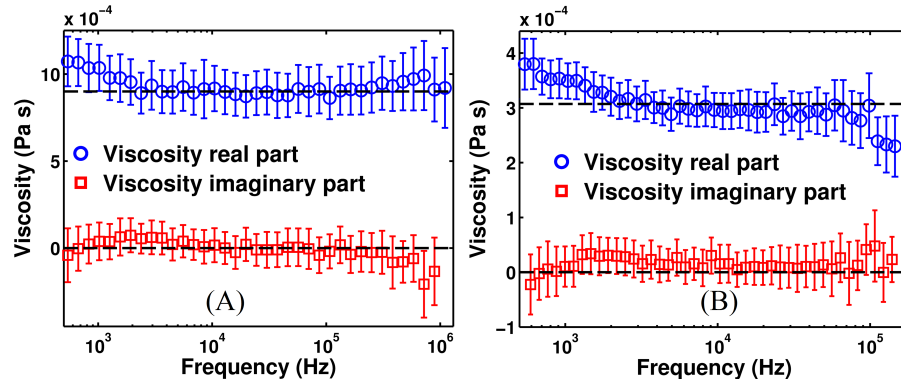


Figure 7.8: Experimental results of the viscosities of water (A) and acetone (B) obtained by the Felderhof Method.

The viscosities of water and acetone in a frequency range of from 500 Hz to about 1 MHz (200 kHz in the acetone case) are shown in Fig. 7.8. The minimum frequency is limited by the high pass filter in the AC detector, which can be improved by using a DC detector. Whereas, the maximum frequency is limited by noise, presumably the shot noise, in the experiments. As discussed in Chapter 4, the shot noise in the silica-acetone system is higher than that in the silica-water system. Thus, the frequency range in which the viscosity of water can be extracted is larger than that in silica-acetone system. The uncertainty of viscosity (the error-bar) is determined from the variance in the results of 1100 and 143 independent measurements for water and acetone respectively. Similar results on water have been reported recently [148, 154].

Our setup can be easily adapted to measure the viscoelasticity of an unknown complex fluid. Silicone oils are suggested to be Maxwell fluids [132]. Polystyrene ($n = 1.58$) and BaTiO_3 ($n = 2.1$) microspheres might be better options than silica microspheres for single beam trapping in silicone oils since refractive index of silicone ($n \sim 1.40$) is too close to that of silica microspheres ($n = 1.46$) to form a stable trap [155]. We are also planning to study the viscoelasticity of polyacrylamide solutions [140, 143, 156, 157], wormlike-micelle solutions [136, 158, 159], and transient polymer networks [160, 161].

Chapter 8

Brownian motion with slip boundary condition

Fluid flow velocity conditions at solid surfaces can have a huge impact on Brownian motion. For example, it is well known that the magnitude of the steady Stokes drag force on a sphere moving at velocity v is reduced from $F_s = 6\pi\eta av$ in the conventional no-slip boundary condition case to $F_s = 4\pi\eta av$ if the sphere has a perfect-slip boundary condition [162–164]. Yet, the detail of the effects of changing boundary conditions on the sphere and/or any other bounding surfaces (different with the boundary effects discussed in Chapter 5 and 6) on Brownian motion over the entire time scales is not well studied. We attempt to shed new light on these effects.

Slippage is usually quantified in terms of an extrapolation length, the so-called slip length. The slip length δ is defined as the distance inside the solid wall where the extrapolated fluid flow profile vanishes. The three boundary conditions is illustrated in Fig. 8.1. In the case of the no-slip boundary condition, $\delta = 0$; for the partial-slip boundary condition δ is finite; and $\delta = \infty$ for the perfect-slip boundary condition. The slip boundary condition can also be characterized by the contact angle θ_c , which in many cases is related to slip length through $\delta = \delta_0(1 + \cos\theta_c)^{-2}$ [33, 165]. δ_0 is an empirical quasiuniversal

length scale, typically obtained from experiments.

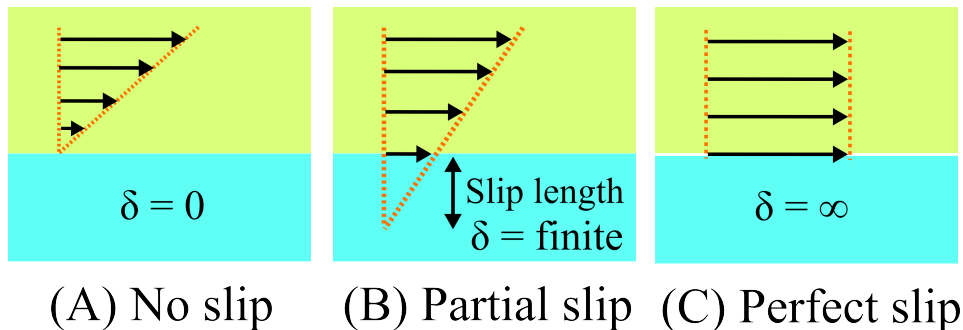


Figure 8.1: Fluid flow boundary conditions at solid-fluid interfaces: (A) no slip, $\delta = 0$ (B) partial slip, δ is finite (C) perfect slip, $\delta = \infty$. The light blue block represents the solid and the light green area indicates the fluid.

In fluid dynamics, the no-slip boundary condition is a conventional assumption, although its microscopic mechanism is still under debate [166]. In the no-slip condition, fluid particles along the plane of the fluid-solid surface have zero velocity with respect to the interface. In other words, the outermost molecules of fluid are stuck to the solid surface perfectly. At macroscopic scales, the no-slip boundary condition is generally valid because in most cases the adhesive forces between the fluid molecules and solid particles are greater than the cohesive forces between the fluid molecules. This force imbalance brings down the fluid velocity to zero relative to the solid surface.

As discussed in Chapter 4 and 6, we assumed the all the solid-fluid interfaces (glass-water and glass-acetone) have no-slip boundary conditions. The contact angle between water and glass typically lies in the range 25° to 29° [29], resulting a slip length of 0.1 nm [33, 165]. Because the particle's

diameter is 10^4 times larger than the slip length, the interface between water and micron-sized glass particles can be approximated with no-slip boundary condition. The contact angle of acetone on glass is typically smaller than that of water on glass [167]. Hence, the interface between acetone and micron-sized glass particles can be approximated with no-slip boundary condition as well.

However, if the slip length is comparable to the dimensions of interest, the no-slip assumption is insufficient and the partial-slip boundary condition must be used [30, 32–34, 168–175]. Slip lengths ranging from nanometers to even micrometers have been reported [30, 168, 169]. In some experiments and simulations, the slip length appears to be independent of shear rate [168, 170], whereas in others it depends upon shear rate [30, 169].

In recent years, superhydrophobic surfaces with large slip lengths (large contact angles $\theta_c \geq 150^\circ$) have been extensively studied [31, 32, 176–178]. The two key features of superhydrophobic surface are low surface energy and micro- or nano-roughness (typical with certain patterns), often called lotus leaf structure. The combination of surface roughness and hydrophobicity can trap an air layer in the depressions on the surface and result in the formation of an air-water interface that is supported by the peaks in the surface roughness. Therefore, the effective slip length can be increased.

In addition, the slip length of fluids on a glass surface can be increased by coating a hydrophobic self-assembled monolayer [179]. Therefore, microspheres with a partial-slip or even a near perfect-slip boundary condition can be created. In this chapter, we will discuss the boundary-condition effects

on Brownian motion for two systems: an unbounded particle with different boundary conditions at its surface, and a no-slip particle near a flat wall with different boundary conditions at the wall's surface. We will first give the theories and followed by numerical predictions with our experimental conditions for each system. In the end, we propose that the boundary condition can be extracted from the motion of a particle, which is similar to the approach of extracting viscoelasticity of fluids from the motion of an immersed particle discussed in Chapter 7.

8.1 Brownian motion of an unbounded microsphere with partial-slip boundary condition

The theory for Brownian motion presented in Chapter 3 assumes the no-slip boundary condition on the particle's surface. In this section, we will study the Brownian motion of an unbounded microsphere with different boundary conditions at its surface, namely different slip lengths.

As discussed in Chapter 3, to study the Brownian motion we just need to know the admittance of the system. The frequency-dependent friction coefficient of a microsphere in a liquid with a slip boundary condition has been studied [164]:

$$\gamma_{slip}(\omega) = \frac{2\pi\eta a (1 + 2\tilde{\delta})(9 + 9\tilde{\alpha} + \tilde{\alpha}^2) + \tilde{\delta}\tilde{\alpha}^2(1 + \tilde{\alpha})}{3(1 + (3 + \tilde{\alpha})\tilde{\delta})} \quad (8.1)$$

where the dimensionless quantities $\tilde{\alpha} = \sqrt{-i\omega\tau_f}$, and $\tilde{\delta} = \delta/a$. In the no-slip limit, $\gamma(\omega)$ reduces to $\gamma(\omega) = \gamma_s(1 + \tilde{\alpha} + \tilde{\alpha}^2/9)$ as $\tilde{\delta} = 0$.

In the perfect-slip limit, $\gamma_{slip}(\omega)$ reduces to

$$\gamma_{p-s}(\omega) = 6\pi\eta a \frac{2 + 2\tilde{\alpha} + \tilde{\alpha}^2/3 + \tilde{\alpha}^3/9}{3 + \tilde{\alpha}} \quad (8.2)$$

The steady drag coefficient is $\gamma_{p-s}(\omega = 0) = 4\pi\eta a$, as $\tilde{\alpha} \rightarrow 0$.

The admittance of a microsphere in a liquid with a slip boundary condition can be obtained from the frequency-dependent friction coefficient through

$$\mathcal{Y}_{slip}(\omega) = \frac{1}{-i\omega m + \gamma_{slip}(\omega) + \frac{K}{-i\omega}}. \quad (8.3)$$

With the admittance known, all the statistical quantities, such as MSD, position PSD, velocity PSD and velocity autocorrelation function and thermal force PSD, describing Brownian motion can be numerically calculated using Eq. (3.11) to Eq. (3.15), although it might be not easy to obtain the analytic solutions.

Here, we give the numerical predictions of a 3 μm diameter, optically trapped microsphere (has the same density as silica, 2000 kg/m^3) in water with different boundary conditions, namely different slip lengths. A trap strength of 150 $\mu\text{N}/\text{m}$ is used in this numerical calculation.

8.1.1 Velocity autocorrelation function

The numerical prediction for velocity autocorrelation function $C_v(t)$ with different boundary conditions on sphere's surface are shown in Fig. 8.2. The red solid line represents the prediction of the VACF in the no-slip limit and the green solid line predicts the VACF in the perfect-slip limit. The

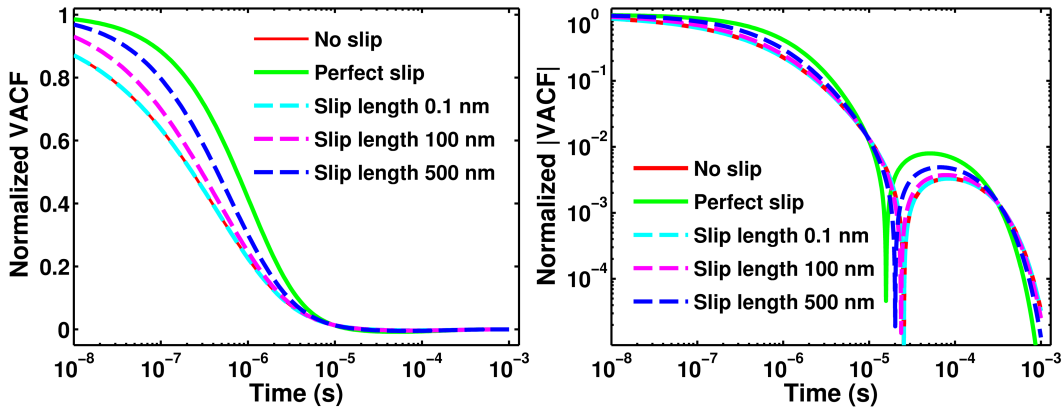


Figure 8.2: The numerical predictions of velocity autocorrelation function of an unbounded microsphere with different boundary conditions. (A), on a log-linear plot; (B), on a log-log plot with absolute value.

dashed lines are the predictions with partial-slip boundary conditions. In particular, the agreement between the VACF with no-slip boundary condition and VACF with a slip length of 0.1 nm (the cyan dashed line) indicates that the interface between glass and water indeed can be assumed to be no-slip in our experiments.

With our current time resolution on VACF (down to 50 ns), the maximum measurable normalized VACF value can be increased from 0.75 in the no-slip case to 0.95 if the microsphere has perfect-slip boundary condition. As shown in Chapter 4, this is similar to the results of a BaTiO_3 microsphere in acetone. Therefore, we can measure the instantaneous velocity of a $3 \mu\text{m}$ silica microsphere in water with our existing setup if silica microspheres have perfect-slip boundary conditions on their surface.

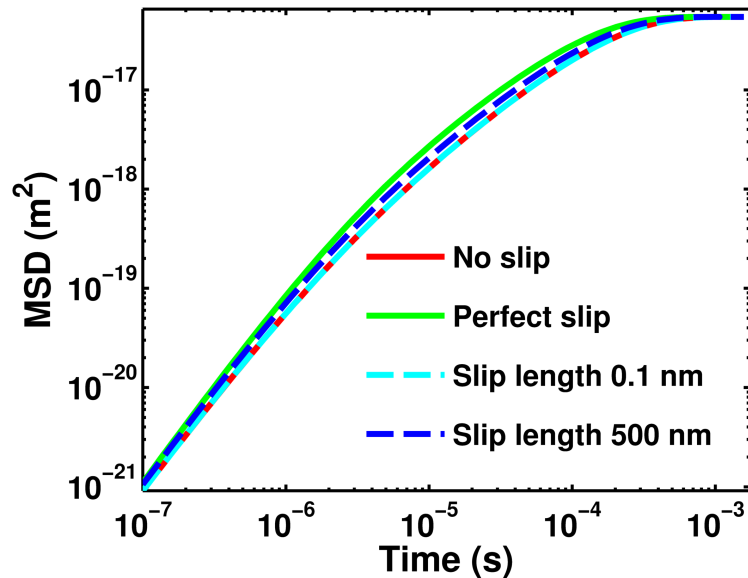


Figure 8.3: The numerical predictions of the mean square displacements of an unbounded microsphere with different boundary conditions.

8.1.2 Mean square displacement

The mean square displacement predictions with different boundary conditions are shown in Fig. 8.3. The slippage on the particle surface results in a less friction force on the particle. Therefore, the MSD increases with increasing slip length. At long time scales, the optical trap confines the particle and causes the MSD to plateau to the same value, which is due to the same trapping strength and is independent of the slippage.

8.1.3 Position power spectral density

The position power spectral density predictions of the particle with different boundary conditions are shown in Fig. 8.4. Interestingly, with increasing

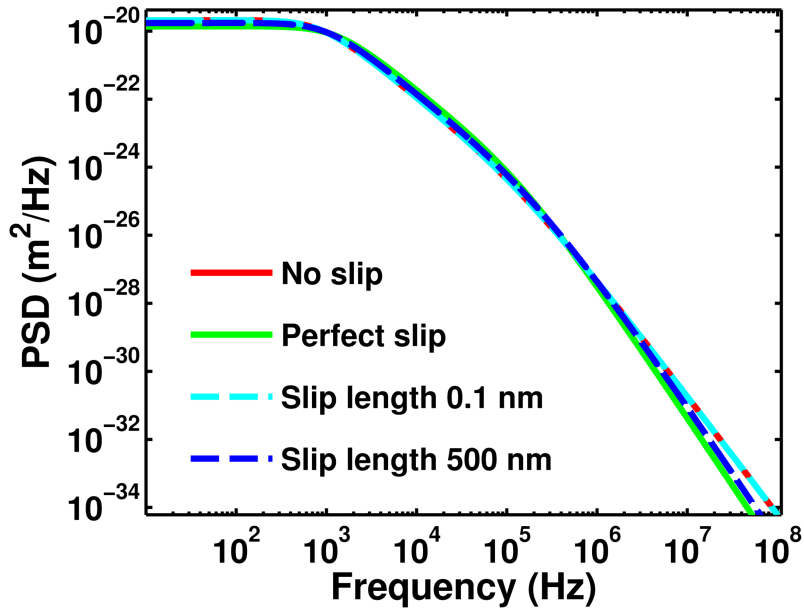


Figure 8.4: The numerical predictions of the position power spectral densities of an unbounded microsphere with different boundary conditions.

slip length, the position PSD is suppressed at low frequencies and high frequencies while it is enhanced at intermediate frequencies. This ensures that the total area under the PSD remains the same as the energy equipartition theory predicts, $\langle x^2 \rangle = k_B T / K$. Overall, the power of the position signal is redistributed towards low frequencies due to the slippage on the particle's surface. This is in favor of precisely measuring the position with a given detection bandwidth.

8.1.4 Velocity power spectral density

The velocity power spectral density predictions with different boundary conditions are shown in Fig. 8.5. The boundary-condition effects on the

velocity PSD are very similar to those on the position PSD. With increasing slip length, the power of the velocity is redistributed towards low frequencies, which facilitates the precise measurements of the instantaneous velocity of a particle with large slip lengths.

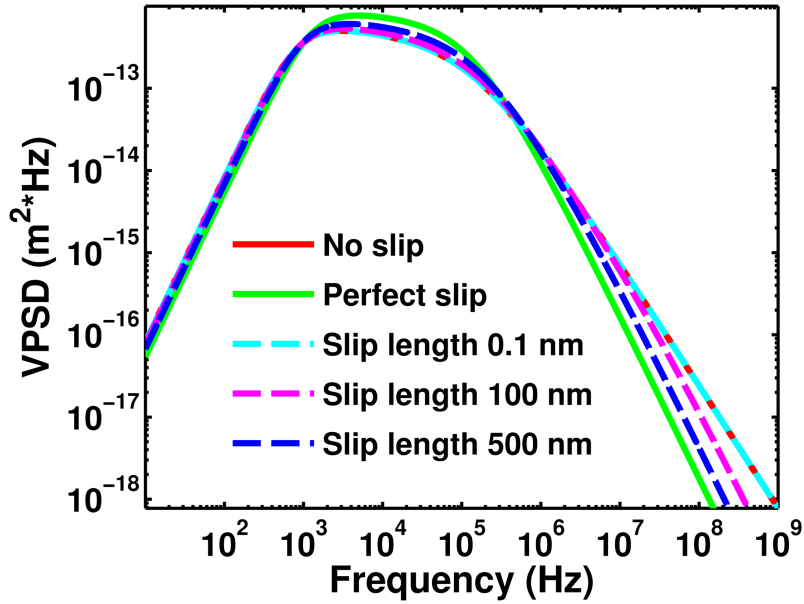


Figure 8.5: The numerical predictions of the velocity power spectral densities of an unbounded microsphere with different boundary conditions.

8.1.5 Thermal force power spectral density

Fig. 8.6 shows the thermal force power spectral density predictions on the sphere with different boundary conditions. The thermal force on the particle with partial (and perfect) slip boundary conditions becomes less colorful, as the thermal force PSD tend to flatten with increasing slip length. Both the DC values of the thermal force spectrum and the drag force decrease with

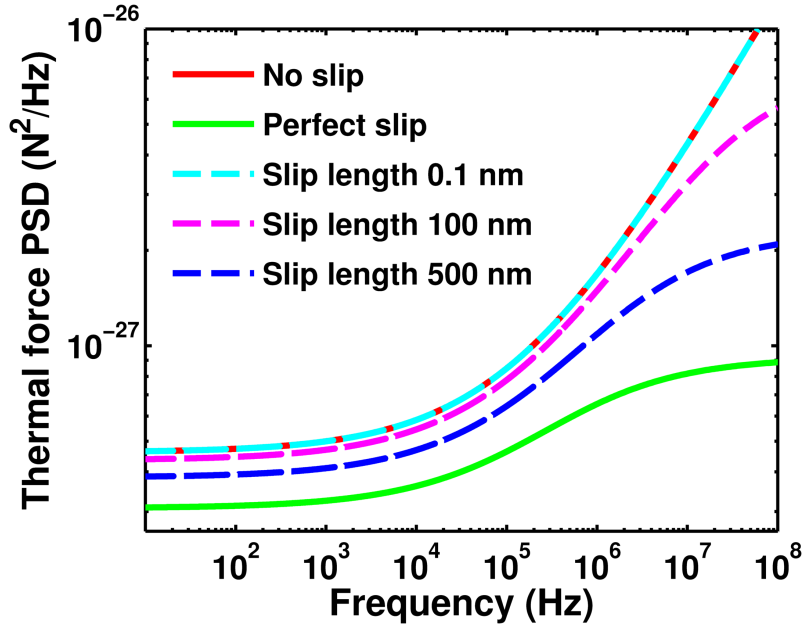


Figure 8.6: The numerical predictions of the velocity power spectral density of an unbounded microsphere with different boundary conditions.

increasing slip length, which is in accordance with the fluctuation-dissipation theorem [10]. The high frequency behavior is significantly affected by the slippage on the particle's surface. The thermal force spectrum with slip boundary conditions no longer has a dependence of $\sqrt{\omega}$ and instead tends to a saturation. In the perfect-slip limit, the thermal force at high frequencies saturates at

$$S_F(\omega) = 48\pi^2\eta ak_B T \quad (8.4)$$

which is 3 times of the corresponding DC value.

In summary, the boundary-condition can drastically affect Brownian motion, which can be utilized to measure the slippage. In the mean time,

these numerical calculations validate the assumption we made in Chapter 4 and 6, regarding the no-slip boundary condition at the glass surface in water and acetone.

8.2 Brownian motion of a no-slip microsphere near a perfect-slip wall

In Chapter 5 and 6, we have discussed the boundary effects on Brownian motion of a microsphere with no-slip boundary condition imposed by a no-slip infinite flat wall. In this section, we will discuss the boundary effects on Brownian motion of a microsphere imposed by a perfect-slip infinite flat wall. It is worth emphasizing that the sphere has the no-slip boundary condition.

The theory for Brownian motion in such system can be obtained similarly to the one presented in Chapter 5. Whereas, the reaction field tensor in this system is different than that for a no-slip boundary wall given in Eq. (5.20) and Eq. (5.21), and has been given by Felderhof [180, 181]. The reaction field tensor element in the parallel direction is

$$R_{\parallel}^{slip}(\mathbf{r}_0, \omega) = \frac{-1}{32\pi\eta h\nu^2} \left[1 - (1 + 2\nu + 4\nu^2)e^{-2\nu} \right] \quad (8.5)$$

and in the perpendicular direction is given by

$$R_{\perp}^{slip}(\mathbf{r}_0, \omega) = \frac{-1}{16\pi\eta h\nu^2} \left[1 - (1 + 2\nu)e^{-2\nu} \right] \quad (8.6)$$

where $\nu = \sqrt{-i\omega\rho_f h^2/\eta} = \sqrt{-i\omega\tau_w}$, τ_w is the time taken for vorticity in the fluid to traverse the distance from the wall to the sphere.

Furthermore, we can give the admittance of particle for both directions in such system as we did in Eq. (5.22) and Eq. (5.23)

$$\mathbf{y}_{slip}^{\perp}(\omega) = \frac{1 + \gamma_s(1 + \tilde{\alpha} + \tilde{\alpha}^2/3)R_{\perp}^{slip}(\mathbf{r}_0, \omega)}{(\gamma_0(\omega) - i\omega m_p) + i\omega(m_f - m_p)\gamma_s(1 + \tilde{\alpha} + \tilde{\alpha}^2/3)R_{\perp}^{slip}(\mathbf{r}_0, \omega)}, \quad (8.7)$$

and in the parallel direction

$$\mathbf{y}_{slip}^{\parallel}(\omega) = \frac{1 + \gamma_s(1 + \tilde{\alpha} + \tilde{\alpha}^2/3)R_{\parallel}^{slip}(\mathbf{r}_0, \omega)}{(\gamma_0(\omega) - i\omega m_p) + i\omega(m_f - m_p)\gamma_s(1 + \tilde{\alpha} + \tilde{\alpha}^2/3)R_{\parallel}^{slip}(\mathbf{r}_0, \omega)}. \quad (8.8)$$

With these, the complete dynamics of the particle can be at least numerically calculated. For rest of the section, we will give the numerical predictions of a variety of statistical quantities for the Brownian motion of no-slip sphere in three cases: unbounded, near a no-slip flat infinite wall, and near a perfect-slip flat infinite wall. These calculations will be used to study both boundary effects and boundary-condition effects. The particle considered here is a 3 μm diameter silica sphere ($\rho = 2.0 \text{ g/cm}^3$) trapped by an optical tweezer with a trap stiffness of 150 $\mu\text{N/m}$, whereas the fluid is water ($\rho_f = 1 \text{ g/cm}^3$, $\eta = 0.9 \times 10^{-3} \text{ Pa}\cdot\text{s}$). In the bounded cases, the sphere-wall separation is set to $h = 3 \mu\text{m}$. Since the boundary effects imposed by a no-slip wall have been investigated thoroughly Chapter 5 and 6, here we just use them as comparisons to the boundary effects imposed by a perfect-slip flat wall.

8.2.1 Position power spectral density

The position power spectral density predictions of the sphere in those three cases are shown in Fig. 8.7. At high frequencies ($> F_w = 1/(2\pi\tau_w)$), the

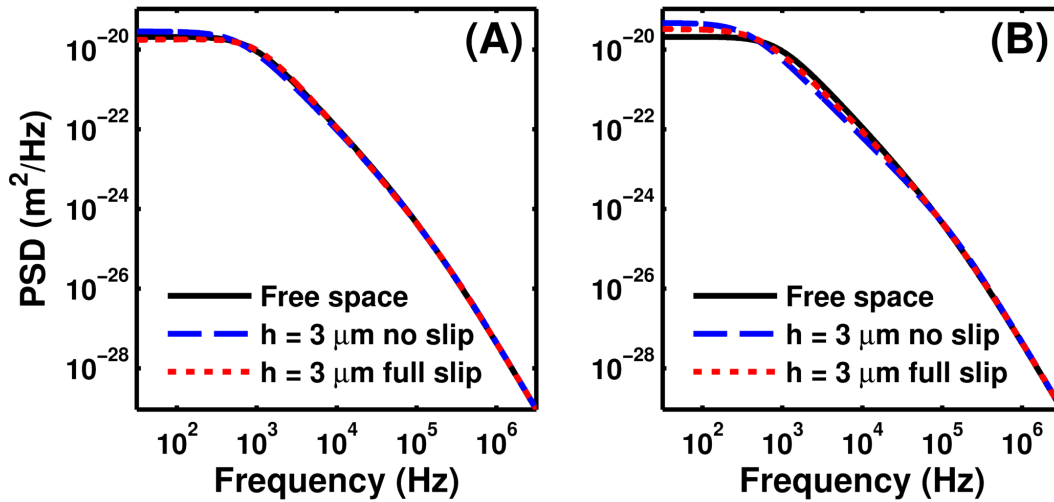


Figure 8.7: The numerical predictions of the position power spectral density of a no-slip microsphere in three cases: unbounded, $3 \mu\text{m}$ away from a flat infinite no-slip wall, and $3 \mu\text{m}$ away from a flat infinite perfect-slip wall. (A) in the parallel direction; (B) in the perpendicular direction.

boundary effects imposed by both no-slip and perfect-slip walls are negligible. In the perpendicular direction, shown in Fig. 8.7(B), the boundary effects imposed by the perfect-slip wall are similar to those imposed by the no-slip wall. However, they are qualitatively different in the parallel direction as shown in Fig. 8.7(A). Unlike the no-slip wall case, the parallel position PSD of the sphere near a perfect-slip wall is suppressed at low frequencies and enhanced at intermediate frequencies.

8.2.2 Velocity power spectral density

Fig. 8.8 shows the velocity power spectral density predictions of the sphere in those three cases. The boundary effects on velocity PSD imposed

by both no-slip and perfect-slip walls are similar to those on the position PSD imposed by the same wall.

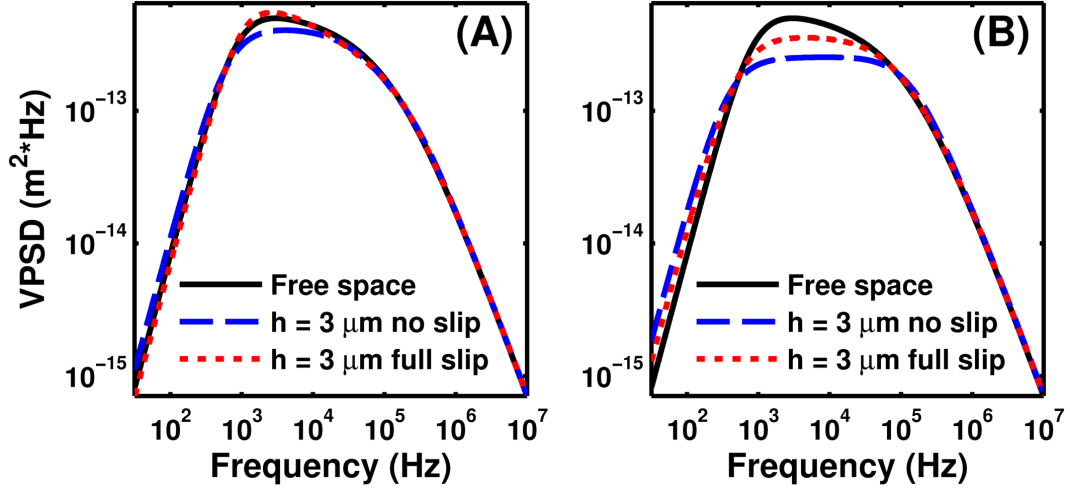


Figure 8.8: The numerical predictions of the velocity power spectral density of a no-slip microsphere in three cases: unbounded, $3 \mu\text{m}$ away from a flat infinite no-slip wall, and $3 \mu\text{m}$ away from a flat infinite perfect-slip wall. (A) in the parallel direction; (B) in the perpendicular direction.

8.2.3 Mean square displacement

The mean square displacement predictions of the sphere in the three cases are shown in Fig. 8.9. At long time scales, the MSDs of each case in both parallel and perpendicular directions plateau to the same value due to confinement caused by the optical trap. As compared to the MSD of an unbounded particle, the MSDs in the perpendicular direction of particle near both no-slip and perfect-slip walls are suppressed (shown in Fig. 8.9(B)), meaning the sphere experience a stronger drag force when move perpendicularly to a wall regardless the boundary condition on the wall surface. However, the mag-

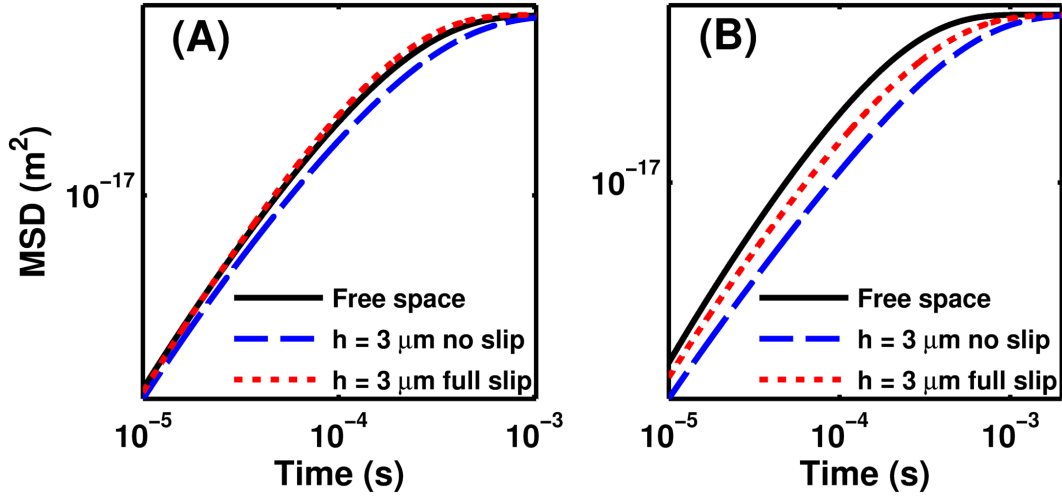


Figure 8.9: The numerical predictions of the mean square displacements of a no-slip microsphere in three cases: unbounded, $3 \mu\text{m}$ away from a flat infinite no-slip wall, and $3 \mu\text{m}$ away from a flat infinite perfect-slip wall. (A) in the parallel direction; (B) in the perpendicular direction.

nitude of the drag force depends on the boundary condition at the wall. In addition to this quantitative dependence on boundary conditions, the drag force on the sphere moving parallel to the wall has a qualitative dependence on the boundary conditions. It is surprising that in the parallel direction, the MSD of the sphere near the perfect-slip wall actually increases as compared to that of an unbounded sphere, which means that the sphere experience less drag force when moving in parallel to a perfect-slip wall as compared to that of an unbounded sphere.

Here, we give the DC values of the drag coefficients of the sphere near a perfect-slip wall in both directions

$$\gamma_{\text{p-s}}^{\parallel} = 6\pi\eta a \frac{1}{1 + \frac{3a}{8h}} \quad (8.9)$$

$$\gamma_{\text{p-s}}^\perp = 6\pi\eta a \frac{1}{1 - \frac{3a}{4h}} \quad (8.10)$$

With these, the diffusion coefficients with first order of a/h in the two directions can be given by Einstein-Stokes relation

$$\mathcal{D}_{\text{p-s}}^\parallel = \frac{k_B T}{6\pi\eta a} \left(1 + \frac{3a}{8h}\right) = D_0 \left(1 + \frac{3a}{8h}\right) \quad (8.11)$$

$$\mathcal{D}_{\text{p-s}}^\perp = \frac{k_B T}{6\pi\eta a} \left(1 - \frac{3a}{4h}\right) = D_0 \left(1 - \frac{3a}{4h}\right) \quad (8.12)$$

The diffusion coefficient $\mathcal{D}_{\text{p-s}}^\parallel$ is actually bigger than the one in bulk. This has been experimentally demonstrated for a sphere moving near a fluid-air interface, which can be considered to be perfect-slip [182].

8.2.4 Velocity autocorrelation function

The numerical prediction of the absolute velocity autocorrelation function $C_v(t)$ (normalized to $\langle(v_\parallel^*)^2\rangle$ and $\langle(v_\perp^*)^2\rangle$ in the parallel and perpendicular directions respectively) of the sphere in the three cases are shown in Fig. 8.10. In the perpendicular direction, the boundary effects imposed by both no-slip and perfect-slip walls cause a more rapid decay in VACF as compared to that in bulk case. However, in the parallel direction, the VACF of a sphere near a perfect-slip wall first decay faster than the one in bulk case followed by slower decay at intermediate time scales.

8.2.5 Thermal force power spectral density

The thermal force power spectral density predictions in the three cases are shown in Fig. 8.11. As discussed in Chapter 5 and 6, the thermal force

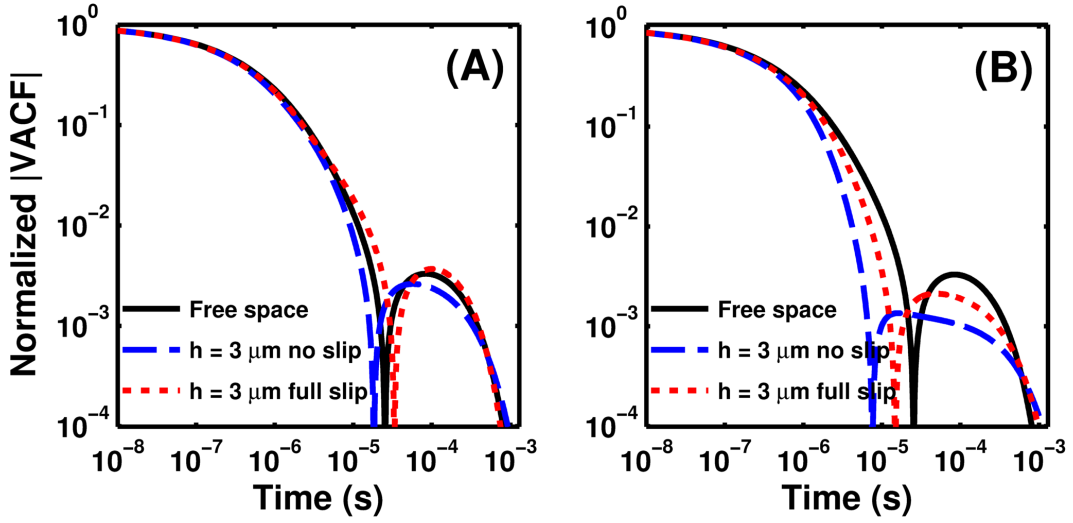


Figure 8.10: The numerical predictions of the velocity autocorrelation function of a no-slip microsphere in three cases: unbounded, $3 \mu\text{m}$ away from a flat infinite no-slip wall, and $3 \mu\text{m}$ away from a flat infinite perfect-slip wall. (A) in the parallel direction; (B) in the perpendicular direction.

loses its color at low frequency when approach to a no-slip wall. It is still the case for a sphere moving perpendicularly near a perfect-slip wall. However, it is qualitatively different in the parallel direction. The thermal force in the parallel direction on a sphere near a perfect-slip wall does not lose its color.

The low frequency behaviors of the thermal force near a perfect-slip wall can be understood by the asymptotic form of the thermal force PSD (one-sided) exerted on the particle $\omega \rightarrow 0$, which is given in the parallel direction by

$$S_{F,\parallel}^{\text{p-s}}(\omega) = 4k_B T \gamma_s \left(\frac{1}{1 + \frac{3a}{8h}} + \frac{64\sqrt{2}h^2}{(8h + 3a)^2} (\omega\tau_f)^{\frac{1}{2}} \right) \quad (8.13)$$

and in the perpendicular direction by

$$S_{F,\perp}^{\text{p-s}}(\omega) = 4k_B T \gamma_s \left(\frac{1}{1 - \frac{3a}{4h}} + \frac{8\sqrt{2}(6h^4 - 5a^2h^2)}{15a^2(4h - 3a)^2} (\omega\tau_f)^{\frac{3}{2}} \right) \quad (8.14)$$

The DC values of $S_{F,\parallel}^{\text{p-s}}$ and $S_{F,\perp}^{\text{p-s}}$ change to $4k_B T \gamma_s \frac{1}{1 + \frac{3a}{8h}}$ and $4k_B T \gamma_s \frac{1}{1 - \frac{3a}{4h}}$ from the bulk value of $4k_B T \gamma_s$ respectively. The change in the thermal force is consistent with the change in the drag force, in accordance with the fluctuation-dissipation theorem [10].

The flatness of the thermal force PSD in the perpendicular direction on a sphere near a perfect-slip flat wall can be understood in the same way for the no-slip wall case. In contrast, this effect is not seen in the parallel direction in the case of a perfect slip plane wall, mathematically seen as $S_{F,\parallel}^{\text{p-s}}$

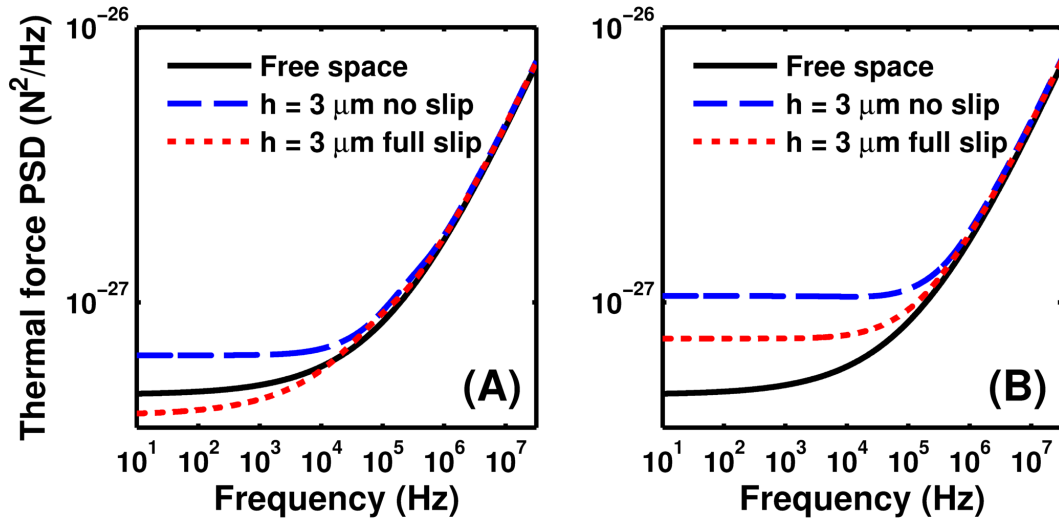


Figure 8.11: The numerical predictions of the thermal force power spectra on a no-slip microsphere in three cases: unbounded, $3 \mu\text{m}$ away from a flat infinite no-slip wall, and $3 \mu\text{m}$ away from a flat infinite perfect-slip wall. (A) in the parallel direction; (B) in the perpendicular direction.

depends on $\sqrt{\omega\tau_f}$. We believe this to be due to constructive interference from the reflected flow, as discussed in Section 5.2.4. More studies are needed to completely understand this effect.

In summary, some conclusions drawn in the Chapter 5 and 6 still hold for the case of a sphere near a perfect-slip wall. For instance, boundary effects imposed by a perfect-slip flat wall occur at time scales shorter than τ_w and frequency scales higher than F_w . In the perpendicular direction, the boundary effects imposed by a perfect-slip wall is only quantitatively different with those caused by a no-slip wall, which can be understood as the no penetration boundary condition does not change for both cases. With the same sphere-wall separation, the boundary effects near a perfect-slip wall are weaker than those near a no-slip wall. However, in the parallel direction, the boundary effects caused by two types of walls are qualitatively different. The boundary effects imposed by a partial-slip flat wall will manifest as a hybrid of the effects caused by a no-slip wall and a perfect-slip wall.

We present two economical methods of achieving partial-slip boundary conditions both on the microspheres and boundaries, namely coverslips or glass fibers. One is to coat the glass surface with a superhydrophobic structure with nano-scale roughness¹, which increases the effective slip length to the order of 100 nm. The other method is to coat the glass with a self-assembled monolayer of phosphonates, whose thickness is typically only a few nanometers². With

¹For instance, HydroFoe coating, <http://lotusleaf.octochemstore.com/>

²For example, Aculon, <http://www.aculon.com/samp-technology.php>

this, we are expecting to achieve a slip length of ~ 10 nm.

Chapter 9

Brownian motion in compressible fluids and non-equilibrium physics study

One has to modify the Maxwell Boltzmann distribution and the energy equipartition theorem to explain the observation shown in Chapter 4, which accounts for the inertia of the entrained fluid. These modifications are unnecessary if the effects of compressibility of the liquid is taken into account [26]. Below time scales on the order of $\tau_c = a/c$, where c is the speed of sound in the liquid and a is the radius of the microsphere, the compressibility of the liquid cannot be neglected and the mean square value of the velocity will approach the energy equipartition theorem $\langle v^2 \rangle = k_B T / m_p$, rather than the modified one $\langle (v^*)^2 \rangle = k_B T / m^*$ observed in Chapter 4. The effective mass will be the mass of particle m_p alone. The time scale τ_c in our experiments is typically around 1 ns, which is not accessible with our current experimental setup.

In this chapter, we will first present the efforts to resolve the compressibility of fluid using a pulsed laser as the detection beam. It is important to note that we assume a no-slip boundary condition in this chapter. In the second part of the chapter, we will briefly discuss the possible further experiments on studying non-equilibrium physics.

9.1 Brownian motion in compressible fluids

As shown in Chapter 4, our current temporal resolution on velocity measurement is around 100 ns ($\gg \tau_c$), which is limited by the position sensitivity and ultimately by the detection beam's shot noise. This temporal resolution does not allow us to resolve the compressibility of the fluids. The absolute shot noise in the detection beam increases with power as \sqrt{P} , while the position signal increases linearly with power P . Therefore, one can increase the position sensitivity by increasing the detection power, which is limited by three facts: the maximum power the detector can handle, the maximum laser power available for detection, and the maximum power on the particles and fluids without causing heating issue. The current commercially available balanced detectors have a power limitation of 5 mW per photodiode (Thorlabs PDB410C for instance). The home-made balanced detector can handle up to 100 mW per photodiode [17]. Continuous wave (CW) lasers typically can only provide power up to ~ 10 W, while a pulsed laser can easily provide much higher peak power and much lower averaged power. The high peak power will reduce the shot noise level thus increase the position sensitivity. The low averaged power reduces heating on the microspheres and fluids and can be well below the detector damage threshold.

For example, by using a 10^{-10} s duration pulsed laser with a peak power of 10^8 W, one can increase the position sensitivity to about 10^{-19} m/ $\sqrt{\text{Hz}}$. This leads to a temporal resolution of 0.1 ns (see Section 3.4), which is much shorter than τ_c , thus we can resolve the compressibility of fluids. Moreover,

the average power of the pulsed laser is only 10 mW, which is well below our detector's damage threshold, and would not heat the particles and fluids. A large particle combined with a low-sound-speed fluid, which result in a large τ_c , are in favor of resolving the fluid's compressibility. Perfluorohexane is probably desired as it has low sound speed (479 m/s) in comparison with that of water (1500 m/s). It is worth noting that the temporal resolution is also limited by the duration of the pulsed laser; hence, a sub-ns pulsed laser is necessary.

9.1.1 Theory for Brownian motion of a microsphere in a compressible fluid

The theory of hydrodynamic interaction presented in Chapter 3 does not take into account the nonzero compressibility of the fluid. In this section, we will give the theory of Brownian motion with compressible effects.

Unlike the theory for a Brownian particle in an incompressible fluid, the theory for Brownian motion with compressible effects is not well developed. Expressions for many statistical quantities of Brownian motion, like MSD, position PSD, velocity PSD, and so on, have not been derived. The normalized velocity autocorrelation function of a microsphere in a compressible fluid in short time limit ($\ll \tau_c$) can be approximated as [26]:

$$A(t) = \frac{\langle v(t)v(0) \rangle}{k_B T / m^*} = 1 + \frac{m_f}{2m_p} \left[\frac{1}{2} - \frac{im^*}{(4m_p^2 - m_f^2)^{1/2}} \right] e^{-ix_1 t / \tau_c} \quad (9.1)$$

$$+ \frac{m_f}{2m_p} \left[\frac{1}{2} + \frac{im^*}{(4m_p^2 - m_f^2)^{1/2}} \right] e^{-ix_2 t / \tau_c},$$

where

$$\begin{aligned} x_1 &= -i\frac{m^*}{m_p} + \left[1 - \frac{m_f^2}{4m_p^2}\right]^{1/2}, \\ x_2 &= -i\frac{m^*}{m_p} - \left[1 - \frac{m_f^2}{4m_p^2}\right]^{1/2}. \end{aligned} \quad (9.2)$$

At very short time scales $t \ll t_c$, Eq. (9.1) approaches $A(0) = 1 + \frac{m_f}{2m_p}$. The short time limit $A(0) \neq 1$ because the normalization factor is $k_B T/m^*$, rather than $k_B T/m_p$.

As discussed in Chapter 3, in order to get the comprehensive theory for Brownian motion of a sphere in a compressible fluid, the admittance for such system is needed and can be obtained from the frequency-dependent friction coefficient, which has been studied [164]:

$$\gamma_{com}(\omega) = \frac{4\pi\eta a (1 + \tilde{\lambda})(9 + 9\tilde{\alpha} + \tilde{\alpha}^2) + 2\tilde{\lambda}^2(1 + \tilde{\alpha})}{3 \quad 2(1 + \tilde{\lambda}) + (1 + \tilde{\alpha} + \tilde{\alpha}^2)\tilde{\lambda}^2/\tilde{\alpha}^2} \quad (9.3)$$

where the dimensionless quantities $\tilde{\lambda} = \frac{a\omega}{\sqrt{-c^2 + i\omega(\zeta + 4\eta/3)/\rho_f}}$, which contains the information for the compressible effects, $\tilde{\alpha} = \sqrt{-i\omega\tau_f}$, c is the speed of sound in the fluid, η and ζ are the shear viscosity and bulk viscosity of the fluid respectively.

In the incompressible limit, corresponding to $\tilde{\lambda} \rightarrow 0$ (because $c \rightarrow \infty$), the drag coefficient $\gamma_{com}(\omega)$ reduces to the one in an incompressible fluid $\gamma_s(1 + \tilde{\alpha} + \tilde{\alpha}^2/9)$, as in Eq. (3.31). The ratio between the two important time scales τ_f and τ_c is $\frac{\rho_f a c}{\eta}$, which is around 10^3 in our experiments, meaning the hydrodynamic effects take place at time scales 10^3 longer than that of the compressible effects. At low frequencies $\omega \ll c/a$, which leads $|\tilde{\lambda}| \ll 1$, thus the compressible effects are negligible.

The admittance of an optically trapped sphere in a compressible fluid can be obtained from the frequency-dependent friction coefficient through

$$\mathcal{Y}_{com}(\omega) = \frac{1}{-i\omega m + \gamma_{com}(\omega) + \frac{K}{-i\omega}}. \quad (9.4)$$

With this, the complete theory of Brownian motion with compressible effects is known at least numerically.

9.1.2 Numerical predictions of Brownian motion in compressible fluids

In this section, we will give our predictions of Brownian motion of a microsphere in a compressible fluid for two systems: a 3 μm diameter silica microsphere in water ($\zeta = 2.4 \times 10^{-3}$ Pa·s, $c = 1500$ m/s) [183] and a 6 μm diameter BaTiO₃ microsphere in acetone ($\zeta = 1.4 \times 10^{-3}$ Pa·s, $c = 1174$ m/s) [183]. The compressible effects time scales τ_c are 1 ns and 2.5 ns for the two systems respectively. The trapping strength 150 $\mu\text{N/m}$ is used in the numerical calculation. This will serve as a guide for the experiments on resolving the fluid's compressibility.

The position power spectral density predictions of the two systems are shown in Fig. 9.1. At low frequencies, the two theoretical predictions overlap nearly perfectly, proving that the compressible effects can be neglected at frequency scales lower than $F_c = 1/(2\pi\tau_c)$. The PSDs enhance at frequencies around F_c due to boundary effects. At frequencies much higher than F_c , these two theories tend to agree with each other. The characteristic frequency scales are $F_{c1} = 160$ MHz and $F_{c2} = 60$ MHz for the two systems: a 3 μm diameter

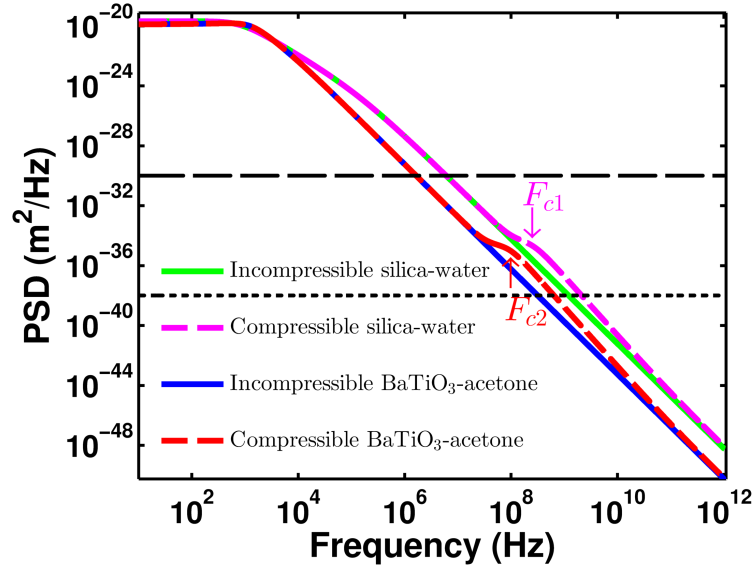


Figure 9.1: The predictions of the position power spectral densities for the two systems: a $3 \mu\text{m}$ diameter silica microsphere in water and a $6 \mu\text{m}$ diameter BaTiO_3 microsphere in acetone. Solid lines are the predictions for incompressible fluids. Dashed lines are the predictions for compressible fluids. The characteristic frequency scales are $F_{c1} = 160 \text{ MHz}$ and $F_{c2} = 60 \text{ MHz}$ for the two systems respectively. The black dashed and dotted lines represent position sensitivity with a level of $10^{-15} \text{ m}/\sqrt{\text{Hz}}$ and $10^{-19} \text{ m}/\sqrt{\text{Hz}}$ respectively.

silica microsphere in water and a $6 \mu\text{m}$ diameter BaTiO_3 microsphere in acetone respectively. The compressible features on position PSD are submersed in our current shot noise (black dashed line, $10^{-15} \text{ m}/\sqrt{\text{Hz}}$). However, by using the pulsed laser mentioned above, the compressible effects become resolvable due to much lower noise level (black dotted line, $10^{-19} \text{ m}/\sqrt{\text{Hz}}$).

The velocity power spectral density predictions for the two systems are shown in Fig. 9.2. The compressible effects on VPSD is similar to the ones on PSD. The two theories give almost the same predictions except at frequencies

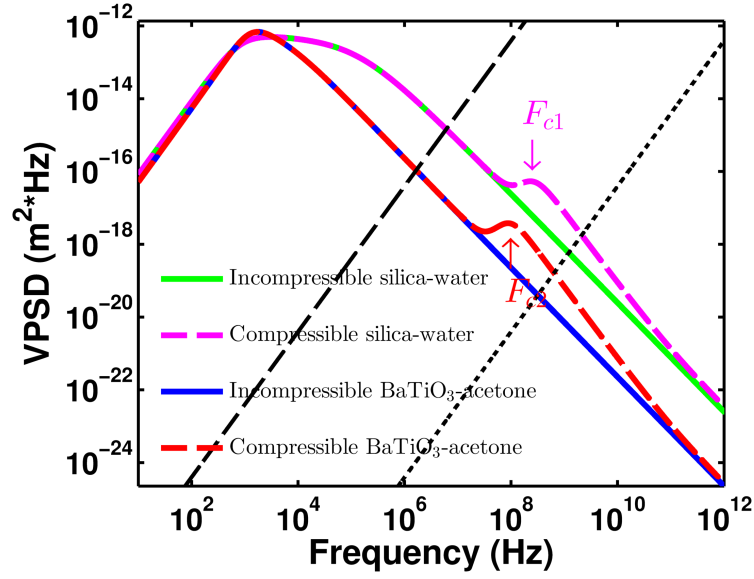


Figure 9.2: The predictions of the velocity power spectral densities for the two systems: a 3 μm diameter silica microsphere in water and a 6 μm diameter BaTiO_3 microsphere in acetone. Solid lines are the predictions for incompressible fluids. Dashed lines are the predictions for compressible fluids. The characteristic frequency scales are $F_{c1} = 160$ MHz and $F_{c2} = 60$ MHz for the two systems respectively. The black dashed and dotted lines represent the noise level with position sensitivities: 10^{-15} m/ $\sqrt{\text{Hz}}$ and 10^{-19} m/ $\sqrt{\text{Hz}}$ respectively.

around F_c . Also, our current noise, represented by the black dashed line, makes the compressible effects on velocity PSD elusive. However, these effects can be resolvable with the pulsed laser.

The mean square displacement predictions for the two systems are shown in Fig. 9.3. At time scales much larger than τ_c , the two predictions agree well with each other, thus the compressible effects on MSD can be neglected. At time scales shorter than τ_c , the compressibility of the fluid changes the MSD slightly.

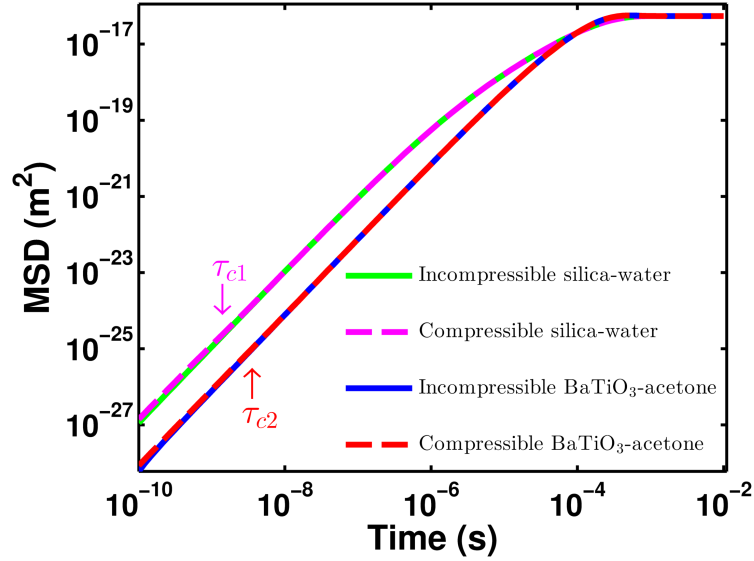


Figure 9.3: The predictions of the mean square displacements for the two systems: a 3 μm diameter silica microsphere in water and a 6 μm diameter BaTiO_3 microsphere in acetone. Solid lines are the predictions for incompressible fluids. Dashed lines are the predictions for compressible fluids.

The velocity autocorrelation function predictions for the two systems, normalized to $k_B T/m^*$, are shown in Fig. 9.4. At time scales longer than τ_c , the two theoretical predictions are equivalent, indicating negligible compressible effects, whereas at time scales shorter than τ_c , the two theoretical predictions deviate from each other. The incompressible theory predicts the velocity variance $C_v(0) = 1$, which is consistent with the modified energy equipartition theorem. In contrast, the compressible theory approaches $C_v(0) = 1 + \frac{m_f}{2m_p}$, which is in accordance with the energy equipartition theorem. The short time approximation for VACF predicted by Eq. (9.1), agrees well with the compressible predictions at time scales much shorter than τ_c . The $C_v(0)$ predicted

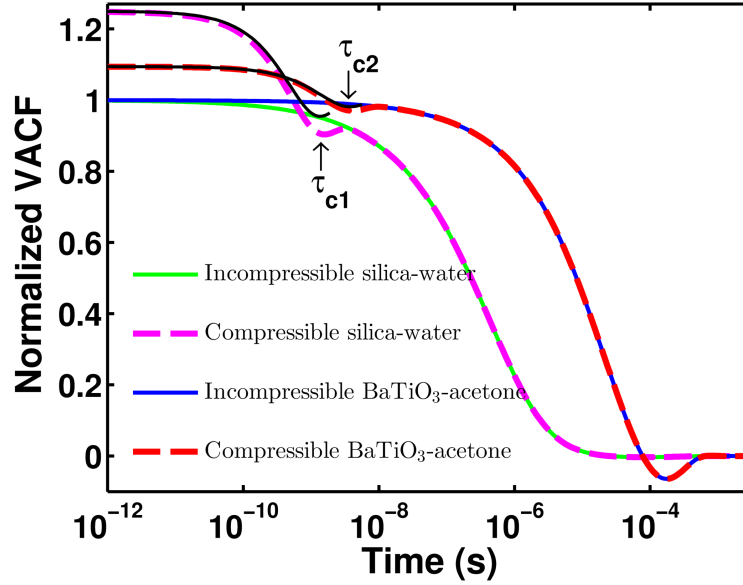


Figure 9.4: The predictions of the velocity autocorrelation functions (normalized to $k_B T/m^*$) for the two systems: a 3 μm diameter silica microsphere in water and a 6 μm diameter BaTiO_3 microsphere in acetone. Solid lines are the predictions for incompressible fluids. Dashed lines are the predictions for compressible fluids. The thin black lines are the short time scales approximation for VACF as given in Eq. (9.1). The compressible time scales are $\tau_{c1} = 1$ ns and $\tau_{c2} = 2.5$ ns for the two systems respectively.

by the compressible theory is 1.1 and 1.25 for the two systems respectively. Due to the compressibility of the fluids, an interesting feature emerging is that the VACF does not monotonically decay. Instead, it oscillates at time scales around τ_c .

The thermal force power spectral densities for the two systems are shown in Fig. 9.5. Similarly to position PSD and velocity PSD, the compressible effects only have impact on the thermal force PSD at frequencies around F_c . At frequencies much lower and much higher than F_c , the compressible

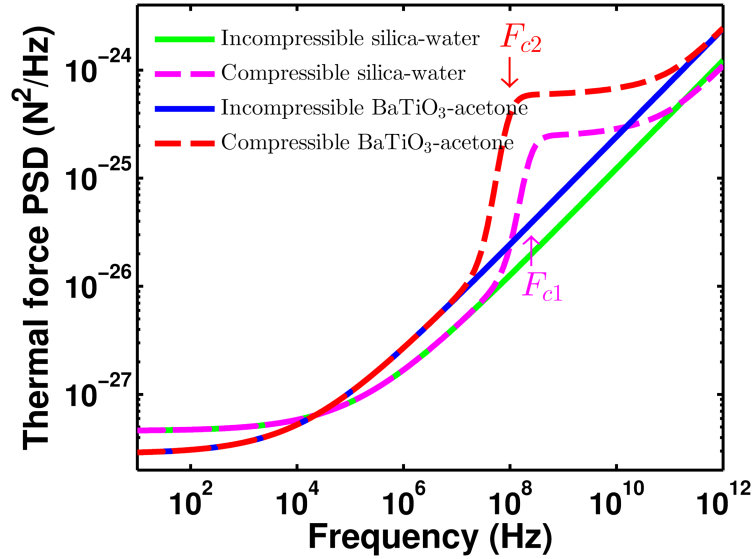


Figure 9.5: The predictions of the thermal force power spectral densities for the two systems: a $3 \mu\text{m}$ diameter silica microsphere in water and a $6 \mu\text{m}$ diameter BaTiO_3 microsphere in acetone. Solid lines are the predictions for incompressible fluids. Dashed lines are the predictions for compressible fluids. The characteristic frequency scales are $F_{c1} = 160 \text{ MHz}$ and $F_{c2} = 60 \text{ MHz}$ for the two systems respectively.

theory gives almost the same predictions as the incompressible theory does.

In summary, at frequencies lower than F_c (or time scales longer than τ_c), the compressible effects on Brownian motion is negligible. Consequently, the incompressible theories presented in Chapter 3 and 5 are good approximations. With our current experimental setup, we are about one decade in both time and frequency domains away from starting to resolve the compressibility, which can be achieved by using a 10^{-10} s duration pulsed laser with a peak power of 10^8 W. The measured velocity distribution and averaged kinetic energy are expected to agree with the Maxwell Boltzmann distribution, and energy

equipartition theorem. It is easier to resolve the compressible effects in the system with 6 μm BaTiO₃ microsphere in acetone due to its larger size of the microsphere and lower sound speed in the fluid as compared to the system with a 3 μm silica microsphere in water.

9.1.3 Experiments toward resolving compressibility of fluids

In this section, we will describe the experimental plans to study Brownian motion with compressible effects in somewhat detail. The simplified schematic of the experiment using pulse probes to resolve compressibility of fluids is shown in Fig. 9.6. The detection laser pulse is split into two pulses by polarization with controllable time delay τ_0 , which can be easily realized by adjusting the difference in optical path length between pulse 1 and pulse 2. In air, 1 ns optical delay time is corresponding to about 30 cm optical path difference. τ_0 , limited by the pulsed laser duration, is one of the limiting factors on the experimental temporal resolution. Therefore τ_0 , as well as the pulse duration, need to be shorter than τ_c . The two probe pulses pass through the trapped particle by a CW beam that is not shown, with a time difference of τ_0 . To cancel out the noise caused by vibration of the cut mirror, the two pulse probes are balanced by the same cut mirror. Polarization is used to guide the two probe pulse into two balanced detectors separately.

The positions of the particle $x(t_0)$ and $x(t_0 + \tau_0)$ can be obtained from detector 1 and 2 respectively. With this, the position autocorrelation function at τ_0 , $C_x(\tau_0) = \langle x(t_0)x(t_0 + \tau_0) \rangle$, can be obtained experimentally by averaging

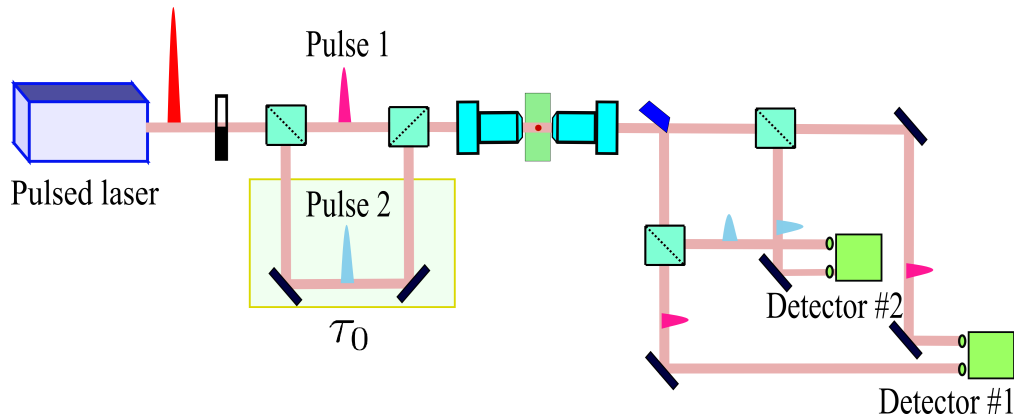


Figure 9.6: The simplified schematic for studying Brownian motion using pulse probes. The laser pulse is split into two pulses, pulse 1 (pink) and pulse 2 (light blue), by polarization with a controllable delay τ_0 . The two pulses pass through a trapped microsphere (by a CW beam which is not shown) with time difference τ_0 and incident onto two balanced detectors.

many measurements with a fixed time delay τ_0 . By changing the optical path length difference thus τ_0 , one can get the $C_x(\tau_0)$ over the entire time domain. The instantaneous velocity of the particle can be estimated using $v(t_0) = (x(t_0 + \tau_0) - x(t_0))/\tau_0$. The velocity autocorrelation function can also be obtained by using four pulse probes instead of two.

Our pulsed laser (Concepts Research Corporation, TO3-1064-5-5) is a passively Q-switched microchip laser with a central wavelength of 1064 nm, a linewidth of 0.28 nm. The pulse duration length (full width at half maximum) is 1.28 ns, measured by the intensity autocorrelation method [184]. The pulse energy, around $5 \mu\text{J}$, results in a peak power of 3 kW. The position sensitivity with this pulsed laser is expected to be around $10^{-17} \text{ m}/\sqrt{\text{Hz}}$, which may still be possible to fully resolve the compressibility of fluids by using large

microspheres and fluids with low sound speed. The pointing noise of this laser, measured by a position sensing detector (Thorlabs, PDP90A), is less than 50 micro-radians in each directions.

In the presence of detection noise, the measured position of the microsphere by two detectors can be expressed as

$$\begin{aligned}x_{1,msr}(t_0) &= x_{1,s}(t_0) + x_{1,n}(t_0), \\x_{2,msr}(t_0 + \tau_0) &= x_{2,s}(t_0 + \tau_0) + x_{2,n}(t_0 + \tau_0),\end{aligned}\tag{9.5}$$

where $x_{1,s}(t_0)$ and $x_{1,n}(t_0)$ are the real position of the microsphere and the noise in the detection system #1 at time t_0 respectively, whereas $x_{2,s}(t_0 + \tau_0)$ and $x_{2,n}(t_0 + \tau_0)$ are the real position of the microsphere and the noise in the detection system #2 at time $t_0 + \tau_0$ respectively. The instantaneous velocity of the trapped Brownian particle at time t_0 is:

$$\begin{aligned}v_s(t_0) &= \frac{x_{2,s}(t_0 + \tau_0) - x_{1,s}(t_0)}{\tau_0} \\&= \frac{x_{2,msr}(t_0 + \tau_0) - x_{1,msr}(t_0)}{\tau_0} - \frac{x_{2,n}(t_0 + \tau_0) - x_{1,n}(t_0)}{\tau_0}\end{aligned}\tag{9.6}$$

In general, $x_{1,n}(t)$ and $x_{2,n}(t)$ should behave similarly but will not be identical due to the two optical paths and the electronics in each system not being exactly the same, which will cause error in the instantaneous velocity measurement. As a result, it is necessary to calibrate the two detection systems.

As shown in Chapter 4 and 6, calibration is not needed in CW beam detection systems. The time difference between two successive measurements

is 5 ns, which is limited by sampling rate of the digitizer (maximum 200 MHz). At such high frequency, the shot noise dominates the classical noise and the instantaneous velocity measurement is immune to low frequency classical noise. This is because the classical noise in a certain data point can be cancelled by the previous data point (or the one followed by). Essentially, each data point serves as a calibration automatically for the next data point, a passive calibration, which can be explained as following. In the presence of detection noise, the positions of the microsphere at at time t_0 and $t_0 + \delta t$ (sampling time interval) measured by the same detection system can be expressed as

$$\begin{aligned} x_{msr}(t_0) &= x_s(t_0) + x_n(t_0), \\ x_{msr}(t_0 + \delta t) &= x_s(t_0 + \delta t) + x_n(t_0 + \delta t), \end{aligned} \tag{9.7}$$

The instantaneous velocity of the trapped Brownian particle at t_0 time can be estimated as:

$$\begin{aligned} v_s(t_0) &= \frac{x_s(t_0 + \delta t) - x_s(t_0)}{\delta t} \\ &= \frac{x_{msr}(t_0 + \delta t) - x_{msr}(t_0)}{\delta t} - \frac{x_n(t_0 + \delta t) - x_n(t_0)}{\delta t} \end{aligned} \tag{9.8}$$

$x_n(t_0 + \delta t) - x_n(t_0)$ is small and dominated by the shot noise when δt is much shorter than $1 \mu s$ in our experiments.

In summary, unlike the CW beam detection mode having the passive calibration, one has to actively calibrate the two detection systems in pulsed detection mode. Calibration can be done by introducing a calibration pulse passing through the trapped particle and incident onto both detectors shortly

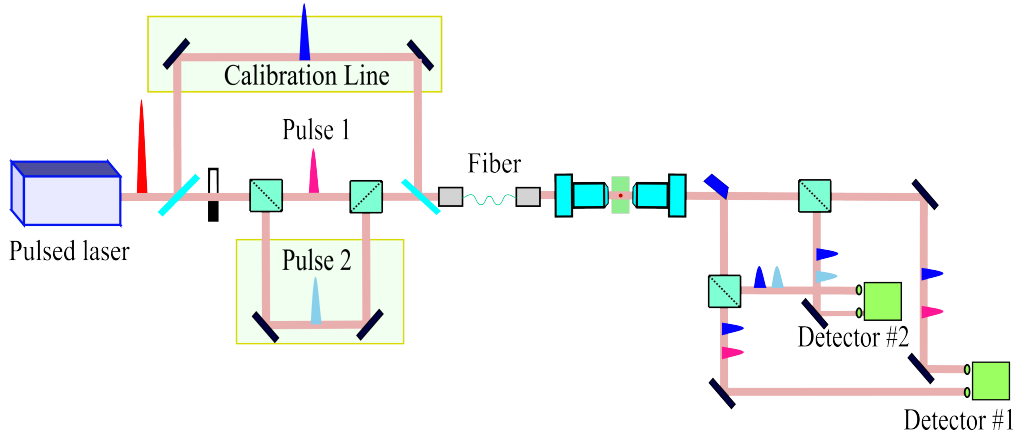


Figure 9.7: The simplified schematic for instantaneous velocity measurements of a Brownian particle using probe pulses with calibration. An unpolarized calibration pulse passes through the trapped microsphere δt later than the pulse 1. One single mode optical fiber is used to assure the probe and calibration pulses have the same optical path incident on the particle.

before (or after) the probe pulses. As shown in Fig. 9.7, the unpolarized calibration pulse (the blue pulse), after passing through the trapped microsphere δt later than the pulse 1, is split into two sub-pulses after going through the trapped microsphere. The two detection systems can be calibrated as the following. The measured position by the two detection systems can be expressed as

$$\begin{aligned}
 x_{1,cali,msr}(t_0 + \delta t) &= x_{1,s}(t_0 + \delta t) + x_{1,n}(t_0 + \delta t), \\
 x_{2,cali,msr}(t_0 + \delta t) &= x_{2,s}(t_0 + \delta t) + x_{2,n}(t_0 + \delta t).
 \end{aligned}
 \tag{9.9}$$

Since the position of the Brownian particle measured by the two detection systems at the same time $t_0 + \delta t$ should be the same, namely $x_{1,s}(t_0 + \delta t) = x_{2,s}(t_0 + \delta t)$, the relative noise difference between two detection systems at

time $t_0 + \delta t$ can be calculated

$$x_{1,n}(t_0 + \delta t) - x_{2,n}(t_0 + \delta t) = x_{1,cali,msr}(t_0 + \delta t) - x_{2,cali,msr}(t_0 + \delta t) \quad (9.10)$$

If both τ_0 and δt is much shorter than 1 μs , the difference among $x_{1,s}(t_0)$, $x_{1,s}(t_0 + \tau_0)$, $x_{1,s}(t_0 + \delta t + \tau_0)$ and $x_{2,s}(t_0)$, $x_{2,s}(t_0 + \tau_0)$, $x_{2,s}(t_0 + \delta t + \tau_0)$ measured in each detection system are small and dominated by the shot noise. The instantaneous velocity of the trapped Brownian particle at time t_0 can be estimated as:

$$\begin{aligned} v_s(t_0) &= \frac{x_{2,s}(t_0 + \tau_0) - x_{1,s}(t_0)}{\tau_0} \\ &= \frac{x_{2,msr}(t_0 + \tau_0) - x_{1,msr}(t_0)}{\tau_0} - \frac{x_{2,n}(t_0 + \tau_0) - x_{1,n}(t_0)}{\tau_0} \\ &= \frac{x_{2,msr}(t_0 + \tau_0) - x_{1,msr}(t_0)}{\tau_0} - \frac{x_{2,cali,msr}(t_0 + \delta t) - x_{1,cali,msr}(t_0 + \delta t)}{\tau_0} \end{aligned} \quad (9.11)$$

Until now, we can measure the instantaneous velocity in the pulse-probe mode since every term in the Eq. (9.11) is measurable. This calibration using a CW laser beam can be understood in a similar way. For convenience, the calibration pulse delay time δt needs to be around 10 ns, corresponding to an optical delay path of 3 m. It is important noting that the probe pulses and calibration pulse need to be temporally well resolved by the detectors. For this reason, balanced detectors are necessary as the quadrant detectors are too slow. A single mode fiber is needed to assure that the probe pulses and calibration pulse have same optical path incident on the trapped particle.

There are a few potential limitations in the pulse probe method. The pulse can not be too strong, otherwise the particle motion would be disturbed

or even brought into deep non-equilibrium regime and the fluid would be broke down. The high peak intensity on the photodiodes might cause saturation in photocurrent production and dielectric breakdown of the fluids.

9.2 Non-equilibrium physics study

The ability to measure the instantaneous velocity will allow direct access to statistics of the energy and entropy exchange between the microsphere and the fluid both in equilibrium and non-equilibrium experiments. Brownian motion, as a model tool, has been used to study nonequilibrium physics in many studies [87, 185–194].

Trapped gold nano-spheres exhibit hot Brownian motion due to strong absorption of laser beam [190, 192, 195]. Hot Brownian motion deviates from the predictions of equilibrium Brownian motion because there is constant energy flow from the microsphere to the fluid [190, 196, 197]. It is much easier to measure motion of a gold particle than that of a dielectric sphere of the same size. This is because gold’s density is much higher, resulting in a longer momentum relaxation time τ_p , as well as a gold nano-sphere has much stronger scattering, resulting in higher optical gain, thus lower shot noise.

Another non-equilibrium situation can be created by moving hosting fluids [193, 194], which could break the symmetry of the velocity distribution and of the velocity dynamics. We can easily apply a known velocity fluid flow using the syringe pump, while studying the motion of the trapped microspheres. The maximum flow rate is limited by the trapping strength, which

can be estimated as $v_{max} = Ka/\gamma_s \sim 10$ mm/s with our experimental conditions. The corresponding Reynolds number is about 10^{-2} , thus linearized Navier-Stokes equation is still a good approximation.

Perhaps a more systematic and controllable experiment is to use an optical pushing force (exerted by a CW beam or a pulsed beam) to bring the microspheres to non-equilibrium. A 71 nN (3 orders of magnitude larger than typical trapping forces) optical kicking force on a microsphere exerted by a pulsed laser has been measured [191]. They observed the particle displaced 208 nm on average before exponentially decaying back to the original position due to optical trapping. However, their 1 ms temporal resolution is far from being able to resolve how the velocity of the sphere decays after the kicking, which requires a temporal resolution of less than τ_p . Interestingly, Felderhof predicts that the velocity decays in a quantum-oscillation like way in short times scales when compressibility of the fluids becomes important [198]. The velocity does not decrease monotonically instead it oscillates, as shown in the Fig. 9.4. If the fluid is sufficiently compressible and its bulk viscosity is sufficiently smaller than its shear viscosity, then the velocity of the particle after being kicked can even change its direction.

With a pump-probe scheme as shown in Fig. 9.8, we are likely to be able to resolve these surprising effects. The kicking pulse is introduced from the side by an optical fiber with a conical shape microlens on the tip¹, whose

¹We have 5 such fibers with a desired wavelength of 1064 nm from LaseOptics corporation (Part number: LF-SM-SC-01-RC/HI-1060-FC/APC)

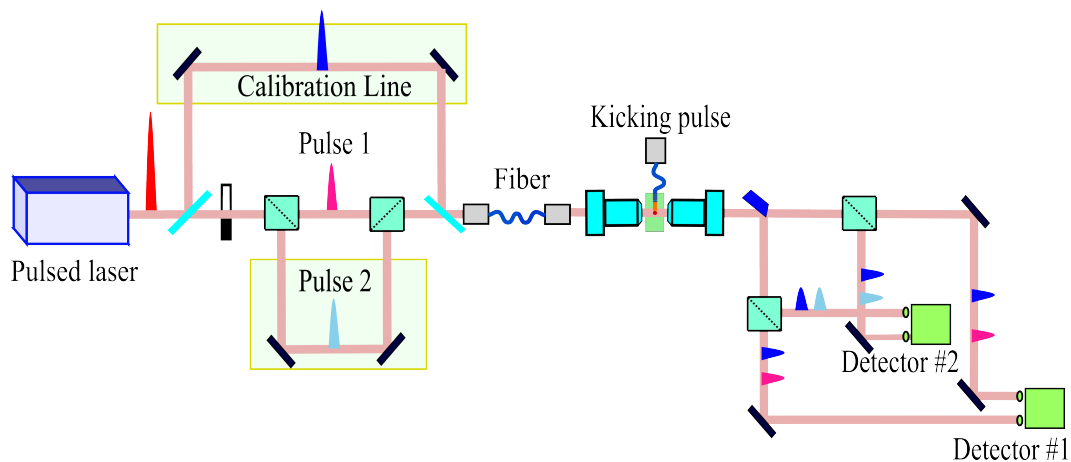


Figure 9.8: The simplified schematic of a “pump-probe” experiment. Based on the pulse probe experiment shown in Fig. 9.7, a kicking pulse is introduced by an optical fiber with a microlens on its tip.

working distance is between 75 to 80 μm . The expected focus spot waist is around 1.5 μm in water. This fiber has a outer diameter of 80 μm , which is the same as the thickness of the flow cell chamber, thus can be sealed in flow cell in the same way as discussed in Chapter 6.

Appendix

Appendix 1

Kubo-Green formula derivation

In this appendix, as an example, we will derive the Kubo-Green formula [80] for a free particle described by the Einstein-Ornstein-Uhlenbeck model [13, 81]. The motion of a free particle in a fluid can be described by the Langevin equation as discussed in Section 3.3.1.1,

$$m_p \dot{v}(t_0 + t) + \gamma_s v(t_0 + t) = F_{th}(t_0 + t). \quad (1.1)$$

By multiplying both sides of the Eq. (1.1) by $v(t_0)$ and taking ensemble average of that, we get

$$m_p \langle v(t_0) \dot{v}(t_0 + t) \rangle + \gamma_s \langle v(t_0) v(t_0 + t) \rangle = \langle v(t_0) F_{th}(t_0 + t) \rangle. \quad (1.2)$$

Due to causality and delta correlation of the thermal force $\langle F_{th}(t_1) F_{th}(t_2) \rangle = \delta(t_1 - t_2)$, one can get $\langle v(t_0) F_{th}(t_0 + t) \rangle = 0^1$. Thus Eq. (1.2) reduces to

$$m_p \frac{d}{dt} \langle v(t_0) v(t_0 + t) \rangle + \gamma_s \langle v(t_0) v(t_0 + t) \rangle = 0. \quad (1.3)$$

¹This is not universal. For example, this cross correlation for a particle in a liquid is nonzero due to non-delta correlated thermal force, as has been experimentally observed [17]. It is worth noting that this does not violate the causality, which can be understand as the following. $v(t_0)$ is correlated to the previous thermal force $F_{th}(t_0 - t)$, and $F_{th}(t_0 - t)$ is correlated to $F_{th}(t_0 + t)$, thus $v(t_0)$ is correlated to $F_{th}(t_0 + t)$.

We multiply both sides of the Eq. (1.3) by $e^{i\omega t}$ and integrate over t from 0 to ∞ . The first term can be simplified by integration by parts. So we get

$$-\frac{k_B T}{m_p} + \left(\frac{\gamma_s}{m_p} - i\omega\right) \int_0^\infty dt e^{i\omega t} \langle v(t_0)v(t_0 + t) \rangle = 0. \quad (1.4)$$

This can be rewritten as

$$\frac{1}{-i\omega m_p + \gamma_s} = \frac{1}{k_B T} \int_0^\infty dt e^{i\omega t} \langle v(t_0)v(t_0 + t) \rangle. \quad (1.5)$$

The left side of the Eq. (1.4) is the admittance of this system, as shown in Eq. (3.20) in Section 3.3.1.1. Therefore, we can get the Kubo-Green formula

$$\mathfrak{Y}(\omega) = \frac{1}{k_B T} \int_0^\infty e^{i\omega t} C_v(t) dt. \quad (1.6)$$

It is important to note that although this general formula is derived within the Einstein-Ornstein-Uhlenbeck model, it can be applied to Brownian motion in liquids and with optical trapping as well, which can not be described by the Einstein-Ornstein-Uhlenbeck model. Furthermore, it is not restricted to the Langevin model or any other specific model either. In fact, it follows from linear response theory.

Bibliography

- [1] Joseph Klafter, MF Shlesinger, and Gert Zumofen. Beyond brownian motion. *Physics Today*, pages 33–39, 1996.
- [2] Robert Brown. Microscopical observations on the particles contained in the pollen of plants; and on the general existence of active molecules in organic and inorganic bodies. *Philosophical Magazine Series 2*, 4(21):161–173, 1828.
- [3] Albert Einstein. Investigations on the Theory of the Brownian Movement. *Annalen der Physik*, 17:549, 1905.
- [4] M. von Smoluchowski. Zur kinetischen theorie der brownschen molekularbewegung und der suspensionen. *Ann. Physik*, 21:756, 1906.
- [5] J Perrin and F Soddy. *Brownian movement and molecular reality*. 1910.
- [6] T. Vicsek. *Fractal Growth Phenomena*. World Scientific, Singapore, second edition, 1992.
- [7] A Einstein. Theoretische bemerkungen über die Brownsche bewegung. *Zeitschrift für elektrochemie und angewandte . . .*, 17(1905):549–560, 1907.
- [8] Paul Langevin. Sur la théorie cinétique du mouvement brownien. *Comptes-rendus de l'Académie des Sciences (Paris)*, 146:530, 1908.

- [9] Don S Lemons, Anthony Gythiel, and I Langevin. Paul Langevin's 1908 paper On the Theory of Brownian Motion. PHYSICS—On the Theory of Brownian Motion A note from M . P . Langevin , presented by M . Mascart . *C.R. Acad. Sci.*, 146(1908):530–533, 1908.
- [10] R Kubo, Home Search, Collections Journals, About Contact, My Iopscience, and I P Address. The fluctuation-dissipation theorem. *Reports on Progress in Physics*, 255, 1966.
- [11] Y. P. Kalmykov W. T. Coffey and J. T. Waldron. *The Langevin Equation: With Applications in Physics, Chemistry and Electrical Engineering*. World Scientific, Singapore, 1996.
- [12] J.V. Noble. Lecture on physics of the human body: The properties of water.
- [13] G E Uhlenbeck and L S Ornstein. On the theory of the Brownian motion. *Physical Review*, 36(5):823–841, October 1930.
- [14] B Lukic, S. Jeney, C. Tischer, A. J Kulik, L Forro, Ernst-Ludwig Florin, B. Lukić, and L. Forró. Direct observation of nondiffusive motion of a Brownian particle. *Physical Review Letters*, 95(16):160601, October 2005.
- [15] Thomas Franosch, Matthias Grimm, Maxim Belushkin, Flavio M Mor, Giuseppe Foffi, Laszlo Forro, and Sylvia Jeney. Resonances arising from

- hydrodynamic memory in Brownian motion. *Nature*, 478(7367):85–88, October 2011.
- [16] Tongcang Li, Simon Kheifets, David Medellin, and Mark G Raizen. Measurement of the instantaneous velocity of a Brownian particle. *Science (New York, N.Y.)*, 328(5986):1673–1675, June 2010.
- [17] Simon Kheifets, Akarsh Simha, Kevin Melin, Tongcang Li, and Mark G. Raizen. Observation of Brownian motion in liquids at short times: instantaneous velocity and memory loss. *Science (New York, N.Y.)*, 343(6178):1493–1496, March 2014.
- [18] Jianyong Mo, Akarsh Simha, Simon Kheifets, and Mark G Raizen. Testing the Maxwell-Boltzmann distribution using Brownian particles. *Optics express*, 23(2):1888–1893, 2015.
- [19] F.M. Exner. Notiz zu Brown’s Molecularbewegung. *Annalen der Physik*, 1900.
- [20] Milton Kerker. Brownian movement and molecular reality prior to 1900. *Journal of Chemical Education*, 51:764, 1974.
- [21] K. Huang. *Statistical Mechanics*. Wiley, 1987.
- [22] Lord Kelvin. On a Decisive Test-Case Disproving the Maxwell-Boltzmann Doctrine regarding Distribution of Kinetic Energy, 1892.

- [23] R. J. Gould. Deviation from a Maxwellian Velocity Distribution in Low-Density Plasmas. *Physics of Fluids*, 14(8):1701, 1971.
- [24] R. J. Gould and M Levy. Deviation from a Maxwellian velocity distribution in regions of interstellar molecular hydrogen. *The Astrophysical Journal*, 1976.
- [25] Donald D. Clayton. Maxwellian relative energies and solar neutrinos, 1974.
- [26] Robert Zwanzig and Mordechai Bixon. Compressibility effects in the hydrodynamic theory of Brownian motion. *Journal of Fluid Mechanics*, 69(01):21, March 1975.
- [27] HA Lorentz. *Abhandlungen über theoretische Physik*. 1907.
- [28] T. Mason and D. Weitz. Optical Measurements of Frequency-Dependent Linear Viscoelastic Moduli of Complex Fluids, 1995.
- [29] Richard Fitzpatrick. Lecture on fluid mechanics.
- [30] Y Zhu and S Granick. Rate-dependent slip of Newtonian liquid at smooth surfaces. *Physical review letters*, 87(9):096105, 2001.
- [31] P. Joseph, C. Cottin-Bizonne, J. M. Benoît, C. Ybert, C. Journet, P. Tabeling, and L. Bocquet. Slippage of water past superhydrophobic carbon nanotube forests in microchannels. *Physical Review Letters*, 97(15):1–4, 2006.

- [32] Chang Hwan Choi, Umberto Ulmanella, Joonwon Kim, Chih Ming Ho, and Chang Jin Kim. Effective slip and friction reduction in nanogated superhydrophobic microchannels. *Physics of Fluids*, 18(8):1–8, 2006.
- [33] David M. Huang, Christian Sendner, Dominik Horinek, Roland R. Netz, and Lydéric Bocquet. Water slippage versus contact angle: A quasiuniversal relationship. *Physical Review Letters*, 101(22):1–4, 2008.
- [34] Zhi Liang and Pawel Keblinski. Slip length crossover on a graphene surface. *The Journal of Chemical Physics*, 142(13):134701, 2015.
- [35] James Clerk Maxwell. *A Treatise on Electricity and Magnetism*. Clarendon Press, Oxford, first edition, 1873.
- [36] P. N. Lebedev. Untersuchungen über die druckkräfte des lichtes. *Ann. d. Phys.*, 6:433, 1901.
- [37] E. F. Nichols and G. F. Hull. A preliminary communication on the pressure of light and heat radiation. *Science*, 14:588, 1901.
- [38] A Ashkin. Acceleration and Trapping of Particles by Radiation Pressure. *Physical review letters*, (4):24–27, 1970.
- [39] A Ashkin and J M Dziedzic. Optical levitation of liquid drops by radiation pressure. *Science (New York, N.Y.)*, 187(4181):1073–5, March 1975.

- [40] A. Ashkin and J. M. Dziedzic. Optical levitation in high vacuum. *Applied Physics Letters*, 28(6):333–335, 1976.
- [41] A. Ashkin, J M Dziedzic, J E Bjorkholm, and S Chu. Observation of a single-beam gradient force optical trap for dielectric particles. *Optics letters*, 11(5):288, 1986.
- [42] A. Ashkin, J. M. Dziedzic, and T. Yamane. Optical trapping and manipulation of single cells using infrared laser beams. *Nature*, 330(6150):769–771, 1987.
- [43] A. Ashkin and J. Dziedzic. Optical trapping and manipulation of viruses and bacteria. *Science*, 235(4795):1517–1520, March 1987.
- [44] A. Ashkin. History of optical trapping and manipulation of small-neutral particle, atoms, and molecules. *IEEE Journal on Selected Topics in Quantum Electronics*, 6(6):841–856, 2000.
- [45] E. a. Cornell and C. E. Wieman. Nobel lecture: Bose-Einstein condensation in a dilute gas, the first 70 years and some recent experiments. *Reviews of Modern Physics*, 74(3):875–893, 2002.
- [46] B. DeMarco. Onset of Fermi Degeneracy in a Trapped Atomic Gas. *Science*, 285(5434):1703–1706, 1999.
- [47] B J Bloom, T L Nicholson, J R Williams, S L Campbell, M Bishof, X Zhang, W Zhang, S L Bromley, and J Ye. An optical lattice clock with

- accuracy and stability at the 10^{-18} level. *Nature*, 506(7486):71–5, February 2014.
- [48] A. Ashkin. Atomic-beam deflection by resonance-radiation pressure. *Physical Review Letters*, 25(19):1321–1324, 1970.
- [49] T.W. Hänsch and A.L. Schawlow. Cooling of gases by laser radiation, 1975.
- [50] A. Ashkin. Trapping of atoms by resonance radiation pressure. *Physical Review Letters*, 40(12):729–732, 1978.
- [51] Bound Resonant Absorbers. Radiation-Pressure Cooling of Bound Resonant Absorbers. 40(25):1639–1642, 1978.
- [52] Steven Chu, J. E. Bjorkholm, A. Ashkin, and A. Cable. Experimental observation of optically trapped atoms. *Physical Review Letters*, 57(3):314–317, 1986.
- [53] A. Ashkin. Applications of laser radiation pressure. *Science (New York, N.Y.)*, 210(4474):1081–1088, 1980.
- [54] A. Ashkin. Forces of a single-beam gradient laser trap on a dielectric sphere in the ray optics regime. *Methods in cell biology*, 55(February):1–27, January 1992.
- [55] Timo a Nieminen, Vincent L Y Loke, Alexander B Stilgoe, Gregor Knöner, Agata M Braczyk, Norman R Heckenberg, and Halina Rubinsztein-

- Dunlop. Optical tweezers computational toolbox. *Journal of Optics A: Pure and Applied Optics*, 9(8):S196–S203, August 2007.
- [56] Yasuhiro Harada and Toshimitsu Asakura. Radiation forces on a dielectric sphere in the Rayleigh scattering regime. *Optics Communications*, 124(5-6):529–541, 1996.
- [57] W H Wright, G J Sonek, and M W Berns. Parametric study of the forces on microspheres held by optical tweezers. *Applied optics*, 33(9):1735–1748, 1994.
- [58] Tongcang Li. *Fundamental Tests of Physics with Optically Trapped Microspheres*. PhD thesis, The University of Texas at Austin, May 2011.
- [59] M K Cheezum, W F Walker, and W H Guilford. Quantitative comparison of algorithms for tracking single fluorescent particles. *Biophysical journal*, 81(4):2378–2388, 2001.
- [60] Dj Pine, a Weitz, M Chaikin, and E Herbolzheimer. Diffusing-Wave Spectroscopy. 60(12), 1988.
- [61] J. X. Zhu, D. J. Durian, J. Müller, D. A. Weitz, and D. J. Pine. Scaling of transient hydrodynamic interactions in concentrated suspensions. *Physical Review Letters*, 68(16):2559–2562, April 1992.

- [62] P. Zakharov, F. Cardinaux, and F. Scheffold. Multispeckle diffusing-wave spectroscopy with a single-mode detection scheme. *Physical Review E - Statistical, Nonlinear, and Soft Matter Physics*, 73(1):1–5, 2006.
- [63] Lulu Liu, Alexander Woolf, Alejandro W. Rodriguez, and Federico Capasso. Absolute position total internal reflection microscopy with an optical tweezer. *Proceedings of the National Academy of Sciences*, 111(52):E5609–E5615, 2014.
- [64] K. Visscher, S.P. Gross, and S.M. Block. Construction of multiple-beam optical traps with nanometer-resolution position sensing. *IEEE Journal of Selected Topics in Quantum Electronics*, 2(4):1066–1076, 1996.
- [65] Frederick Gittes and Christoph F. Schmidt. Interference model for back-focal-plane displacement detection in optical tweezers. *Optics letters*, 23(1):7–9, January 1998.
- [66] M W Allersma, F Gittes, M J DeCastro, R J Stewart, and C F Schmidt. Two-dimensional tracking of bacterial motility by back focal plane interferometry. *Biophysical journal*, 74(2 Pt 1):1074–1085, 1998.
- [67] A. Pralle, M Prummer, E L Florin, E H Stelzer, and J K Hörber. Three-dimensional high-resolution particle tracking for optical tweezers by forward scattered light. *Microscopy research and technique*, 44(5):378–86, March 1999.

- [68] Simon F. Tolic-Norrelykke, Erik Schaffer, Jonathon Howard, Francesco S. Pavone, Frank Julicher, and Henrik Flyvbjerg. Calibration of optical tweezers with positional detection in the back focal plane. *Review of Scientific Instruments*, 77(10):103101, 2006.
- [69] Christian Tischer, Stephan Altmann, Samo Fisinger, J. K. Heinrich Horber, Ernst H. K. Stelzer, and Ernst-Ludwig Florin. Three-dimensional thermal noise imaging. *Applied Physics Letters*, 79(23):3878, 2001.
- [70] J N Munday and F Capasso. Precision measurement of the Casimir Lifshitz force in a fluid. *Phys.Rev.A*, 75:60102, 2007.
- [71] Prerna Sharma, Shankar Ghosh, and S. Bhattacharya. Microrheology of a sticking transition. *Nature Physics*, 4(12):960–966, October 2008.
- [72] Prerna Sharma, Shankar Ghosh, and S. Bhattacharya. A high-precision study of hindered diffusion near a wall. *Applied Physics Letters*, 97(10):104101, 2010.
- [73] Chungil Ha, H.D. Ou-Yang, and Hyuk Kyu Pak. Direct measurements of colloidal hydrodynamics near flat boundaries using oscillating optical tweezers. *Physica A: Statistical Mechanics and its Applications*, 392(17):3497–3504, September 2013.
- [74] Rongxin Huang. *Browian motion at fast time scales and thermal noise imaging*. PhD thesis, University of Texas at Austin, 2008.

- [75] Isaac Chavez, Rongxin Huang, Kevin Henderson, Ernst Ludwig Florin, and Mark G. Raizen. Development of a fast position-sensitive laser beam detector. *Review of Scientific Instruments*, 79(10):1–4, 2008.
- [76] Simon Kheifets. *High-sensitivity tracking of optically trapped particles in gasses and liquids: observation of Brownian motion in velocity space*. PhD thesis, University of Texas at Austin, 2014.
- [77] Texas Instruments. Transimpedance considerations for high-speed amplifiers.
- [78] Tongcang Li, Simon Kheifets, and Mark G. Raizen. Millikelvin cooling of an optically trapped microsphere in vacuum. *Nature Physics*, 7(7):527–530, March 2011.
- [79] S. Chandrasekhar. Stochastic problems in physics and astronomy. *Reviews of Modern Physics*, 15(1):1–89, 1943.
- [80] V. Balakrishnan. *Elements of nonequilibrium statistical mechanics*. CRC Press, 2008.
- [81] G. E. Uhlenbeck C. M. Wang. On the Theory of the Brownian Motion-ii. *Reviews of Modern Physics*, 17(2-3):323–342, 1945.
- [82] E. J. Hinch. Application of the Langevin equation to fluid suspensions. *Journal of Fluid Mechanics*, 72(03):499, March 1975.

- [83] HJH Clercx and P Schram. Brownian particles in shear flow and harmonic potentials: A study of long-time tails. *Physical Review A*, 46(4):1942–1950, 1992.
- [84] P Schram and IP Yakimenko. On the theory of Brownian motion in compressible fluids. *Physica A: Statistical Mechanics and its ...*, 260:73–89, 1998.
- [85] Branimir Lukić, Sylvia Jeney, Željko Sviben, Andrzej Kulik, Ernst-Ludwig Florin, and Laszlo Forro. Motion of a colloidal particle in an optical trap. *Physical Review E*, 76(1):011112, July 2007.
- [86] R J Henery. The generalized Langevin equation and the fluctuation-dissipation theorems, 1971.
- [87] R Kubo. Brownian motion and nonequilibrium statistical mechanics. *Science (New York, N.Y.)*, 233(4761):330–4, July 1986.
- [88] B.U. Felderhof. Linear response theory of the motion of a spherical particle in an incompressible fluid. *Physica A: Statistical Mechanics and its Applications*, 166(3):492–504, 1990.
- [89] B U Felderhof. Effect of the wall on the velocity autocorrelation function and long-time tail of Brownian motion in a viscous compressible fluid. *The Journal of chemical physics*, 123(18):184903, November 2005.
- [90] L. D. Landau. *Fluid mechanics*. Elsevier/Butterworth-Heinemann, Amsterdam, 2004.

- [91] A. B. Basset. On the Motion of a Sphere in a Viscous Liquid. *Philosophical Transactions of the Royal Society A: Mathematical, Physical and Engineering Sciences*, 179(January):43–63, January 1888.
- [92] BJ Alder and TE Wainwright. Velocity autocorrelations for hard spheres. *Physical review letters*, 18(June):988–990, 1967.
- [93] B. J. Alder and T. E. Wainwright. Decay of the velocity autocorrelation function. *Physical Review A*, 1(1):18–21, 1970.
- [94] Robert Zwanzig and Mordechai Bixon. Compressibility effects in the hydrodynamic theory of Brownian motion. *Journal of Fluid Mechanics*, 69(01):21, 1975.
- [95] Simon F. Nørrelykke and Henrik Flyvbjerg. Harmonic oscillator in heat bath: Exact simulation of time-lapse-recorded data and exact analytical benchmark statistics. *Physical Review E - Statistical, Nonlinear, and Soft Matter Physics*, 83(4):1–10, 2011.
- [96] Kirstine Berg-Sørensen and Henrik Flyvbjerg. Power spectrum analysis for optical tweezers. *Review of Scientific Instruments*, 75(3):594, 2004.
- [97] Thomas Franosch and Sylvia Jeney. Persistent correlation of constrained colloidal motion. *Physical Review E*, 79(3):031402, March 2009.
- [98] K G Libbrecht and E D Black. Toward quantum-limited position measurements using optically levitated microspheres. *Physics Letters A*, 321(2):99–102, January 2004.

- [99] Todd P. Meyrath. *Experiments with Bose-Einstein condensation in an optical box*. PhD thesis, The University of Texas at Austin, May 2005.
- [100] Megan T Valentine, Nicholas R Guydosh, Braulio Gutiérrez-Medina, Adrian N Fehr, Johan O Andreasson, and Steven M Block. Precision steering of an optical trap by electro-optic deflection. *Optics letters*, 33(6):599–601, 2008.
- [101] Matthias Grimm, Sylvia Jeney, and Thomas Franosch. Brownian motion in a Maxwell fluid. *Soft Matter*, 7(5):2076–2084, 2011.
- [102] Kirstine Berg-Sørensen and Henrik Flyvbjerg. The colour of thermal noise in classical Brownian motion: a feasibility study of direct experimental observation. *New Journal of Physics*, 7:38–38, February 2005.
- [103] Anita Jannasch, Mohammed Mahamdeh, and Erik Schäffer. Inertial Effects of a Small Brownian Particle Cause a Colored Power Spectral Density of Thermal Noise. *Physical Review Letters*, 107(22):228301, November 2011.
- [104] Jianyong Mo, Akarsh Simha, and Mark G. Raizen. Broadband boundary effects on brownian motion. submitted.
- [105] Sir Horace Lamb. *Hydrodynamics*. University Press, 1916.
- [106] John Happel and Howard Brenner. *Low Reynolds Number hydrodynamics with special applications to particulate media*. Springer, 1983.

- [107] Md Shamsul Alam, Katsuya Ishii, and Hidenori Hasimoto. Slow motion of a small sphere outside of a circular cylinder, 1980.
- [108] S Wakiya. Effect of a plane wall on the impulsive motion of a sphere in a viscous fluid. *Journal of the Physical Society of Japan*, 1964.
- [109] Toshiyuki Gotoh and Yukio Kaneda. Effect of an infinite plane wall on the motion of a spherical. *Journal of Chemical Physics*, 76(6):15, 1981.
- [110] B U Felderhof. Effect of the wall on the velocity autocorrelation function and long-time tail of Brownian motion. *The journal of physical chemistry. B*, 109(45):21406–21412, November 2005.
- [111] Akarsh Simha, Jianyong Mo, and P. J. Morrison. Under preparation.
- [112] D. Bedeaux and P. Mazur. Brownian motion and fluctuating hydrodynamics. *Physica*, 76(2):247–258, September 1974.
- [113] B.U. Felderhof. Force density induced on a sphere in linear hydrodynamics. *Physica A: Statistical Mechanics and its Applications*, 84(3):569–576, January 1976.
- [114] B.U. Felderhof. Corrections to “Effect of the Wall on the Velocity Autocorrelation Function and Long-Time Tail of Brownian Motion”. *J. Phys. Chem. B*, 110(26):63317, 2006.
- [115] K.H. Lundberg, H.R. Miller, and R.L. Trumper. Initial conditions, generalized functions, and the laplace transform troubles at the origin. *IEEE Control Systems Magazine*, 27(1):22–35, February 2007.

- [116] F. L. Yang. A formula for the wall-amplified added mass coefficient for a solid sphere in normal approach to a wall and its application for such motion at low Reynolds number. *Physics of Fluids*, 22(12), 2010.
- [117] Sangjin Ryu and Paul Matsudaira. Unsteady motion, finite Reynolds numbers, and wall effect on *Vorticella convallaria* contribute contraction force greater than the stokes drag. *Biophysical journal*, 98(11):2574–2581, June 2010.
- [118] H. B. Eral, J. M. Oh, D. Van Den Ende, F. Mugele, and M. H G Duits. Anisotropic and hindered diffusion of colloidal particles in a closed cylinder. *Langmuir*, 26(25):16722–16729, 2010.
- [119] Rei Tatsumi and Ryoichi Yamamoto. Velocity relaxation of a particle in a confined compressible fluid. *The Journal of chemical physics*, 138(18):184905, May 2013.
- [120] Katsuhiko Ishii, Toshiaki Iwai, and Hui Xia. Hydrodynamic measurement of Brownian particles at a liquid-solid interface by low-coherence dynamic light scattering. *Optics express*, 18(7):7390–7396, 2010.
- [121] M. a. Plum, J. Rička, H. J. Butt, and W. Steffen. Anisotropic hindered motion close to an interface studied by resonance-enhanced dynamic light scattering. *New Journal of Physics*, 12, 2010.
- [122] Mauricio D. Carbajal-Tinoco, Ricardo Lopez-Fernandez, and José Luis

- Arauz-Lara. Asymmetry in Colloidal Diffusion near a Rigid Wall. *Physical Review Letters*, 99(13):138303, September 2007.
- [123] Peter Huang and Kenneth S. Breuer. Direct measurement of anisotropic near-wall hindered diffusion using total internal reflection velocimetry. *Physical Review E - Statistical, Nonlinear, and Soft Matter Physics*, 76:1–4, 2007.
- [124] Kyu Pak Hyuk. Observation of a colloidal particle dynamics nearby flat wall using oscillating optical tweezers. *Journal of the Korean Physical Society*, 56(31):977, March 2010.
- [125] Sylvia Jeney, Branimir Lukić, Jonas a. Kraus, Thomas Franosch, and László Forró. Anisotropic Memory Effects in Confined Colloidal Diffusion. *Physical Review Letters*, 100(24):240604, June 2008.
- [126] Rongxin Huang, Isaac Chavez, Katja M. Taute, Branimir Lukić, Sylvia Jeney, Mark G. Raizen, and Ernst-Ludwig Florin. Direct observation of the full transition from ballistic to diffusive Brownian motion in a liquid. *Nature Physics*, 7(7):576–580, March 2011.
- [127] Jacob N. Israelachvili. *Intermolecular and Surface Forces*. Elsevier Science, Burlington, 2010.
- [128] Michael A Bevan and Dennis C Prieve. Direct measurement of retarded van der Waals attraction. 1(4):7925–7936, 1999.

- [129] A. Pralle, E. L. Florin, E. H K Stelzer, and J. K H Hörber. Local viscosity probed by photonic force microscopy. *Applied Physics A: Materials Science and Processing*, 66:71–73, 1998.
- [130] Eric Lauga, Willow R DiLuzio, George M Whitesides, and Howard a Stone. Swimming in circles: motion of bacteria near solid boundaries. *Biophysical journal*, 90(2):400–412, 2006.
- [131] Guanglai Li, Lick-Kong Tam, and Jay X Tang. Amplified effect of Brownian motion in bacterial near-surface swimming. *Proceedings of the National Academy of Sciences of the United States of America*, 105(47):18355–18359, November 2008.
- [132] Patrick Oswald. *Rheophysics, the deformation and flow of matter*. Cambridge University Press, Cambridge New York, 2009.
- [133] Erwin Frey and Klaus Kroy. Brownian motion: A paradigm of soft matter and biological physics. *Annalen der Physik (Leipzig)*, 14(1-3):20–50, 2005.
- [134] T. Mason, K. Ganesan, J. van Zanten, D. Wirtz, and S. Kuo. Particle Tracking Microrheology of Complex Fluids. *Physical Review Letters*, 79(17):3282–3285, October 1997.
- [135] Thomas G Mason. Estimating the viscoelastic moduli of complex fluids using the generalized Stokes-Einstein equation, 2000.

- [136] F Cardinaux, L Cipelletti, F Scheffold, and P Schurtenberger. Microrheology of giant-micelle solutions, 2002.
- [137] T a Waigh. Microrheology of complex fluids. *Reports on Progress in Physics*, 68(3):685–742, March 2005.
- [138] Alison Yao, Manlio Tassieri, Miles Padgett, and Jonathan Cooper. Microrheology with optical tweezers. *Lab on a chip*, 9(17):2568–75, September 2009.
- [139] Todd M. Squires and Thomas G. Mason. Fluid Mechanics of Microrheology. *Annual Review of Fluid Mechanics*, 42(1):413–438, January 2010.
- [140] Daryl Preece, Rebecca Warren, R M L Evans, Graham M Gibson, Miles J Padgett, Jonathan M Cooper, and Manlio Tassieri. Optical tweezers: wideband microrheology. *Journal of Optics*, 13(4):044022, April 2011.
- [141] Manlio Tassieri, R M L Evans, Rebecca L Warren, Nicholas J Bailey, and Jonathan M Cooper. Microrheology with optical tweezers: data analysis. *New Journal of Physics*, 14(11):115032, November 2012.
- [142] E Bertseva, D Grebenkov, P Schmidhauser, S Gribkova, S Jeney, and L Forró. Optical trapping microrheology in cultured human cells. *The European physical journal. E, Soft matter*, 35(7):63, July 2012.
- [143] Angelo Pommella, Valentina Preziosi, Sergio Caserta, Jonathan M Cooper, Stefano Guido, and Manlio Tassieri. Using optical tweezers for the

- characterization of polyelectrolyte solutions with very low viscoelasticity. *Langmuir : the ACS journal of surfaces and colloids*, 29(29):9224–30, July 2013.
- [144] Yuriy L. Raikher, Victor V. Rusakov, and Régine Perzynski. Brownian motion in a viscoelastic medium modelled by a Jeffreys fluid. *Soft Matter*, 9(45):10857, 2013.
- [145] Ben Fabry, Geoffrey N. Maksym, James P. Butler, Michael Glogauer, Daniel Navajas, and Jeffrey J. Fredberg. Scaling the microrheology of living cells. *Physical Review Letters*, 87(14):1–4, 2001.
- [146] C. Oelschlaeger, M. Cota Pinto Coelho, and N. Willenbacher. Chain flexibility and dynamics of polysaccharide hyaluronan in entangled solutions: A high frequency rheology and diffusing wave spectroscopy study. *Biomacromolecules*, 14(10):3689–3696, 2013.
- [147] B U Felderhof. Estimating the viscoelastic moduli of complex fluids from observation of Brownian motion of a particle confined to a harmonic trap. *The Journal of chemical physics*, 134(20):204910, May 2011.
- [148] P. Domínguez-García, Frédéric Cardinaux, Elena Bertseva, László Forró, Frank Scheffold, and Sylvia Jeney. Accounting for inertia effects to access the high-frequency microrheology of viscoelastic fluids. *Physical Review E*, 90(6):1–5, 2014.

- [149] H. A. Barnes, J. F. Hutton, and K. Walters. *An introduction to rheology*. Elsevier Science Publishers, Amsterdam, The Netherlands, 1989.
- [150] Yu. L. Raikher and V. V. Rusakov. Theory of Brownian motion in a Jeffreys fluid. *Journal of Experimental and Theoretical Physics*, 111(5):883–889, December 2010.
- [151] B U Felderhof. Estimating the viscoelastic moduli of a complex fluid from observation of Brownian motion. *The Journal of chemical physics*, 131(16):164904, October 2009.
- [152] R. M L Evans, Manlio Tassieri, Dietmar Auhl, and Thomas a. Waigh. Direct conversion of rheological compliance measurements into storage and loss moduli. *Physical Review E - Statistical, Nonlinear, and Soft Matter Physics*, 80(1):8–11, 2009.
- [153] Manlio Tassieri, Graham M. Gibson, R. M L Evans, Alison M. Yao, Rebecca Warren, Miles J. Padgett, and Jonathan M. Cooper. Measuring storage and loss moduli using optical tweezers: Broadband microrheology. *Physical Review E - Statistical, Nonlinear, and Soft Matter Physics*, 81(2):1–5, 2010.
- [154] Pablo Domínguez-García, Flavio M. Mor, László Forró, and Sylvia Jeney. Exploiting the color of Brownian motion for high-frequency microrheology of Newtonian fluids. 8810:881015, September 2013.

- [155] M.-C. Yang. Some Rheological Measurements on Magnetic Iron Oxide Suspensions in Silicone Oil. *Journal of Rheology*, 30(5):1015, 1986.
- [156] WM Kulicke, R Kniewske, and J Klein. Preparation, characterization, solution properties and rheological behaviour of polyacrylamide, 1982.
- [157] Mamdouh T. Ghannam and M. Nabil Esmail. Rheological properties of aqueous polyacrylamide solutions. *Journal of Applied Polymer Science*, 69(8):1587–1597, August 1998.
- [158] John van Zanten and Karl Rufener. Brownian motion in a single relaxation time Maxwell fluid. *Physical Review E*, 62(4):5389–5396, October 2000.
- [159] N. Willenbacher, C. Oelschlaeger, M. Schopferer, P. Fischer, F. Cardinaux, and F. Scheffold. Broad Bandwidth Optical and Mechanical Rheometry of Wormlike Micelle Solutions. *Physical Review Letters*, 99(6):068302, August 2007.
- [160] G. H. Koenderink, M. Atakhorrami, F. C. MacKintosh, and C. F. Schmidt. High-frequency stress relaxation in semiflexible polymer solutions and networks. *Physical Review Letters*, 96(13):1–4, 2006.
- [161] Joris Sprakel, Jasper van der Gucht, and Martien a. Cohen Stuart. Brownian particles in transient polymer networks. *Physical Review E*, 77(6):061502, June 2008.

- [162] Basset Alfred Barnard. *A Treatise on hydrodynamics, Volume II, Chapter 21*. Cambridge University Press, London, 1888.
- [163] A.M. Albano, D. Bedeaux, and P. Mazur. On the motion of a sphere with arbitrary slip in a viscous incompressible fluid. *Physica A: Statistical Mechanics and its Applications*, 80(1):89–97, January 1975.
- [164] A. Erba, R. Podgornik, and R R Netz. Viscous compressible hydrodynamics at planes, spheres and cylinders with finite surface slip. *The European physical journal. E, Soft matter*, 32(2):147–64, June 2010.
- [165] Roman S. Voronov, Dimitrios V. Papavassiliou, and Lloyd L. Lee. Boundary slip and wetting properties of interfaces: Correlation of the contact angle with the slip length. *Journal of Chemical Physics*, 124(20):1–10, 2006.
- [166] Michael A. Day. The no-slip condition of fluid dynamics. *Erkenntnis*, 33(3):285–296, 1990.
- [167] Dimitri Janssen, Randy De Palma, Stijn Verlaak, Paul Heremans, and Wim Dehaen. Static solvent contact angle measurements, surface free energy and wettability determination of various self-assembled monolayers on silicon dioxide. *Thin Solid Films*, 515(4):1433–1438, 2006.
- [168] R. Pit, H. Hervet, and L. Léger. Direct experimental evidence of slip in hexadecane: solid interfaces. *Physical Review Letters*, 85(5):980–983, 2000.

- [169] V S Craig, C Neto, and D R Williams. Shear-dependent boundary slip in an aqueous Newtonian liquid. *Physical review letters*, 87(5):054504, 2001.
- [170] J Baudry and E Charlaix. Experimental Evidence for a Large Slip Effect at a Nonwetting Fluid - Solid Interface. *Langmuir*, (4):5232–5236, 2001.
- [171] Chang Hwan Choi, K. Johan a Westin, and Kenneth S. Breuer. Apparent slip flows in hydrophilic and hydrophobic microchannels. *Physics of Fluids*, 15(10):2897–2902, 2003.
- [172] Elmar Bonaccorso, Hans-Jürgen Butt, and Vincent S J Craig. Surface roughness and hydrodynamic boundary slip of a newtonian fluid in a completely wetting system. *Physical review letters*, 90(14):144501, 2003.
- [173] C. Neto, V. S J Craig, and D. R M Williams. Evidence of shear-dependent boundary slip in newtonian liquids. *European Physical Journal E*, 12(SUPPL. 1):59–62, 2003.
- [174] Christophe Cheikh and Ger Koper. Stick-slip transition at the nanometer scale. *Physical review letters*, 91(15):156102, 2003.
- [175] Pierre Joseph and Patrick Tabeling. Direct measurement of the apparent slip length. *Physical Review E - Statistical, Nonlinear, and Soft Matter Physics*, 71(3):1–4, 2005.
- [176] Hitoshi Ogihara, Jing Xie, Jun Okagaki, and Tetsuo Saji. Simple method for preparing superhydrophobic paper: Spray-deposited hydropho-

- bic silica nanoparticle coatings exhibit high water-repellency and transparency. *Langmuir*, 28(10):4605–4608, 2012.
- [177] Dong Song, Robert J. Daniello, and Jonathan P. Rothstein. Drag reduction using superhydrophobic sanded Teflon surfaces. *Experiments in Fluids*, 55(8), 2014.
- [178] Alexander L. Dubov, Sebastian Schmieschek, Evgeny S. Asmolov, Jens Harting, and Olga I. Vinogradova. Lattice-Boltzmann simulations of the drag force on a sphere approaching a superhydrophobic striped plane. *The Journal of Chemical Physics*, 140(3):034707, 2014.
- [179] M. Chinappi and C. Casciola. Intrinsic slip on hydrophobic self-assembled monolayer coatings. *Physics of Fluids*, 22(4):1–8, 2010.
- [180] B U Felderhof. Spectrum of position fluctuations of a Brownian particle bound in a harmonic trap near a plane wall. *The Journal of chemical physics*, 136(14):144701, April 2012.
- [181] B. U. Felderhof. Hydrodynamic force on a particle oscillating in a viscous fluid near a wall with dynamic partial-slip boundary condition. *Physical Review E*, 85(4):046303, April 2012.
- [182] G. M. Wang, R. Prabhakar, and E. M. Sevick. Hydrodynamic Mobility of an Optically Trapped Colloidal Particle near Fluid-Fluid Interfaces. *Physical Review Letters*, 103(24):248303, December 2009.

- [183] Andrei S Dukhin and Philip J Goetz. Bulk viscosity and compressibility measurement using acoustic spectroscopy. *The Journal of chemical physics*, 130(12):124519, March 2009.
- [184] Diels Jean-Claude and Rudolph Wolfgang. *Ultrashort Laser Pulse Phenomena(Second Edition)*. Academic Press, 2006.
- [185] G. M Wang, E. M Sevick, Emil Mittag, Debra J Searles, and Denis J Evans. Experimental demonstration of violations of the second law of thermodynamics for small systems and short time scales. *Physical Review Letters*, 89(5):50601, July 2002.
- [186] G D’Anna, P Mayor, a Barrat, V Loreto, and Franco Nori. Observing brownian motion in vibration-fluidized granular matter. *Nature*, 424(6951):909–912, 2003.
- [187] A. Imparato, L. Peliti, G. Pesce, G. Rusciano, and A. Sasso. Work and heat probability distribution of an optically driven Brownian particle: Theory and experiments. *Physical Review E - Statistical, Nonlinear, and Soft Matter Physics*, 76(5):1–4, 2007.
- [188] T. Speck, V. Blickle, C. Bechinger, and U. Seifert. Distribution of Entropy Production for a Colloidal Particle in a Nonequilibrium Steady State. 30002, 2007.
- [189] V. Blickle, T. Speck, C. Lutz, U. Seifert, and C. Bechinger. Einstein relation generalized to nonequilibrium. *Physical Review Letters*, 98(21):1–4,

2007.

- [190] Daniel Rings, Romy Schachoff, Markus Selmke, Frank Cichos, and Klaus Kroy. Hot Brownian Motion. *Physical Review Letters*, 105(9):8–11, August 2010.
- [191] Thue B Lindballe, Martin V G Kristensen, Kirstine Berg-Sørensen, Søren R Keiding, and Henrik Stapelfeldt. Pulsed laser manipulation of an optically trapped bead: averaging thermal noise and measuring the pulsed force amplitude. *Optics express*, 21(2):1986–96, January 2013.
- [192] G. Falasco, M. V. Gnann, D. Rings, and K. Kroy. Effective temperatures of hot Brownian motion. 032131:11, 2014.
- [193] Yoshishige Katayama and Ryutaro Terauti. Brownian motion of a single particle under shear flow. *European Journal of Physics*, 17(3):136–140, 1999.
- [194] Hiroshi Orihara and Yoshinori Takikawa. Brownian motion in shear flow: Direct observation of anomalous diffusion. *Physical Review E*, 84(6):1–5, 2011.
- [195] Faeghe Hajizadeh and S Nader S Reihani. Optimized optical trapping of gold nanoparticles. *Optics express*, 18(2):551–9, January 2010.
- [196] Laurent Joly, Samy Merabia, and Jean-Louis Barrat. Effective temperatures of a heated Brownian particle. 50007, 2011.

- [197] D. Chakraborty. Velocity autocorrelation function of a Brownian particle. *The European Physical Journal B*, 83(3):375–380, October 2011.
- [198] B. U. Felderhof. Backtracking of a sphere slowing down in a viscous compressible fluid. *The Journal of chemical physics*, 123(4):044902, July 2005.

Vita

Jianyong Mo was born in Huzhou China on September 28th, 1985, the son of Falin Mo and Yuee Xu. He completed his high school education from Changxing Middle School in 2005. He received the Bachelor of Science degree in Physics from the University of Science and Technology of China in 2009. He entered the graduate school at the University of Texas at Austin in 2009 and joined professor Mark Raizen's group right away. He got married with Juan Li on May 5th, 2013. His daughter, Emily Xinyu Mo, was born on May 11th, 2015.

Permanent address: 40 Huangliangwan
Heping Town, Changxing County
Huzhou, Zhejiang, 313103, China

This dissertation was typeset with L^AT_EX[†] by the author.

[†]L^AT_EX is a document preparation system developed by Leslie Lamport as a special version of Donald Knuth's T_EX Program.